Imaging an Intra-continental Subduction in Central Asia with Teleseismic Receiver Functions

Dissertation zur Erlangung des Doktorgrades im
Fachbereich Geowissenschaften der
Freien Universität Berlin

vorgelegt von
Felix Michael Schneider
Mai 2014

Tag der Disputation: 27. Juni 2014

Mitglieder der Prüfungskommision:

Erstgutachter:	Prof. Dr. Rainer Kind	(FU Berlin, GFZ-Potsdam)
Zweitgutachter:	Prof. Dr. Frederik Tilmann	(FU Berlin, GFZ-Potsdam)
Kommisionsvorsitz:	Prof. Dr. Serge A. Shapiro	(FU Berlin)
	apl. Prof. Edward Sobel, PhD	(Uni Potsdam)
	Dr. Xiaohui Yuan	(GFZ-Potsdam)

Abstract

Beneath the Pamir and Hindu Kush mountains an earthquake zone is observed in 80 to 300 km depth. It resembles in form and intensity the intermediate depth seismicity in subduction zones, where lithosphere is recycled in the Earth's mantle. The fundamental tectonic concept of subduction is well established for convergent margins including an oceanic plate. The Pamir, however, is situated in an intra-continental setting and is formed during a continent-continent collision. This thesis aims to contribute to the investigation of the active tectonic process underlying the local occurrence of the seismicity in upper mantle depths. The field experiment for this study was performed in the framework of the multidisciplinary TIPAGE project from 2008 to 2010 and included large parts of the Pamir, the adjacent Tajik Depression and the Southern Tien Shan. The receiver function technique was applied to detect and locate seismic discontinuities in the subsurface in order to perform seismic imaging. The results clearly attest to an intra-continental subduction. Beneath the Pamir, the subducting plate is of Eurasian provenance. A southerly dipping 10 to 15 km thick low velocity zone could be resolved along a north-south profile in the eastern Pamir framing the earthquake zone in the upper mantle. This low velocity zone appears to be connected to the lower crust north of the seismic zone indicating subduction of crustal material in north to south direction. West of this north-south profile the zone of intermediate depth seismicity describes an arc changing its strike from east-west beneath the eastern Pamir to north-south beneath the western Pamir. Thereby the dipping direction of the slab changes from due south to due east. The geometry of this slab is confirmed by various receiver function cross sections. Towards western direction the subducted slab is connected to the crust of the Tajik Depression, indicating that the slab is the western extension of the Tajik Depression plate. Since the crustal thickness of the Tajik Depression is determined to at least 40 km, a continental composition for the crust of the Tajik Depression is inferred even though its underlying mantle lithosphere appears to be thin. The crustal thickness is mapped for the whole region. The resulting Moho map shows a 65 to 75 km thick crust in the Pamir and a 40 to 45 km thick crust in the surrounding basins. The arcuate subduction of the Tajik Depression plate and its eastern extension is reflected by characteristic Moho depth anomalies along the arc.

Zusammenfassung

Unterhalb der Gebirgsformationen des Pamir und des Hindukush wird in einer Tiefe von 80 bis 300 km eine Erdbebenzone beobachtet. Diese gleicht in Form und Intensität den mitteltiefen seismisch aktiven Zonen von Subduktionszonen, bei denen Lithosphäre in den Erdmantel abtaucht. Das für die Plattentektonik grundlegende Konzept der Subduktion ist sicher bestätigt für ozeanische Lithosphäre. Der Pamir befindet sich hingegen in einer kontinentalen Kollisionszone. Die vorliegende Arbeit stellt einen Beitrag zur Untersuchung des aktiven tektonischen Prozesses dar, der für das Auftreten der mitteltiefen Erdbeben in dieser Region verantwortlich ist. Für diese Untersuchung wurde in den Jahren von 2008 bis 2010 im Rahmen des TIPAGE-Projekts eine Messkampagne in weiten Teilen des Pamir, des benachbarten Tadschikischen Beckens und des Südlichen Tien Shans durchgeführt. Die Methode der Receiver Funktionen, die Grenzflächen im Untergrund lokalisiert, wurde zur seismischen Bildgebung verwendet. Die Ergebnisse zeigen deutlich, dass eine innerkontinentale Subduktionszone vorliegt. Die unterhalb des Pamir subduzierte Platte ist eurasischer Herkunft. Entlang eines in Nord-Süd Richtung verlaufenden Messprofils konnte eine in südliche Richtung einfallende, 10 bis 15 km mächtige Zone verringerter seismischer Geschwindigkeit detektiert werden, die die Erdbebenzone im oberen Mantel umgibt. Diese Niedriggeschwindigkeitszone ist mit der unteren Kruste nördlich der seismisch aktiven Zone verbunden, was auf von Norden nach Süden subduziertes krustales Material schließen lässt. Westlich des Nord-Süd Messprofils beschreibt die Erdbebenzone einen Bogen, mit einer sich von Ost-West nach Nord-Süd ändernden Streichrichtung. Die Einfallsrichtung der Seismizitätszone ändert sich entlang des Bogens entsprechend von Süd nach Ost. Die Geometrie der subduzierenden Platte konnte mit der Methode der Receiver Funktionen entlang zahlreicher Querschnitte bestätigt werden. In westlicher Richtung ist die subduzierte Kruste mit dem Tadschikischen Becken verbunden. Dies lässt darauf schließen, dass es sich bei der subduzierten Platte um den östlichen Ausläufer des Tadschikischen Beckens handelt. Da die Krustenmächtigkeit im Tadschikischen Becken ausschließlich Werte von über 40 km zeigt, wird eine kontinentale Krustenzusammensetzung angenommen, auch wenn der lithosphärische Mantel niedrige Mächtigkeit aufweist. Die Krustenmächtigkeit wurde für die gesamte Region kartiert. Im Pamir wird eine Krustenmächtigkeit von 65 bis 75 km bestimmt, wobei in den umgebenden Becken Krustendicken von

40 bis 45 km auftreten. Die bogenförmige Subduktionszone spiegelt sich in der Krustenmächtigkeitsverteilung durch charakteristische Anomalien entlang des Subduktionsbogens wieder.

Contents

1. Introduction

The continental collision zone of India and Eurasia is the area on Earth where, since Cenozoic times, the highest mountains are rising and the Earth's crust is deforming most. This collision is ongoing since roughly 50 million years. Both opponents in the collision are different in lithospheric strength. Before India collided, the lithosphere of the Eurasian southern margin had been already weakened throughout a long history of oceanic subduction and accretion of micro plates. In contrast India is a relatively rigid block. Indian lithosphere underthrusts large parts of the Eurasian crust beneath Tibet, which has been observed by different seismic methods as body wave tomography (Tilmann et al., 2003; Li et al., 2008), surface wave tomography (Priestley et al., 2006; Pandey, 2013) or receiver functions (Nábělek et al., 2009; Kind and Yuan, 2010). The upper crust of the Indian plate is thereby scraped off and forms the Himalaya mountain range. Deforming and translating forces are transferred to the Eurasian crust, resulting in distributed internal shortening in a large zone north of the collision front.

The Eurasian internal crustal shortening involves various mechanisms, such as lithospheric thickening, lateral escape or lithospheric stacking. Thickening and lateral escape can both occur in ductile and brittle lithospheric state, in pure shear and simple shear manner, along transfer faults, by crustal flow or through uplifting and erosion. A further shortening mechanism is recycling of crustal material into the mantle. For this, different scenarios are known such as delamination and subduction. Continental crust is less dense than the mantle, since it has differentiated from oceanic crust and mantle material over many eons and accumulated lighter material. Thus in most cases the continental crust does not subduct and stays up during collision.

However, exhumation of ultra-high pressure metamorphic rocks testifies that continental crust is capable to subduct to great depth despite of its buoyancy (Chopin, 1984; Hacker et al., 2006; Okay et al., 1989). One possible scenario for subduction is the transformation of lower crust: Due to crustal thickening the lower crust is subject to high pressures that causes its eclogitization, which reverses the buoyancy and thus may drive the subduction (Molnar and Gray, 1979; Krystopowicz and Currie, 2013). For the collision of India and Eurasia seismic observations in Tibet indicate on the Indian side underplating of lower continental crust (e.g. Nábělek et al. (2009)) combined with lower crustal eclogitization

(Hetényi et al., 2007), and on the Eurasian side subduction of continental lithosphere (e.g.Kind et al. (2002); Kumar et al. (2005)). However, there has been no direct observation of subducting continental crust in the Indian-Eurasian collision zone so far.

In the Pamir region, which is situated on the western syntaxis of the collision zone, the total amount of crustal shortening that occurred during the Cenozoic is higher than in Tibet, since a similar amount of total convergence has been accommodated over a much smaller distance. Considering the relation of present to pre-Cenozoic crustal thicknesses, these extremely high amounts of crustal shortening in the Pamir yield realistic scenarios that require some sort of vertical crustal excess (Schmidt et al., 2011). Thus, the Pamir is seen to be a possible candidate where subduction of continental crust may occur (Burtman and Molnar, 1993). This assumption is mainly based on the observation of vigorous intermediate-depth seismicity in 70 to 250 km depth, which is very uncommon in intra-continental settings. Moreover, findings of crustal xenoliths of clearly Eurasian provenance in the south-eastern Pamir testify that crustal rocks have resided at least at 90 km depth in this region (Hacker et al., 2005).

To investigate this area we performed a seismic experiment, which was embedded in the framework of the multidisciplinary TIPAGE project. From 2008 to 2010 seismological data have been collected to produce images of the subsurface of this region to gain insights in the geometry and characteristics of this possible zone of intra-continental subduction. The latest geophysical investigations from local data in the Pamir were conducted in the 1970s Beloussov et al. (1980). Due to the politically unstable situation in Tajikistan no field campaigns were possible in this region for a long time. The collected data set provides the first modern, digital passive seismic data of this region. For this thesis, the receiver function technique was applied to the data to resolve discontinuities of seismic velocities in the underground. Such discontinuities exist at the base of the crust, plate boundaries, inner-crustal material changes or the mantle transition zone.

This thesis is structured as follows:

First the geological history and present day observations are reviewed and the data set is introduced (Chapter 2 and 3). The next chapter is dedicated to the receiver function (RF) method, that uses P-to-S (P-RF) and S-to-P (S-RF) converted waves from teleseismic sources (Chapter 4). Chapter 5 is gives a large scale overview by presenting and discussing results from various P-RF and S-RF cross sections. In Chapter 6, I focus on the observation of a low velocity zone in the upper mantle that coincides with the intermediate-depth seismicity in this region. This feature is resolved by P-RFs along the North-South profile in the

eastern Pamir. We interpret the P-RF signal as crustal subduction. Various tests and modeling are performed and discussed to ensure the reliability of the observation and to receive some parameters as thickness and velocity-contrast of the subducted crust. In Chapter 7 the average crustal velocity ratio v_p/v_s and the crustal thickness is deduced for the observation area using the slant stacking method of Zhu and Kanamori (2000). The crustal thickness map for the Pamir and the surrounding basins is also independently derived from S-RFs. Both methods as well as forward modeling of P-RFs yield with consistent results. Discussion and further interpretation of the results are given in the concluding Chapter 8.

The results presented in Chapter 6 "Seismic imaging of subducting lower continental crust" have been published in an article of the same title in *Earth and Planetary Science Letters* in August 2013 (Schneider et al., 2013). This includes figures 6.1, 6.2, 6.4, 6.5, 6.6, 6.15 6.16, 6.17 and 6.18 as well as the text paragraphs describing the forward modeling in section 6.5.

2. Geology

2.1. The Pamir - Part of the Indian-Eurasian collisional belt

The Pamir mountains were build through the continental collision of India and Eurasia. In the India-Eurasia collisional belt they form the north-western promontory of the so called "roof of the world", the Tibet-Himalaya orogen.

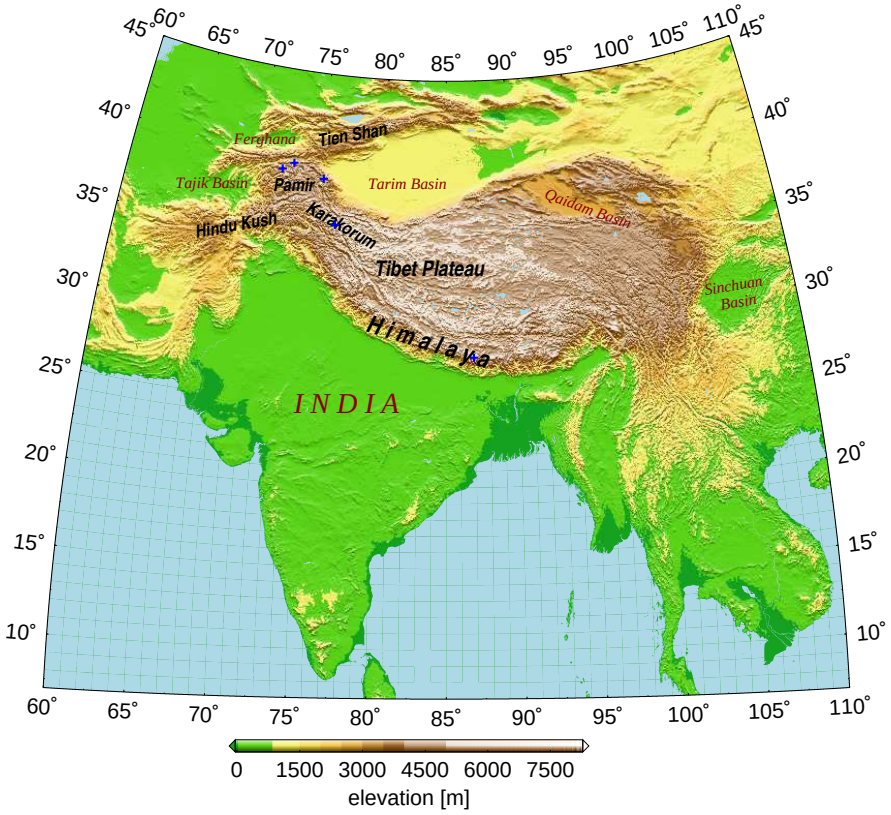

Figure 2.1.: Topographic map, showing the Indian-Asian collision zone.

The continental collision of India and Eurasia resulted in the largest zone of crustal deformation in the world. The area of high elevation originating from this collision includes the Himalaya, the Tibetan Plateau, the Karakorum, the

Pamir, the Hindu Kush and the Tien Shan. Even areas further north, like Mongolia and southern Siberia, are affected and elevated as a result of this "Biggest Crash on Earth" (Kind and Yuan, 2010).

The relative positions of India with respect to Eurasia before and during the collision could be reconstructed from paleomagnetic data (Molnar and Tapponnier, 1975), see figure 2.2. It shows the northward drift of India from 71 Ma to present. A rapid decrease of the relative velocity is seen in the data between 50 and 35 Ma, which is interpreted as evidence for an onset of the India-Asia collision at 55–50 Ma.

In Patriat and Achache (1984) three phases of the Indian drift are identified: In the first phase (70-52 Ma) India was approaching continuously northward to Eurasia with a mean velocity of 15 to 20 cm/yr. In the second phase, lasting from 52 to 36 Ma, Patriat and Achache describe the northward motion of India as "rather erratic", showing several changes in direction and a reduction of the mean northward velocity to less than 10 cm/yr. In a third phase from 36 Ma to present the northward motion became again more regular with a constant convergence rate of about than 5 cm/yr.

Timing of the Indian-Asian collision

The exact dating of the collision is still subject of discussion as well as the shape and northern extend of India before the collision, referred to as "Greater India" (Ali and Aitchison, 2012; van Hinsbergen et al., 2012b).

Estimates on the timing of the collision, that is defined as the closure of Tethys, range between 65 Ma (Ding, 2005) (from obducted oceanic rocks at 65 Ma) to 34 Ma (Ali and Aitchison, 2005) (deduced from the locations of India and Asia, and a limitation to the size of Greater India within Gondwana), while the most authors prefer a collision age of 52-50 Ma (van Hinsbergen et al., 2011).

Van Hinsbergen et al. (2012b) suggest that India underwent major N-S extension after rifting from Gondwana and before the collision with Eurasia. In this scenario, the northern part of India rifted away and formed an Tibetan-Himalayan micro-continent, that collided at around 50 Ma. The "hard" India–Asia collision of the cratonic Indian continental lithosphere occurred in this model later, at around 25–20 Ma.

This suggestion is similar to the approach described by Aitchison et al. (2007). They propose that India first collided with an intraoceanic arc at 55 Ma followed by the continent-continent collision between India and Asia in the Oligocene ($\leq$ 35 Ma).

While Ali and Aitchison argue that the northern extent of India is limited to fit in the composition with Africa, Arabia and Madagascar to Gondwana

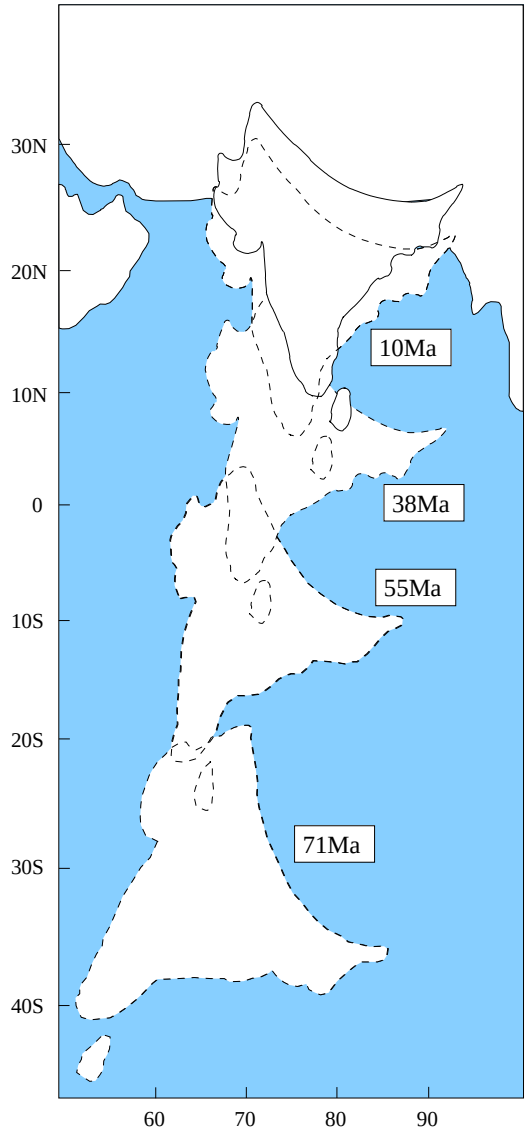

Figure 2.2.: Northward motion of India with respect to Eurasia from 71 Ma to present (redrawn from Molnar and Tapponnier (1975)).

van Hinsbergen et al. believe in a much larger Greater India to explain a collision of India with Asia at 50 Ma together with its position relative to Eurasia.

2.2. Tectonic divisions of Pamir and correlation to Tibet

The Pamir is thought to consist of the same collage of continental terranes as Tibet that have been accreted to the southern border of Eurasia prior to the Indian Eurasian collision (Yin and Harrison, 2000). A simplified model for the pre-collisional history of Tibet is shown in Figure 2.3.

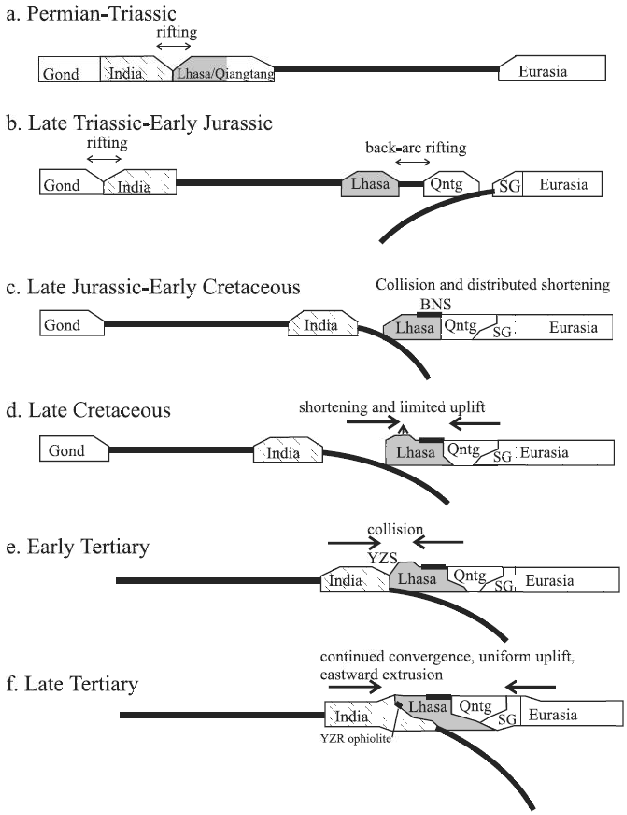

Figure 2.3.: Precollisional history of Tibet from (Haines et al., 2003). YZS: Yarlung Zangbo Suture, BNS: Bangong-Nujiang Suture, SG: Songpan-Ganzi, Gond: Gondwana, Qntg: Qiangtang.

Tibet consists of east-west trending belts that are namely (from north to south) the Kunlun terrane, Songpan-Ganzi, Qiangtang and Lhasa. The Songpan-Ganzi terrane is a flysch complex, whereas Qiangtang and Lhasa originate from Gondwana and have been rifted and drifted towards Asia in the Permians to early

Jurassic.

The belts are separated from each other by suture zones that host oceanic rocks, remnants of the oceanic plates, which have been subducted in between the continental terranes. In Fig. 2.4 A the terranes and the separating sutures are shown. The Kunlun Suture (KS) separates the Kunlun from Songpan-Ganzi terranes, the Jingsha Suture is in between Songpan-Ganzi and Qiangtang terranes and the Bangong-Nujiang Suture separates Qiangtang from Lhasa. Finally, the Indus-Yarlang Suture is the boundary between India and Eurasia.

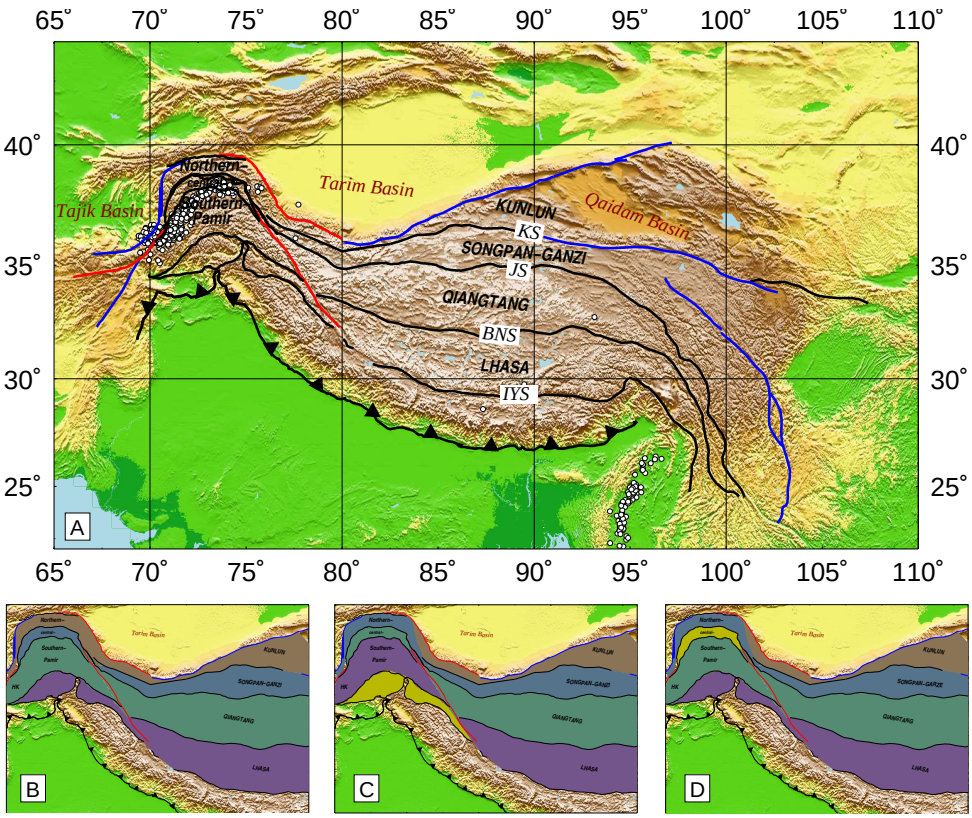

Figure 2.4.: A: Suture zones dividing continental terranes in Pamir and Tibet. Sutures and thrust faults are marked with black lines. Red lines show the position of dextral and blue lines the locations of sinistral strike slip faults, respectively. White dots show the epicenters of earthquakes located in deeper than 100 km depth from a global catalog (Engdahl et al., 1998).; B-D: Possible correlations between Tibet and Pamir landmasses.

The Pamir is also composed of east-west trending tectonic divisions: The Northern Pamir is bounded by the Main Pamir Thrust in the north and the Tanymas Suture in the south. The Central Pamir is situated between the Tanymas Suture and the Rushan Pshart zone. The Southern Pamir lies south of the Rushan

Pshart zone and north of the Shyok Suture. The southernmost part of Eurasia, north of the Indian plate is the Kohistan-Ladakh arc, which lies south of the Shyok Suture and north of the Indus-Yarlung Suture, which is also referred to as Main Mantle Thrust.

There is an ongoing debate on how these tectonic divisions of Pamir and Tibet correlate to each other (Cowgill, 2010; Robinson et al., 2012). In Fig. 2.4 B - D three different scenarios are depicted.

Cowgill introduces in his publication two correlation scenarios referring to the models of the corresponding authors:

- In scenario 1 the Northern Pamir is correlated to Kunlun terrane, the Central Pamir to Songpan-Ganzi, the Southern Pamir to Qiangtang and Kohistan Ladakh Arc to Lhasa. This correlation scenario refers to Burtman and Molnar (1993), Searle (1996) and Yin and Harrison (2000).
- In scenario 2 the correlations are shifted by one terrane with respect to scenario 1: The northern Pamir translates into the Songpan-Ganzi, the Central Pamir translates into Qiangtang and the Southern Pamir into Lhasa. This correlation scenario refers to Schwab et al. (2004) and Lacassin et al. (2004).

Scenario 2 requires larger magnitudes of relative displacement than scenario 1. Furthermore the Kunlun Terrane in Tibet and the Kohistan-Ladakh arc on the Pamir side remain without counterpart in the Pamir and Tibet, respectively.

A third scenario has been proposed by Robinson et al. (2012):

- In scenario 3 the Central Pamir is a separate terrane without counterpart in Tibet. The northern Pamir translates into Songpan-Ganzi as in scenario 2, whereas the Southern Pamir correlates to Qiangtang and Kohistan Ladakh translates into Lhasa as in scenario 1.

2.3. Northward displacement of Pamir with respect to Tibet

Through the collision of India and Eurasia the shape of the sutures have been strongly deformed. The correlation of the Pamir and Tibetan belts and sutures indicates that structures in the Pamir were translated northward by around 300 km with respect to Tibet. Thereby the crust connecting the Tajik and Tarim basins disappeared (Burtman and Molnar, 1993; Robinson et al., 2004) leading to the hypothesis that the Eurasian continental lithosphere is subducted along the Pamir's deformation front, which is today formed by the Main Pamir Thrust (MPT) (Burtman and Molnar, 1993; Hamburger et al., 1992; Sobel et al., 2013).

At its eastern and western flanks the northward motion of the Pamir is accommodated by thrust and strike slip faults. At the western flank the Darvas Fault

is thought to accommodate left-lateral strike slip displacement (Abers et al., 1988) or is described as thrust fold (Thomas et al., 1993), while at the eastern flank, right-lateral displacement is accomodated by the Karakorum Fault and the Kashgar Yensh Transfer System (KYTS) (Cowgill, 2010; Sobel et al., 2011).

Cowgill (2010) concludes from geological evidences that the northward motion of the Pamir can be described as a combination of radial thrusting with a strike slip component at the Darvaz Fault and dextral-slip transfer faulting at the KYTS marking the western flank and eastern flanks of the Pamir, respectively, see Fig 2.5.

The northward motion of the Pamir with respect to stable Eurasia has resulted in the closure of the Tajik-Yarkand Basin. The Alai Valley, which separates the Pamir and the Tien Shan, forms the last remnant of the Tajik-Yarkand sedimentary basin that used to link the Tarim Basin in the East with the Tajik Depression in the West (Strecker et al., 2003; Burtman and Molnar, 1993; Coutand et al., 2002).

2.4. Present day surface deformation

By geodetic measurements using Global Positioning System (GPS), the present day deformation is observed at the earth surface. Figure 2.6 shows a compilation of the obtained velocity vectors from Zubovich et al. (2010) and Ischuk et al. (2013). Further campaigns are described in Reigber et al. (2001); Yang et al. (2008); Abdrakhmatov et al. (1996); Mohadjer et al. (2010).

The GPS arrows show a decrease in velocity by at least 10 and possibly 15 mm/yr (Zubovich et al., 2010) at the Main Pamir Thrust. While in the eastern Pamir the highest rate of shortening is observed in north-south direction, towards the north-western edge, at the transition between Darvaz Fault and Main Pamir Thrust, the principle direction of motion and shortening at the surface is in SSE to NNW direction. Supposing that this shortening rate at the MPT is caused by overthrusting of the Pamir and intra-continental subduction, this rate leads to an inferred length of the subducted slab of 250 - 375 km since 25 Ma, which is the approximate time of the onset of deformation in this region (Thomas et al., 1993; Sobel et al., 2013).

As in the geological records, on the eastern and western edges of the Pamir the velocity field shows an asymmetric behavior. In the western Pamir a counter-clockwise rotation of velocity vectors is evident. This confirms the kinematic model introduced by Cowgill (2010), (see Fig. 2.5). The average northward components of the Pamir and the Tajik Depression show a difference of 10 ± 1 mm/yr, which may be located at the sinistral Darvaz Fault (Ischuk et al., 2013). In contrast, at the eastern flank no dextral shear is observed between Tarim and Pamir,

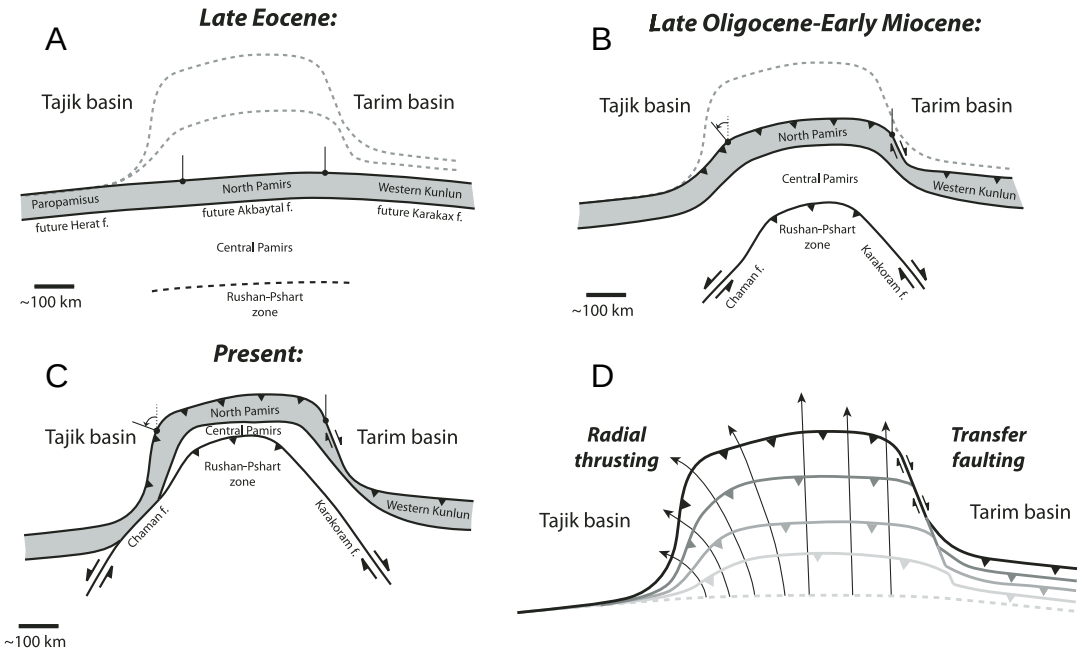

Figure 2.5.: Evolution of the Pamir. A-C: Different stages of northward motion from A: late Eocene (∼30 Ma), B: late Oligocene/ early Miocene (∼23 Ma), C: situation today. Through the northward motion of Pamir the basin area connecting Tajik and Tarim basins is overthrusted. In Miocene or later times, the western margin experiences counter clockwise rotation as indicated by the marks and observed in rock records by Thomas et al. (1994). D: Kinematic model of asymmetric deformation: at the western margin northward motion is accomodated by transfer faulting. (Figure modified from Cowgill (2010)).

whereas the eastern margin shows from geological mapping offsets of at least 200 km since 20 Ma at the transpressional MPT-Kumtag oblique thrust fault system (Sobel and Dumitru, 1997) later referred to as KYTS (Cowgill, 2010). This means, that the relative motion between Pamir and Tarim has, in geological time-scales, stopped recently. Also it appears that thrusting in this region has stopped. Nowadays Tarim and Pamir move northwards with the same velocity and show divergence in east-west direction of 5±1 mm.
While the Pamir does not show much internal north-south shortening, in east-west direction a 5-10 mm/yr extension occurs within the Pamir. The Tajik Depression accommodates a comparable amount of east-west shortening (Ischuk et al., 2013) manifested in the Vakhsh fold and thrust belt (Leith and Alvarez, 1985).

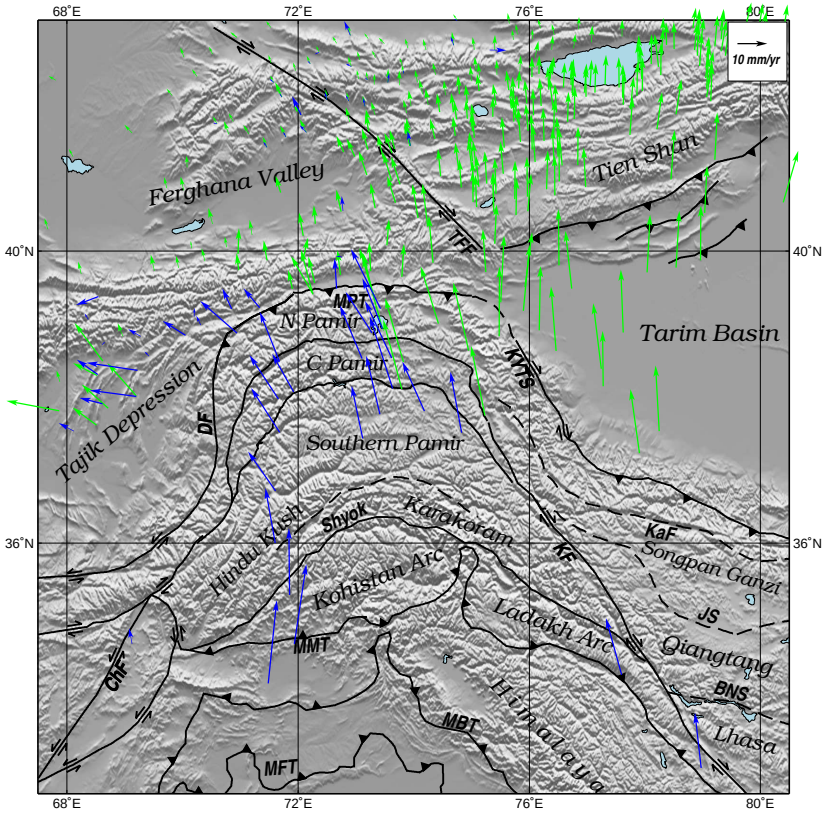

Figure 2.6.: Map showing tectonic divisions of the Pamir and its surrounding and GPS velocities (green arrows from Zubovich et al. (2010), blue arrows from Ischuk et al. (2013)). Sutures and Faults: BNS: Bangong-Nujiang Suture, ChF: Chaman Fault, DF: Darvas Fault, HeF: Herat Fault, JS: Jinsha Suture, KaF: Karakax Fault, KF: Karakorum Fault, KYTS: Kashgar-Yecheng Transfer System, MBT: Main Boundary Thrust, MFT: Main Frontal Thrust, MMT: Main Mantle Thrust, MPT: Main Pamir Thrust, TFF: Talas-Ferghana Fault. Geological information were provided from Sippl (2012).

2.5. Intermediate depth seismicity

The Pamir-Hindu Kush region hosts a zone of intermediate depth seismicity of depths down to 300 km (Sippl et al., 2013b). Usually earthquakes at intermediate depths occur in regions where oceanic subduction takes place for at least 10 Ma (Pegler and Das, 1998). In contrast, the intermediate depth seismicity in the Pamir-Hindu Kush can not easily be linked to oceanic plate subduction, since it is situated in a intra-continental setting. The occurrence of intermediate depth earthquakes in such an environment is quite unique, and particularly, it is an outstanding feature within the Indian-Asian collision zone. In Fig. 2.4 A the earthquake epicenters from depths between 100 and 300 km depth are plotted, which are listed in the global earthquake catalog compiled by Engdahl et al. (1998). Beneath Tibet only a few single earthquakes are observed below 100 km. Only at the syntaxis of the Indian indenter earthquake zones in this depth range are observed. While in the south-eastern zone the intermediate depth seismicity is attributed to subducting oceanic lithosphere confirmed by active volcanism (Searle et al., 2007), the Pamir is located far away from any oceanic plate. However, models exist also for the Pamir that attribute the Pamir seismic zone to an remnant and far displaced oceanic slab (Pegler and Das, 1998) or to subduction of a remnant ocean basin (Chatelain et al., 1980).

In map view, this intermediate depth seismic zone forms a narrow S-shaped band of approximately 450 km length from the Hindu Kush in northeastern Afghanistan to the eastern Pamir. The hypocenters of these mantle earthquakes form two separated Wadati-Benioff zones, one beneath the Pamir and one beneath the Hindu Kush (Burtman and Molnar, 1993; Fan et al., 1994; Negredo et al., 2007; Pegler and Das, 1998). N-S oriented cross sections reveal opposite dips for both zones. High resolution earthquake locations from the TIPAGE deployment, resolve the seismicity in the Pamir as a curviplanar arc dipping to the south in the eastern Pamir and bending to an eastward dipping direction beneath the south-western Pamir. The resulting geometry of the intermediate-depth earthquake zone beneath the Pamir and Hindu Kush is described by Sippl et al. (2013b). His results for the Pamir are compiled in Fig. 2.7. Fig. 2.7 A shows the map view of the earthquake hypocenters and the positions of the five cross sections shown in the Fig. 2.7 B. The locations of the cross sections were chosen perpendicular to the strike of the seismic zone. The deepest earthquakes of the Pamir arc are observed in 240 km depth at its south-western termination. Here, the seismic zone has the steepest dip angle of 90°. In the depth range 80-150 km the dip angle is with around 50° approximately the same for all cross sections. At the western termination, the earthquake zone is dipping clearly due east rather than due south. Following the arc towards north eastern direction, the dipping direction changes from eastwards to southwards. However at the eastern termination the earthquake zone is limited to the upper

150 km. The 3D geometry of the Pamir seismic zone is sketched in Fig. 2.7 C. The seismic zone beneath the Hindu Kush (not shown here) appears to be separated from the Pamir zone. It is a more complex structure, that is less smooth compared to the Pamir zone. It strikes roughly in east-west direction. The inclination angle is very steep and dipping direction is north to north-west.

2.6. Proposed models

To explain the observation of different dipping directions for the intermediate depth seismic zone beneath the Hindu-Kush and the Pamir a variety of models had been proposed. Following Pegler and Das (1998), they can be divided in two groups of models, those models that imply that the intermediate-depth seismicity beneath the Pamir have a different origin from that beneath the Hindu Kush (two-slab models) and those models that propose that the intermediate-depth seismicity beneath the Pamir and Hindu Kush have a common origin, namely a contorted slab (one slab models).

One slab models

One slab models of a single, contorted slab were proposed by Billington et al. (1977), Pegler and Das (1998) and Pavlis and Das (2000). All of these authors promote the idea, that oceanic lithosphere is responsible for the intermediate depth earthquakes, that has been subducted northwards and was then contorted during the continental collision. While the model of Pegler and Das (1998) (shown in Fig. 2.8 d) explain the contortion by the right lateral motion along the Karakorum Fault at the eastern flank of the Pamir, Pavlis and Das (2000) propose that the zone of intermediate depth seismicity marks the northern boundary of the Indian indenter that pushes ahead a decoupled and neutrally buoyant composition of oceanic and continental crust (shown in Fig. 2.8 c). The contortion towards the eastern Pamir is explained by differential mantle flow induced by the underplating of Indian mantle lithosphere.

Two slab models

Two-slab models are proposed by Chatelain et al. (1980), Roecker (1982), Burtman and Molnar (1993), Fan et al. (1994) and Negredo et al. (2007). While Chatelain et al. (1980) also proposed subduction of oceanic crust postulating the existence of an remnant ocean basin subducted southwards beneath the Pamir, Roecker (1982) and Burtman and Molnar (1993) conclude from tomographic and other geophysical observations that continental crust might be subducted beneath the Hindu Kush and Pamir, respectively. The conceptual model of

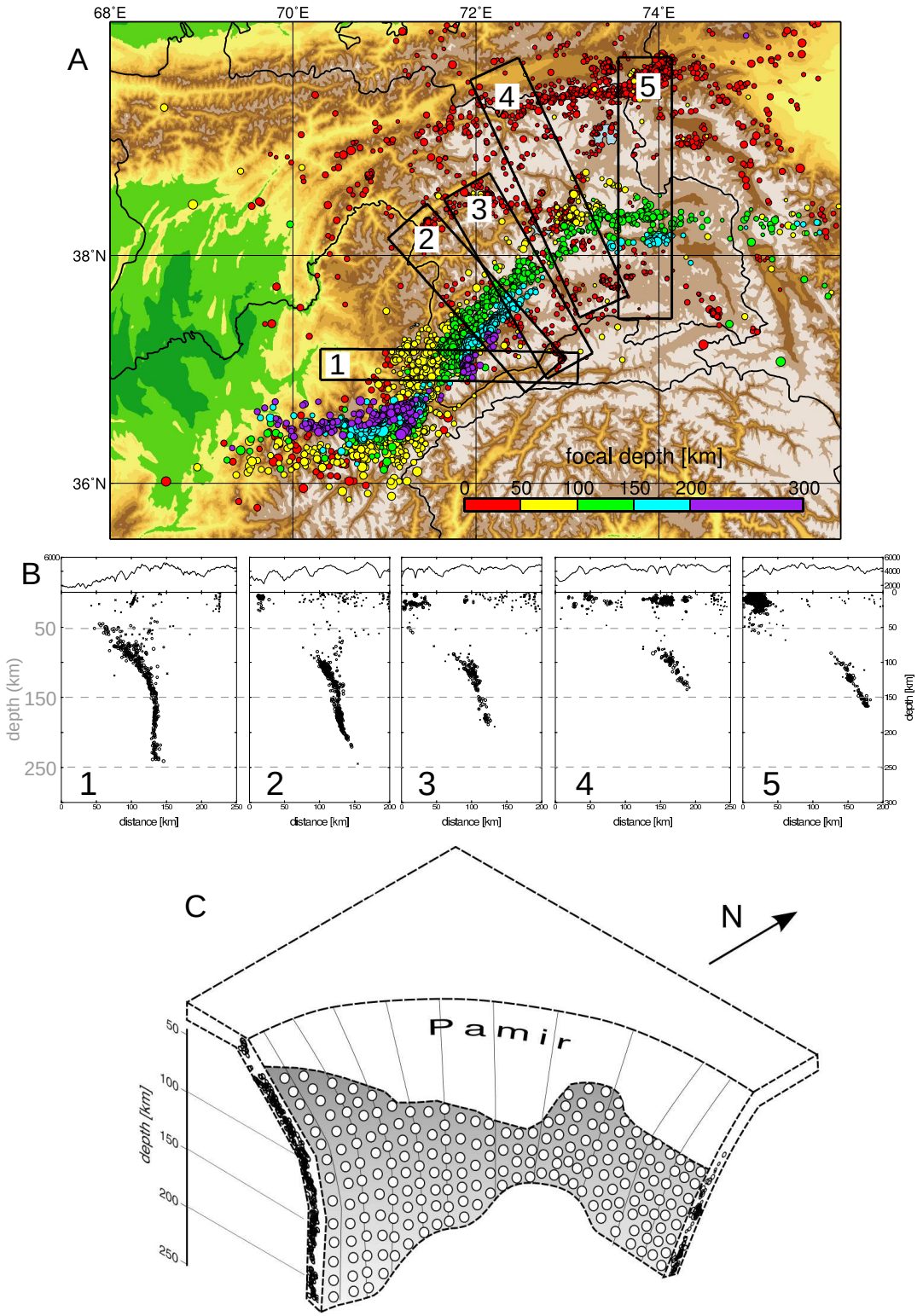

Figure 2.7.: Intermediate depth seismicity as located from the TIPAGE dataset by Sippl et al. (2013b). The map in the upper figure shows the positions of the cross sections. The middle panel shows cross sections and the lower panel shows a schematic model of the zone of intermediate depth seismicity inferred from the locations.

two opposing subducting slabs drawn by Burtman and Molnar (1993) is shown in Fig. 2.8 a. Fan et al. (1994) came up with the idea that the Indian indenter and the Eurasian slab may collide in the upper mantle beneath the Pamir. Negredo et al. (2007) show in their geodynamic model a curviplanar arc for the Eurasian slab and a north dipping Hindu-Kush (see Fig. 2.8 b), which resembles at least for the Pamir the observations of the geometry of the seismicity as detected by Sippl et al. (2013b).

The geodynamic models proposed within the publications that resulted from the TIPAGE project (Sippl et al., 2013b,a; Schneider et al., 2013) promote such a curviplanar arc configuration for the subduction beneath the Pamir, which is inferred from the highly resolved geometry of the seismic zone (Sippl et al., 2013b), earthquake tomography (Sippl et al., 2013a) and receiver functions (Schneider et. al, 2013; and this thesis). Since the Hindu Kush is located outside of the TIPAGE deployment a unequivocal model for the Hindu Kush is not provided. However, since the previously proposed one slab models assume a originally northward subduction scenario those models can be excluded by our observations.

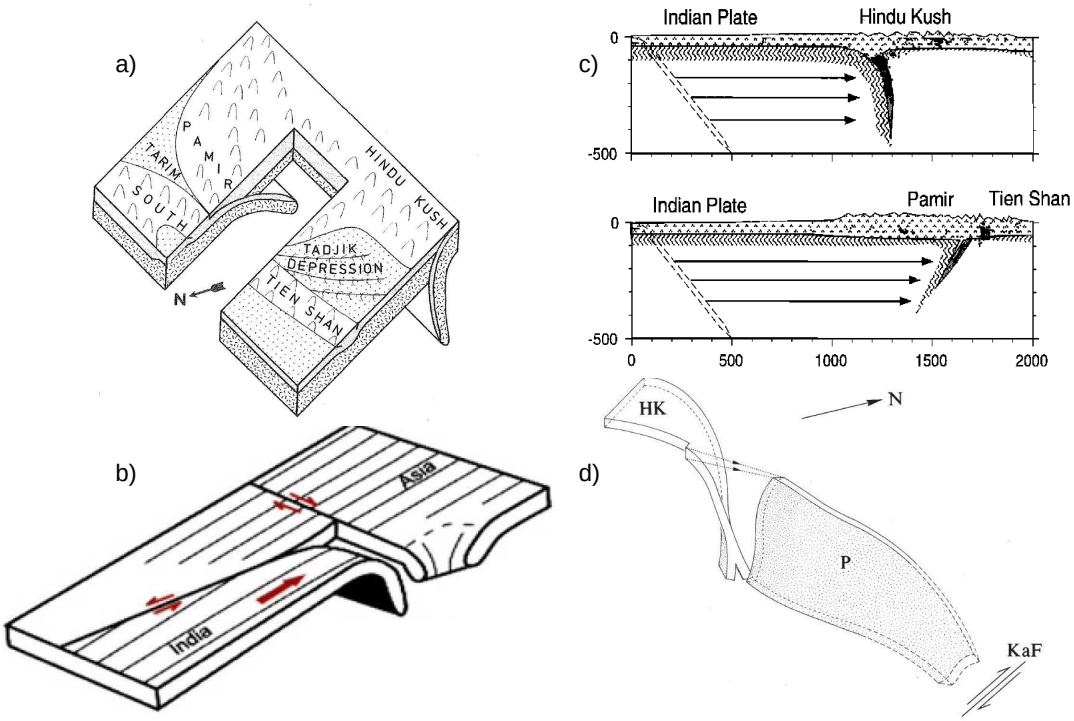

Figure 2.8.: Conceptual tectonic models proposed for the Pamir-Hindu Kush region. The two slab models shown here are proposed by Burtman and Molnar (1993) (a) and Negredo et al. (2007) (b). One slab models have been proposed by Pavlis and Das (2000) (c) and Pegler and Das (1998) (d). In model c) a remnant neutrally buoyant oceanic slab has been displaced northward and contorted by differential mantle flow, whereas in model d) the slab is contorted by right-lateral motion along the Karakorum Fault (KaF).

3. Dataset

A station map with the locations of all seimic stations used within this study is shown in Fig. 3.1. Data collection (GIPP stations) was done in cooporation with local geoscientific partners from Tajikistan (Geological Institute, Tajik Academy of Sciences) and Kirgistan (Central-Asian Institute of Applied Geosciences). The data set was complemented with data from a Chinese deployment and from permanent stations in Tajikistan.

TIPAGE deployment

The data from the TIPAGE forming the heart of the data that are used in this thesis. They were collected from 2008 to 2010. Within the framework of the multidisciplinary Tien Shan Pamir Geodynamic program (TIPAGE) we were running a temporary network of 32 broadband and 8 short period seismic stations across the Pamir. Thereby two different network configurations have been realized.

In the first year 24 stations (P01-P24) were set up in the eastern Pamir forming a 350 km long north-south profile, with a station spacing of approximately 15 km. This network geometry was designed mainly for receiver function processing. The profile crosses the zone of intermediate depth earthquakes, all major sutur zones of the Pamir, the Main Pamir thrust, the Alay Valley and the Southern Tien Shan. Regarding to this geological features it is oriented almost perpendicular to their strikes. In order to be able to use the network in this configuration also for local earthquake locations and tomography, 16 further stations were deployed distributed over the whole investigation area.

In the second year we rearranged the deployment in order to get an equally distributed network with a station spacing of approximately 40 km. The second year geometry was chosen to enhance the resolution of methods that need distributed stations such as tomography and earthquake location.

Further data

The dataset was extended with data from two further field campains conducted by groups of the GFZ. First, data from a temporary network in the Ferghana Valley in Kyrgyzstan, which ran for one year from 2009 to 2010 (Haberland et al.,

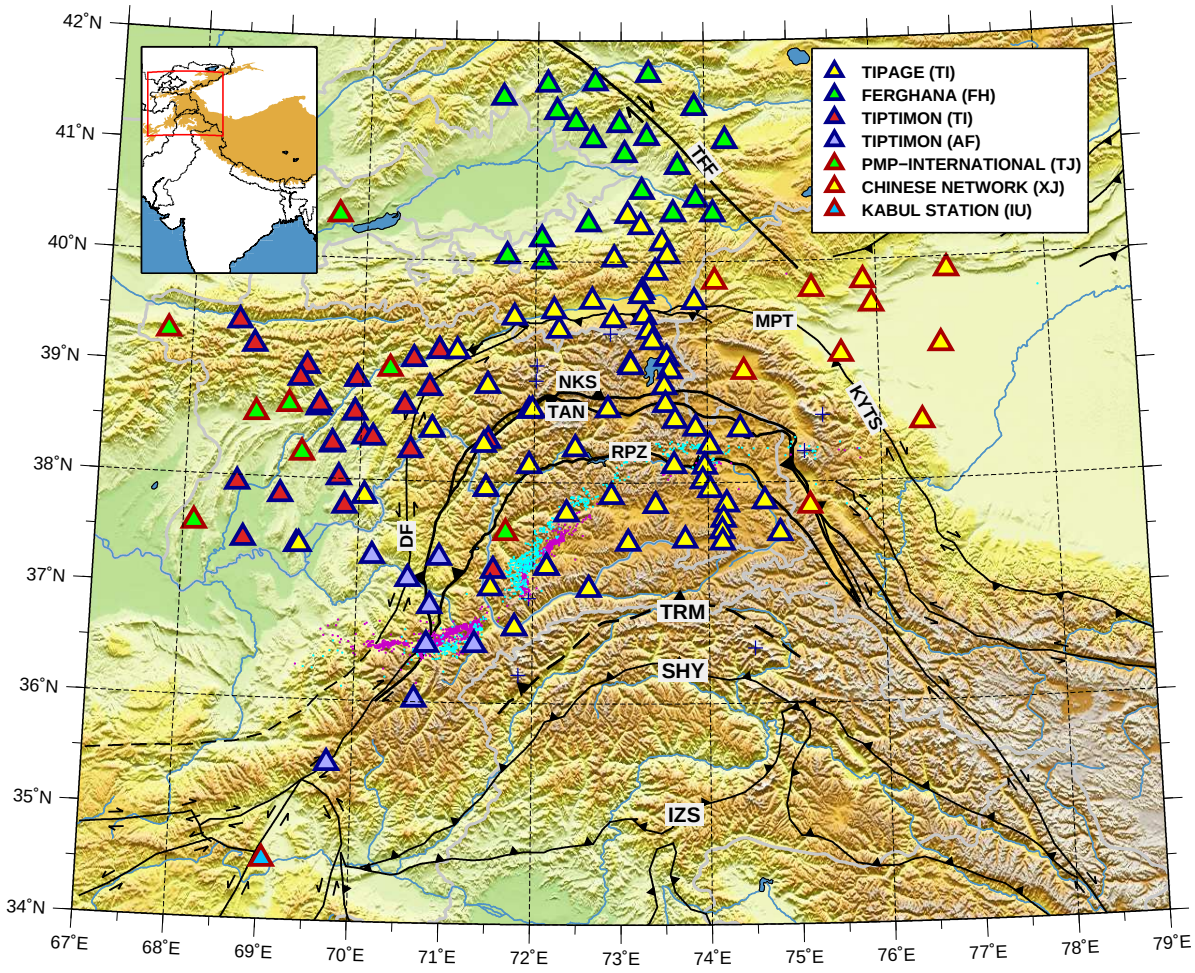

Figure 3.1.: Map showing the geological features and locations of stations used. Blue triangles are stations deployed by the GFZ provided by the Geophysical Instrument Pool Potsdam (GIPP). Red triangles show locations of stations from other networks. Sutures and faults marked in the map are (from north to south): Talas Fergana Fault (TFF), Main Pamir Thrust (MPT), Northern Pamir/Kunlun Suture (NKS), Tanymas Suture (TAN), Kashgar-Yensh Transfer System (KYTS), Rushan Pshart Zone (RPZ), Darvaz Fault (DF), Tirich Mir Zone (TRM), Shyok Suture (SHY) and Indus-Zangbo Suture (IZS). Cyan and purple dots are the earthquake hypocenters in 100-150 km and 150-300 km depth ranges from Sippl et al. (2013b). Inset map shows the Indian-Eurasian collision zone. Altitudes exceeding 3000 m are highlighted in brown, including Tibet, Himalaya, Pamir and Tien Shan.

2011) were added. Recently a new data set is collected in the framework of the TIPTIMON project (Kufner et al., 2013). The first year of data from this experiment have also been processed and included in the analysis. These two dataset complement the TIPAGE data towards the basin areas west and north of the Pamir.

Furthermore, data from permanent stations in Tajikistan have been provided by the seismological survey of Tajikistan (PMP international) that were already included in the design of the TIPAGE deployment. Further data from a Chinese network in the Chinese Pamir and the Tarim basin (XJ) complement the dataset in the eastern neighborhood of the Pamir.

A list of all stations with coordinates, instrument types and network codes is given in tables C.1 and C.2 in Appendix C.

4. Receiver function method

To investigate the upper mantle and cross crustal structure in the Pamir, we use the receiver function method as it is described in Kind et al. (2012).

With help of receiver functions (RFs) discontinuities in seismic velocities can be imaged. To identify the seismic discontinuities the RF method makes use of seismic wave signals that are generated at seismic discontinuities through conversion of seismic wave from one wave type to another. We use seismic waves originating from the teleseismic regime (30°-95° epicentral distance), which allow for the far-field assumption of plane wave propagation and do not show further waveform complication from the core mantle boundary (see Fig. 4.1).

A RF is a time series that is transformed from the original seismic traces. They are defined in such a way that a positive amplitude in a RF represents a Moho-like velocity contrast in the Earth. That means, that a layer with a slower seismic velocities is located above a layer with a faster velocity. This situation is given at the crust mantle boundary, where the crust ($v_s \approx 3.75\ km/s$) is situated on top of the upper mantle ($v_s \approx 4.5\ km/s$). A negative amplitude in the receiver function is produced in case of the opposite situation, where slower seismic velocity is located above a faster one, separated by a discontinuity. This situation is given for example at the lithosphere asthenosphere boundary (LAB), where a reduction of seismic velocity is observed in the asthenosphere.

One advantage of analyzing earthquakes from the teleseismic regime is that the waves reach the investigation area from below and thus the points where conversion of P-to-S or S-to-P waves occur (piercing points) are close to the receiver. RFs can be constructed from P or S wave types as leading mother phase and are called herein P-RF and S-RF, respectively. For P-RFs the entire teleseismic regime 30°-90° is used (see Fig. 5.1(a) in section 5.1.1), while for S-RFs the useful regime is further restricted to 55°-85° (Fig. 5.5(a) in section 5.2.1).

The arrival times of the different wave types (phases) in dependence of the epicentral distance is displayed in Fig. 4.2. Besides the main phases also the converted Ps and Sp and $SKSp$ phases are marked originating from the crust mantle boundary at 68 km depth, which was chosen apply for the Pamir. The windows used for receiver function analysis are marked. Since the direct P wave is the fastest wave, the coda of P which is used for P-RFs is unperturbed over a wide distance range. In contrast, the precursor range of S, used for S-RF is

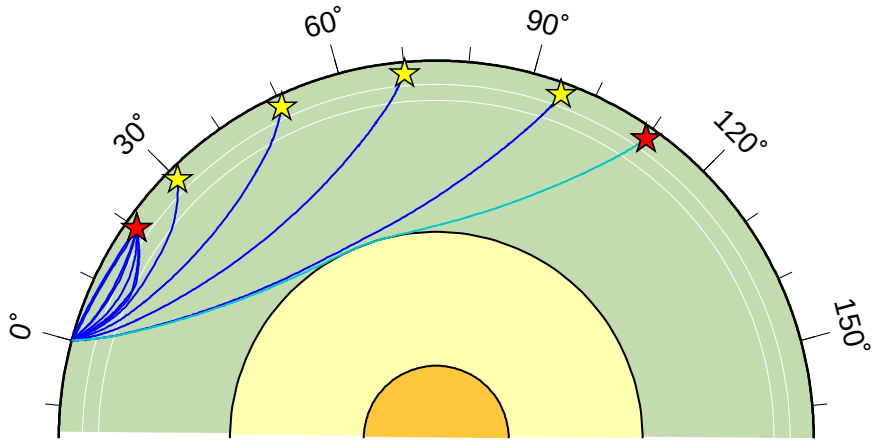

Figure 4.1.: Ray paths (blue lines) for earthquakes with hypocenters (yellow stars) in the teleseismic regime 30°-95° used for receiver function analysis. Red stars and corresponding lines show earthquakes and ray paths from outside of the used teleseismic regime. The seismic receiver is supposed to be 0°. At 20° the far-field assumption of plane waves is not valid. Events with larger distances than 95° interact with the core-mantle-boundary, which can result in a complicate waveform.

limited towards large distances by SKS arrivals. The PKiKP arrivals are weak in amplitude and hence do not disturb the analysis. However, S-to-P conversions at the Moho only occur for events with larger distances than 55°. Thus the distance range for events used for S-RF analysis is limited to 55°-85°. SKS and SKSp phases have also been used for the S-RF method.

A zoom into the two windows used for P- and S-RFs is shown in Fig. 4.3. Here all arrival times are shown with respect to the mother phase (P or S) that is set to 0. Relevant arrival times for P-RFs of global phases (P, PcP and PP) as well as of waves converted at the Moho (Ps and the crustal reverberations $PpPs$, $PpSs$ and $PsSs$) are shown in Fig. 4.3 (a) and (b). The same pictures are drawn for the relevant arrival times for S-RFs in Fig. 4.3 (c) and (d). Here, besides the global S, $PKiKP$ and SKS-phases, arrival times of converted waves from the Moho are Sp and the multiple reverberations $SpPp$ $SsPp$ and $SsSp$. Comparing Fig. 4.3 (a) and (b) with Fig. 4.3 (c) and (d) its obvious, that for P-RFs the direct Ps-phase and the multiples are both in the P-coda, while for S-RFs direct Sp and multiples are separated from each other.

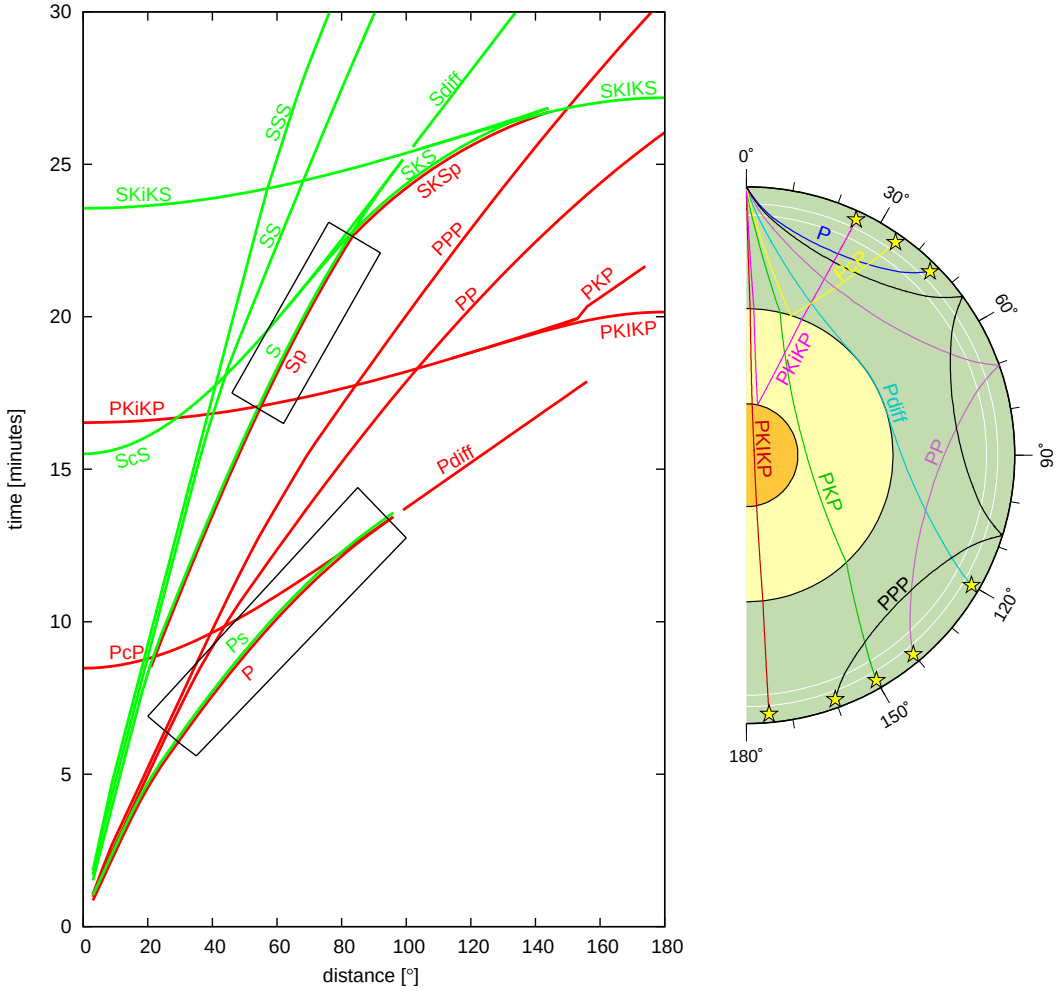

(a) (b)

Figure 4.2.: (a): Theoretical arrival times of seismic body waves of an earthquake in dependence of the distance. The windows used for P and S-RFs are marked. Longitudinal (P-) wave arrivals are marked in red, transversal (S-) wave arrivals are marked in green. All arrival times were calculated using the $TauP$ toolkit (Crotwell et al., 1999) with the IASP91 model. Besides the direct phases also phases of P-to-s (Ps) and S-to-p (Sp and $SKSp$) waves converted at a 68 km deep Moho are marked. (b): For all direct compressional wave phases the nomenclature is explained by example paths. The nomenclature of the direct shear wave phases is analogue to those of direct compressional waves. K and I denote compressional waves running in the liquid outer and the solid inner core, respectively. The lower case letters c and i denote reflections at the outer and inner core.

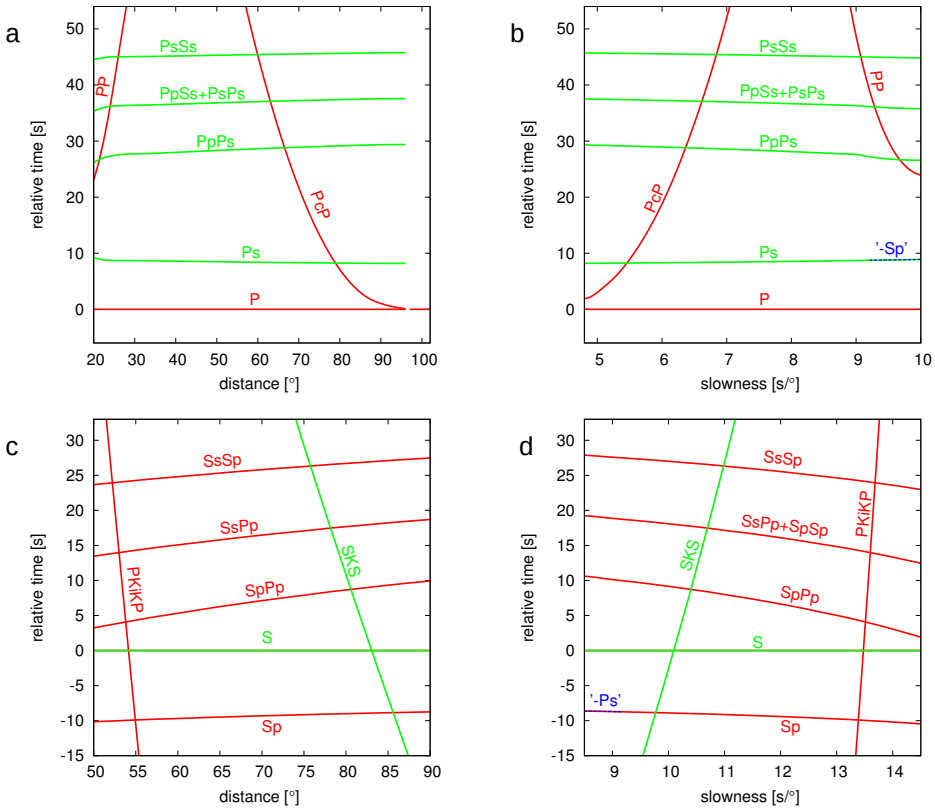

Figure 4.3.: Arrivals of converted phases from the direct wave (Ps and Sp) and from multiple crustal reverberations (XxXs and XxXp). Time is given as a delay time with respect to the arrival time of the mother phase (P or S). In (a) and (b) P is the mother phase; in (c) and (d) it is S. In (a) and (c) arrival times are given in dependence of the distance for a 30 km hypocenter depth. Conversions take place at the Moho of a 68 km thick crust. The blue phases in (b) and (d) labeled '$-Sp$' and '$-Ps$' are the negative arrival times of Sp and Ps phases relative to the S and P arrival, respectively. They show that P and S receiver functions are comparable if the arrival times are corrected for the slowness (moveout correction). All arrival times were calculated using $TauP$-toolkit (Crotwell et al., 1999).

4.1. Conversion

Similar to light, seismic waves are refracted and reflected at discontinuities of the wave speed. However, compared to the propagation of light waves, which is described as a purely transversal wave, for seismic waves, as body waves in a continuous medium, an additional degree of freedom exists that allows for excitation of different wave types - longitudinal (P-) and transversal (S-) waves. Here P stands for pressure or primary wave and S for shear or secondary wave. Besides the seismic wave energy is split up into refracted and reflected energy at discontinuities, a part of the incoming seismic wave energy gets converted into the complementary body wave type, i. e. a part of P wave energy gets converted to S wave energy (P-to-S conversion) or vice versa (S-to-P conversion). The waveforms of the converted and original (mother-) waves resemble each other, and are only scaled in amplitude, because the converted wave is excited by the original wave. Only differences in the transmission of converted and mother wave above the seismic discontinuity could alienate the two phases from each other, which is treated as negligible.

In Fig. 4.4 a simple model for the process of conversion is illustrated. Here the case of Ps conversion at a positive and a negative velocity contrast, that is orientated horizontally below the surface is shown. We call a velocity contrast positive if the velocity above is lower compared to the velocity below such as the crust mantle boundary (Moho). Analogously, we call the velocity contrast negative if the velocity above is higher than the velocity below such as the lithosphere asthenosphere boundary.

In this simplified model perception the S-wave gets excited as consequence of the refraction of the mother phase: The refraction causes a change of direction of the particle motion at the discontinuity. This directional change leads to a force roughly perpendicular to the particle motion opposite to the directional change. The released energy can be partitioned in reflected and a transmitted waves of different modes. The particle motion of the transmitted shear mode is roughly perpendicular to the wave propagation is excited.

This model perception given here is not precise, but it is helpful to predict intuitively the sign of the converted wave. To describe the problem in a physically precise way the transmission, reflection and conversion coefficients of a plane wave in a continuous medium allowing for shear and compressional waves at a discontinuity has to be computed, that can be done analytically by solving the equations of Zoeppritz (1919). Solving this equation reveals that the amplitude of both S-to-P and P-to-S conversion are determined by the shear wave velocity contrast. Thus P-RF and S-RF are two independent methods that observe the same thing, namely discontinuities in the S-velocity structure below a seismic receiver.

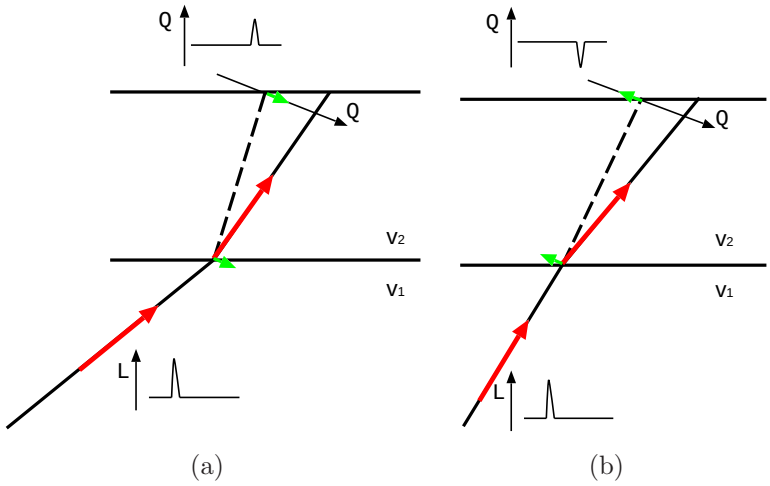

(a) (b)

Figure 4.4.: Simplified model perception for P-to-S conversion at a positive velocity contrast (Moho-like, i.e. $v_1 > v_2$) resulting in a positive peak on the Q-component (a) and for negative velocity contrast ($v_1 < v_2$) (b). Red Arrows denote particle motion of the P-wave, whereas green arrows denote the particle motion of the S-wave.

The RF processing explained below, isolates the arrival times of the converted wave energy with respect to the main phase. Each three component seismogram is transformed into a receiver function, that is a time series, where positive and negative amplitudes are identified with positive and negative velocity contrasts in the earth below the receiver. The seismic discontinuities can further be localized as sources of converted wave energy.

4.2. Separation of primary and converted wave energy

For the calculation of RFs three component receivers are used, recording the particle motion on a vertical (Z) and two horizontal components, directed to north (N) and east (E). To separate the converted and the mother waves from each other, a separation of P and S waves is needed, that is achieved by a rotation of the coordinate system, see Fig. 4.5.

First, the (Z, N, E) coordinate system is rotated around the Z axis, into the (Z, R, T) system. The rotation angle θ is the back azimuth of the arriving P wave. The radial (R) and tangential (T) components are aligned radial and perpendicular to the surface-path of the incoming wave. Thus an isolation of the horizontal shear (SH) energy is achieved, which is registered on the T component.

Mathematically, this is expressed by

$$\begin{pmatrix} Z \\ R \\ T \end{pmatrix} = \begin{pmatrix} 1 & 0 & 0 \\ 0 & \cos(\theta) & \sin(\theta) \\ 0 & -\sin(\theta) & \cos(\theta) \end{pmatrix} \begin{pmatrix} Z \\ N \\ E \end{pmatrix} .$$

In the second step, in order to separate the P and vertical shear (SV) energy, a further coordination transformation is performed. The transformation of the (Z, R, T) to (L, Q, T) system is written by the matrix equation:

$$\begin{pmatrix} L \\ Q \\ T \end{pmatrix} = \begin{pmatrix} V_{LZ} & V_{LR} & 0 \\ V_{QZ} & V_{QR} & 0 \\ 0 & 0 & 1 \end{pmatrix} \begin{pmatrix} Z \\ R \\ T \end{pmatrix} .$$

The new components L and Q register the longitudinal (L) and vertical shear wave (Q, for German "quer") particle motion, respectively.
The simplest way of choosing the transformation matrix is a second rotation around the T axis by the incidence angle of the arriving P-wave. Additionally, the Q-component is defined to point radially in opposite direction from the source. That is why a factor -1 is multiplied to the V_{QZ} and V_{QR}.
In this case, the components are given by

$$\begin{aligned} V_{LZ} &= cos(i)\,, & V_{LR} &= -sin(i)\,, \\ V_{QZ} &= -sin(i)\,, & V_{QR} &= -cos(i)\,. \end{aligned}$$

The incidence angle and the back azimuth for each event can be calculated directly from the data by diagonalizing the covariance matrix, as described in the following section. Alternatively, theoretical angles can be calculated from the event and receiver locations using a global earth model, such as IASP91 (Kennett and Engdahl, 1991). This can be achieved using the method of Buland and Chapman (1983) as implemented in the TauP toolkit (Crotwell et al., 1999).

An theoretically more precise way to choose the transformation matrix taking into account free surface effects is proposed by Kennett (1991). The elements of the transformation matrix are then given by

$$\begin{aligned} V_{LZ} &= \frac{1 - 2\,p^2\,v_s^2}{q_p\,v_p}, & V_{LR} &= \frac{-2\,p\,v_s^2}{v_p}, \\ V_{QZ} &= -2\,p\,v_s, & V_{QR} &= \frac{-1 + 2\,p^2\,v_s^2}{q_s\,v_s}\,, \end{aligned}$$

where

$$q_p = \sqrt{\frac{1}{v_p^2} - p^2} \qquad \text{and} \qquad q_s = \sqrt{\frac{1}{v_s^2} - p^2}$$

denote the vertical slownesses of the P and S waves, respectively. Interestingly the consideration of the surface effects shows, that the incidence angle of the P wave is only dependent from the S-velocity at the surface (see Appendix A). This can be used to estimate the surface shear wave speed v_s from a measured incidence angle (Saul et al., 2000; Svenningsen and Jacobsen, 2007).

4.3. Determining the back azimuth and incidence angle from the data

The back azimuth and the incidence of an an incoming plane wave can be measured by determining the direction of maximum polarization of the incoming wave registered at three components (Kanasewich, 1983; Stammler, 1992).

Therefore the *covariance matrix* of the three components is calculated in a time window around the onset. The eigenvector of the largest eigenvalue points into the direction of the maximum polarization.

The *covariance matrix* $\mathbf{C}$ of the three components $X = (x_1, ..., x_n)$, $Y = (y_1, ..., y_n)$ and $Z = (z_1, ..., z_n)$ is defined as

$$\mathbf{C}(X, Y, Z) = \begin{pmatrix} \sum x_i^2 & \sum x_i y_i & \sum x_i z_i \\ \sum x_i y_i & \sum y_i^2 & \sum y_i z_i \\ \sum x_i z_i & \sum y_i z_i & \sum z_i^2 \end{pmatrix} \tag{4.1}$$

.

The covariance matrix is composed of auto and cross-correlation entries. Since the matrix is symmetric and real it can be diagonalized and the resulting eigenvectors are orthogonal to each other. In the diagonalized form, the cross-correlation entries of $\mathbf{C}$, correlating different components with each other, are zero. Thus, in the eigenvector system the particle movements are separated from each other and the eigenvector with the largest eigenvalue points in the direction of the maximum polarization. Thus, if $\mathbf{v} = (v_Z, v_N, v_E)$ is the eigenvector of $\mathbf{C}$ with the largest eigenvalue, the back-azimuth θ and inclination angle i can be

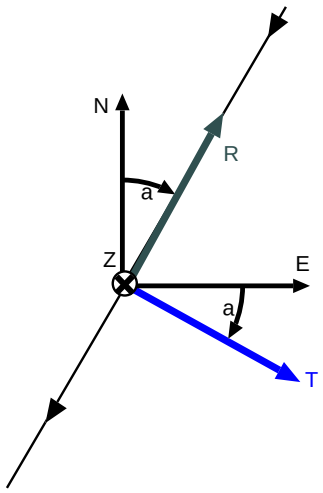

(a) Rotation from (Z, N, E) to (Z, R, T) coordinate system for an event located in the north-east of the seismic receiver: The coordinate system is rotated around the Z axis by the back-azimuth of the event.

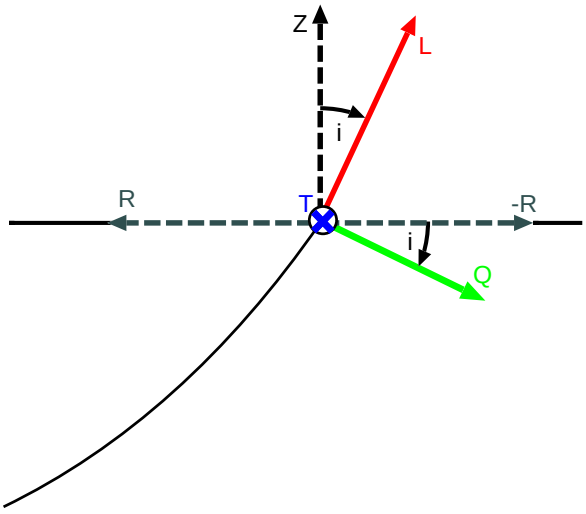

(b) Transformation from (Z, R, T) to (L, Q, T) coordinate system: The R component is inverted and the coordinate system is rotated around the T-axis by the incidence angle of the event.

Figure 4.5.: Separation of wave types by two transformation steps.

calculated by

$$\theta = \arctan(v_E/v_N) + 180^\circ \quad (4.2)$$
$$i = \arccos(v_Z)\,. \quad (4.3)$$

4.4. Excursus: Comparison of theoretical and measured azimuths

To compare the results of the measured and theoretical azimuthal values, for each event the difference

$$\Delta A = A_{data} - A_{theo} \quad (4.4)$$

is calculated, where A_{data} is the azimuth value determined from the data and A_{theo} is the theoretical azimuth value.
In figure 4.6 ΔA values for ca. 15000 event registrations from 85 stations are sorted and plotted. The median value of all stations and all events in the network is $-3^\circ \pm 10^\circ$, where the error is derived from the interquartile range $(Q_{75} - Q_{25})$ of the distribution. This value is the mean deviation of measured and theoretical azimuths averaged over all stations and events from the network. The value corresponds to the mean magnetic declination in the Pamir region, that is 3.4° at the $(38N, 74E)$, see figure 4.7 for illustration. This is expected, since the stations were directed to the magnetic north pole.
By comparison of theoretical and measured azimuths, for each seismometer, the azimuthal deviation is calculated. In this way misdirected seismometers can be identified. In the TIPAGE deployment, 3 stations (P04, KIR9 and F10) were wrongly directed to south instead of north, see figure 4.8. For correction, the horizontal components of this 3 stations have been rotated by 180°.

4.4.1. Comparison to magnetic declination

The mean magnetic declination for all locations of stations used in Fig. 4.6 is calculated from the International Geomagnetic Reference Field (IGRF) (Finlay et al., 2010). The average value is for our network is

$$\delta_{av} = \sum_{i=1}^{N} \frac{\delta(lat_i, lon_i)}{N} = 3.8 \pm 0.5^\circ\,. \quad (4.5)$$

The spatial variation of the IGRF in the Pamir region is plotted in Fig. 4.9. It is ranging from 3.0° in the southeast to 4.8° in the northwest. On the right column

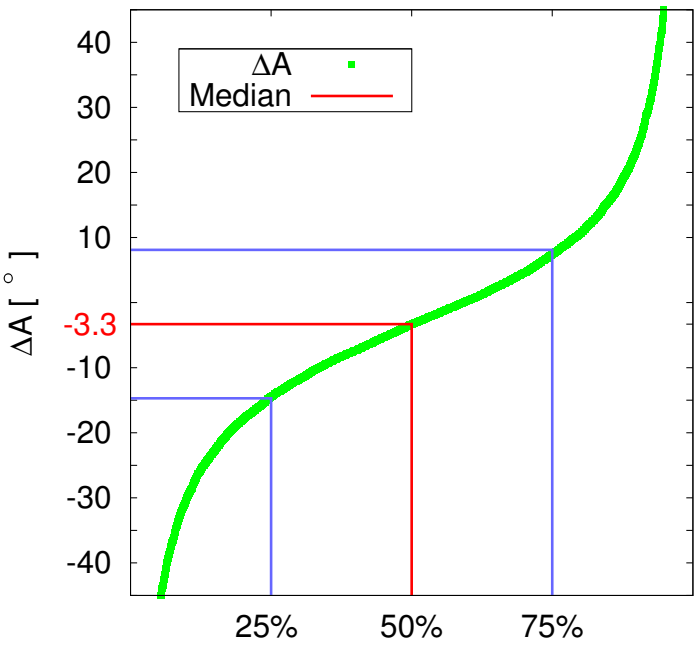

Figure 4.6.: Distribution of ΔA for all stations and all events except misoriented stations P04, KIR9 and F10.

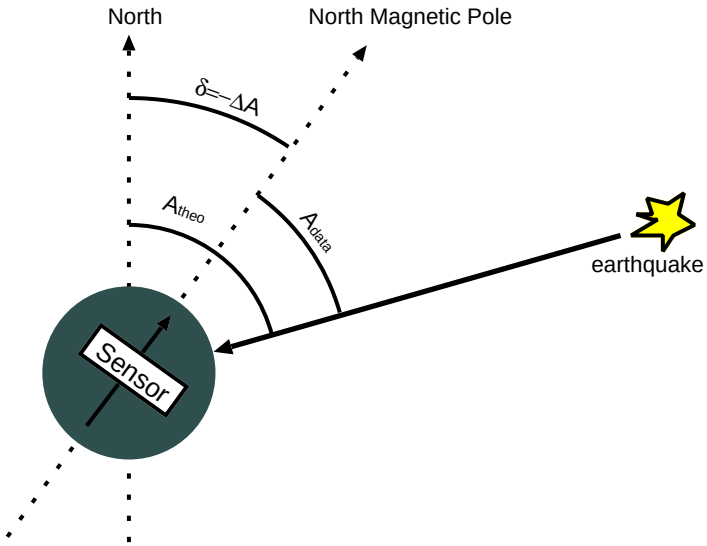

Figure 4.7.: Relation of sensor orientation and event azimuth: Since A_{data} is measured with respect to the sensor orientation, which is aligned due magnetic north, whereas A_{theo} is given with respect to true north, the declination can be deduced from the difference.

in Fig. 4.9 ΔA of 3 sub-regions is plotted. The stations of the regions are plotted with blue, green and red colors, where the IRGF model shows a declination of 3.0° to 3.5°, 3.5° to 4.0° and 4.0° to 4.8°, respectively. The resulting declinations for the three region are ($\delta = -\tilde{\Delta A}$)

$$\delta_{blue} = 1.2 \pm 10^{\circ} \tag{4.6}$$
$$\delta_{green} = 4 \pm 10^{\circ} \tag{4.7}$$
$$\delta_{red} = 5 \pm 10^{\circ}\,, \tag{4.8}$$

showing an increase in declination from southeast to northwest as expected from the IGRF model. However, the variance of ΔA as measured from the Q_{25} and Q_{75} quantiles is with ±10 quite high.

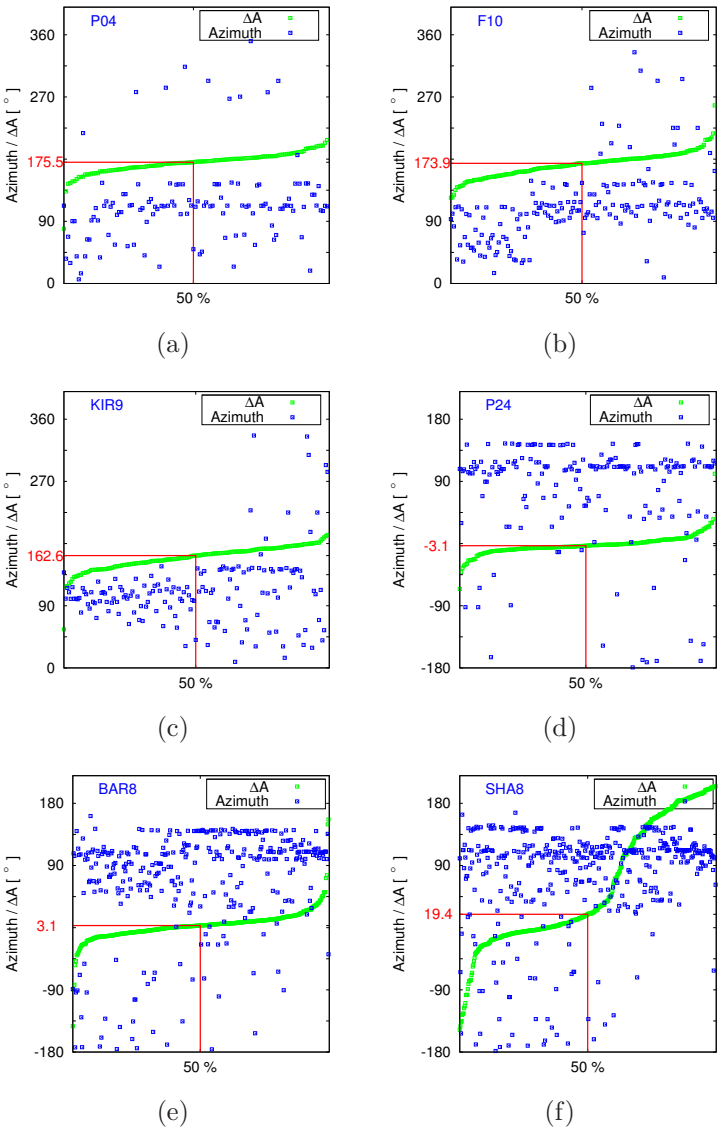

Figure 4.8.: Examples for comparison of the measures azimuth and the theoretical azimuth for individual stations. The Median of the ΔA distributions is calculated. ΔA and the theoretical azimuths are plotted with green and blue symbols, respectively. For the three stations P04, F10 and KIR9 in figures (a - c) a 180° misorientation of the seismometer could be recognized. For stations P24 and BAR8 (figures (d) and (e)), the median of ΔA matches the magnetic declination of ca. 3°. In figure (f), the distribution is asymmetric, probably due to shallow lateral structure variations such as a dipping layer.

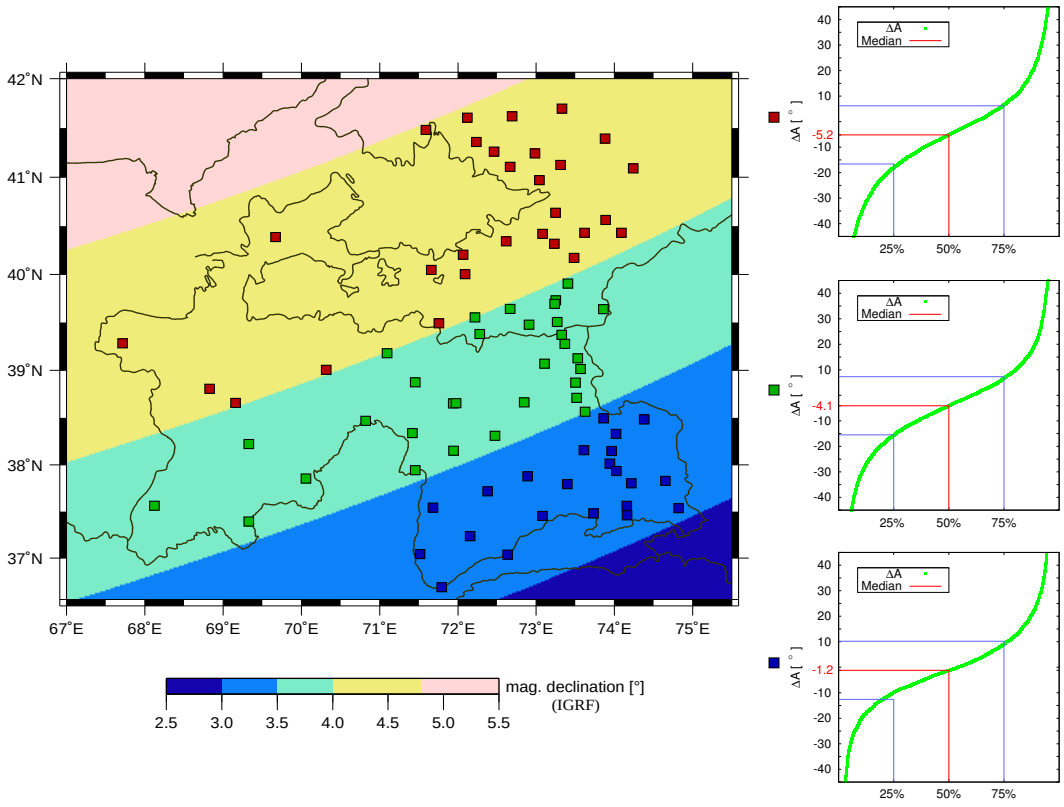

Figure 4.9.: Comparison of the magnetical declination with the difference of measured and theoretical event azimuths (ΔA). Left: Magnetical declination from the IGRF model. Right column: ΔA sorted for all events of stations in three region, marked with blue green and red symbols in the map.

4.5. Deconvolution

The final step after separating the primary and converted wave energy from each other is to identify the arrival times of converted wave energy. The time series of the converted wave has to be scanned in order to detect the signature of the mother phase.

In the following the case of P-to-S converted waves is discussed. It can be simply assigned to the case of S-to-P conversions by changing Q and L components.

To identify the P-to-S converted wave energy on the Q-component, the P wave characteristic recorded in the L-component is deconvoluted from this signal. The idealized process is illustrated by the sketch in Fig. 4.10. The source time function of the L component is used to determine its inverse, which is folded to both, the L and Q component. In the idealistic case, this maps the waveform recorded on the L component to a spike. On the Q-component the P-to-S converted energy from each converter has the same waveform as the P wave recorded on the L-component but with smaller amplitude and shifted in time, depending on the converter depth.

Applying L^{-1} to the Q component let each P-wave signature contained on the Q-component be transformed to a spike. The quality of the deconvolution can be checked by regarding the spike that is generated by applying L^{-1} to L. Thus the converted signal is increased in amplitude and simplified. By this process positive and negative spikes are produced depending on the sign of the velocity contrast. The arrival times of converted signals on the Q component relative to the arrival of the main phase on the L component is a strictly monotonic function of the depth of the converter, see section 4.7.

In reality, the duration of the source-time function of the event is much larger than the delay times of the converted waves. Thus the converted signals are hidden in the source time function. Furthermore the signal can be disturbed by noise. A more realistic situation as the idealized sketch in Fig. 4.10 is illustrated in Fig. 4.11. The Q component in Fig. 4.11(b) is constructed artificially by folding the L-component taken from a real record with the the Greens function displayed in figure 4.11(a). Even with this simple Greens function the timing of converted phases is hardly possible by just comparing Q and L components.

The result of deconvolution of L from Q, (that is applying the inverse filter of L to the L and Q component) is shown in figure 4.11(c)). In this semi synthetic test, the Q component reveals both, the maximum and minimum positions and the amplitudes of the Greens function. The sharpness of the spikes on the Q-component is determined by the sharpness of the spikes on the deconvolved L component.

In Fig. 4.12 the real Q component for the same event is shown and used for the deconvolution. It shows two strong converters at 8.5 s and 9.5 s. The strongest

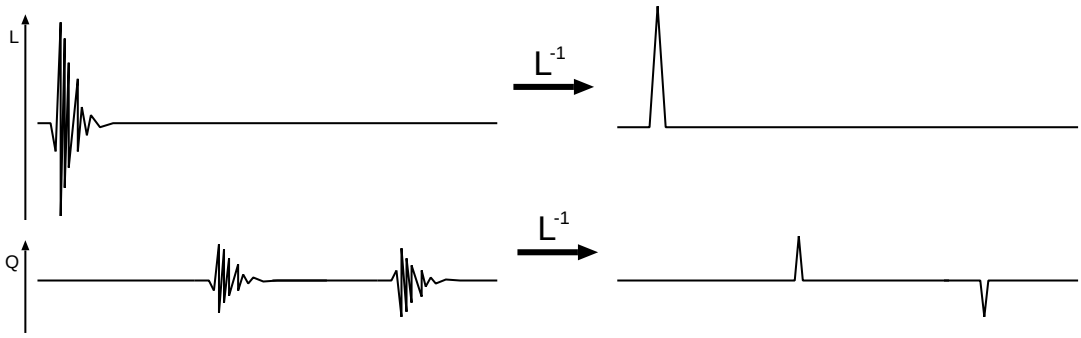

Figure 4.10.: Sketch illustrating the deconvolution. Left side: L-component containing the mother waveform and Q-component with converted wave energy represented as the same waveform shifted and with smaller or inverse amplitudes. The L^{-1} spiking filter is calculated from the mother waveform on the L-component and folded to L and Q. On the right side the resulting deconvolved waveforms are sketched. The deconvolved Q component is defined as the P-receiver function.

phase at 8.5 s phase is probably the Moho-phase.

A mathematical description of the deconvolution method used for this thesis is given in appendix B.

4.6. Plain summation

The purpose of the deconvolution described in the previous sections is to remove the source waveform of a seismic event. Once the effects of the source and near source structure are removed, only the response of the receiver side structure remains in the signal, which is the objective of the investigation. Plain summation, as described by Kumar et al. (2010) is a simple method to remove the source side effects which is applicable if many records are available. In this method from each 3 component seismogram the L-, Q- and T-components are shifted together, in order to align all maxima of the absolute value of the L-components. In case the maximum absolute value belongs to a negative amplitude on the L-component, all three components are inverted. All components are normalized to the maximum of the L-component. Then all L-, Q- and T-components are summed either after moveout correction (see section 4.8) or through CCP stacking (see section 4.9). In the three resulting summations of L-, Q-, and T-components the source side effects are removed statistically. Through summation of many records from different source regions at the same station the amplitudes caused by different source regions interfere destructively, while the receiver side signals are the same for all events and thus interfere constructively.

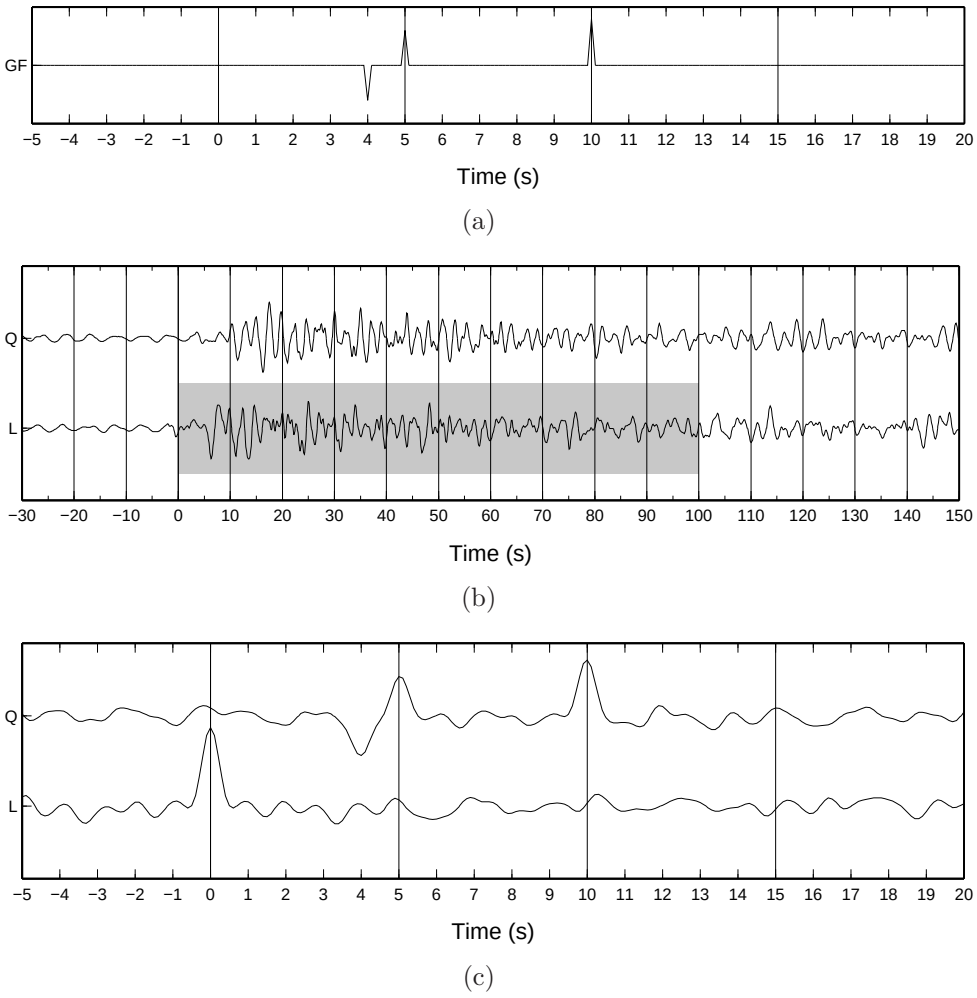

Figure 4.11.: Illustration for deconvolution method. In (a) a Greens function in displayed. In (b) a L-component is displayed that has been measured from a teleseismic event. The Q component has been produced artificially by folding the L-component with the Greens function in (a). Figure (c) shows the result of deconvolution of the L and Q components.

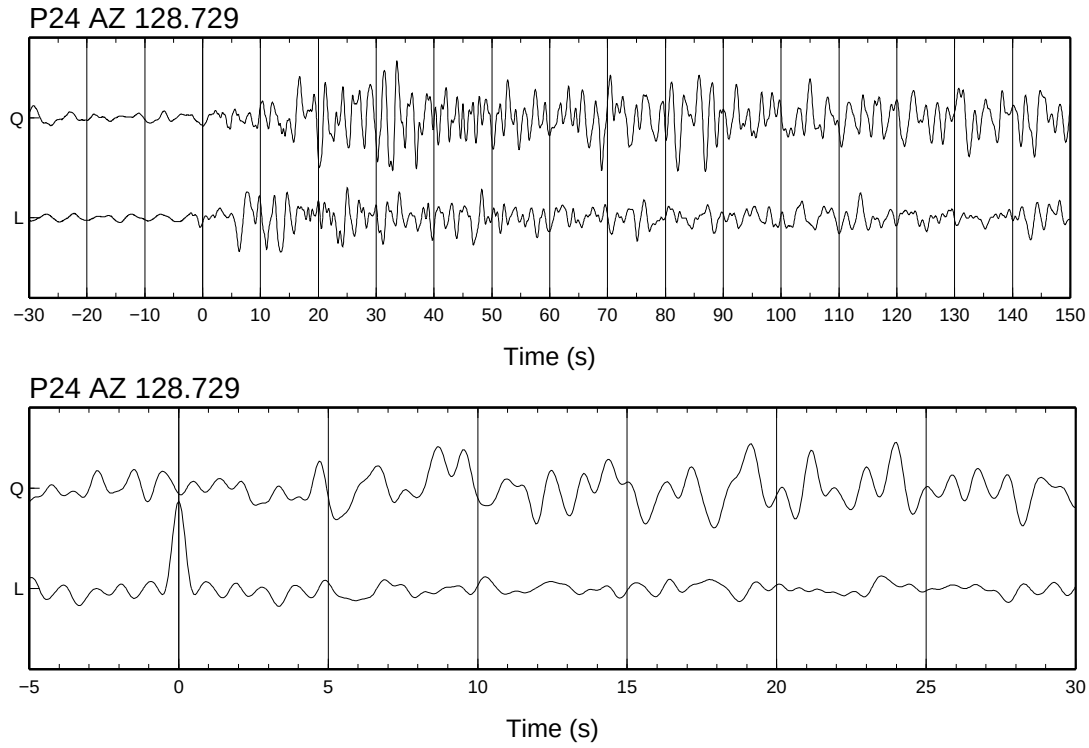

Figure 4.12.: Upper panel: Real data example of L and Q component, measured at station P24 from a teleseismic event. The L-component is identical to the L-component in Fig. 4.11.

An example for one station is shown in Fig. 4.13. In the summation trace of the L-components, shown in the top panel of the left image, the result of the source normalization is displayed. The summation trace consists mainly of a singular pick at $0s$, which is desired. For this image 211 events were summed. In the Q-component a clear Moho phase at 8.5 s is evident as well as a negative LAB phase at 14 s.

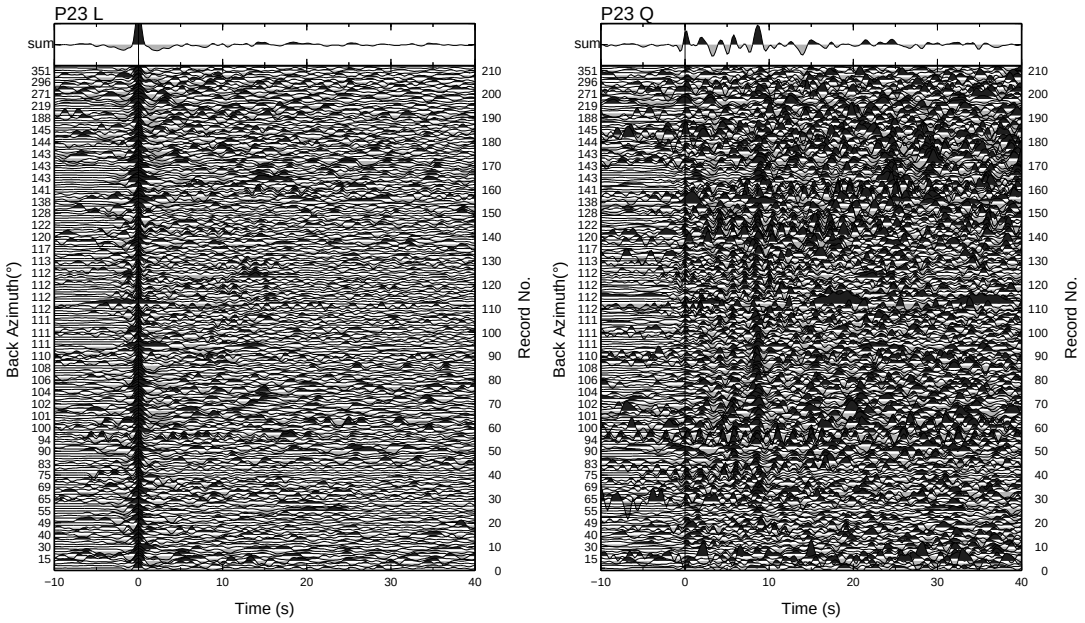

Figure 4.13.: L and Q component of station P23. Traces are shifted to align the maximum of the absolute value of L. All traces are normalized to this maximal deviation of zero. All traces are low pass filtered with a corner frequency of 1 s.

4.7. Delay time depth assignment

To interpret the receiver functions the relation between the delay-times and the conversion depth is needed. Therefore, the approach of a plane incident wave and horizontally layered velocity structure is made. The delay times are resulting from the different P and S wave travel times (t_p and t_s) along their ray paths and an initial delay t_D of direct and converted wave due to the path difference. This is illustrated in figure 4.14. Here a two layered model is shown. The delay time of the converted S wave arrival with respect to the P wave arrival

is given by

$$\Delta t = t_s - t_p + t_D \,, \tag{4.9}$$

where

$$t_p = \sum_i \frac{h_i}{v_{p,i} \cos \alpha_i} \qquad \text{and} \tag{4.10}$$

$$t_s = \sum_i \frac{h_i}{v_{s,i} \cos \beta_i} \tag{4.11}$$

are the P and S travel times from the discontinuity to the surface along their ray paths, respectively.
The horizontal distances of the direct P wave piercing point x_p and the P-to-S conversion point x_s measured from the station are given by

$$x_p = \sum_i h_i \tan \alpha_i \qquad \text{and} \tag{4.12}$$

$$x_s = \sum_i h_i \tan \beta_i \,. \tag{4.13}$$

The initial delay between the P wave and the converted S wave at the discontinuity is given by the horizontal travel time of the incident P wave from the P piercing point to the S conversion point. This can be calculated by

$$t_D = p\, x_D = p\,(x_p - x_s) \,, \tag{4.14}$$

where

$$p = \frac{\sin \alpha_i}{v_{pi}} = \frac{\sin \beta_i}{v_{si}} \tag{4.15}$$

is the (horizontal) slowness of the waves. Using the identities $1 = \sin^2 + \cos^2$ and $\tan = \frac{\sin}{\cos}$ from equations 4.9 - 4.15 follows directly

$$\Delta t = \sum_i h_i \left(\frac{\cos \beta_i}{v_{si}} - \frac{\cos \alpha_i}{v_{pi}} \right) \,, \tag{4.16}$$

which can be also expressed in terms of slowness by

$$\Delta t = \sum_i h_i \left(\sqrt{v_{si}^{-2} - p^2} - \sqrt{v_{pi}^{-2} - p^2} \right) . \tag{4.17}$$

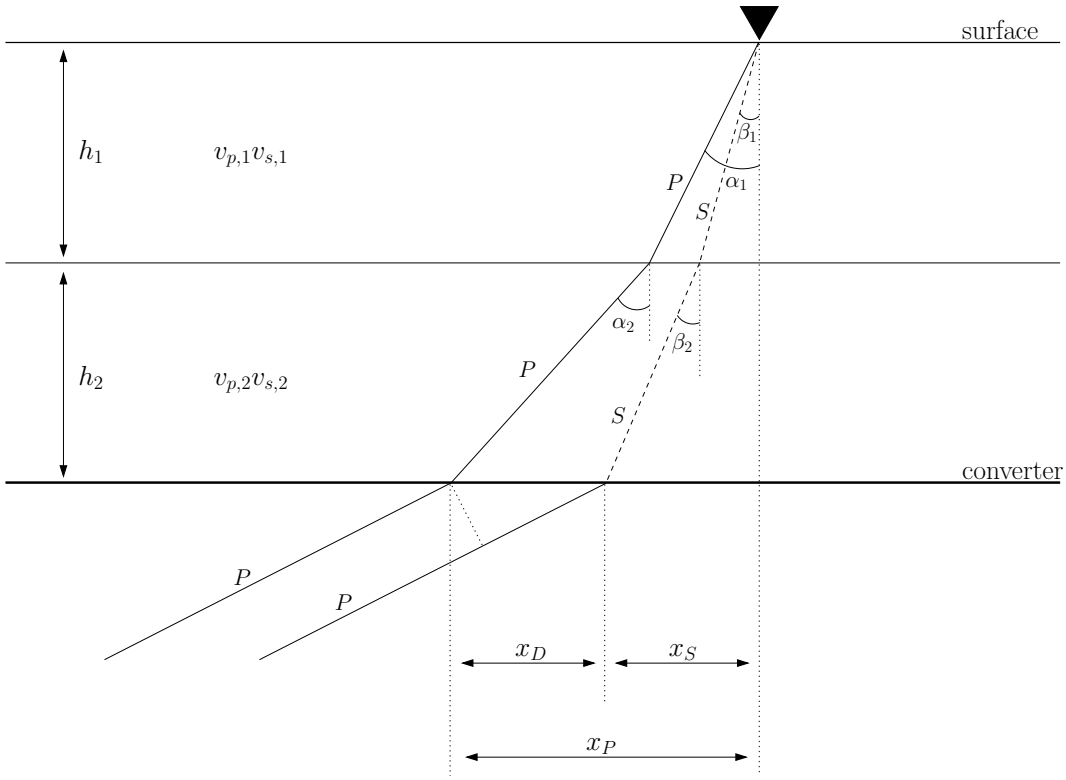

Figure 4.14.: Ray paths of waves attributed to direct P and direct converted Ps phases. Due to different incidence angles of P and S waves the paths are different, which has to be taken into account by calculating the differential travel time t_D that the P wave needs to travel the distance x_D in horizontal direction. The delay time of Ps with respect to P is thus composed on the P- wave travel times in each layer above the converter minus the sum of the S-travel times in each layer above the converter and the differential travel time t_D.

4.7.1. Travel time and vertical slowness

Expression 4.17 can be also directly deduced regarding the wave fronts rather than the ray paths. Snapshots of the wave-fronts at three different times are needed to deduce the delay-time: at the time t_0 where the incident P-wave reaches the point at the converter vertically below the station, and the two times $t_{v,p}$ and $t_{v,s}$, at which the P and S wave fronts reach the station. This situation is shown for a single layer in Fig. 4.15. The distances, that the S and P wave fronts have to travel in their propagation direction to reach the surface, starting from the discontinuity below the station are

$$D_s = h\,\cos\beta \qquad \text{and} \tag{4.18}$$

$$D_p = h\,\cos\alpha. \tag{4.19}$$

Thus the delay times is

$$\Delta t = \frac{D_s}{v_s} - \frac{D_p}{v_p}\,. \tag{4.20}$$

Defining the (velocity dependent) vertical slownesses

$$q_p = \frac{cos\alpha}{v_p} = \sqrt{v_{si}^{-2} - p^2} \qquad \text{and} \tag{4.21}$$

$$q_s = \frac{cos\beta}{v_s} = \sqrt{v_{pi}^{-2} - p^2} \tag{4.22}$$

$$\tag{4.23}$$

and generalizing equation 4.20 to a multiple layered situation leads to

$$\Delta t = \sum_i h_i\,(q_{s,i} - q_{p,i})\,. \tag{4.24}$$

In equation 4.24 it is evident, that the delay time is the time that two plane waves need to pass in vertical direction through a layered medium. This can be easily adapted to multiple reflections.

Multiple reflections

In RFs besides the amplitude of direct converted phases, amplitudes of multiple reverberated phases occur, which are reflected between surface and the Moho, see figure 4.16. For P-RFs, these multiple phases arrive after the Ps phase. The two most important multiple phases are $PpPs$ and $PpSs$. The first one has two P legs and one S leg. Thus the delay time between the direct P arrival (1 P

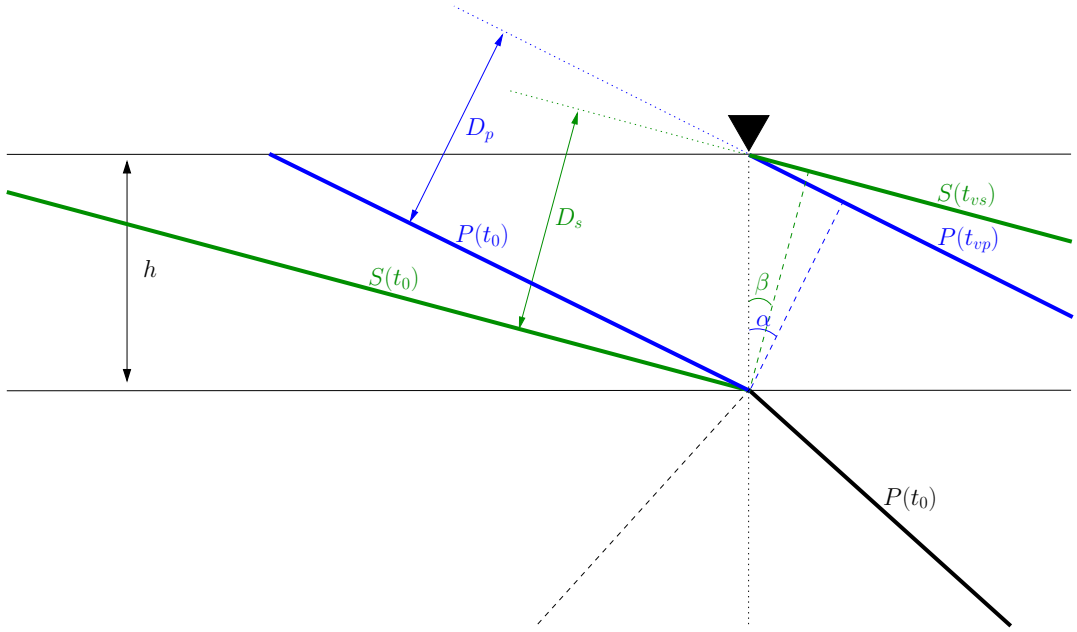

Figure 4.15.: Wave fronts for a planar incident P wave. At $t = t_0$ the wave reaches the point vertically below the station. At $t = t_{vp}$ and $t = t_{vs}$ the P and Ps wave fronts arrive at the station, respectively.

leg) and the $PpPs$ phase is

$$\Delta t_{ppps} = \sum_i h_i \left(\underbrace{2\, q_{p,i} + q_{s,i}}_{pPs} - \underbrace{q_{p,i}}_{P} \right) = \sum_i h_i \left(q_s + q_p \right). \tag{4.25}$$

Analogously, the delay time for $PpSs$ with one P and two S legs is

$$\Delta t_{ppss} = \sum_i h_i \left(\underbrace{q_{p,i} + 2\, q_{s,i}}_{pSs} - \underbrace{q_p}_{P} \right) = 2 \sum_i h_i q_s \,. \tag{4.26}$$

4.8. Moveout correction

In order to enhance the signal to noise ratio of converted Ps phases for each station the summation traces of many single event receiver functions traces are calculated. Since the assignment from delay time to depth is dependent on the slowness of the event the effect of different slownesses has to be corrected. Therefore, a reference slowness is chosen (6.4 $^\circ/s$). The time axes of traces with

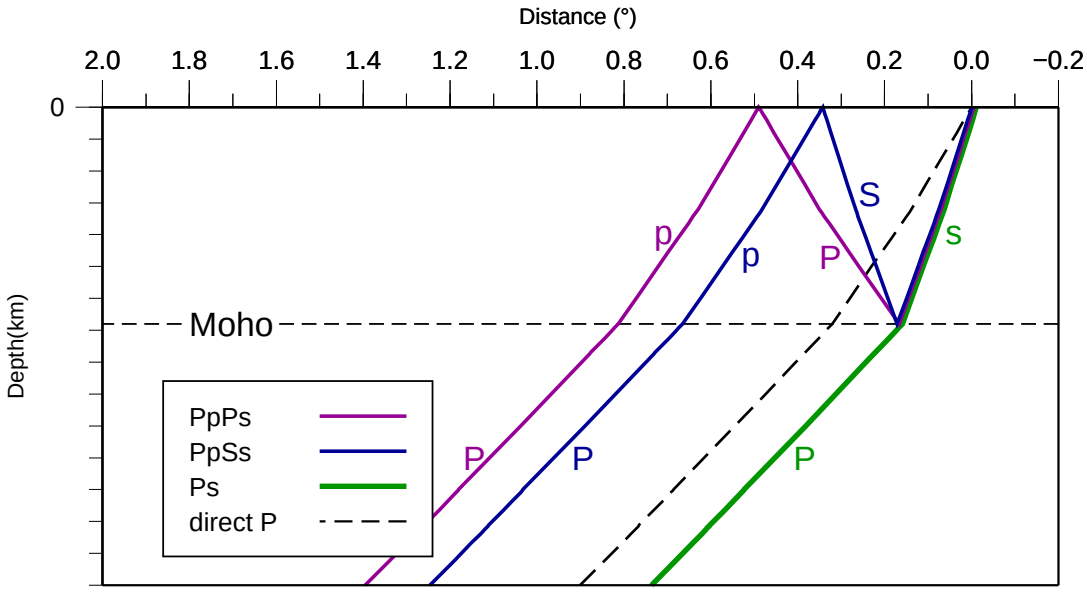

Figure 4.16.: Ray paths of P, direct converted Ps and crustal multiple $PpPs$ and $PpSs$ phases. Ray paths are calculated with $TauP$ (Crotwell et al., 1999) and a 1D velocity model with a 68 km thick crust.

smaller slownesses are stretched and time axes of traces with higher slownesses are compressed such that all Ps phases become parallel to the P arrival. The stretching or compression functions are calculated theoretically using an 1D reference model (IASP91). The moveout correction can also be applied for the multiple $PpPs$ or $PpSs$ phases. Here the moveout functions differ from that of the Ps phase.

An example illustrating this step is shown in Fig. 4.17. Theoretical seismograms are calculated using the Haskell matrix method (code of T. Shibutani Shibutani et al. (1996)). The upper panels show the summation trace. As model for the forward calculation a modified IASP91 model with a 60 km thick crust was chosen. Fig. 4.17(a) shows the calculated traces without moveout correction. In the summation traces the Moho and multiple phases are strong while the 410 and 660 phases disappear.

Fig. 4.17(b), (c) and (d) show the same traces moveout corrected for Ps, $PpPs$ and $PpSs$ phases, respectively. In Fig. 4.17(b) the phases of the direct Ps conversions of the Moho and also (more recognizable) of the 410 and 660 discontinuities are aligned and can be thus be identified in the summation traces. The multiple phases $PpPs$ and $PpSs$ get incoherent and thereby the amplitudes get reduced. In panels (c) and (d) the $PpPs$ and $PpSs$ multiple phases of the Moho get aligned and enhanced in the summation traces.

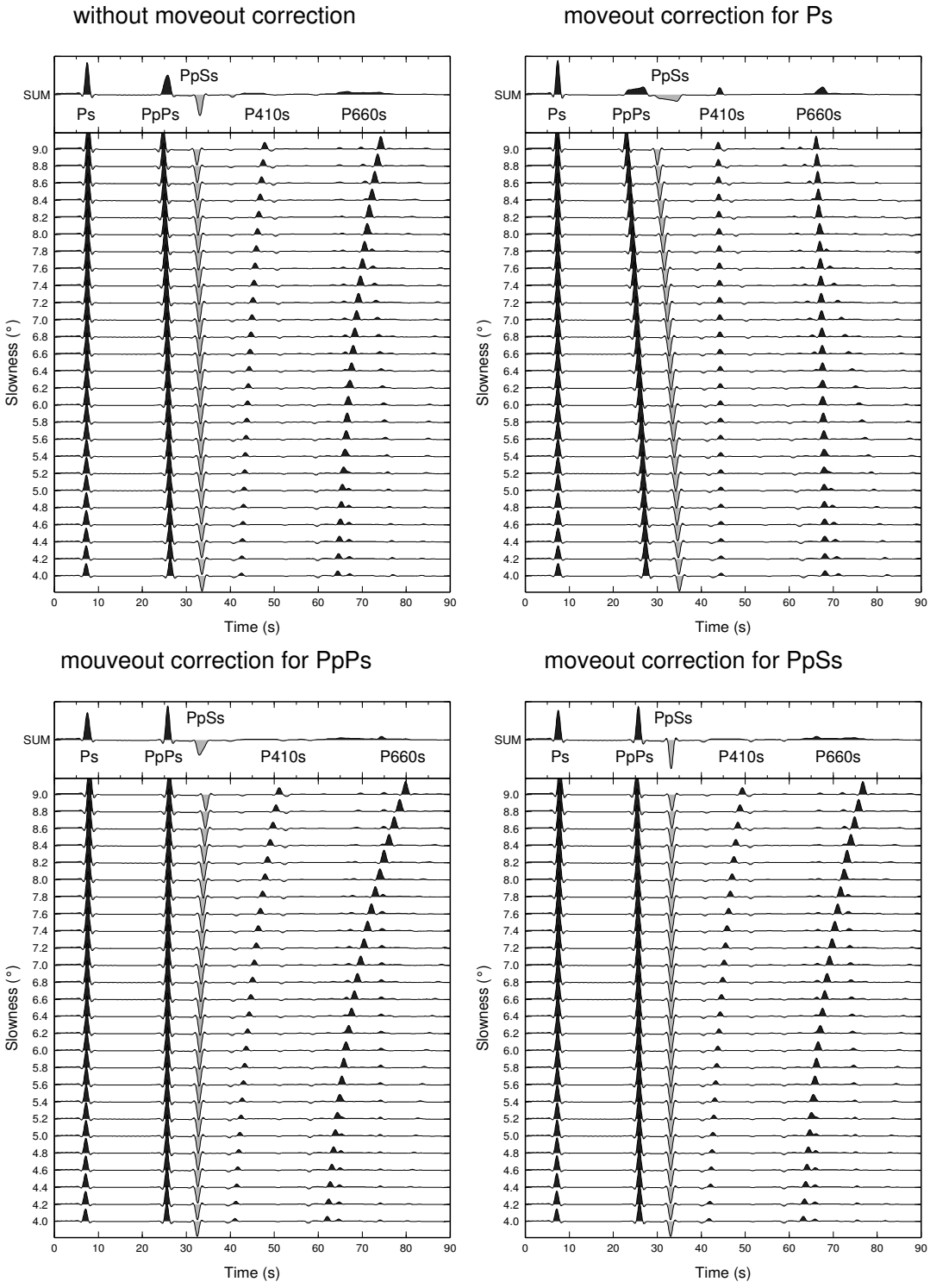

Figure 4.17.: Moveout correction for summation of individual traces. Upper left: synthetic P-RFs with different slownesses without moveout correction. Upper right and lower panels show moveout corrected traces for Ps, $PpPs$ and $PpSs$ phases. The target trace can be enhanced in amplitude. Particularly the $P410s$ and $P660s$ phases can only be clearly observed in the summation trace when the Ps moveout correction is applied.

4.9. Migration

In order to create depth sections from receiver functions of many stations that are typically arranged in a linear profile, the receiver functions are back projected along their ray paths. In this way every amplitude of the RF time traces are converted into a color-coded point in a 2D plane. This is done, taking into account the delay time depth assignment formula 4.17 applying a 1D velocity model that is applicable for the region. We use a modified version of the IASP91 model (Kennett and Engdahl, 1991) with a 68 km thick crust as one dimensional reference model.

In the following paragraphs the basic principle of common conversion point (CCP) stacking and a migration technique taking into account scattered waves as realized in the Fortran code of Xiaohui Yuan (e.g. used in Yuan et al. (2000)) is reviewed.

4.9.1. Common conversion point stacking

Starting from the station, for each event ray tracing of P and S waves with corresponding azimuth and slowness values is performed using a 1D Earth model. Between each depth step of the velocity model in which the P and S velocities are constant the rays are straight lines with a slope determined by the slowness of the ray and P or S- velocity of the depth layer. The ray paths are calculated from the station into depth (see Fig. 4.18(a)). The 2D plane is divided into a grid in x_i (lateral, along the section) and z_j (depth) direction. Typically a 2×2 km grid is used. For each receiver function trace a loop for depth is performed. Starting at the surface ($z = 0$), the code calculates for P and S rays the horizontal distances that they cover within each depth step of the velocity model.

Let z_k be the current depth step of the loop and v_l be the corresponding velocity layer for the depth z_k. To get the horizontal distances r_{sz} and r_{pz} of S and P wave at the depth z_k all horizontal distances from the layers of the velocity model v_i with $i \leq l$ are summed:

$$r_{pz}(k) = \sum_{i=1}^{l(k)} h_i * \tan \alpha_i \tag{4.27}$$

$$r_{sz}(k) = \sum_{i=1}^{l(k)} h_i * \tan \beta_i, \tag{4.28}$$

where h_i are the thicknesses of the layers of the velocity model. The thickness

of the lowest layer of the velocity model h_l has to be reduced to the distance between layer v_{l-1} of the velocity model to z_k (see Fig. 4.18(a)):

$$h_l = z_k - \sum_{i=1}^{l-1} h_i. \tag{4.29}$$

α_i and β_i are the incidence angles of P and converted S waves at layer i of the velocity model, respectively. The tangent of the incident angles can be determined from the ray parameter and the velocity at depth by

$$\tan\alpha_i = \frac{\sin\alpha_i}{\cos\alpha_i} = \frac{\sin\alpha_i}{\sqrt{1-\sin^2\alpha_i}} = \frac{p\ v_{p,i}}{\sqrt{1-p^2\ v_{p,i}^2}} \tag{4.30}$$

Here, in the last equal sign, Snell's law

$$\frac{\sin\alpha_k}{v_{p,k}} = p = const. \tag{4.31}$$

was applied, and similar

$$\tan\beta_i = \frac{p\ v_{s,i}}{\sqrt{1-p^2\ v_{s,i}^2}}\ . \tag{4.32}$$

For each depth z_i, $r_{sz}(i)$ is the distance from the station, where a possible wave conversion takes place (see Fig. 4.18(a)). Thus the corresponding amplitude of the receiver function has to be added to the grid cell of this position.
The times of P and S waves to reach the surface from depth z_i are

$$t_{pz}(k) = \sum_{i=1}^{l(k)} \frac{h_i}{\cos\alpha_k} \cdot \frac{1}{v_{p,i}} \tag{4.33}$$

$$t_{sz}(k) = \sum_{i=1}^{l(k)} \frac{h_i}{\cos\beta_k} \cdot \frac{1}{v_{s,i}}\ . \tag{4.34}$$

To calculate the corresponding delay time between P and S arrival, also the initial delay time between the arrival of the P waves at the positions r_{pz} and r_{sz}

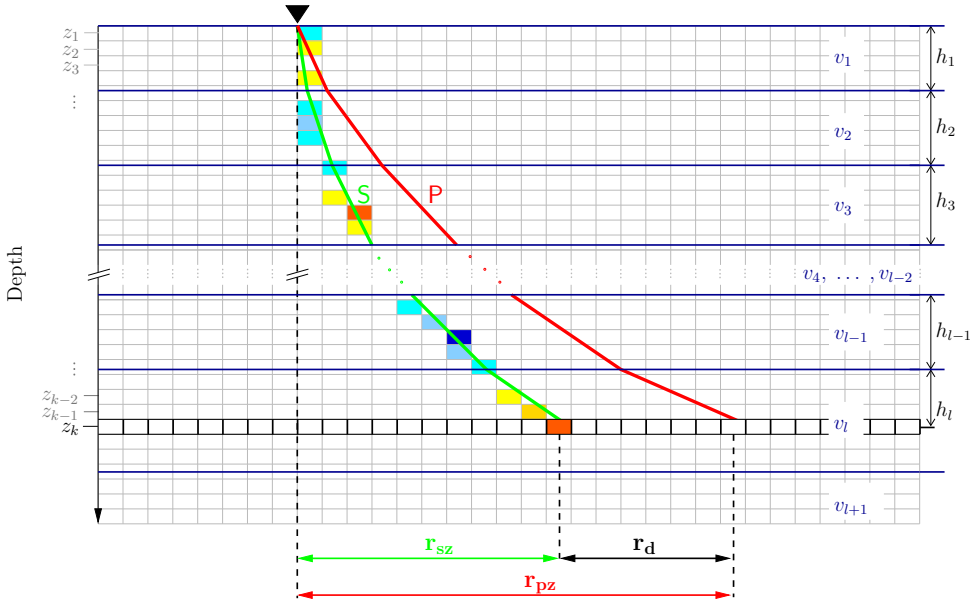

(a) Ray tracing on a 2D grid in case of $\alpha_{ev} = 0$. Here r_{sz}, r_{pz} and r_d are equal to x_{sz}, x_{pz} and x_d, respectively.

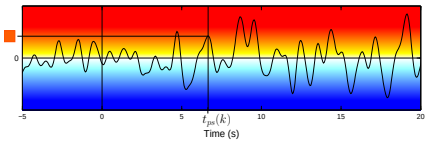

(b) Color coding of RF amplitudes.

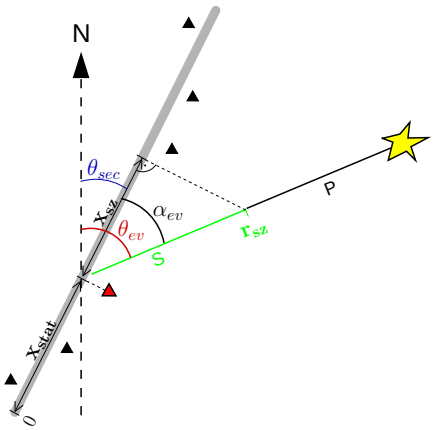

(c) Projection of RF amplitudes on the section line. Grey line: projection plane; θ_{sec}: azimuthal direction of the section; θ_{ev}: azimuth of the event; α_{ev}: angle of event with respect to the section (needed for the projection)

Figure 4.18.: CCP stacking procedure. For each receiver function a loop for depth is performed. For each depth z_k, r_{sz} and r_{pz} are calculated (a) and the amplitude of the corresponding time $t_{ps}(k)$ is plotted color coded on this position. In (the standard) case of $\alpha_{ev} \neq 0$, the distance r_{sz} is projected on the section plane (c).

are needed. It is calculated from the difference distance r_d between r_{pz} and r_{sz}, by multiplying it with the horizontal slowness p:

$$r_d = r_{pz} - r_{sz} \tag{4.35}$$
$$t_d = r_d \cdot p. \tag{4.36}$$

The delay time between P and S arrival from a converter at depth z_k is

$$t_{ps}(k) = t_{sz}(k) + t_d(k) - t_{pz}(k) \tag{4.37}$$

The amplitude at $t = t_{ps}(k)$ is taken from the receiver function. In the last step, the radius r_{sz} is projected on the section plane. (See Fig. 4.18(c)). Therefore the angle of the event with respect to the section line α_{ev} is determined from the azimuthal orientation of the section θ_{sec} and the back azimuth of the event θ_{ev}. The projected position of the converter is then given by

$$x_{sz} = r_{sz} \cos \alpha_{ev}. \tag{4.38}$$

The RF amplitude is added to the grid cell at the position (x_{sz}, z_k).

4.9.2. Migration with scattered waves

A further approach implemented in the code is the back projection along the range of a Fresnel zone, which defines a lower bound of seismic resolution.
The radius of the Fresnel zone depends on the depth h and wavelength λ:

$$r_{Fresnel} = \sqrt{\frac{1}{2}\lambda\, h + \frac{1}{16}\lambda^2}\,, \tag{4.39}$$

where the wavelength $\lambda = T * v_s$ depends on the S-velocity and the dominant period T of the signal.
In this approach, for each RF at each depth for all positions

$$\{(x_{sz} + i \cdot \Delta s; y_{sz})|_{i \in \{-n,..,n\}}\} \tag{4.40}$$

the delay time t_{ps} is calculated and the corresponding amplitude is added to the grid cell, see Fig. 4.19(a). Here, Δs is the lateral grid cell intervall. Thus all

possible scatterers are taken into account as possible sources for the recorded signal. In Fig. 4.19(b) the functionality is demonstrated. Fig. 4.19(b) A and C show the resulting images for one RF trace recorded at one station, while Fig. 4.19(b) B and D show the resulting images for RF traces recorded at 10 lateral distributed stations. The converter of the model used for calculating the synthetic RFs are depicted as black lines in each plot. In A and B the converter is horizontally oriented while in C and D the converter is inclined. For many stations and many RF-traces constructive interference at the converting layers enhances the signal at the real converting structures.

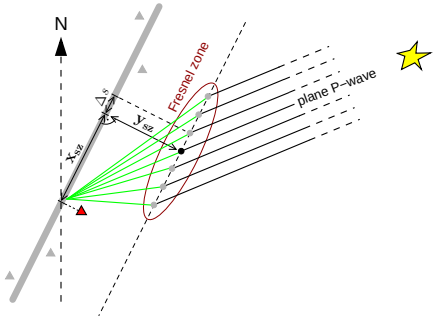

(a)

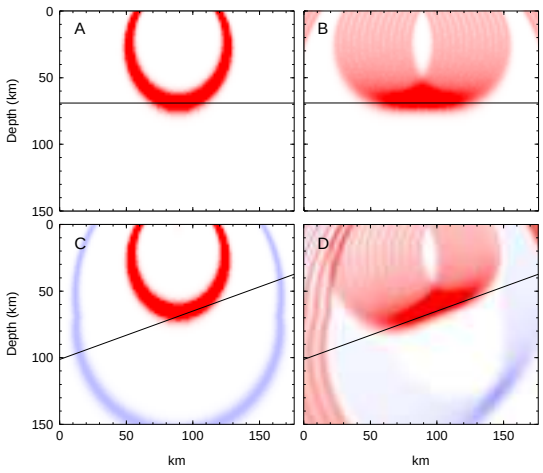

(b)

Figure 4.19.: Migration method taking into account scattered waves. a) Schematic sketch for the migration technique taking into account all scatterer within one Fresnel zone. b) Migration results for one synthetic event with horizontally oriented Moho (A and B) and tilted Moho (C and D), registered at one single station (A and C) and at multiple stations (B and D). For multiple registrations constructive interference enhances the signal at the location of the real structure.

5. Observations from seismic cross sections

5.1. P-Receiver functions

5.1.1. Event selection for P-Receiver functions

As sources for the P-receiver function (P-RF) analysis high quality records of earthquakes with teleseismic epicentral distances are selected. Therefore, from the time span of the deployments, all seismic events of the earthquake catalog published by the National Earthquake Information Center (NEIC) of the U.S. Geological Survey, with epicentral distances between 30° and 95° and magnitudes larger than 5.5 M_w, have been visually inspected and selected if the signal to noise ratio was high enough.

A total number of 22614 records from teleseismic earthquakes have been selected and processed. In Fig. 5.1(a) the hypocenter locations of the teleseismic events are shown. Fig. 5.1(b) and Fig. 5.1(c) show the slowness and azimuth distribution of the events. Most of the detected events originate at the subduction zones in Japan and Indonesia and thus are coming from eastern directions. The maximum number of events were recorded for back azimuths around 110°. Nevertheless there are also few events reaching the investigation area from western directions.

In Fig. 5.2 all receiver functions from the TIPAGE deployment are shown, sorted according to the slowness of the events, binned and summed in slowness intervals of 0.1 $s/°$. Comparing this figure to the theoretical relative arrival times in Fig. 4.3, the observed phases can be identified. The direct Moho Ps phase and 410 and 660 Ps phases can be traced. However, the 410 discontinuity seems to interfere with the $PsSs$ multiple, which is normally considered to be very weak. Furthermore the $PpPs$ and $PpSs$ multiple phases and the PP phase can be traced in this representation. Between 10 s to 15 s a strong negative phase is observed. However, it is difficult to decide whether this phase originates from the lithosphere-asthenosphere boundary (LAB) or if it is caused by inner crustal reverberations. Another negative phase is observed parallel to the 660 phase between 58 s and 65 s. Since this phase shows clearly the moveout of a direct Ps conversion, it is likely caused by a discontinuity within the mantle

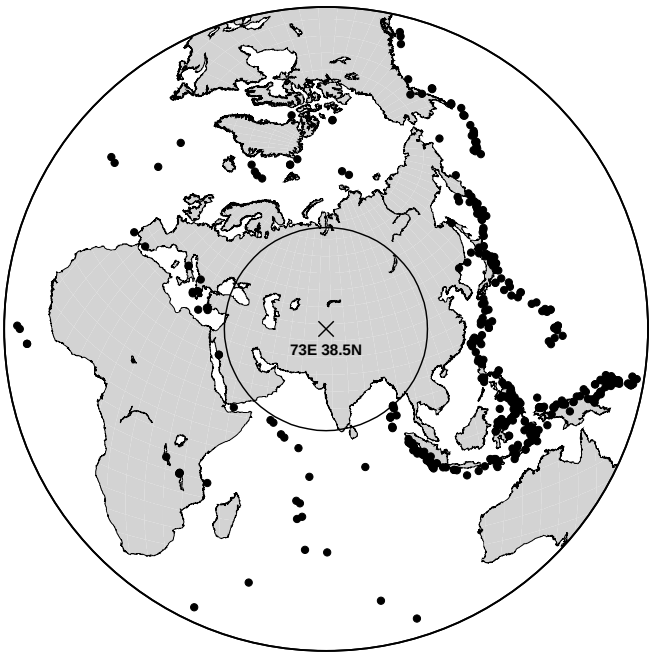

(a) Teleseismic events used for the P-RF analysis

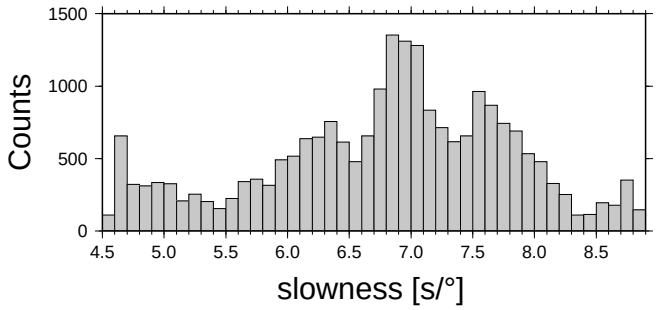

(b) Histogram showing the distribution of slownesses.

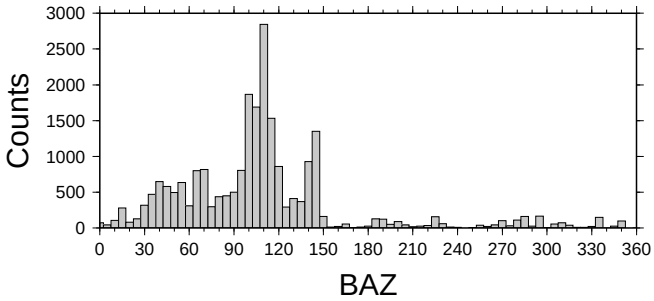

(c) Histogram showing the distribution of azimuths.

Figure 5.1.: Epicenter distribution and statistics of the teleseismic events that have been selected and used to calculate RF at at least one station of our network

transition zone. The corresponding depth is 570 km-580 km.

5.1.2. P-Receiver functions on individual seismic stations

The receiver function processing was performed for each station individually. First, all P wave seismograms were bandpass filtered using a butterworth filter with $0.5s$ and $30s$ as corner periods. Then the events were inspected and selected visually, before the receiver function processing as described in chapter 4 was applied. In the selection and inspection step additional high pass filters (20 s, 15 s, 10 s, 7.5 s or 5 s) were applied individually if needed. In figure 5.3 receiver functions at some exemplary stations are shown.

The figures show moveout corrected individual receiver functions sorted by back azimuth of the event at the station. For moveout correction a reference slowness of 6.4 s/° was chosen. In the top panel the normalized sum of all moveout corrected traces is shown.

At most stations, the Moho phase can be clearly identified, while the interpretation of the other phases is difficult by inspecting them station-wise. At stations P07 and P23, located in the eastern Allay valley and the eastern Pamir, the Moho phases are observed at 8.3 and 8.7 s, respectively. Station BRC9 located in the western Pamir shows two possible amplitudes that can be interpreted as Moho, one at 8 and one at 11.3 s (see also discussion in section 7.4.2). A much earlier time for the Moho conversion is observed for stations in the Tajik Depression as station SHAA, where the Moho amplitude is detected at 5.7 s. Further analysis for individual stations and the determination of crustal thickness and the average crustal velocity ratio v_p/v_s is presented and discussed in chapter 7.

By CCP stacking, the receiver functions from each station are combined with the results of neighboring stations. In this manner phases can be correlated laterally and distinguished from local effects or spurious noise sources. Results from CCP stacking are presented in the following sections and in chapter 6.

5.1.3. South-north mantle cross section

In Fig. 5.4 the cross section along the north south profile is shown, including the upper mantle and the mantle transition zone. This cross section was created by CCP Fresnel zone stacking as described in section 4.9.2. The main global converting discontinuities, namely the Moho, the 410 and the 660 discontinuities, can be recognized clearly. In the Southern Pamir, the Moho is observed in a depth of ∼75 km. Beneath the Central Pamir, the crustal thickness is decreasing to ∼65 km. We observe two positive converters that can be interpreted as Moho beneath the Northern Pamir. The shallower one is at 62 km depth and the

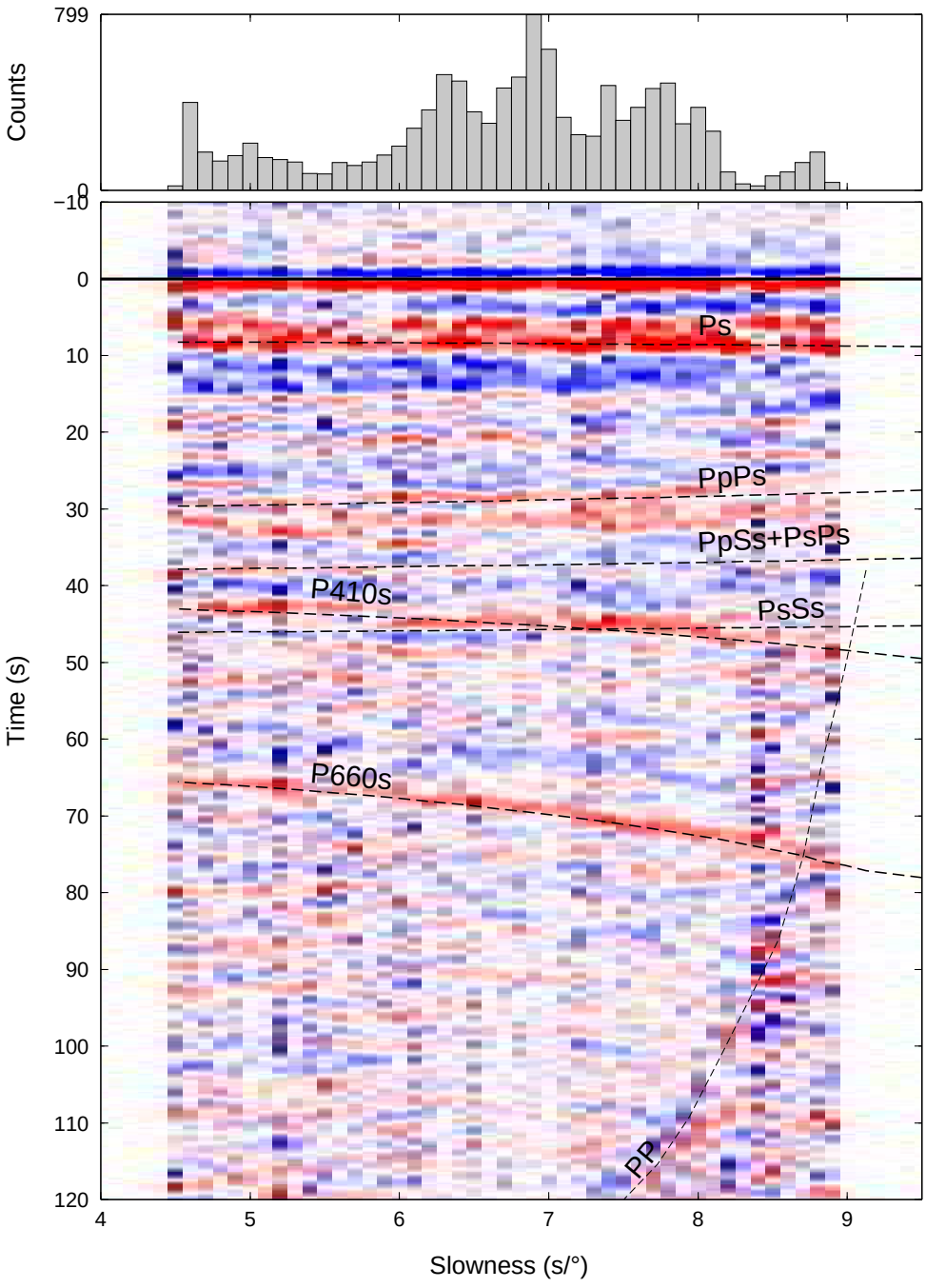

Figure 5.2.: Stack of all P-receiver functions from the TIPAGE deployment sorted by the slowness of the teleseismic wave at the receiver. Theoretical arrival times of direct phases and crustal multiples have been calculated for a 68 km thick crust and upper and lower boundaries of the mantle transition zone in 410 and 660 km depth. Further strong amplitudes in the slowness range 7.5-8.5 between 70 and 120 s could be matched with theoretical PP arrivals.

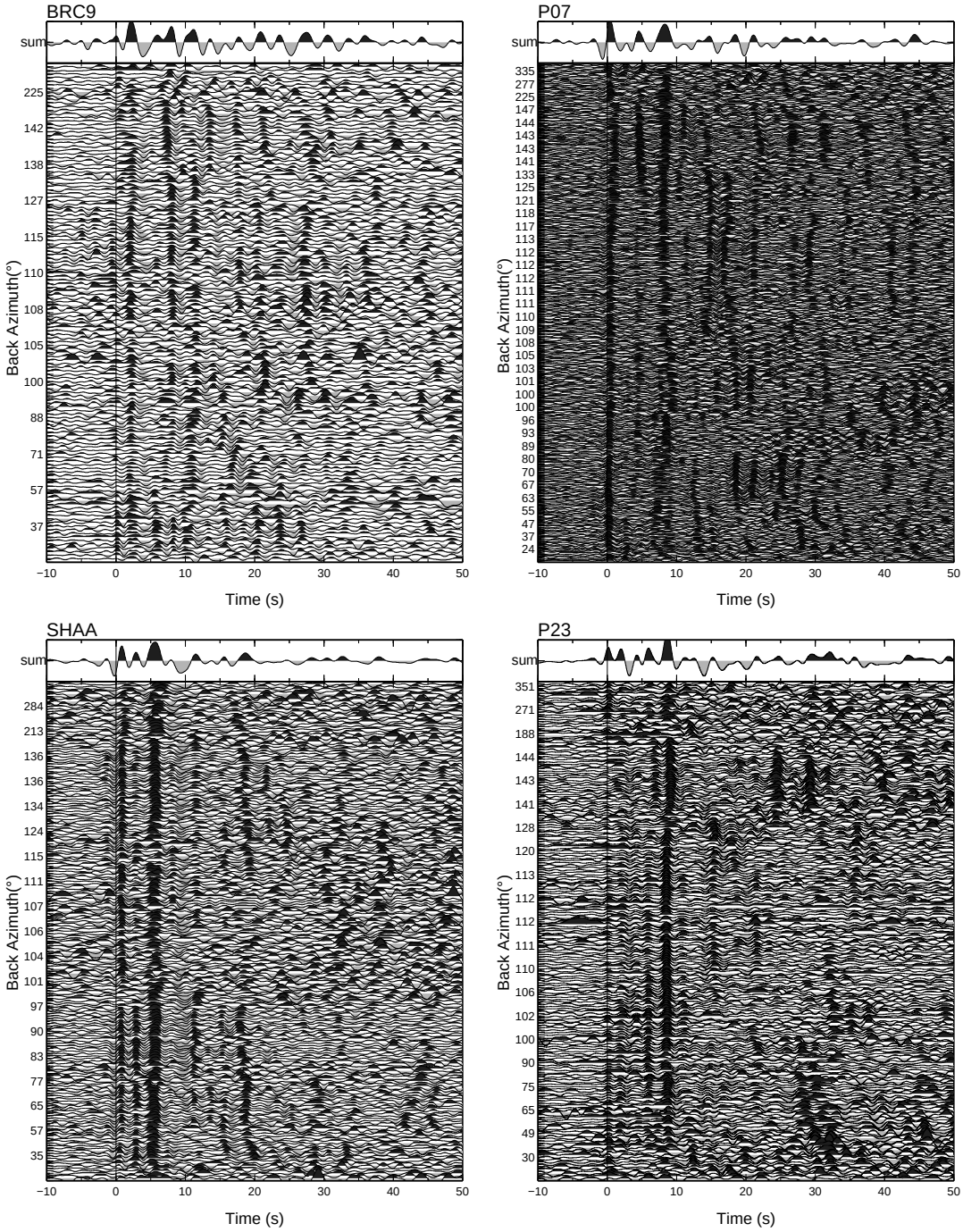

Figure 5.3.: Exemplary results from stations located in the Allay Valley (P07), eastern South Pamir (P23), western Central Pamir (BRC9), and in the Tajik Depression (SHAA). Station locations with names are given in Fig. 7.5(a) on page 120.

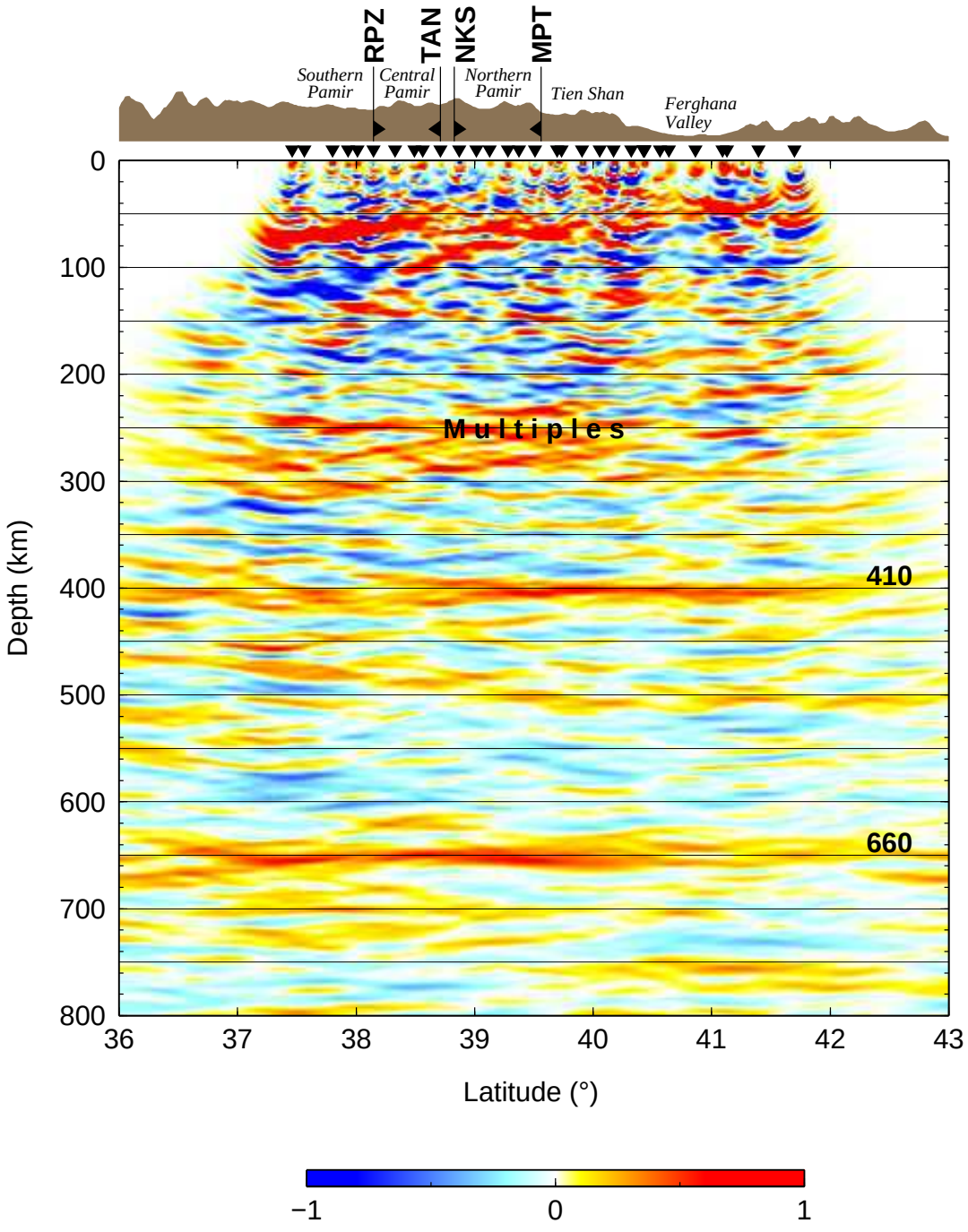

Figure 5.4.: Common conversion point (CCP) image of Q-component receiver functions (QRF) along the N-S main profile. Receiver functions were stacked in the Fresnel zone range. Positive velocity contrasts such as the Moho are shown in red colors, negative velocity contrasts in blue colors. Faults and sutures marked: Main Pamir thrust (MPT), Northern Pamir / Kunlun Suture (NKS), Tanymas Suture (TAN), Rushan Pshart Zone (RPZ).

deeper one at 80 km depth. Crustal thickness and the observation of two Moho phases is discussed in more detail in chapter 7 and section 7.4.2.

At the deepest position of the Moho in the central Pamir the positive converter can be followed continuously towards the south to approximately 100 km. This structure is interpreted as subducting Eurasian crust and will be discussed in more detail in the chapter 6. Towards the north the Moho depth is decreasing to approximately 65 km beneath the Tien Shan. North of the Tien Shan the crustal thickness is decreasing rapidly to 45 km beneath the Fergana basin.

Beneath the southern Pamir a negative phase is observed in approximately 120 km depth. It can be interpreted as the Indian lithosphere asthenosphere boundary (LAB). Often the LAB phase is hidden by the conversions of crustal multiple reverberations. However, since the crust in the study area is very thick the crustal reverberations are expected to occur later. Thus they will be displayed as spurious signals at deeper depths.

The theoretical arrival times of the two strongest multiples ($PpPs$ and $PpSs$) for a 68 km thick crust are between 27.5 s and 38 s (see Fig. 4.3 in chapter 4), which corresponds to the depth range between 250 km and 350 km. In Fig. 5.4 the strong signals in this depth range are labeled as *Multiples*.

The mantle transition zone is clearly visible through the respective discontinuities at 410 km and 660 km (410 and 660 discontinuity). However, the 410 discontinuity seems to shallow a bit beneath the southern Pamir. As it also can be corrupted by $PsSs$ multiple phase (see Fig. 5.2) it is difficult to interpret this pattern.

The 660 discontinuity is not corrupted by multiple phases. A negative converter as observed in the representation in Fig. 5.2 is only observed in a Latitude range from 37° to 38° . This indicates, that the phase observed in Fig. 5.2 is a local discontinuity that might be caused by subduction of lithosphere.

5.2. S-Receiver functions

The S-Receiver functions (S-RFs) method is an observation method independent from P-RFs that observes in principle the same thing, namely velocity contrasts in the S-velocity structure. Since compared to P-waves the frequency content of S-waves is shifted to longer periods, in principle the resolution of S-RFs is lower than the resolution of P-RFs. However, since the observation is independent from P-RFs it is capable to confirm P-RF observations in case of uncertainty. Moreover, compared to P-RFs there are some advantages of the S-RF method, that are described in the following.

First, since the S-RF method uses S-to-P converted waves that arrive in advance to the main S wave at the seismic station, the method has the advantage that the

crustal conversion phases are separated from the crustal multiple reverberations that arrive after the main S phase.

Thus, in situations in which for P-RFs direct conversion phases are overlain by multiple reverberations, S-RFs can increase the resolution and avoid misinterpretations of multiple phases in P-RFs.

A second difference is that the incidence angles of the S-to-P converted phases are larger than the incidence angles of P-to-S converted waves, which results in larger distances of the conversion points from the stations. This leads to less resolution below a single station. The advantage is, however, that the investigation area of a seismic network increases compared to P-RFs, since conversions that take place at large distance offsets from the stations can be observed. For example in case of the TIPAGE deployment the Moho conversion beneath the Hindu Kush can be deduced from stations in the Tajik Depression using S-Receiver functions (see section 7.5), which is not possible using P-RFs.

5.2.1. Event selection for S-Receiver functions

A useful range of epicentral distances for calculation of S-RFs is 55° to 85° (Yuan et al., 2006). Fig. 5.2.1 shows the epicenters of the events of this distance range that were selected from the NEIC catalog for S-RF-analysis. Since the events used for S-RFs are a subset of the events used for P-RFs, as for P-RFs, the most events have azimuths from eastern to southeastern directions, emerging at the subduction zones in Indonesia and Japan and the histogram for the azimuthal distribution looks very similar. However, the azimuthal coverage is worse, since some areas with at least few P-RF events are not covered at all by S-RFs. The larger incidence angles of the S-to-P converted waves are also reflected in the slownesses of the events, that are, compared to the P-RFs, shifted to higher values and ranging from 9.4 $s/°$ to 13.6 $s/°$.

5.2.2. Piercing Points

For S-Receiver functions the conversions points are located far away from the stations compared to the conversion points of P-RFs. This is due to the large incidence angle of S-to-P converted waves. Therefore the resolution of the observation is dependent on the azimuthal distribution of the earthquakes. In Fig. 5.6 the number of S-to-P conversion points, that are used for the observations, is shown per $1° \times 1°$ squares. The conversion points have been calculated and counted in two depth layers (68 km and 110 km depth.) Since most events are coming from around 40° and 110° (see Fig. 5.2.1c), the area of resolution is shifted from the station locations towards eastern directions. In deeper depths the shift gets stronger and the conversion points become more

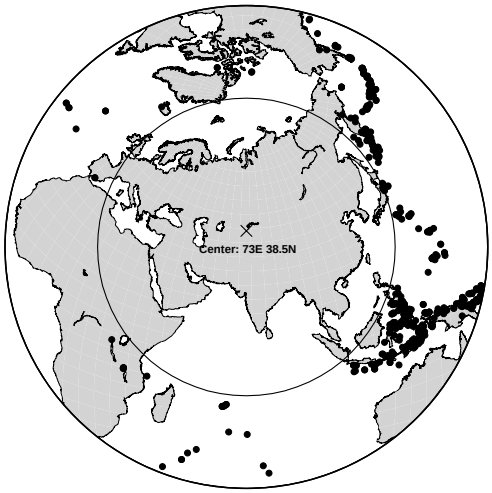

(a) Teleseismic events used for the S-RF analysis

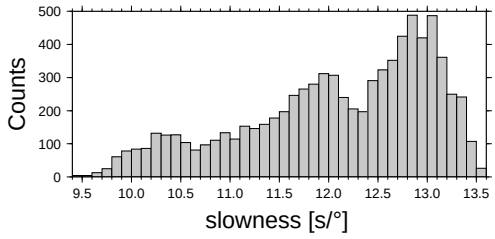

(b) Histogram showing the distribution of slownesses.

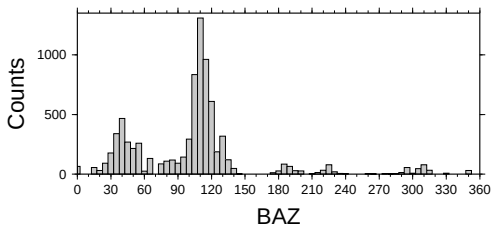

(c) Histogram showing the distribution of azimuths.

Figure 5.5.: Epicenter distribution and statistics of the teleseismic events that have been selected and used to calculate S-RF at at least one station of our network

distributed. Therefore $1^\circ \times 1^\circ$ squares with high number of conversion points are getting less frequent in 110 km than in 68 km depth, but the absolute number of squares with more than 20 conversion points is higher. In both, the 68 km and 110 km depth maps the areas where S-to-P conversions are located fill some areas where no stations are situated, as for example in northern Afghanistan (around 37.5°N, 71°E).

5.2.3. Distance stack

To present the data, the upper panel of Fig. 5.7 shows all S-RFs that pierce the Moho in the area of the Pamir. The S-RFs have been binned and stacked in distance intervals of 0.5°. The piercing points in 68 km depth for each S-RF were determined and only those S-RF traces selected that have piercing point coordinates in the latitude and longitude ranges from 35.0° to 39.5° and from

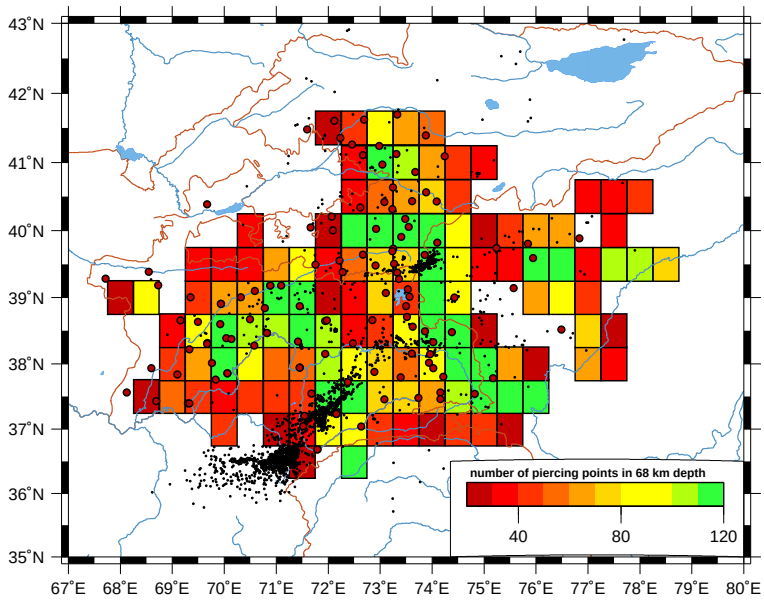

(a)

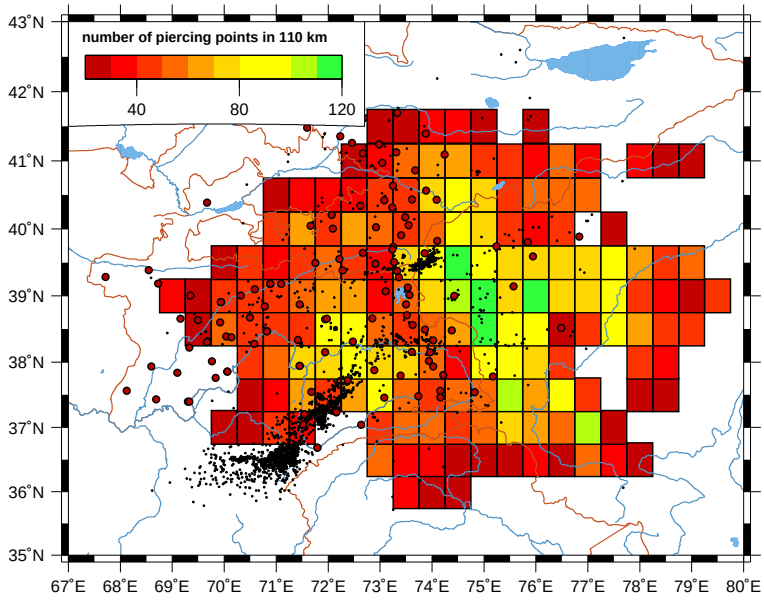

(b)

Figure 5.6.: Number of Sp conversion points in 68 and 110 km depth. Only squares with more than 20 piercing point per square are shown. Red circles show the station locations. Black dots are the earthquakes epicenters from Sippl et al. (2013b) with magnitudes M_w larger than 3.

71.0 to 75.0, respectively.

For comparison, the lower panel of the figure shows synthetic S-RFs processed in the same way as the data. The synthetic seismograms were computed with the reflectivity algorithm (Fuchs and Müller, 1971) implemented by Kind (1985) using the 1D velocity model shown in the upper right plot in Fig. 5.7. Travel times of conversion phases are plotted on top (dashed lines), deduced from this model using the software *TauP* (Crotwell et al., 1999).

In this representation, the S-RF data are plotted relative to the S-arrival times. The S-to-P converted phases, labeled as Smp, SLp, $S410p$, are identified as the conversions at the Moho, the lithosphere-asthenosphere-boundary (LAB) and the 410 discontinuity, respectively. These phases are precursor to the S-arrival. Thus they have negative arrival times. The phases with positive arrival times, labeled as $SPvmp$, $SPnp$ and $SPmp$, are crustal reverberations of S waves that have been converted to P waves at the surface. ScS and SKS phases are S-waves that have been reflected at the core-mantle boundary or passed the liquid core as compressional(K)-waves, respectively. Conversions of ScS to P waves at the Moho, the 410- and 660-discontinuities are labeled as $ScSmp$, $ScS410p$ and $ScS660p$, respectively. In the data an additional phase is observed with the moveout of an ScS-to-P converted wave. The depth of a converter that produces an ScSp-phase that match the observation has been determined by modeling to 1100 km. The appearance of a seismic discontinuity in this depth has been reported before and interpreted to be caused by subducted lithosphere (Vinnik et al., 2001; Deuss and Woodhouse, 2002).

The Moho signal from the data is much more heterogeneous than in the synthetic seismograms. In the distance range from 57° to 67° a strong anomaly in the Moho depth is present. The forward modeling does not show this anomaly, thus it probably can not be explained using a 1D velocity model with a laterally constant Moho depth. This anomaly can either be an error in the processing or be produced by the 3D structure and the lateral variations of the Moho or the presence of a subducting slab. In the following section this observation is further analyzed.

5.2.4. Comparison of a cross section for different slowness ranges

In the distance stack in Fig. 5.7 the Moho phase shows a strong anomaly for epicentral distances smaller than 64°. To identify the reason for this strong offset, in the following, S-RFs cross sections with different slowness ranges are compared. Events from epicentral distances of 64° have an slowness of about $12.4 s/°$. For equal focal depths, events from larger distances have smaller slownesses and vice versa.

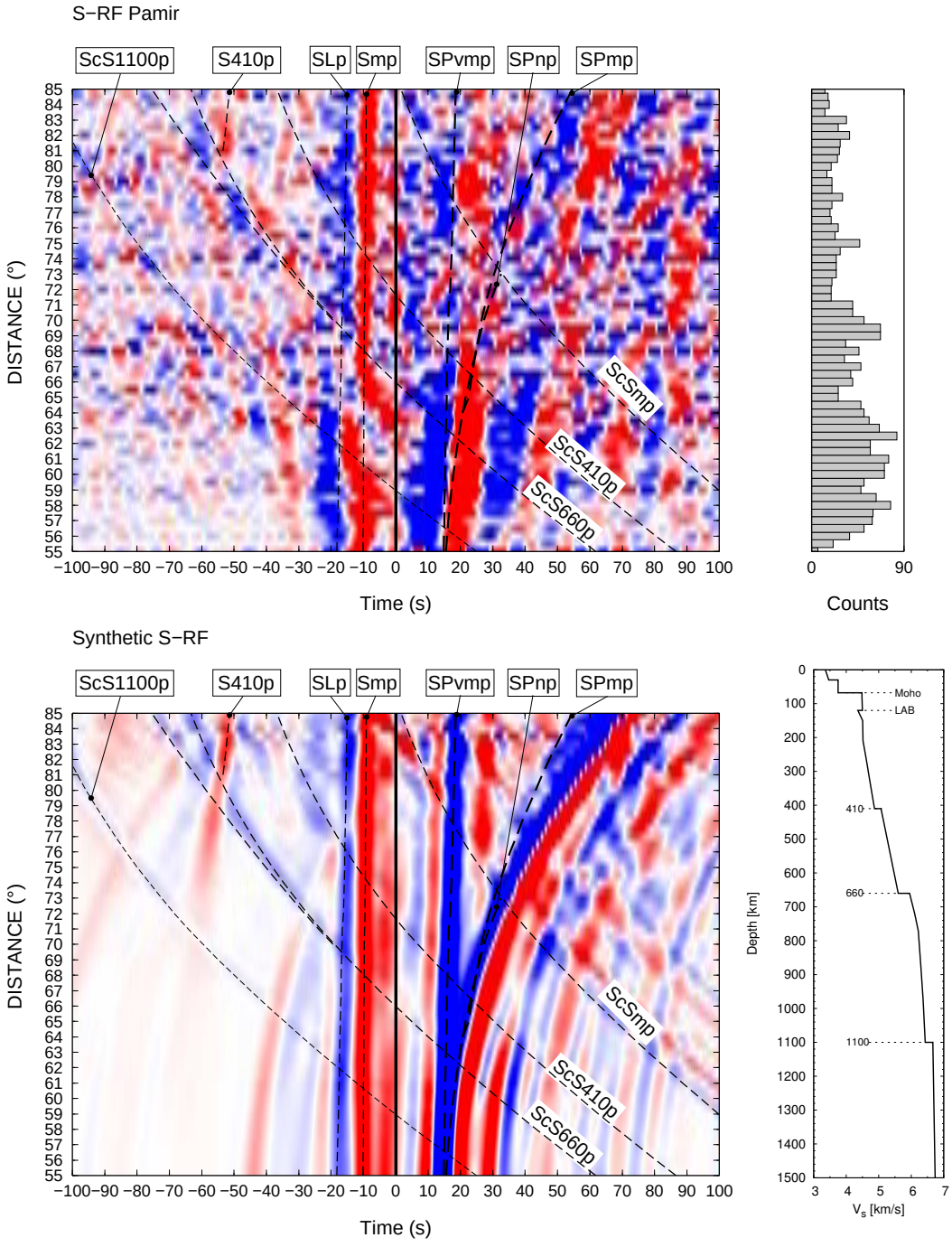

Figure 5.7.: Observed and synthetic S-RFs for the Pamir. Above: Observed S-RFs binned in distance ranges of 1° and summed. Latitude and longitude ranges of the piercing points at 68 km depth are from 35.0° to 39.5° and from 71.0 to 75.0, respectively. The number of seismograms that have been summed in a distance bin is shown in the histogram on the right side.Below: Synthetic S-RFs calculated from the 1D model shown in the right figure. The phases are identified using *TauP* and the arrival times are plotted on top of observed and synthetic S-RFs.

In Fig. 5.8 west-east and south-north cross sections are shown from a center latitude of 37.5°N and a center longitude of 73.0°E, respectively. In the first row, the slowness range has not been limited, whereas in the second and third rows the slowness range has been limited to slownesses smaller and larger than 12.4 $s/°$. Comparing the cross sections in the second and third rows, a strong difference of the Moho signal is obvious in a longitude range from 72.0° to 73.5° and in a latitude range from 36.5° to 38.0° . For slownesses smaller than 12.4 $s/°$, the Moho signal can be traced at 70 to 80 km depth. This is also the dominant Moho depth phase in the first row, where events with all slownesses are used. However in the two cross sections, from events with larger slownesses a positive (red) phase is present in >100 km depth and a strong negative (blue) phase is present in 150 km depth, whereas the Moho phase in 70 to 80 km depth is more diffuse and discontinuous. In both the west-east and in the south-north cross sections the two phases in 100 and 150 km depth terminate in northern and western directions at the locations of intermediate depth seismicity. This is the position where the Indian indenter is supposed to be located (Sippl et al. (2013a), Fig.10). Thus a high velocity zone (HVZ) as observed from the two phases can be interpreted as the presence of underthrusting lithosphere of India. The presence of Indian Lithosphere beneath large parts of the Tibetan plateau has been reported from independent methods as tomography (Tilmann et al., 2003; Li et al., 2008), receiver functions (Kind and Yuan, 2010) and surface wave tomography (Priestley et al., 2008), which is compatible with a northward extent of the India indenter as far as the southern Pamir.

Forward modeling

To understand why the observation is restricted to small slownesses we perform forward modeling using RAYSUM (Frederiksen and Bostock, 2000), which is capable to model 2D structures with inclined layers.

The two phases that are observed for large slownesses show an inclination towards western and northern directions. Thus in the forward modeling an inclined high velocity zone (HVZ) has been included in the model. The direction of inclination has been chosen to west-northwest (290°) and the inclination angle to 23°. In Fig. 5.9 the forward modeling results are shown. The intersections of the model layers with the cross sections at the positions of the receiver are shown as black lines in Fig. 5.9(b). The geometry of events is restricted to two Azimuth ranges (110° and 40°), since the data are dominated by these two azimuths. For both azimuths, the whole slowness range of the data is used.

Fig. 5.9(a) shows the resulting traces from forward modeling for events with 110° back azimuth. The Moho phase is the strong positive phase between 5s and 10s. The HVZ is represented as the two seismic phases between 10 s and 30 s. The inclination of the HVZ causes an amplitude inversion for events with

small slownesses. This is also observable in the cross sections in the first row of Fig. 5.9(b). Here, the modeling is performed for one station only . If more than one station is contributing to the cross section, the amplitude inversion can cause a annihilation of the phases . However, when only large slownesses are taken into account the phases with inverse amplitudes are removed. An inclination of the Moho can cause the Moho to be invisible for events with large slownesses for the given station event geometry. In the forward modeling an inclination of the Moho east-southeast has been chosen. The Moho phase vanishes for large slownesses and events with a back azimuth of 110° (Fig. 5.9(a) and last row of (b)). Since the Indian indenter is supposed to terminate around 38.5°N the events from 40° do not show converted phases from the indenter since the offset of the conversion points is too far north. In the RAYSUM code lateral terminations of layers are not provided. Thus the northern continuation of the HVZ is shaded.

The forward modeling shows, that the observation of two deep phases only for large slownesses, as shown in Fig. 5.8, can be caused by an inclined HVZ south and east of the zone of intermediate depth seismicity. The vanishing of the Moho signal can be caused by an inclination of the Moho.

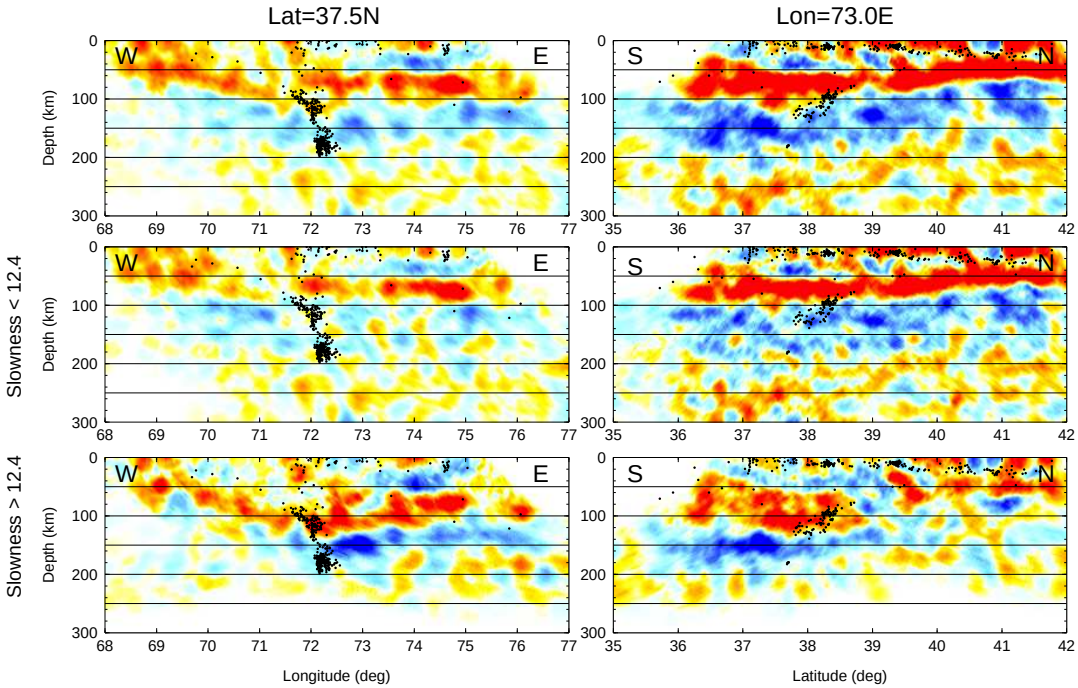

Figure 5.8.: S-RF cross sections in W-E direction along the parallel north line at 37.5° (left side) and in S-N direction along the 73.0°E meridian (right side). The sections have been computed for teleseismic waves from different slowness ranges. First row: S-RFs from all events are summed. Second row and third row: only S-RFs from waves with slownesses smaller and larger than 12.4s/° have been used, respectively.

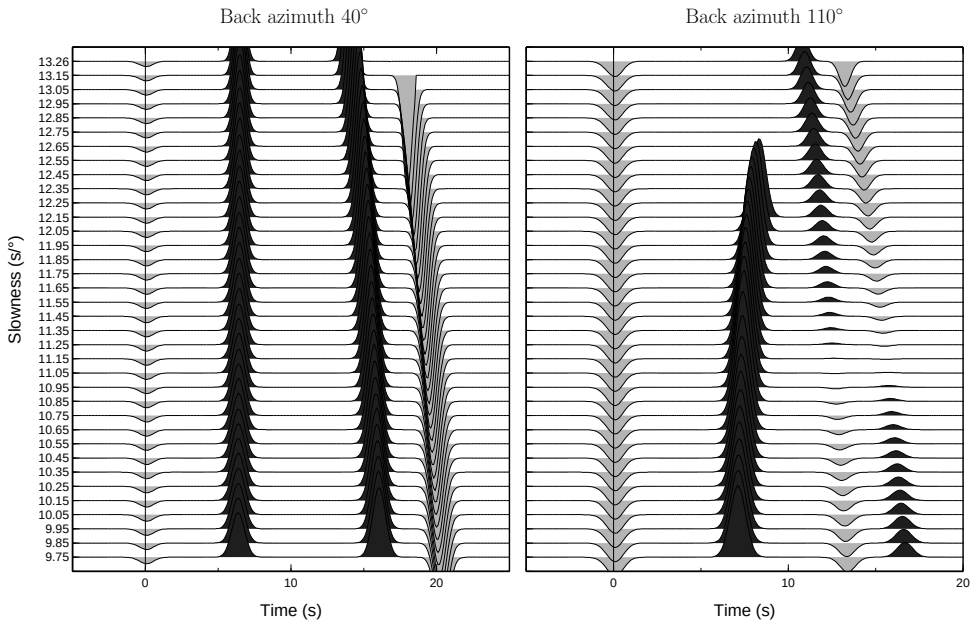

(a)

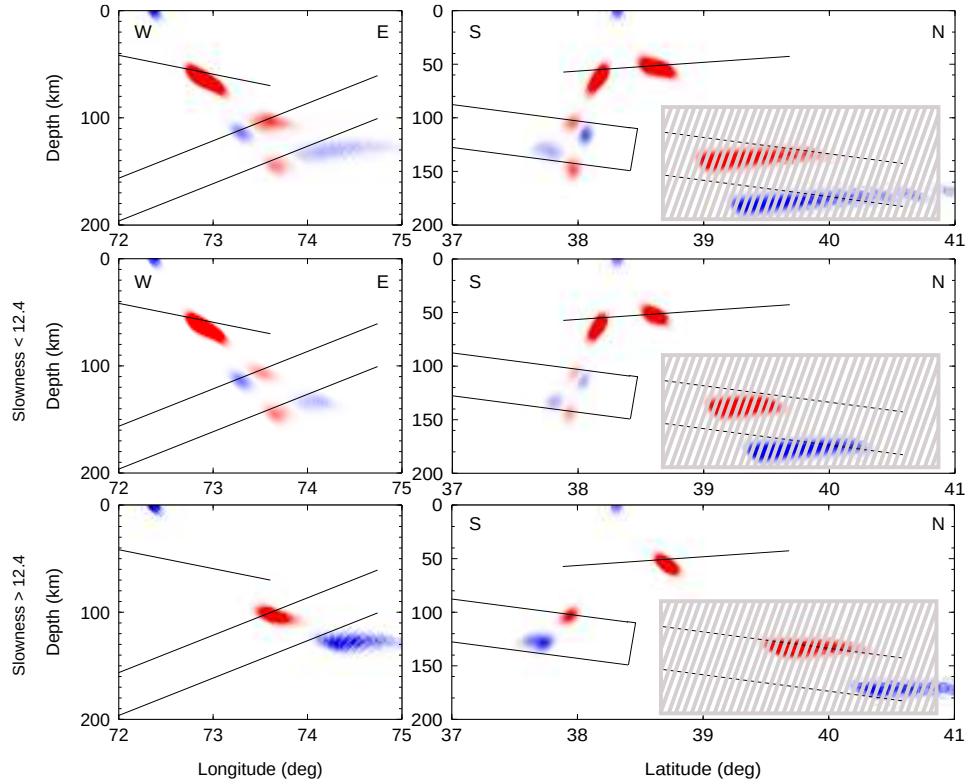

(b)

Figure 5.9.: S-RF forward modeling results for a high velocity zone (HVZ) in the upper mantle that is inclined in western and northern direction. a: S-RF traces for events with 40° (left) and 110° (right) back azimuths and different slownesses. b: Migrated cross sections of the synthetics. The Figure compilation is analogue to Fig. 5.8. In the S-N cross section the HVZ-amplitudes north of 38.5 are shaded since the Indian indenter is supposed to stop here. These amplitudes belong to the seismic waves with back azimuths of 40°. In the W-E cross sections only amplitudes from waves with 110° back azimuths are plotted.

5.3. P- and S-Receiver function cross sections

In this section P-RF and S-RF cross sections along the same section paths are shown and compared. Both methods are complementary to each other. On the one hand, since both methods have slightly different advantages and difficulties the comparison of both independent observations can confirm each other, since it is unlikely that both methods show spurious signals with the same sign at the same location. On the other hand, the comparison can prevent misinterpretations of spurious signals as for example the multiple phases of P-RFs. Furthermore the observation area of P-RFs and S-RFs is different due to different moveout of the rays.

Fig. 5.10 shows the positions of the cross sections that are compared in this section. Cross sections 1 and 2 are west-east (W-E) and west-northwest-east-southeast (WNW-ESE) cross sections passing through the south-western part of the Pamir slab. Section 3 is a south-north (S-N) cross section passing through the Hindu-Kush slab. Sections 4 and 5 are S-N cross sections east of the profile, at the locations where the piercing point density is highest for P-RFs and S-RFs, respectively. The latter are passing the Pamir slab close to its eastern termination.

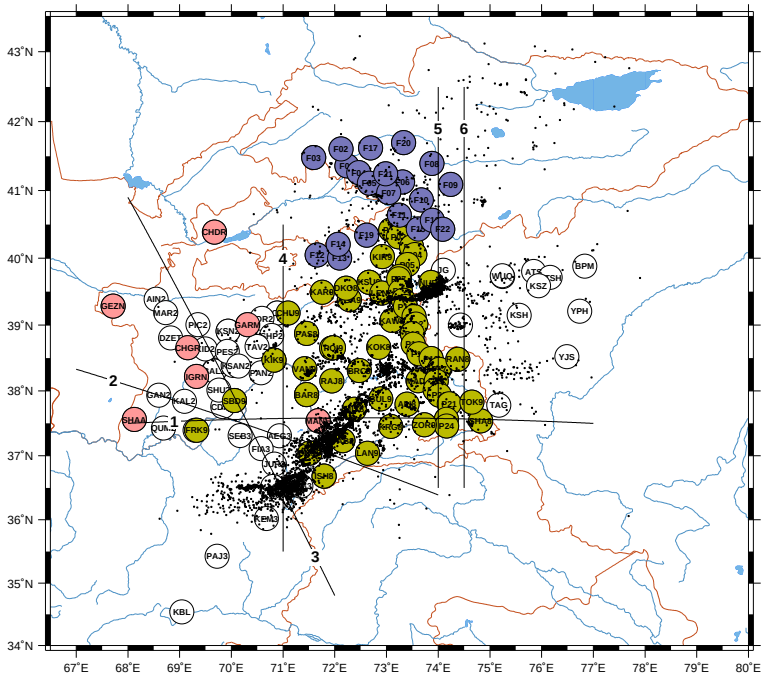

Figure 5.10.: Map showing locations of seismic stations and cross sections.

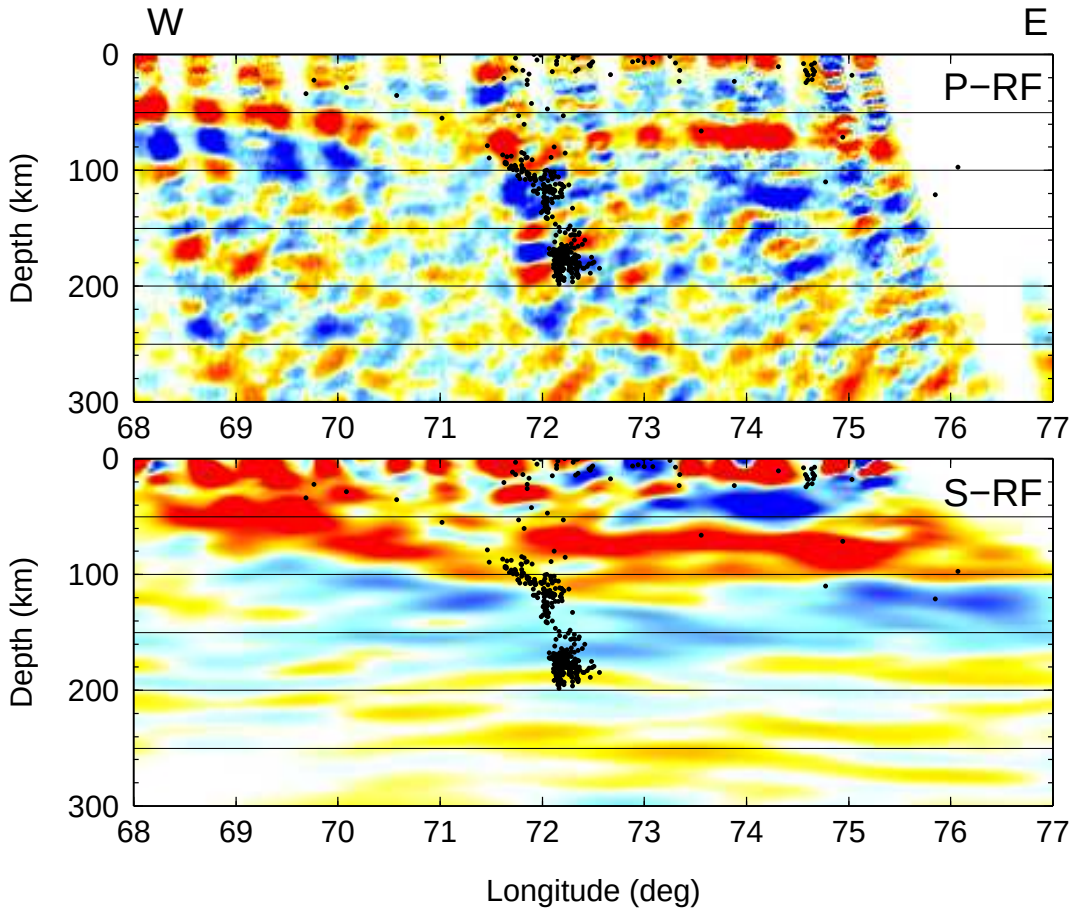

Figure 5.11.: P-RF (upper panel) and S-RF (lower panel) cross section in W-E direction (Line 1 in Fig. 5.10). Conversions with up to 50 km offset from the section line are plotted. Bluish colors and reddish colors show negative and positive RF amplitudes, respectively. The P-RF cross section is gained from CCP stacking along the ray path. A lateral boxcar smoothing filter with a diameter of 20 km has been applied. The S-RFs have been migrated using Fresnel zone stacking technique. No further filter was applied.

5.3.1. West-east cross section

The W-E cross section shown in Fig. 5.11 has its center along the 37.5°N circle of latitude. Conversions with offsets up to 50 km from the center line are plotted. In the P-RF- cross section the Moho and a parallel running negative phase are observed clearly. Both phases are dipping towards the Pamir. Around 71°E the phases cannot be observed due to a lack of stations at this location. In the S-RF cross section, however, this gap is filled due to the larger incidence angles of the Sp converted waves. In this image, the positive and negative phases are observed as well. It shows that the Moho of the Tajik Depression is connected to the zone of intermediate depth seismicity. Since the negative phase is also observed in S-RFs the negative phase in the P-RFs is very likely caused by direct conversion and not by multiple reverberations alone. Thus it is interpreted as the lithosphere asthenosphere boundary (LAB).

The interpretation of this part of the cross section is that it shows the subduction of the Tajik Depression beneath the Pamir in west to east direction. The lithosphere of the Tajik Depression is imaged with a thickness of 80 km which appears to be very thin, whereas the crust with at least 40 km appears to be thick. Thus the mantle lithosphere has only a thickness of about 40 km. This observation is quite enigmatic, since such thin mantle lithosphere is typical for oceanic lithosphere (Gung et al., 2003), whereas the crustal thickness is too thick for oceanic crust. Thus, if the Tajik Depression is a continental plate, parts of the mantle lithosphere may have been removed. As a mechanism, lithospheric thinning in back-arc regions of oceanic subduction zones as described for example by Currie et al. (2008) may apply here, since the southern boundary of Eurasia has a long pre-collisional history of subduction of the Tethys ocean. The observed steep angle of the subduction supports the observation of thin lithosphere, since a thick mantle lithosphere would bear a high flexure rigidity, which would probably avoid steep angle subduction.

East of 70°E, the cross section passes the Southern Pamir. Here we observe a Moho in around 70 km depth. In the S-RF cross sections a strong negative phase is imaged in the crust beneath the eastern part of the Southern Pamir. This indicates a low velocity zone in the crust. The location of this observation correlates to high surface heat flow reported by Duchkov et al. (2001), a strong conductivity anomaly (Sass et al., in press; Sass, 2013) and low seismic P-velocities combined with high v_p/v_s values in the mid-to lower crust reported by Sippl et al. (2013a). The conductivity anomaly is interpreted as partially molten crust, which is consistent with the low seismic wave speeds observations from tomography as well as from S-RFs. In the P-RF cross section around 74°N in 30 km depth a negative signal is observable, that is comparatively small but consistent. The weakening of the signal in P-RF compared to the S-RF signal is possibly caused by destructive interference of direct Ps phases with multiples

from the sedimentary layer.

As discussed in the previous section in the S-RF image two signals implying the presence of an inclined high velocity zone are observable in the upper mantle beneath the Southern Pamir. This is interpreted as underthrusting Indian lithosphere colliding with the slab of the Tajik Depression at the zone of intermediate depth seismicity. Towards the east a negative converter is observed by S-RFs in 120 km depth to the east of 75°N. In the P-RF cross section a strong negative phase is observed in 120 km depth between 74°N and 75°N. The P-RF phase however can also be caused by multiple reverberations of the strong negative converter at 30 km depth. The negative phase in the S-RF cross section at 120 km depth is interpreted as lithosphere asthenosphere boundary of Tarim.

5.3.2. West-northwest - east-southeast cross section

The cross section shown in Fig. 5.12 intersects the intermediate depth seismic zone perpendicular to strike in WNW to ESE direction. The intermediate depth earthquakes show a continuous arc in this projection. As in Fig. 5.11 the P-RF and S-RF cross sections show west of the earthquake zone clear negative and positive signals from the bottom of the lithosphere and the Moho, respectively. The observation of the signals in the P-RF image terminates at 70°E, whereas the S-RF show the continuation of the signal in the P-RF image. The shallow western termination of the earthquake zone lies between the Moho signal in 90-100 km depth (only observed by S-RFs) connected to the west to the Tajik Depression and a shallower Moho signal connected to the east with the Moho beneath the Pamir (observed by P-RF and S-RF). Since the upper end of the earthquake zone is situated on top of a Moho signal, the earthquakes seem to originate from within a layer of the Tajik Depression crust. Since the earthquakes are forming a continuous arc, this cross sections suggests, that the crustal layer is going down to at least 250 km depth. However, here the crustal layer is too thin to be resolved with the given station geometry. In chapter 6 results along the S-N-cross sections are discussed in detail, where a crustal layer can clearly be resolved hosting the intermediate depth earthquakes along the S-N seismological profile. East of the earthquake zone P-RF and S-RFs consistently show a negative phase at 150 km east of 72°E depth which might originate from underthrusting India.

5.3.3. Cross sections passing the Hindu Kush seismic zone

Fig. 5.13 shows cross sections passing the Hindu Kush seismic zone in two different directions. In the projection shown in Fig. 5.13(a) the Hindu Kush seismic zone appears as an arc dipping in NNE direction, while in the S-N cross section

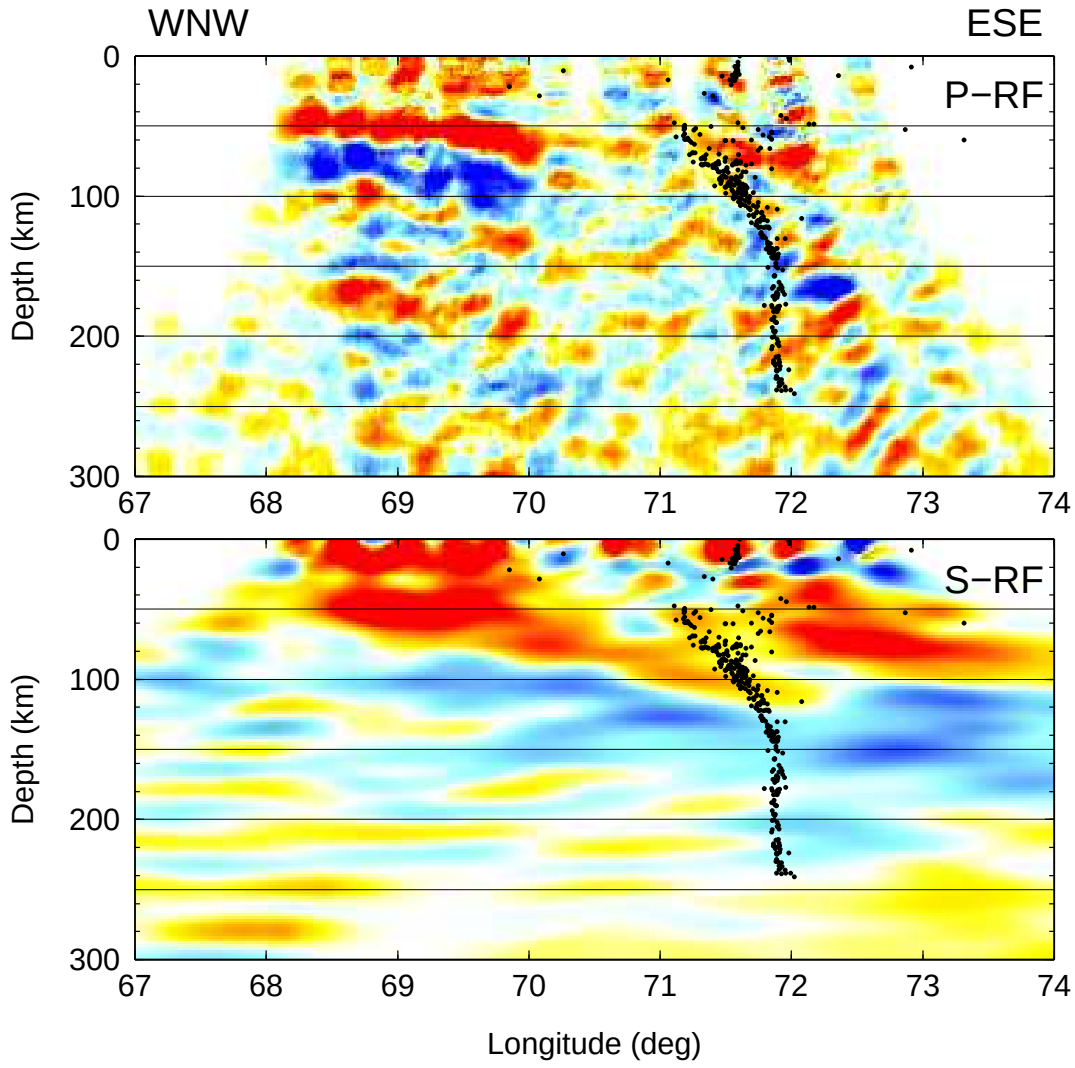

Figure 5.12.: Comparison of P-RF and S-RF cross section in WNW-ESE direction (Line 2 in Fig. 5.10). Black dots show the locations of intermediate depth earthquakes (Sippl et al., 2013b). Conversions with up to 50 km offset from the section line are plotted. Bluish colors and reddish colors show negative and positive RF amplitudes, respectively.

in Fig. 5.13(b) the seismic zone appears much more complicated.

In both directions, the P-RF sections show clear signals only north of 38°N . Here, at the north western edge of the Pamir, the Moho is observed to be at 50 to 60 km depth. South and north of 38.5°, where the crustal thickness reaches with ∼50 km a local minimum, the Moho appears to be inclined and deepening towards SSW and NNE, respectively. In the P-RF sections no structures can be resolved in the latitude range from 36.8°N to 38°N , because in this range the cross sections pass through northern Afghanistan, where either no stations could be deployed so far (north of 37.5°N) or for the deployed stations (south of 37.5°N) only a small amount of data was available at the time when this analysis has been done. Between 36°N and 36.8°N the P-RFs show a positive conversion at ∼70 km depth that can be interpreted as Moho. This phase lies in between a shallower seismic cluster in 40-60 km depth and the upper end of the Hindu Kush seismic zone in intermediate depths > 75 km.

S-RF conversions are also present in the area below 38°N (see Fig. 5.6). Since the stations that have been deployed in Afghanistan are short period stations, the S-RF shown here are exclusively conducted from data recorded at stations deployed in Tajikistan.

Between 37.4° and 39.5° the S-RF Moho phase has a large amplitude and shows an inclination of about 12° and is deepening due south. The Moho signal from P-RFs and S-RFs north of 38°N deviate from each other. This can be caused by the inclined conversion layers, since the CCP stacking code causes an aberration for inclined conversion layers the converters at too deep and too shallow depths for P-and S-RFs, respectively. South of 37.4° the Moho phase gets weaker and it seems to split into two Moho-signals. One positive phase is running in constant depth (in 80-90 km depth) and the other is running to deeper depths into the mantle. A negative phase can be observed running parallel to the deeper Moho phase at 90 to 150 km depth. Both positive and negative phases connect the Moho and LAB in the Tajik Depression with the lower part of the Hindu Kush seismic zone.

This observation suggests that the Tajik Depression is subducting in southern direction beneath the Hindu Kush. However, the geometry of the Hindu Kush seismic zone does not agree with the position of the imaged boundaries. In Fig. 5.13(a) the seismic zone appears to be opposed to the subducting plate of the Tajik Depression. Fig. 5.13(b) shows that the seismic zone has a kink at the location where the plate boundaries reach the earthquake zone. The form of the seismic zone and the location of the converter suggest that the material (slab ?) hosting the earthquakes was deformed by a collision with the subducted plate of the Tajik Depression in about 150 km depth. In contrast to the Pamir seismic zone, the Hindu Kush seismic zone seems not to be hosted in the crust of the Tajik Depression. At least the upper 140 km appear as a NNE-ward inclined

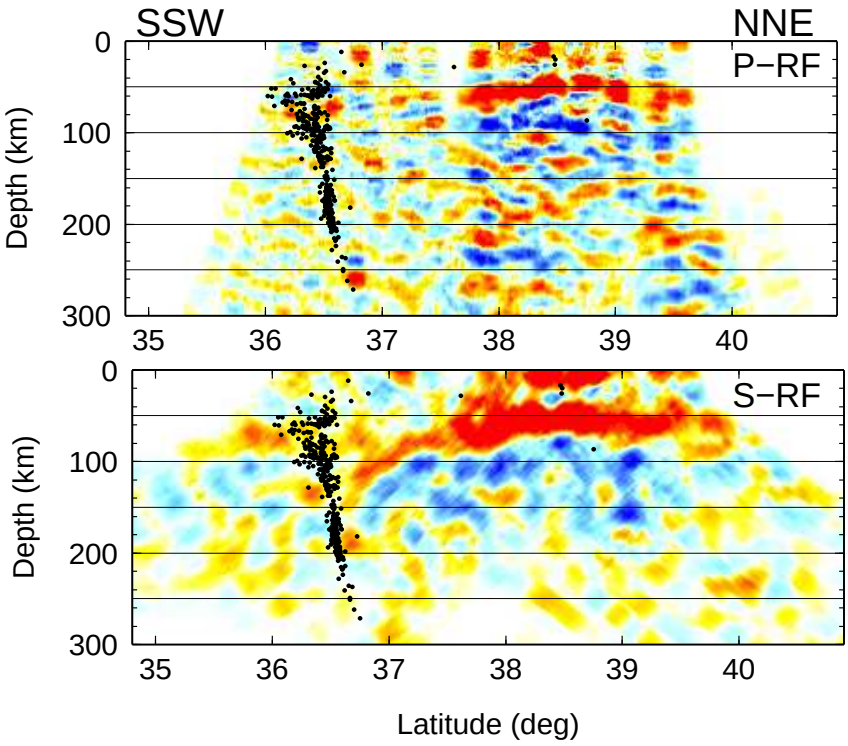

(a) Line 3

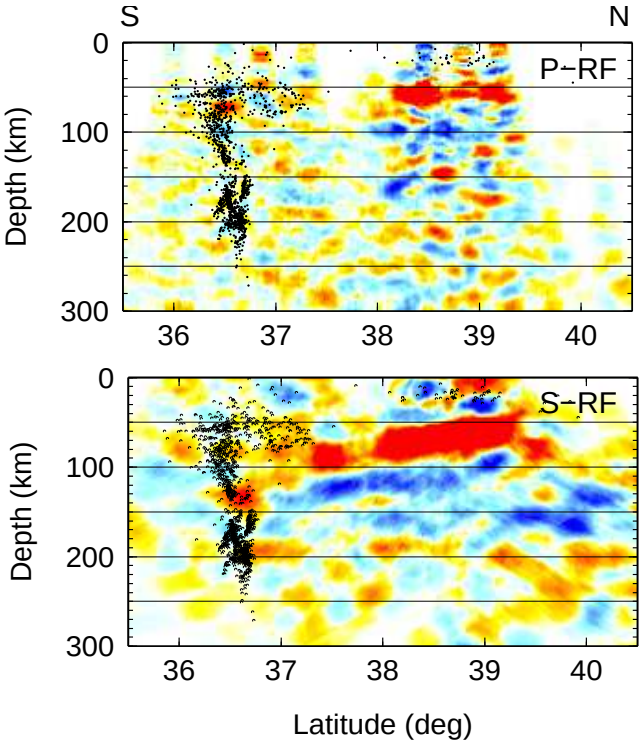

(b) Line 4

Figure 5.13.: SSW-NNE (Line 3 in Fig. 5.10) (a) and S-N (Line 4 in Fig. 5.10) (b) cross sections cutting through the Hindu Kush seismic zone obtained from P-RFs and S-RFs as labeled. Beneath the Tajik Depression P-RF and S-RFs show consistent converters of the Moho (red) and LAB (blue). Between 36.5° and 38° only the S-RFs show a signal due to a lack of data in P-RFs for this region.

zone that has an opposing dipping direction to the observed phases associated to the plate of the Tajik Depression. This geometry suggests that the material hosting the earthquakes is originating from southern direction and belongs to a separate slab, as suggested e.g. by Burtman and Molnar (1993).

5.3.4. South-north cross sections at 74°E and 74.5°E

The S-N cross sections along the 74°E and 74.5°E are located at the highest piercing point density in our network east of the seismic profile. For P-RFs and for crustal structures in the S-RF cross section the piercing points are more concentrated at 74°E, whereas in deeper depths a higher S-RF piercing points density is at 74.5°E. In the P-RF cross section in the upper mantle in 90 to 150 km depth a pair of phases can be resolved indicating a narrow low velocity zone (LVZ) dipping from 38.5°N due south. That LVZ is interpreted as subducting crust which is discussed in detail in chapter 6. The offset between intermediate depth seismicity and the LVZ is caused by aberration in the CCP stacking caused by the inclination of the conversion layers (see section 6.2).

In the S-RF cross sections along the 74.5°E meridian (lower panel of Fig. 5.14(b)) between 38.5°N and 39.5°N two Moho phases are observed. The upper one is imaged at 38.5°N at about 75 km depth and shallowing to 50 km at 395°N, the lower one is imaged at 39.5°N at 65 km depth dipping due south to 100 km depth at 38.8°N. This observation from S-RFs confirms the observation of subduction of Eurasian crust beneath the Pamir. Moreover in the S-RF cross section we observe a negative converter running parallel to the Moho phase in deeper level at 95 km to 130 km depth. This converter is interpreted as LAB and indicates a thickness of the mantle lithosphere of about 30-40 km which is consistent with the thickness that is observed in the E-W cross section for the Tajik Depression.

In Fig. 5.14(a) south of 38.0°N a positive converter at 100 km depth and a negative converter at 150 km depth are interpreted as the Indian indenter, as discussed in section 5.2.4. Further east in Fig. 5.14(b) this phase is defocused.

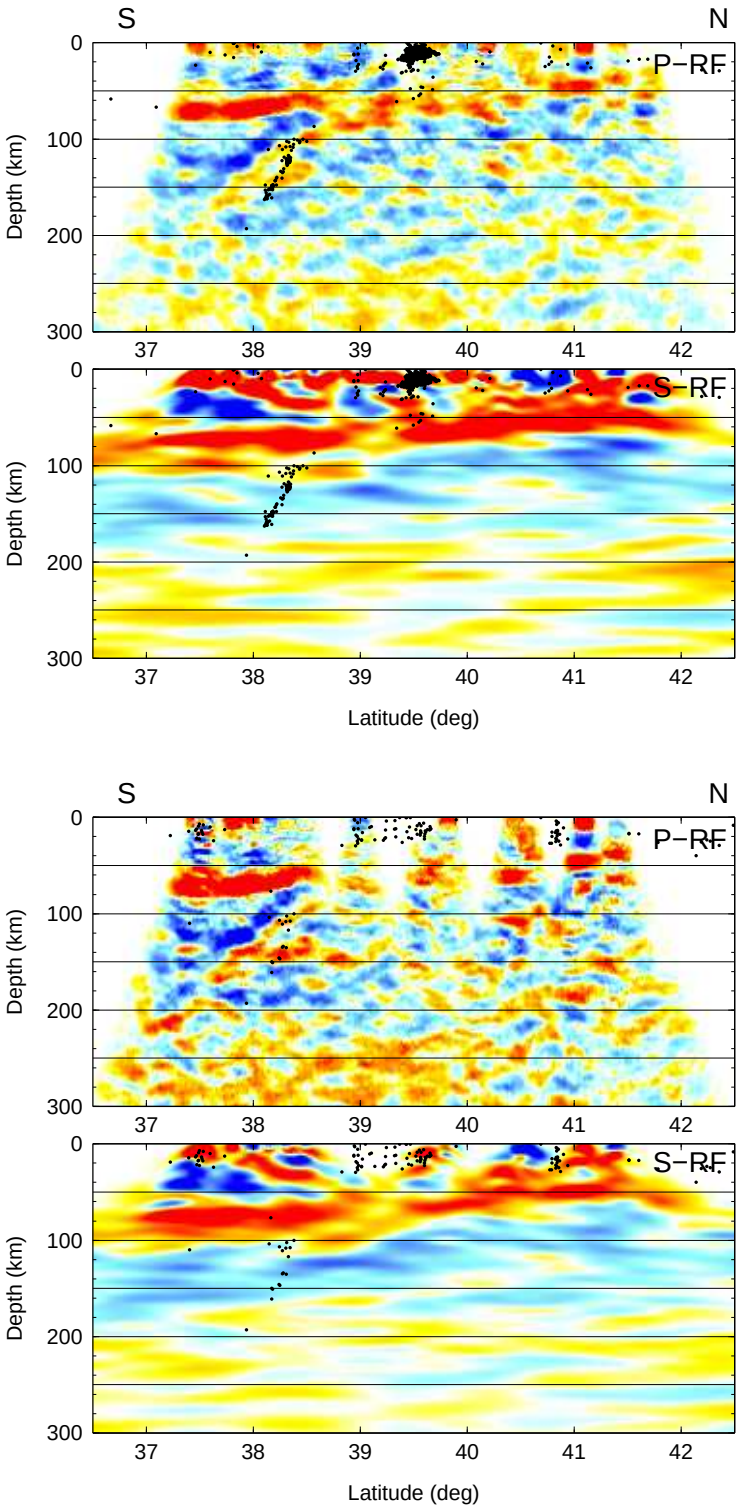

Figure 5.14.: S-N cross section at 74° (Line 5 in Fig. 5.10) (above) and 74.5° (Line 6 in Fig. 5.10) (below), the meridians with the highest piercing point densities at 100 km depth for P-RF and S-RFs, respectively. While along 74.5°, the LAB phase of the south-dipping slab is resolved best, the P-RFs image at this longitude is incomplete, since the P-to-S conversion points are located further east. The P-RFs resolve a south dipping narrow low velocity zone (LVZ) between 37.5° and 38.5° interpreted as subducted crust and discussed in detail in chapter 6.

5.4. Crustal cross sections from S-Receiver functions

In this section crustal cross sections gained from S-RFs are shown. Since in the Pamir the structure of the crust is quite complicated, in P-RFs not much crustal phases can be interpreted, since direct phases are often masked through destructive interference with multiples from intra-crustal converters. On the one hand for S-RFs the resolution is lower due to lower frequency, but on the other hand the observation is less biased from indirect phases.

In the crust of the Pamir, we observe two principal mechanisms of deformation due to collision. While compression and thrusting is observed in N-S direction, extension is observed in E-W direction (Ischuk et al., 2013), probably due to gravitational collapse and a decoupling of the upper crust from mid to lower crust. The high topography imposes a high potential energy, which can relax through motion of crustal material towards the Tajik Depression as presumed for the Shakhdara dome (Stübner et al., 2013b).

In Fig. 5.15 the locations of the cross sections are shown. The S-RF cross sections show evidence for the existence of a detachment in mid-crustal layer in the western Pamir. Towards the eastern Pamir the signature of the detachment layer fades out.

In the cross sections A-A' following the 72° meridian, the blue negative phase in around 20 km depth is clearly visible along the entire profile. A negative amplitude in RFs stands for an upper boundary of a low velocity zone. It can be thus caused by a transition between ductile and brittle behavior of the crust. This is confirmed by the strong correlation with the lower bound of upper crustal seismicity. I interpret this phase as the detachment layer, that decouples upper crustal deformation from deformation below. A detachment has been presumed by Stübner et al. (2013b) beneath the Shakhdara dome and by Hamburger et al. (1992) beneath Peter the first range. The 72° meridian passes the Shakhdara between 36.8° and 37.8°. At this location a shallowing of the detachment is observed.

In cross section B-B' along 73°, this phase is still present but more diffuse. In section C-C' at 74° in the eastern Pamir, this phase is restricted to a small area around the Main Pamir thrust. In the latitude range 38°-39° no negative phase of comparable strength is observed, while south of 38° a strong negative phase is observable in deeper depth ($>$ 30 km). Only in a small range around 37.4 a negative phase in comparable depth ($\sim$ 20 km) is observed.

Section D-D' and E-E' are oriented in west-east direction. The first intersects along strike with the Main Pamir thrust, while the second one is at 38.3, passing a nest of shallow crustal earthquakes in central Pamir. In the D D' profile strong correlation between the earthquakes and a negative phase is observed.

The earthquakes are the aftershocks of the M_w 6.7 Nura earthquake in 2008 (Schurr et al., 2013). The E-E' at 38.3° clearly shows an inclination of the negative phase towards west. At 73° the eastern limit of the detachment layer is observed, which coincides roughly with the transition from western to eastern Pamir. In the eastern Pamir a deeper negative phase is observed in 50 km depth, that is however likely of different origin.

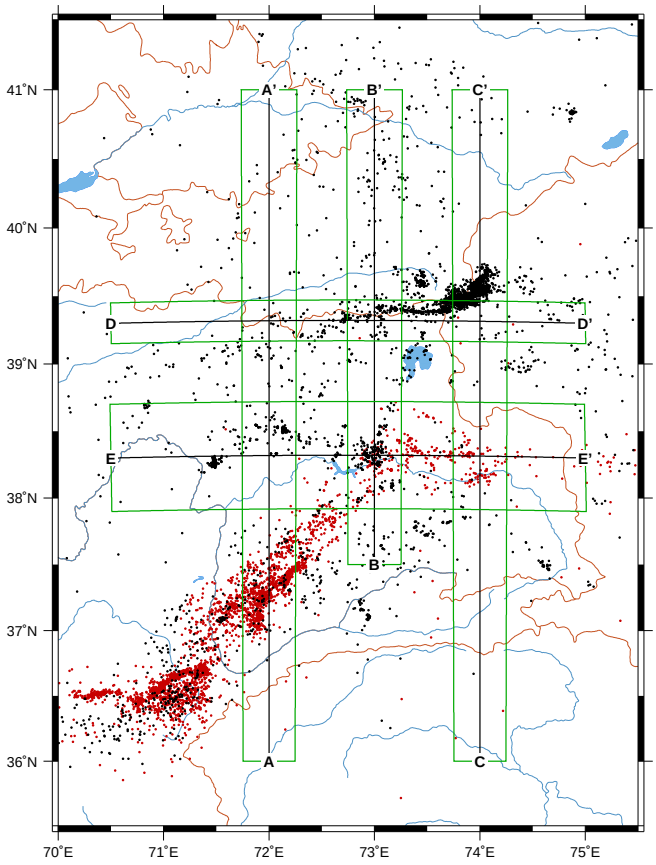

Figure 5.15.: Map showing the location of crustal sections from S-Receiver functions (black lines) The green boxes show the regions of epicenters from Sippl et al. (2013b) projected on the corresponding cross section.

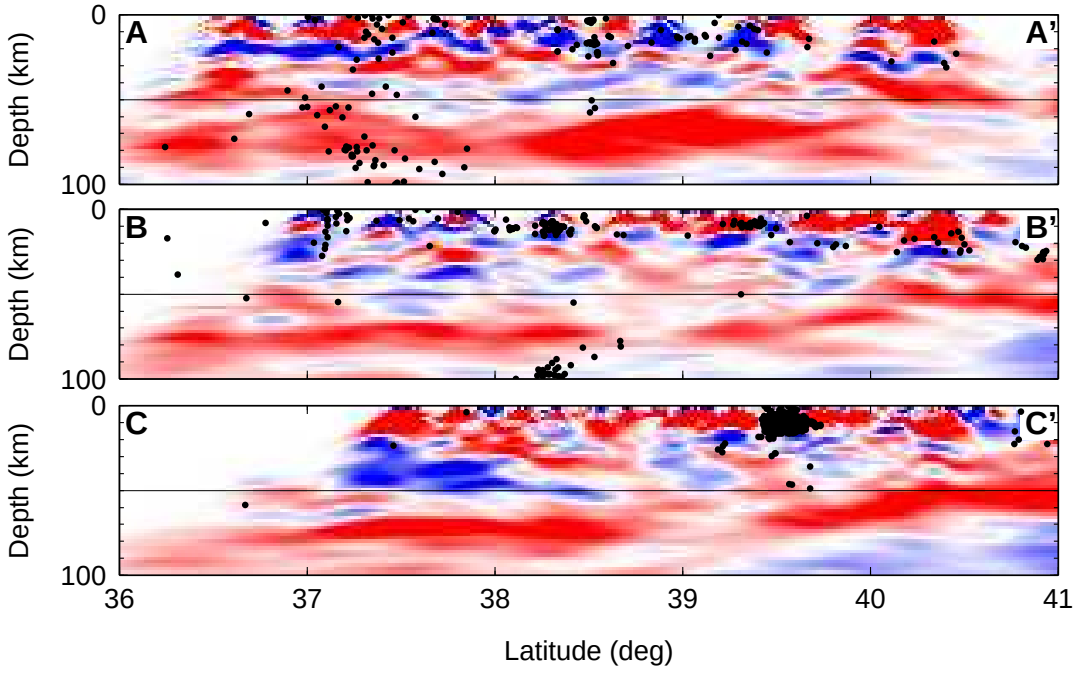

(a) S-RF cross section in S-N direction

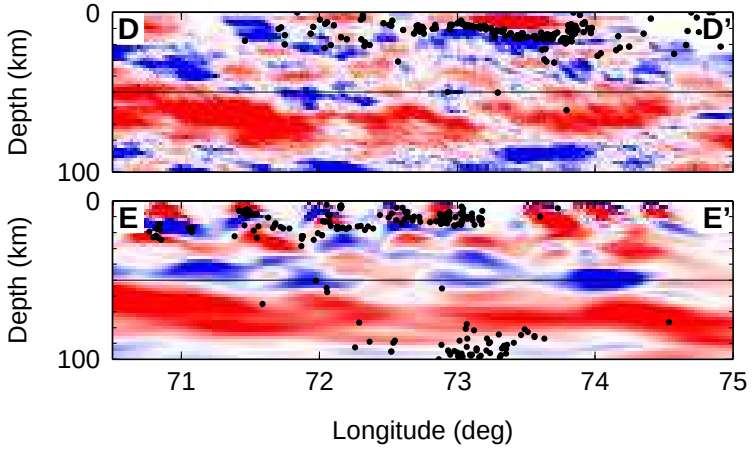

(b) SRF cross section in W-E direction

Figure 5.16.: Crustal S-RF cross section. In mid-crustal depth strong correlation between a negative (blue) converter and the crustal seismicity is observed.

6. Seismic imaging of subducting lower continental crust

Most results presented in this chapter have been published in an article of the same title published in *Earth and Planetary Science Letters* in August 2013 (Schneider et al., 2013).

In this chapter I focus on the observation of a low velocity zone in the upper mantle that can be resolved from P-RFs. P-RF cross sections along the TIPAGE seismic profile are presented that are gained from CCP stacking method as reviewed in section 4.

Using the standard procedure of stacking the Q component of the P-receiver functions and assuming horizontally layered structures, besides the Moho depth and its lateral variation a pair of dipping converters running parallel in the upper mantle with opposite amplitudes is imaged. The converters are interpreted as the signature of a south dipping low velocity zone. However, by comparing the dipping converter to the position of the intermediate depth seismicity a deviation of the positions is evident. This deviation can be traced back to an aberration due to the assumption of horizontally oriented converters. Since the ray geometry of P to S converted waves at inclined converters differ significantly to those of P to S converted waves at horizontally layered structures (such as the Moho) the standard CCP method displays the amplitudes of inclined converters at laterally shifted positions that appear at too shallow depths.

This motivated us to test and apply a modified version of the CCP method that was adopted for inclined converting structures as introduced by Li and Yuan (2003) and described by Kawakatsu and Watada (2007). Synthetic tests are performed to qualify the deviation and to test for which dipping angles the deviation becomes significant.

Moreover we recognize that a significant part of the converted energy from the dipping interfaces is seen on the T-component. This has also been observed by Abe et al. (2011). They imaged the strongly inclined Philippine Sea slab beneath Japan by P-RF migration. Therefore we show and compare Q and T component cross sections of the dipping slab.

Applying the modified CCP stacking method we perform a self consistent routine to pick the positions of the converters in cross sections of the Q and T components if they show the pre-assumed inclination angle. The resulting

model shows the earthquake hypocenters in intermediate-depth located within the south dipping LVZ.

The amplitude of the converted energy on the T component depends on the azimuth of the event relative to the strike of the slab. An inversion of the amplitudes occurs that can be modeled in synthetic seismograms and that is also observed in the data.

Knowing the dipping geometry of the slab it is possible to isolate the converted energy. A multiple step rotation procedure is introduced for this purpose and applied to the data. The success of the rotation procedure gives an additional validation for the existence of the slab.

6.1. Depth sections along the South-north profile

Fig. 6.1 shows the S-N cross section along the TIPAGE profile. The main converters are marked by dashed lines. A prominent southward dipping structure is evident in the uppermost mantle south of the MPT. The dipping structure consists of two parallel phases with a negative phase above and a positive phase below. The two phases define a low velocity zone (LVZ) that dips towards the south, slightly offset from the deep seismicity in this cross section. However, since the CCP section assumes horizontally layered discontinuities, strongly dipping structures are not properly reconstructed. They tend to shift to shallower positions.

6.2. CCP stacking for inclined conversion layers

In the previous section results from CCP stacking from our data along the main TIPAGE profile were shown. A south dipping slab was observed, which is imaged with an inclination angle of more than 30°.

However, the standard CCP stacking method assumes that the converted waves emerge from horizontal discontinuities. This method works well for the localization of horizontal structures such as the Moho, the LAB or the 410 and 660 discontinuities mantle transition zone. However for strongly inclined structures such as the observed slab, the ray geometry of incoming and converted waves changes significantly. This is illustrated in Fig. 6.2. Here the ray geometries for an incoming P-wave and the converted S-wave are compared for a horizontally oriented converter and a 45° inclined converter. Incidence and conversion angles are calculated for a drop from a 8 km/s P-wave velocity below to an S-wave velocity of 4.15 km/s above the discontinuity, as may assumed to be realistic for the boundary between crustal material and the mantle. In case of the horizontally converted structure (left image) the converted S-wave emerges

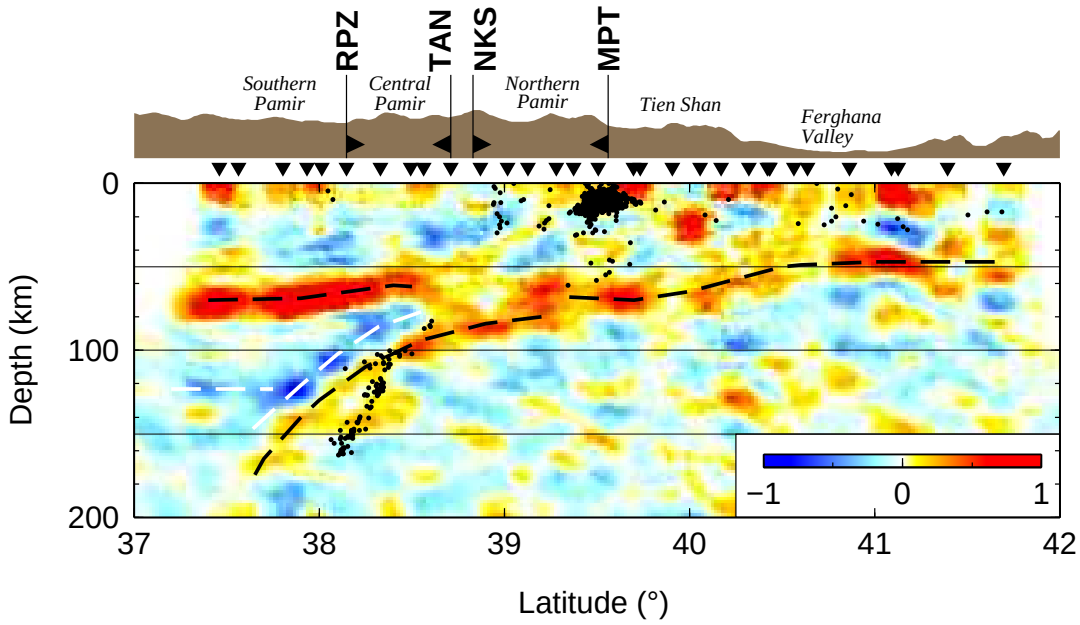

Figure 6.1.: Common conversion point (CCP) image of Q-component receiver functions (QRF) along the N-S main profile. Receiver functions were stacked along their ray paths . Positive velocity contrasts such as the Moho are shown in red colors, negative velocity contrasts in blue colors. Main converters are traced with dashed lines. Between 37.6° and 38.5° a double phase of positive and negative amplitudes is traced interpreted as boundaries of a low velocity zone (LVZ). Stacking along the ray path only yields a clearer image of the subducted LVZ than stacking in the Fresnel zone range (compared to Fig. 5.4). Faults and sutures marked: Main Pamir thrust (MPT), Northern Pamir / Kunlun Suture (NKS), Tanymas Suture (TAN), Rushan Pshart Zone (RPZ).

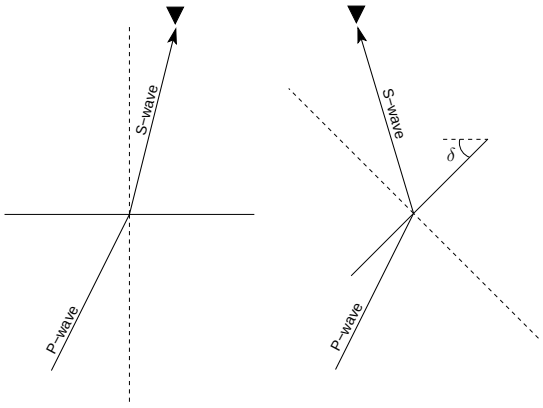

Figure 6.2.: Ray geometries for horizontally oriented and inclined conversion layer

from a position left from the station, whereas in case of an inclined structure the S-wave emerges from a position right from the station. This effect has to be taken into account, when we project converted wave energy back to its real position.

In order to migrate signals from inclined structures a correction in the stacking algorithm is introduced. This is necessary since the direction of the converted S-waves is strongly dependent from the inclination of the converter. Even if the contrast of P- or S-velocity (v_p or v_s) is not very large, the effect of dipping conversion interface is large since the conversion angle depends on the quotient of v_s above the interface to v_p below the interface.

6.2.1. Rotation in coordinate system of inclined converter

For the calculation of the converted ray from an inclined conversion layer a rotation of the coordinate system is performed, which is illustrated in Fig. 6.3 for the simplest case that the back azimuthal direction of the event has the same direction as the strongest inclination of the conversion layer (e.g. the event back azimuth direction is perpendicular to the strike).

The initial situation of the problem is shown in Fig. 6.3 a). A P-wave with an incidence angle i_1 reaches the conversion layer that is inclined with the angle δ. The direction of a converted phase at the inclined converter is calculated with two coordinate transformations. First, the coordinate system is rotated by -δ, which causes the image to rotate by $+\delta$ and the inclination angle to be 0. If the back azimuth of the event is not perpendicular to the strike, a second rotation is performed to align the coordination system to the ray plane in order to receive the 2D situation shown in Fig. 6.3 b). In the new coordinate

system the inclination and conversion angles of P and S wave with respect to the horizontal conversion layer is calculated. In the rotated coordinate system the P-wave has the incidence angle of $i_2 = i_1 + \delta$. The conversion angle i_3 is calculated using Snell's Law. Then the inverse rotation transformations are applied to receive the incoming P-ray in its original position as shown in Fig. 6.3 c). The incidence angle of the converted ray is calculated. In the simple case displayed in the Fig. 6.3 the conversion angle is $i_4 = i_3 - \delta$. However, in the general case, where the incoming ray does not come from directions perpendicular to the strike, the back rotation in azimuthal direction is causing the ray of the converted to be outside of the ray plane of the P-wave. Furthermore for the CCP stacking the ray tracing in the 1D reference model is performed using i_4 and the corresponding slowness and azimuth values. Note that in the illustrated example in Fig. 6.3 the P wave reaching the subsurface below the station from the left side is causing a converted S-wave that is traveling in the opposite direction.

6.2.2. Synthetic tests

We conducted synthetic experiments to test the CCP stack of receiver functions assuming horizontal and dipping converters. We used the RAYSUM (Frederiksen and Bostock, 2000) code to compute radial Q-component receiver functions (QRF) and transverse T-component receiver functions (TRF) for models involving a horizontal Moho and a dipping low-velocity zone (LVZ) with dip angles of 30°, 45° and 65°, respectively (Fig. 6.4). The dipping LVZ produces a double phase with the negative one above and the positive one below, marked by black lines in each figure. The structures are reconstructed by CCP stacking of QRF and TRF, assuming horizontal and dipping converters, respectively. In the QRF, both the Moho and the LVZ are visible, whereas in the TRF only the dipping LVZ is present. For both QRF and TRF, an aberration in the reconstruction of the dipping slab phase assuming horizontal converters already exists for a 30° dip and increases with increasing dip angle. Assuming horizontal converters, the dipping interface tends to be shifted to a shallower position. The dipping phases have been properly reconstructed by assuming dipping converters with corresponding dips. Interestingly, a strongly dipping interface changes its polarity in the QRF, which may reduce the coherence in the CCP stack section.

The synthetic tests show, that the inclination angle of inclined LVZ are imaged with too small inclination angle assuming horizontally layered structures. A recognizable deviation is already observed for inclination angles of 30°. Thus, if in the standard-CCP method structures are imaged with an inclination angles larger than 30°, the real inclination of the structure is expected to be higher.

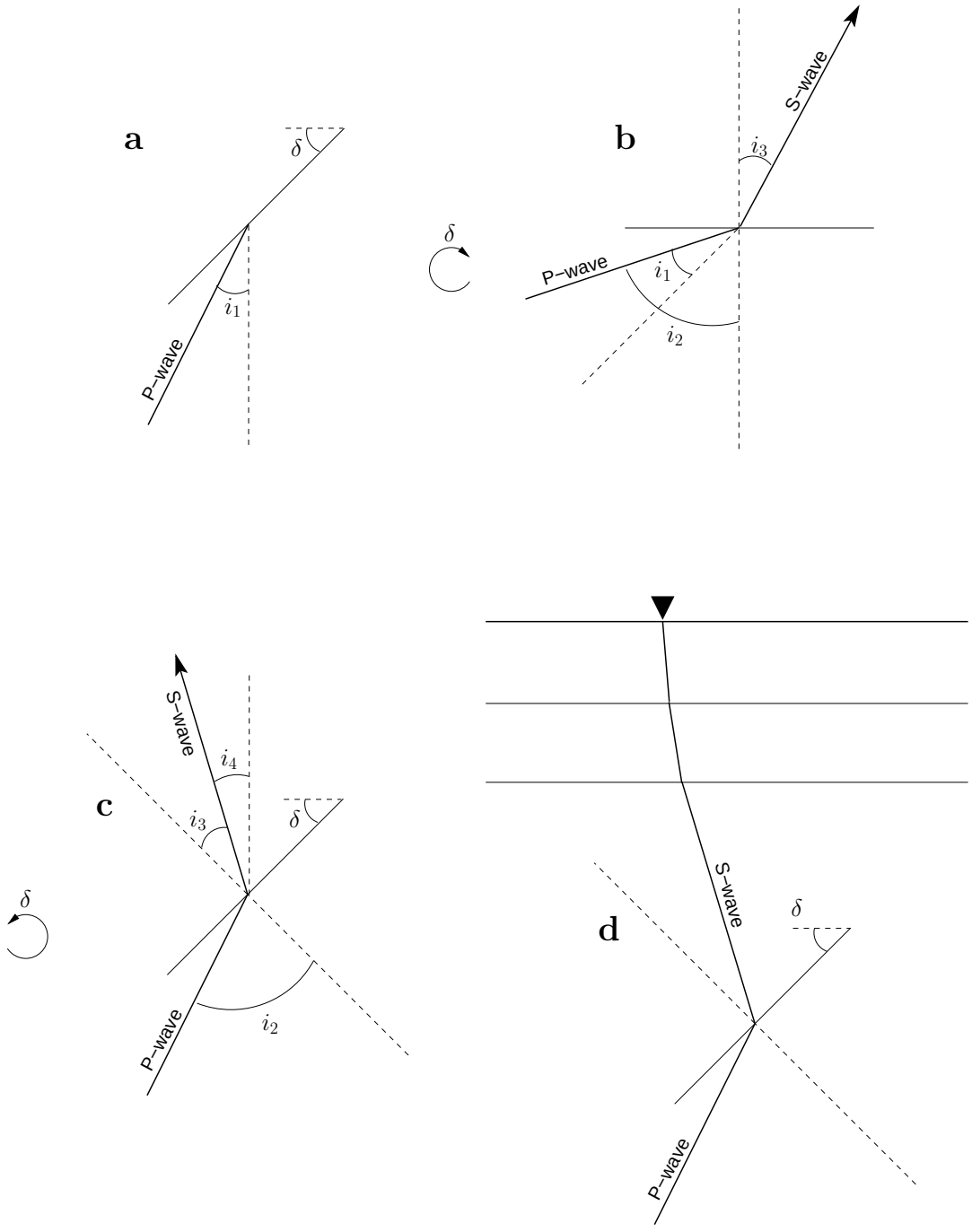

Figure 6.3.: Performing CCP stacking for inclined conversion layers using a 1D reference model: (a) P wave with incidence angle i_1 at an inclined conversion layer (inclination angle δ), (b) rotation of the coordinate system in order to determine i_2 and i_3; (c) back rotated coordinate system to determine i_4, (d) perform ray tracing and CCP stacking as for the case of horizontal layered structure with i_4 and corresponding slowness and azimuth values.

Furthermore the synthetic test show, that a significant part of the converted energy of the LVZ is recorded on the transversal (T) component (see Fig. 6.4 and Abe et al. (2011)).
However, the amplitude of the T-component depends on the side from which the waves reaches the inclined converter. It shows a 2π- periodicity with respect to the back azimuth of the events. For rays perpendicular to the strike no converted energy is projected on the T-component. For example, for a south-dipping (e.g. dipping in the 180° direction) discontinuity, amplitudes on the T-component from events with azimuths in the $0° - 180°$ range have opposite sign to the amplitudes from events with azimuths in the $180° - 360°$ range. Thus, using TRFs the amplitudes for one of the two ranges have to be inverted in the CCP stacking algorithm or only events from one side have to be taken into account. The dipping direction of the slab either has to be assumed or can be deduced from the polarity of the TRF observation.

6.2.3. Q- and T-Receiver function profiles for inclined converters

Fig. 6.5 shows the Q and T-component receiver functions that have been stacked assuming an inclination of 65°. In both cross sections the LVZ is resolved clearly. However, the TRFs show even clearer results for the inclined structure since horizontal converters such as the Moho do not produce signals on the transverse component. Using the pre-assumption of inclined conversion layers the apparent position of the LVZ matches the hypocenter location. It connects the intermediate depth seismicity to the base of the crust just below and south of the MPT. It provides clear evidence for a southward subduction configuration for the eastern Pamir. Tectonic models for the Pamir-Hindu-Kush seismic zone with a single originally north-dipping overturned slab of Indian provenance can thus be discarded. However, it appears that the inclination angle of the LVZ is increasing with depth. Therefore we can not trust the position of the LVZ on every depth level. In order to reconstruct the entire position of the LVZ in the next section a CCP stacking series is performed for different pre-assumed inclinations and the model is constructed in a self-consistent way by picking the locations of structures that are imaged in the pre-assumed inclination angle.

6.2.4. Reconstruction of the dipping low-velocity zone

Strictly the migration shown in Fig. 6.5 is valid only for structures with an inclination angle of about 65°. Interfaces with other dips are shifted to wrong positions. Figure 6.6 shows the CCP stacks of QRF and TRF along the linear array assuming different inclination angles ranging from 0° (horizontally layered)

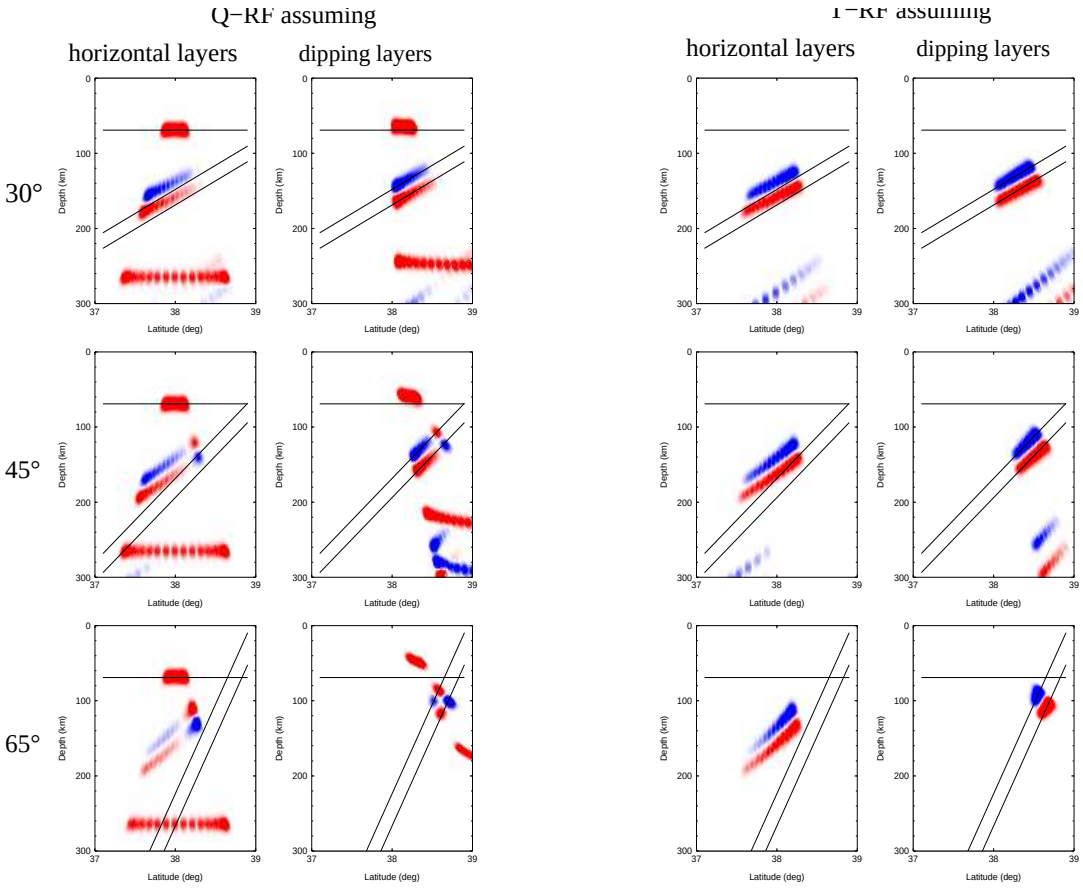

Figure 6.4.: Synthetic migration test for a single station assuming an inclined geometry of the slab. The discontinuities of the input model are depicted as black lines. The slab dips to the south (180°). Synthetics are calculated for events with a slowness of 6.4 s/° and back azimuths between 0° and 180° with an increment of 10°. Since the model is symmetric (2.5D), events from back azimuths between 180° to 360° and those from back azimuths between 0° and 180° would be identical for the QRFs, and would sum to zero for the TRFs.

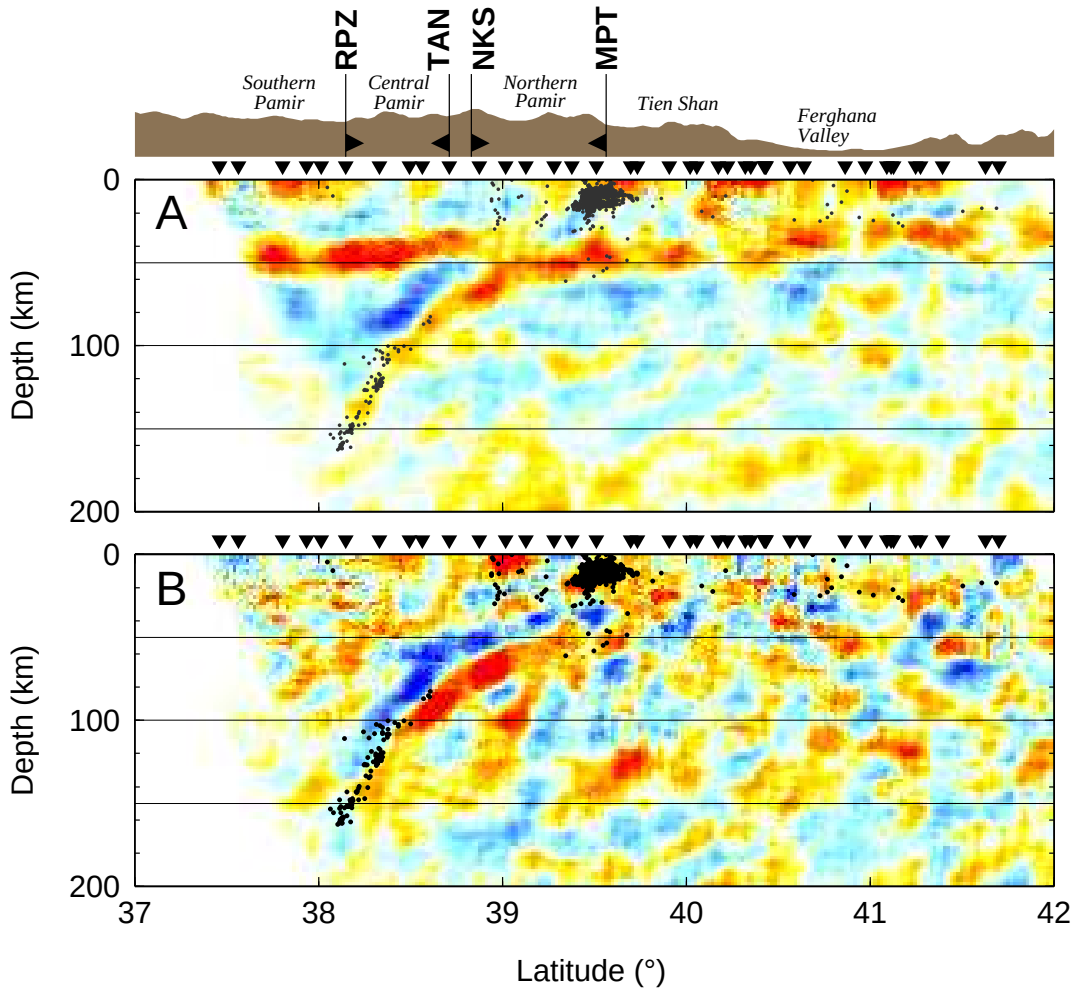

Figure 6.5.: Migrated CCP stack receiver function cross sections assuming 65° inclined conversion interfaces. Q-component and T-component RF are shown in (A) and (B), respectively. The same processing on the CCP stacked data was applied as in Fig. 2.

to 65°. The model is constructed in a self-consistent way: from each cross-section locations of structures imaged with the pre-assumed inclination angle are picked and displayed in the right column. The summation of all images is displayed in the bottom figure.

The resulting image shows two parallel running phases, the upper one with negative and the lower one with positive amplitude dipping to the south. The inclination angles increase with depth from 30° around 80 km depth to 65° around 150 km depth. Circles mark the locations of the earthquake hypocenters occurring between 73° and 75°E (Sippl et al., 2013b). The dipping LVZ coincides with the location of the Wadati-Benioff zone indicated by the hypocenters. We interpret the LVZ as crustal material of Eurasian origin that is subducting due to south.

6.3. Polarity inversion of receiver functions at inclined converters

6.3.1. Polarity inversion in synthetic tests

Synthetic tests show that for dipping structures the signal on the transverse component of the receiver functions (TRFs) changes the sign of the amplitudes depending on the direction from which seismic waves arrive at the inclined converter relative to the dipping direction. For strongly inclined layers QRFs also show inverse amplitudes, depending on the inclination angle of the P-wave and the dipping geometry of the slab.

In Fig. 6.7 forward modeled receiver functions are shown using a simple one layered crust with a horizontally orientated Moho and a 45° inclined LVZ in the upper mantle. The horizontally layered Moho produces only a signal on the Q component at $\sim 8\ s$ in Fig. 6.7 C. The direct Ps phases from the upper and lower bound of the LVZ are observed on Q and T components (Fig. 6.7 C and F) ranging from 12 s to 16 s and from 14 s to 20 s, respectively. For both, Q and T components the polarity of the LVZ phases changes. The polarity for the QRFs shows reversed amplitudes for events from northern direction (300°-360° and 0° - 60°). In the CCP stacked sections (Fig. 6.7 A and B), the phases showing different polarity are separated from each other. For the Q-component the position of the polarity change depends on the inclination angle of the converter. It occurs on the up-dip side of an inclined converter if the inclination angle is larger than the incidence angle of the seismic event.

For a south-dipping LVZ, the polarity change on the T-component occurs for every inclination angle at 0° and 180°. Therefore it is easier to separate phases with opposing polarities for TRFs than for QRFs. Phases of opposing back-

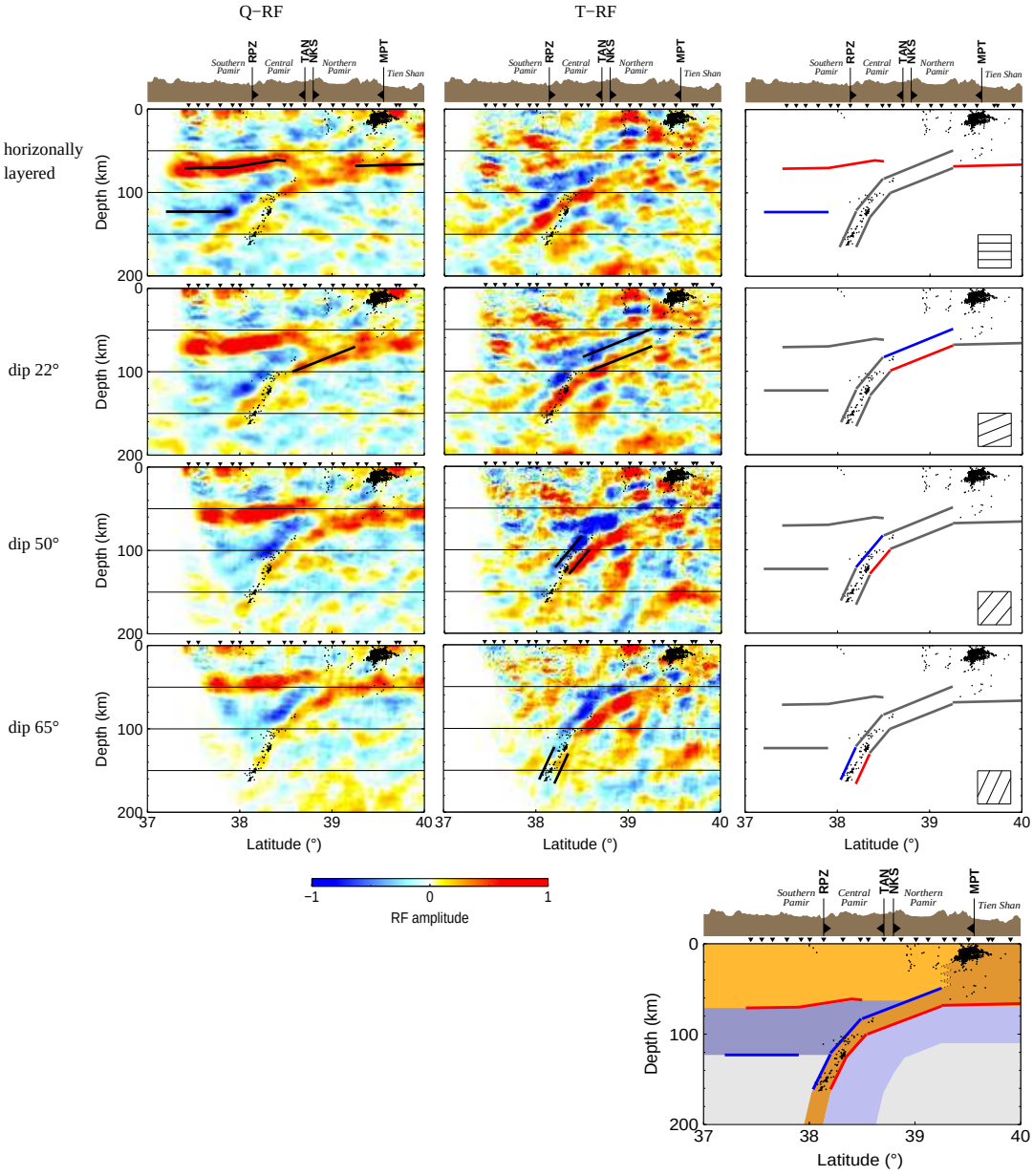

Figure 6.6.: Migrated cross sections along the TIPAGE main seismic profile assuming different inclination angles of the converters. The assumed angles are depicted on the left. In the left and middle columns the amplitudes of the Q- and T-components are shown, respectively. For the T-component only events from the east (azimuthal angles 0°-180°) are taken into account. In the right column the positions of the conversion boundaries corresponding to the relevant dip angle are highlighted in red (positive converters) and blue (negative converters). The bottom figure shows the amalgamation of all picked elements from the right columns.

azimuths would sum to zero and thus annihilate each other in the CCP section, if they were not separated or inverted.

6.3.2. Separation of TRFs from western and eastern azimuths

In Fig. 6.8 the observed and CCP stacked receiver functions from events arriving from western directions are compared to those from eastern directions. For these figures the amplitudes were not inverted. Only few events are coming from western directions (180°-360°). Nevertheless the LVZ is imaged very clearly. The image with events only from eastern directions (0°-180°) differs hardly from the Fig. 6.5 (b), where all TRFs are summed with inverted amplitudes. This is due the events geometry, see Fig. 5.1(a) and Fig 5.1(c). Since much more events are coming from eastern directions, the cross section in Fig. 6.5 (b) are dominated by those events. In Fig. 6.8 B showing the TRFs from eastern directions (0° - 180°) a dipping positive (red) converter is observed together with a negative (blue) blue converter running parallel at slightly shallower depths. In contrast in Fig. 6.8 A showing the TRFs from events with western azimuths the polarity is flipped and we observe the negative (blue) south dipping converter below the positive one. This is what was expected from the synthetic tests. In the isotropic case energy is only transferred to the T-component for inclined structures and if the event azimuth is not strictly in line with the dipping direction. The amplitude of the energy transferred to the T-component depends on the side from which the seismic wave arrives at the inclined converter.

6.4. Separating conversion energy from a dipping converter

In the synthetic tests as well as in the data it was shown that the converted energy from the dipping interface is partitioned on the Q and the T component of the receiver functions. Furthermore, inversions of the amplitudes occur on both components but for different situations as discussed in the previous section. The amplitudes of the Q component get reversed for strongly inclined interfaces for events coming from the up-dip direction in the case that the inclination of the interface is larger than the incidence angle of the event. The T component shows reversed amplitudes comparing events arriving at the dipping plane from opposite sides relative to the dipping direction. For example a south dipping conversion layer produces opposite TRF-amplitudes for events from eastern and western directions.

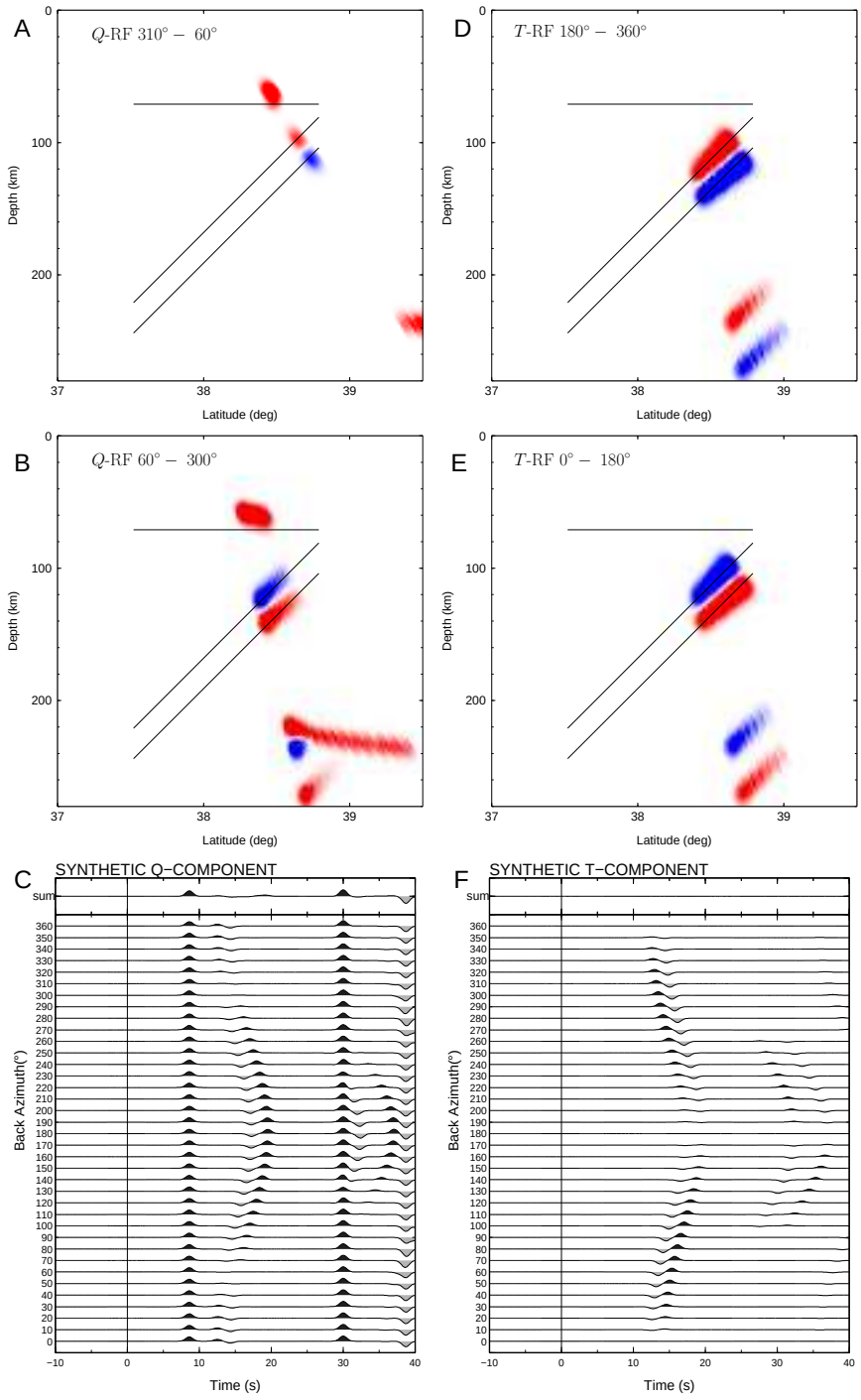

Figure 6.7.: Polarity flip for a dipping LVZ for Q-RF (A-C) and T-RF(D-E). In C and F synthetic Q and T component traces are plotted for the whole 360° azimuth range. In (a) Q-RFs from northern directions are separated showing the inverted signal. In (b) Q-RFs from 60° to 300° are migrated showing the normal polarity. In (d) and (e) migrated TRFs are shown from western and eastern directions, respectively.

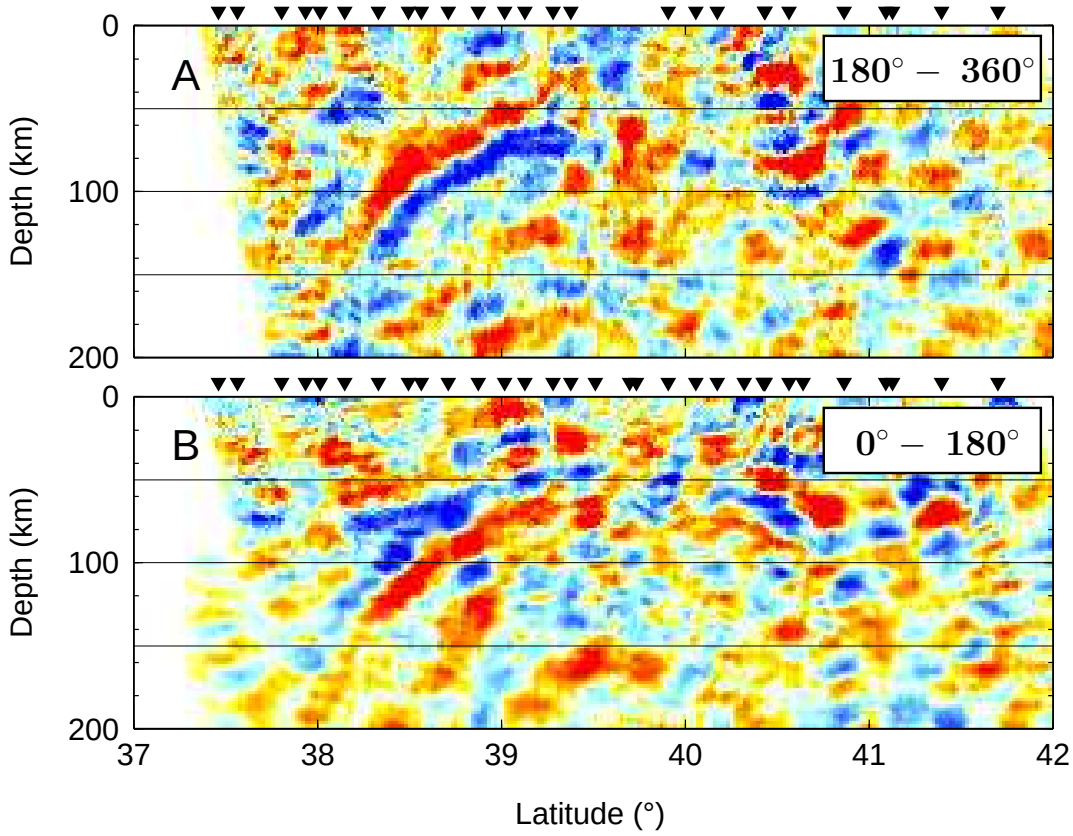

Figure 6.8.: S-N cross sections along main TIPAGE profile showing transversal component receiver functions (TRFs) from western direction (A) and from eastern direction (B).

However, in principle it is possible to choose a coordinate system for each RF in such a way that the amplitudes of the converted energy is recorded only on one component and has a defined sign, only depending on the sequence of the velocities below and above the velocity contrast. Therefore the geometry of a ray at an inclined converter has to considered.

In case of horizontally orientated structures the azimuthal propagation direction of incoming, refracted and converted waves are the same, the ray plane is given by the Z-R or L-Q plane which is perpendicular to the surface. The intersection line of the ray plane and the surface is identically to the projection of the rays on the surface along the vertical Z-axis. As consequence in case of an isotropic earth, the converted energy is also released in the Z-R plane polarized in direction of the Q-component.

For inclined conversion layers the situation changes. In Fig. 6.9 A the ray geometry for an inclined converter is sketched. The incident P-wave (green) is refracted and converted. The rays of incident, converted and refracted waves are all in the ray plane perpendicular to the surface of the inclined conversion layer. Since the converter is inclined, also the ray plane is inclined with the consequence, that the azimuthal direction of propagation changes. Thus, the azimuthal direction of incoming and converted rays differ from each other. The conversion energy that is used for receiver functions is in terms of both propagation and polarization directions restricted to the ray plane of incident and converted rays.

To account for this situation and to reveal a new component that bears the conversion energy with a defined sign a rotation is introduced with respect to the new ray plane that results from the inclined conversion plane. The geometry of the conversion plane has to be assumed in advance, then each receiver function is rotated to reveal components in and perpendicular to the ray plane.

6.4.1. Rotation procedure

In this section the rotation is explained that is sketched in Fig. 6.9. This rotation is performed for the three components of the receiver functions after the deconvolution in the LQT system.

1. In the first step, the rotation from the receiver functions are rotated from LQT system used for the deconvolution back into the ZRT and ZNE systems. For this rotation the theoretical incidence and azimuth angles are used.
2. In the 2nd step the ZNE is rotated around the Z component in the $ZR'T'$ system with the R' component pointing in direction of the new azimuthal propagation direction of the converted wave, see Fig. 6.9 A. The converted ray is calculated using the rotation procedure explained in

section 6.2.1. From the converted and the incoming ray (green and red lines in Fig. 6.9) the ray plane and its intersection with the surface is calculated to determine the direction of R'.

3. In the 3rd step the angle between the ray plane and the surface is determined and the coordinate system is rotated around the R' axis, as sketched in Fig. 6.9 B. In the resulting $Z'R'SH$, the Z' and SH components are situated in and perpendicular to the ray plane, respectively.
4. In the last step the angle between the Z' and the ray of the converted wave is calculated and a rotation around the SH component is performed to transform $Z'R'$ into L' and SV components, respectively (see Fig. 6.9 C).

6.4.2. Synthetic tests

The rotation procedure is tested for synthetic seismograms computed as described in section 6.2.2. Fig. 6.10 shows the individual traces of the synthetic seismograms before and after applying the rotation procedure described in the previous section in the two upper and the two lower panels, respectively. On the Q- and T-components the inclined converter is reflected in the amplitudes between 12 s and 20 s. Both Q- and T-component show signals and amplitude inversions as described in section 6.3. After applying the rotation procedure the conversion energy from the dipping converter is only visible on the SV component (lower left panel). The SH (lower right panel) component does not show amplitudes in the corresponding time interval.

The synthetic tests show that by pre-assuming the geometry of the converter the conversion amplitudes can be separated. In Fig. 6.11 migrated cross sections of the synthetic seismograms are shown. The discontinuities of the model used to calculate the synthetic traces are marked as black lines. The LVZ is dipping due south. Since the inclination angles of the converters are taken into account for the CCP stacking (as described in section 6.2) the phases of the inclined LVZ appear on the proper positions, while the Moho is imaged at a too-shallow position. For the T component only events from eastern directions are used for migration, since they would sum to zero with the events from western directions. After the rotation procedure the SV component contains all direct conversion energy and no energy is left on the SH component. For the cross section events from all azimuths are included.

6.4.3. Application to data

In this section, the method for separation of the converted energy from inclined converters that has been introduced and tested in the previous two sections is

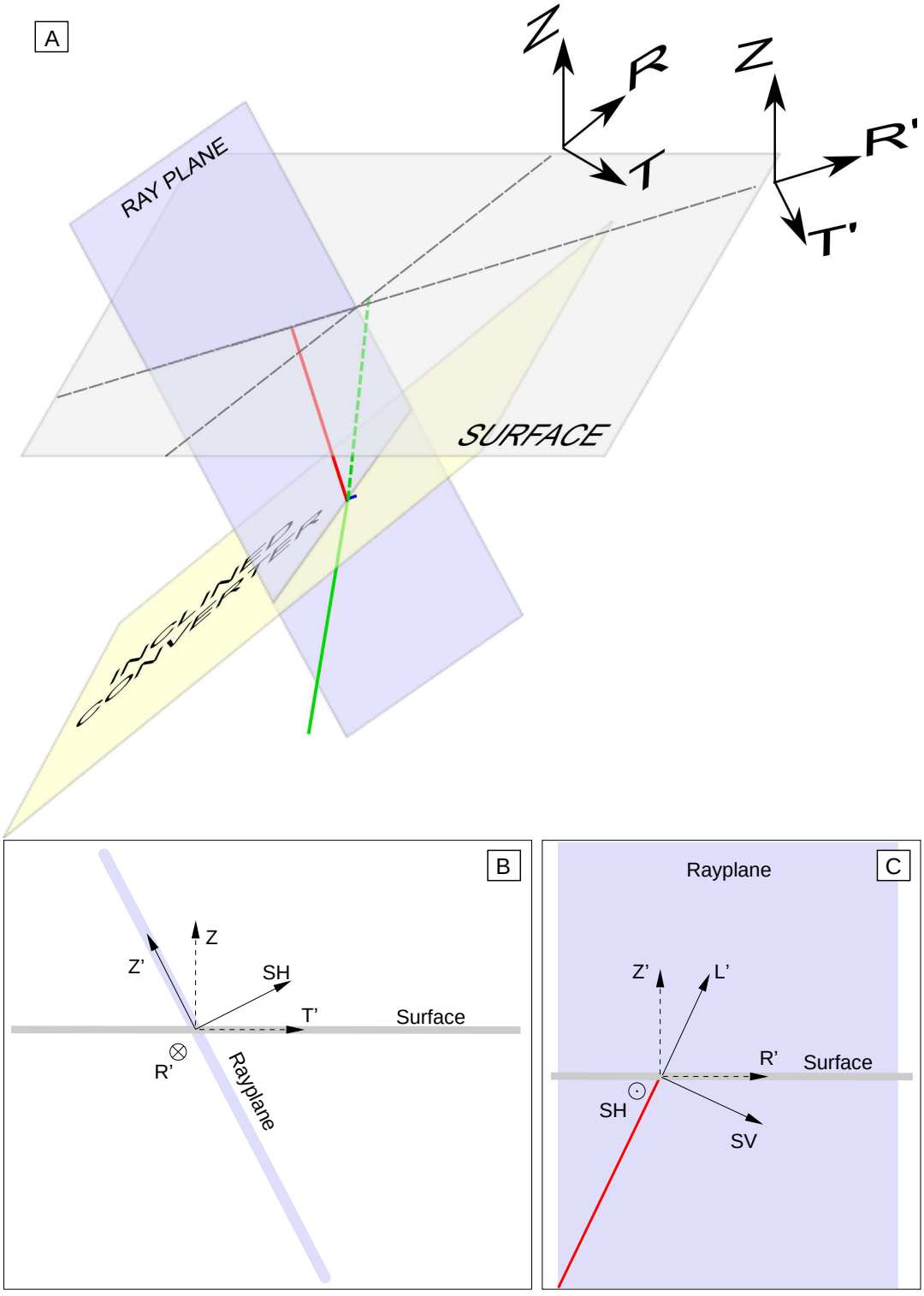

Figure 6.9.: Rotation procedure for the geometry of an ray at an inclined conversion layer. Green and red lines are the rays of incident and converted waves. For horizontally oriented converters the ray plane is spanned by the Z and R directions. For inclined conversion layers the ray plane is inclined and rotated. R' is defined by the intersection of the ray plane and the surface.

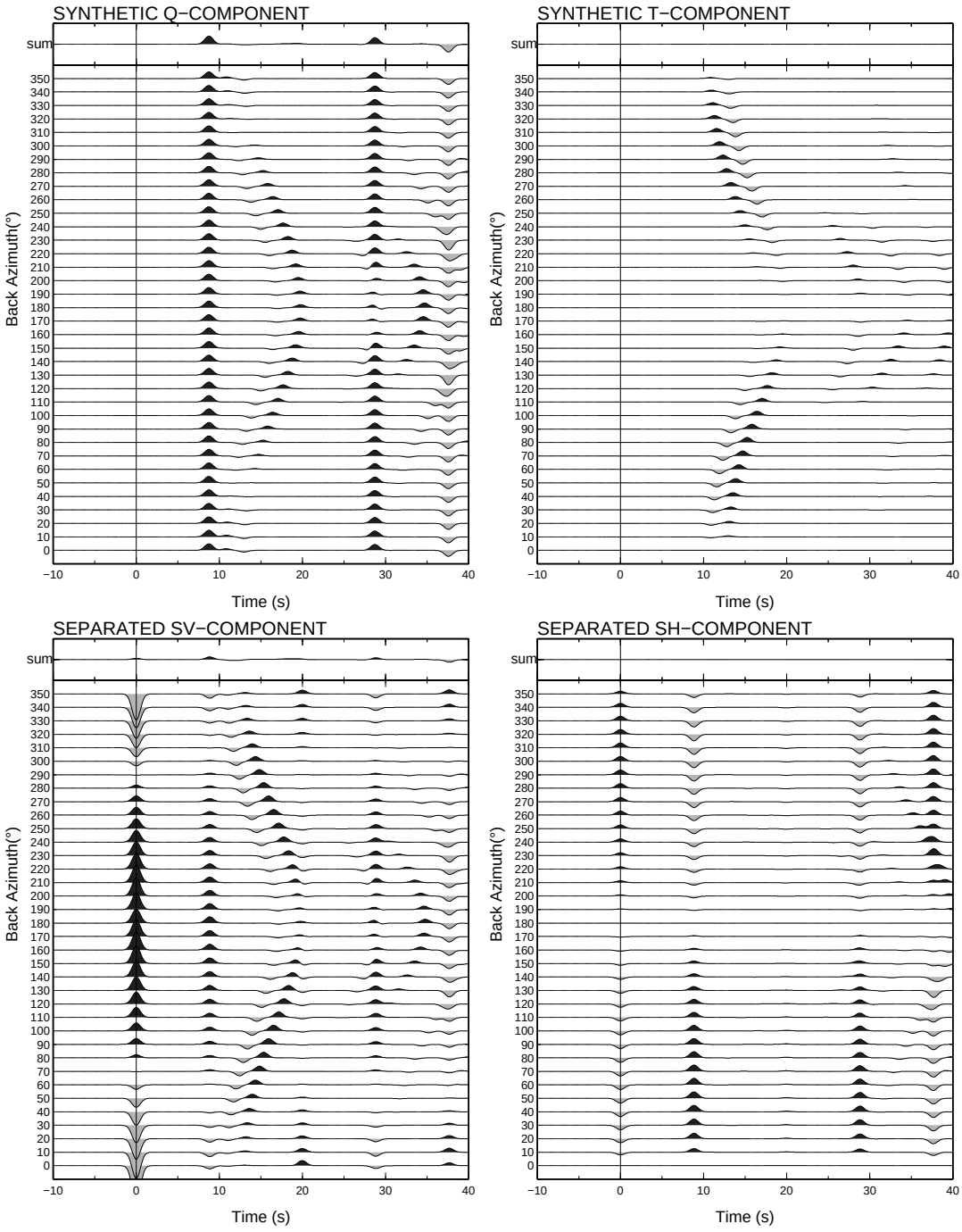

Figure 6.10.: Synthetic tests for the separation of converted energy from inclined converters. The upper two panels show the individual traces of Q and T component receiver functions, the lower two panels show the SV and SH components after the separation has been performed. In the lower two components directly converted energy from the inclined converted is only present in the SV component.

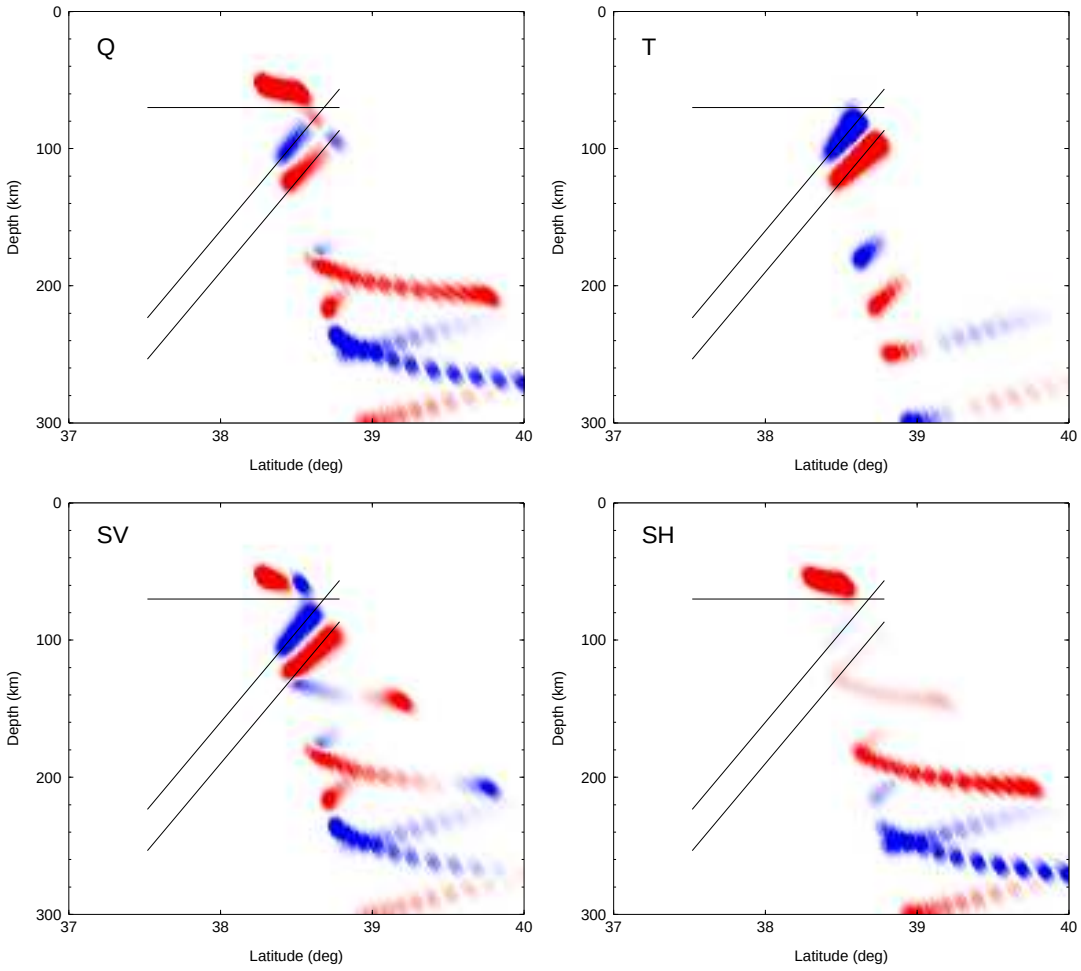

Figure 6.11.: CCP stacked results for the synthetic tests shown in Fig. 6.10. The inclination of the converters has been taken into account in the CCP stacking as described in section 6.2. While in the *LQT* system energy from the inclined converters is projected on both Q- and T-components, in the new coordinates the converted energy is only present on the SV component. For the T-component only events from back azimuths 0°-180° are plotted, while for SV and SH components RFs from all azimuths are stacked.

applied to the data. First, the application for a single station is shown. The application for a cross section along the S-N profile follows in the second step.

Application for single station P18

Fig. 6.12 shows the individual traces of Q and T components of the P-RFs at station P18. This station is located on top of the LVZ in the eastern Pamir. The time interval where the LVZ phases are observed at this station is marked by a blue rectangle. In the summation trace of the Q component a positive amplitude is visible at 15 s (marked by an arrow). This is the delay time at which the lower boundary of the LVZ is observed at 110°, which is the dominant back azimuth in the event distribution. For smaller back azimuths the delay time is decreasing. On the T component the amplitudes of the LVZ are inverted. At 15 s a negative amplitude is observed in the summation trace. At smaller 13 s a positive amplitude is observed. This positive amplitude can be clearly traced from back azimuths of 145° to 0 ° back azimuths. Thereby the delay time is changing from 13.5 s to 9 s. This phase emerges from the upper boundary of the LVZ.

The SV-SH separation procedure is performed for a south-dipping slab with an inclination of 50°. The resulting SV and SH components are shown in the lower two images in Fig. 6.12. The amplitude inversion of the T-Component is corrected in the SV component. The double phase can clearly be traced for back azimuths ranging from 145° to 0°, while in the SH component the amplitude of these phases are low.

In Fig. 6.13 migrated cross sections of the same data are shown. In this representation the dipping phase is observed at 100 km depth. On the Q component the signal is weak and the T component shows reversed polarity. The SV component shows the clearest result.

Application on S-N profile

The rotation procedure to separate the converted energy from the inclined converter is applied to the profile stations. In Fig. 6.14 the resulting S-N cross sections of migrated SV and SH components are shown (lower two panels) in comparison with the Q and T components (upper panels). For all data the same geometry of a 50° inclined slab dipping due south has been assumed. The SV components shows the clearest result. The double phase can be traced clearly from 50 down to 150 km depth In the upper part of the slab, shallower than 100 km depth, some conversion energy from the inclined layer is also observable on the SH component. Here the assumed value of 50° is too high (see previous section), which leads to not perfect separation of the conversion energy.

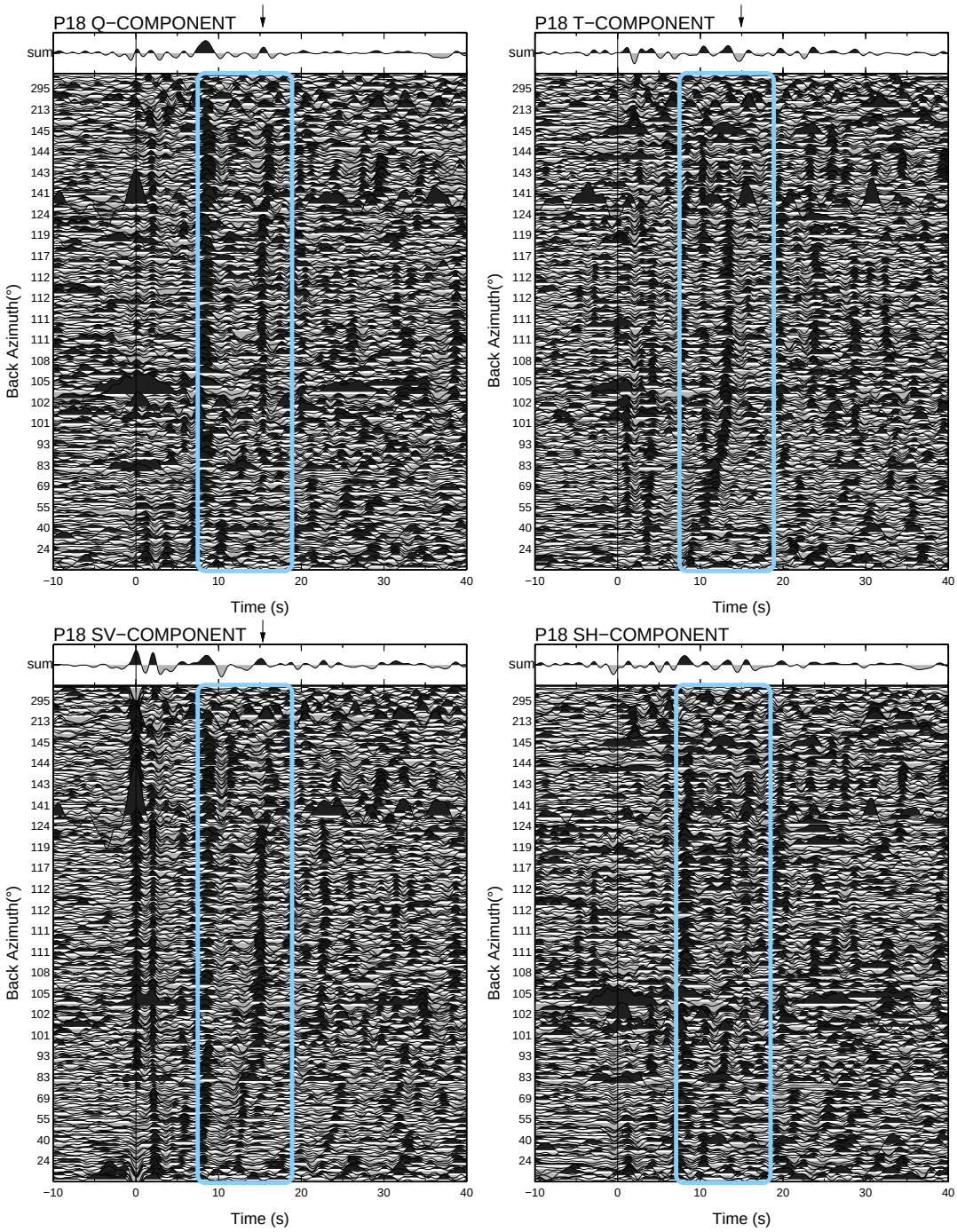

Figure 6.12.: Individual traces of P-RFs for station P18 sorted by the back azimuth. The upper panels in each image show the summation trace. The data are low pass filtered with a corner frequency of 2 s. The upper left and right images show the Q and T component RFs used as input for the rotation procedure to separate the energy from inclined converters. As dipping direction 180° (due south) and as inclination angle 50° have been assumed to construct the SV and SH components shown in the two lower panels.

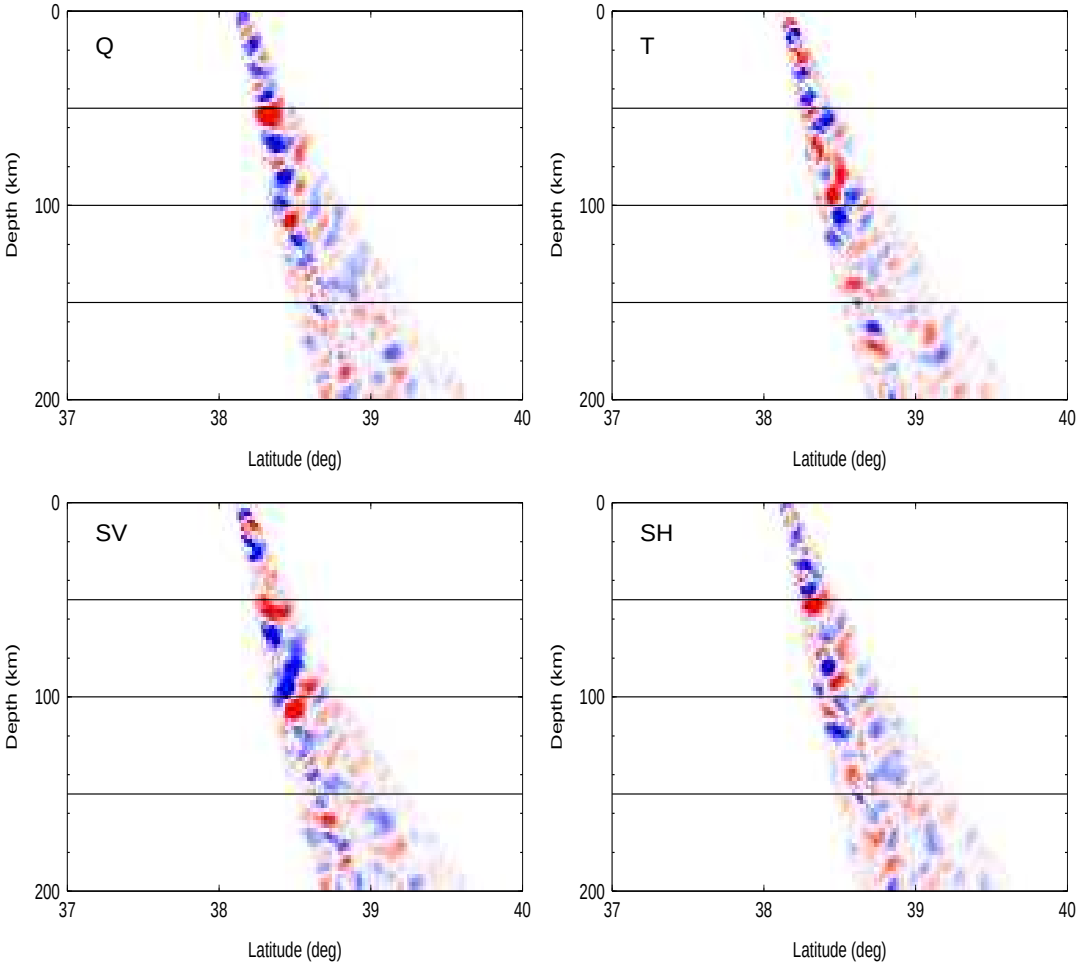

Figure 6.13.: Same data as shown in Fig. 6.12, migrated using CCP cross section for inclined converters. The inclined LVZ is observed in Q and T component at 100 km depth. In the SV component the signal is shown clearly, while most of the energy has been removed from the SH component.

The existence of the south-dipping low velocity zone could be confirmed by this method, since applying theoretically computed rotation angles for the assumed geometry of the slab resulted in an increase in coherence and the isolation of the conversion energy on one component.

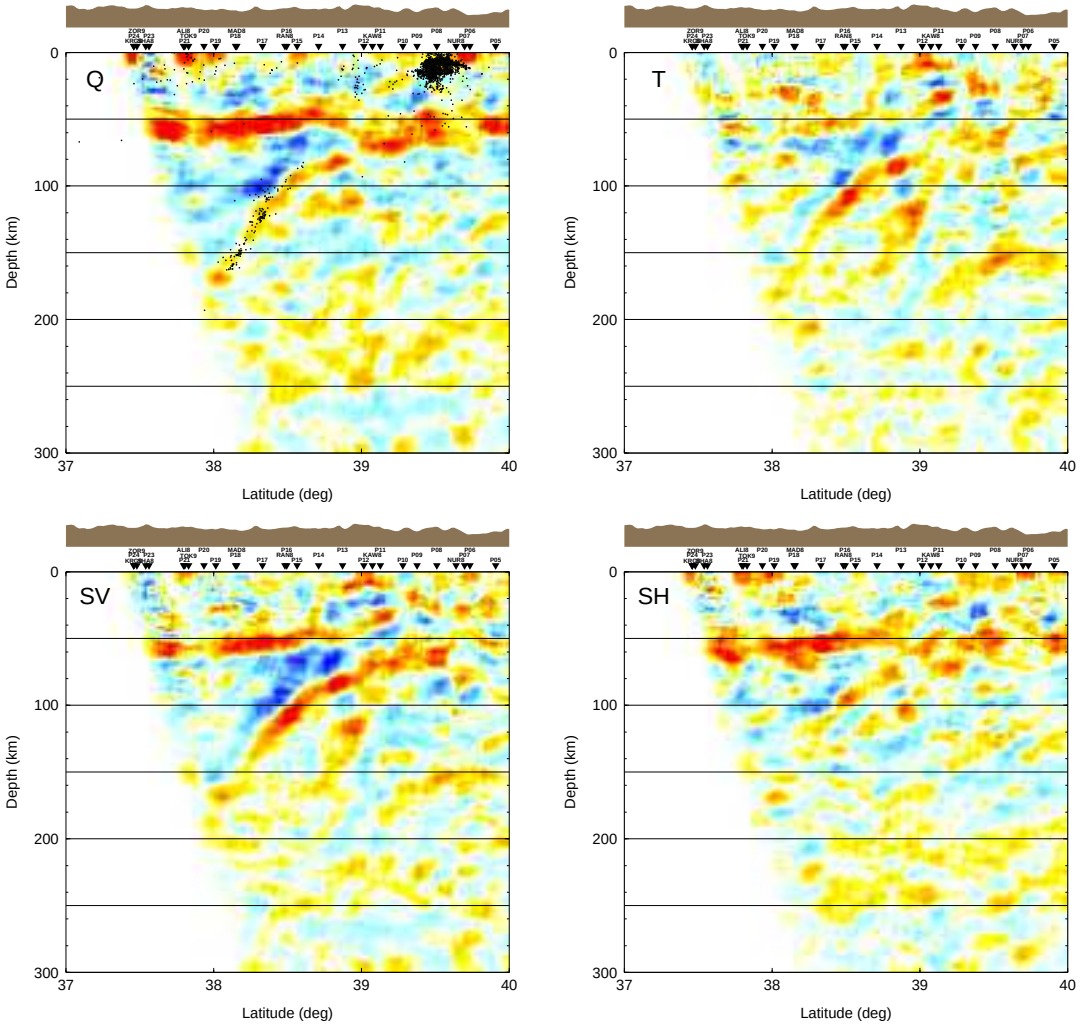

Figure 6.14.: S-N cross sections along the profile for the latitude range imaging the LVZ. Above: Q and T components, below SV and SH components after applying the rotation procedure described in section 6.4.1 to isolate the conversion energy from an inclined converter on the SV component.

6.5. Forward modeling of the LVZ

The basic characteristics of the double phase imaging the LVZ are determined by forward modeling. An example of the comparison between observed and synthetic receiver functions at station P18, located in the southern part of the linear array, imaging the LVZ at around 100 km depth is given in Figs. 6.15 and 6.16.

By modeling the double phase we obtained a thickness of the low velocity zone of 10.5 ±1 km at station P18. At five further stations in the vicinity of P18, the LVZ phases could be identified in the TRFs with back azimuths ranging from 30° to 110°. The LVZ thickness appears to vary laterally between 10 and 15 km (for estimation of error and lateral variation see section 6.5.2). Amplitude modeling of the Moho Ps phase in the QRFs and the double phase in the TRFs, reveals the velocity contrast between the LVZ and the surrounding mantle at 100 km depth to be only slightly smaller compared to the velocity contrast at the Moho ($\Delta v_{LVZ} = 0.97 \Delta v_{Moho}$), implying that the velocity in the LVZ is very similar to the velocity of the lower crust.

6.5.1. Comparison of synthetic and observed RFs for the entire azimuth range

Fig. 6.15a and c shows all the individual QRF- and TRF-traces of station P18, sorted by back azimuth. The summation traces are shown in the upper panels. In the QRF the Moho at ∼8 s is the dominant phase. The double slab phase with negative–positive polarities is clearly seen at 10–15 s in the TRF, and can also be recognized in the individual QRF traces. We calculated the synthetic QRF (Fig. 6.15b) and TRF (Fig. 6.15d) with the RAYSUM code (Frederiksen and Bostock, 2000) using a simple three layered regional model, including a 10.5 km thick LVZ that dips to the south at an angle of 50° and a 65 km thick crust with a flat Moho (illustrated by the black lines in Fig. 6.16a–d). The values of slowness and back azimuths for the synthetic RFs were chosen identical to those of the observed RFs. The majority of the RFs have back azimuths of 0–180°. Few events come from the west (see Fig. 5.1.1). Furthermore, the same post-processing as for the observed data (low pass filter and deconvolution) is applied to the synthetics.

Moho conversions are observed in the QRFs at 8 s. The first multiple phase ($PpPs$) of the Moho (at 29 s) is very (to the point of being invisible) weak in the observed RFs due to noise, lateral heterogeneity or a crust–mantle transition gradient. Surprisingly, the second multiple (PpSs) is clearly visible, though at reduced amplitude.

The primary phases of the dipping layers are well matched by both synthetic

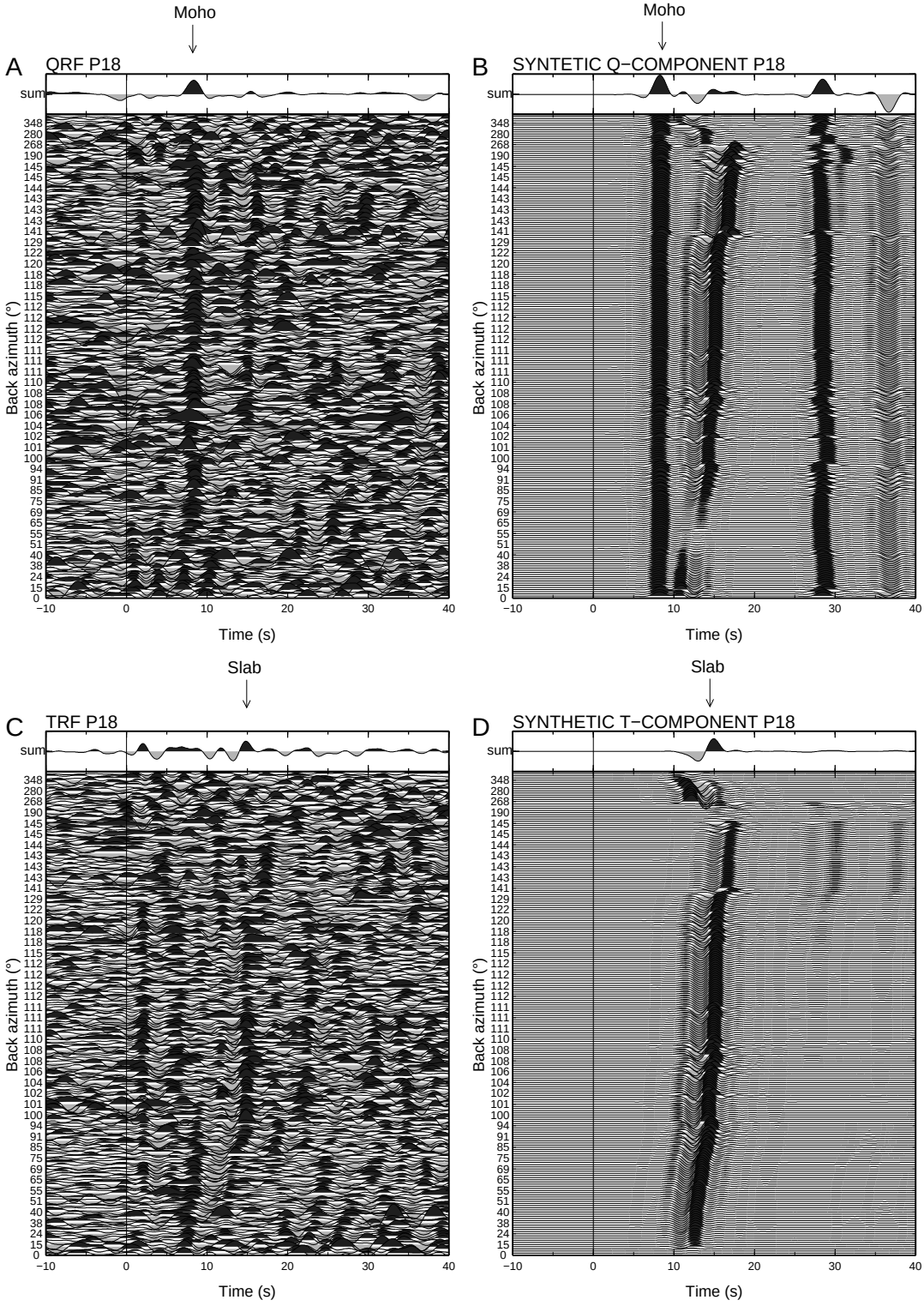

Figure 6.15.: Comparison of observed receiver functions and synthetics for station P18. Traces are low pass filtered with a cut-off period of 3 s.

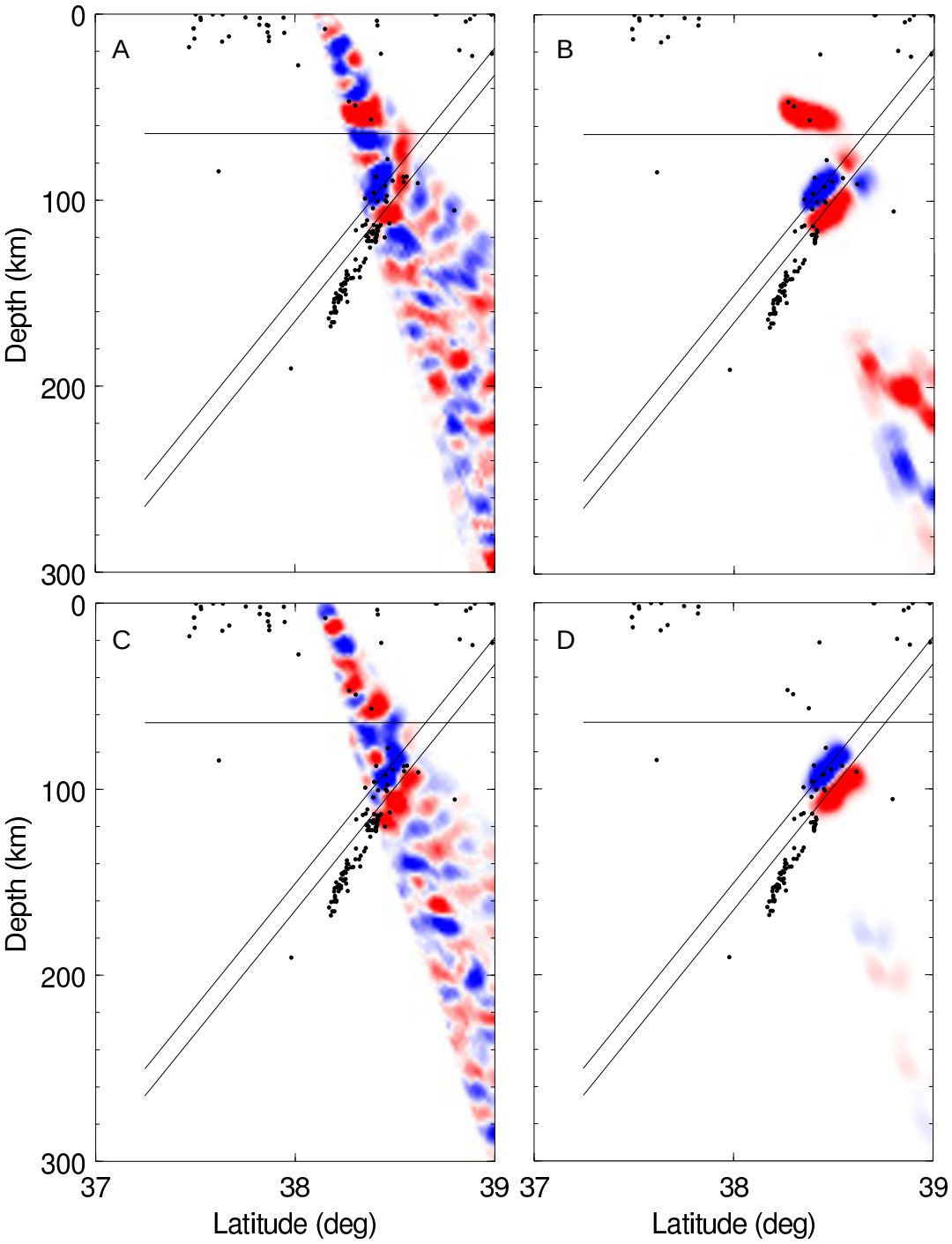

Figure 6.16.: Migrated observed QRFs (A) and TRFs (C), and synthetic QRFs (B) and TRFs (D) for station P18. The traces are migrated assuming 50° dipping conversion layers.

QRFs and TRFs between 10 s at 0° azimuth and 16 s at 180° azimuth. Although too few TRFs from western back azimuths (σ) are available to verify the polarity flip of the inclined phase seen in the synthetics, there are sufficient RFs recorded that show both quadrants in the east to have the same polarity, ruling out anisotropy, which would show a 2σ symmetry. Thus, the waveform modeling verifies the existence of a dipping LVZ. Fig. 6.16a–d shows the comparison of the CCP stack observed and synthetic QRFs and TRFs assuming converters inclined at an angle of 50°. The amplitude of the QRFs changes its sign on the inclined interface, which may explain the reduced coherence of the reconstructed dipping phase in the QRFs compared to the TRFs.

6.5.2. LVZ thickness

The thickness of the LVZ and its lateral variation is estimated by forward modeling. For Fig. 6.17 A and B forward modeling of the LVZ phases has been performed for varying v_p/v_s inside the LVZ and varying inclination angle, respectively. The minimum unit of thickness difference that can be distinguished visually by comparing the synthetic TRFs with the data is 0.5 km, which is thus given as the error for each model. A linear dependency between modeled thickness and v_p/v_s is observed. In a realistic v_p/v_s range from 1.7 to 1.8 the LVZ thickness ranges between 9.5 and 11.8 km. Different inclination angle also affect the thickness result. A realistic range for the dip is 50° ± 10° (see section 6.4.3). In this range, the LVZ thickness can be estimated to be 10.5 +/- 1 km.

To estimate the lateral variation of the LVZ measurement the TRF conversion phases of the LVZ at 6 stations as seen in a back azimuth range from 30° to 110° have been stacked and analyzed, shown in Fig. 6.17C. For each station, the leading negative phases were aligned at 0 s and stacked. The delay time between negative and positive conversions corresponds to the thickness of the LVZ. Starting with the forward modeling at station P18, the thicknesses of the LVZ at the different stations were linearly extrapolated, taking into account the delay times at each station relative to the delay time at station P18. The resulting thicknesses are given at the left side of each trace. In this way, the LVZ thickness is estimated to be 10-15 km. The stations used for the thickness analysis are P17, MAD8, P18, P19, P20 and ALI8, whose locations are shown in Fig. 6.17 D as black filled triangles.

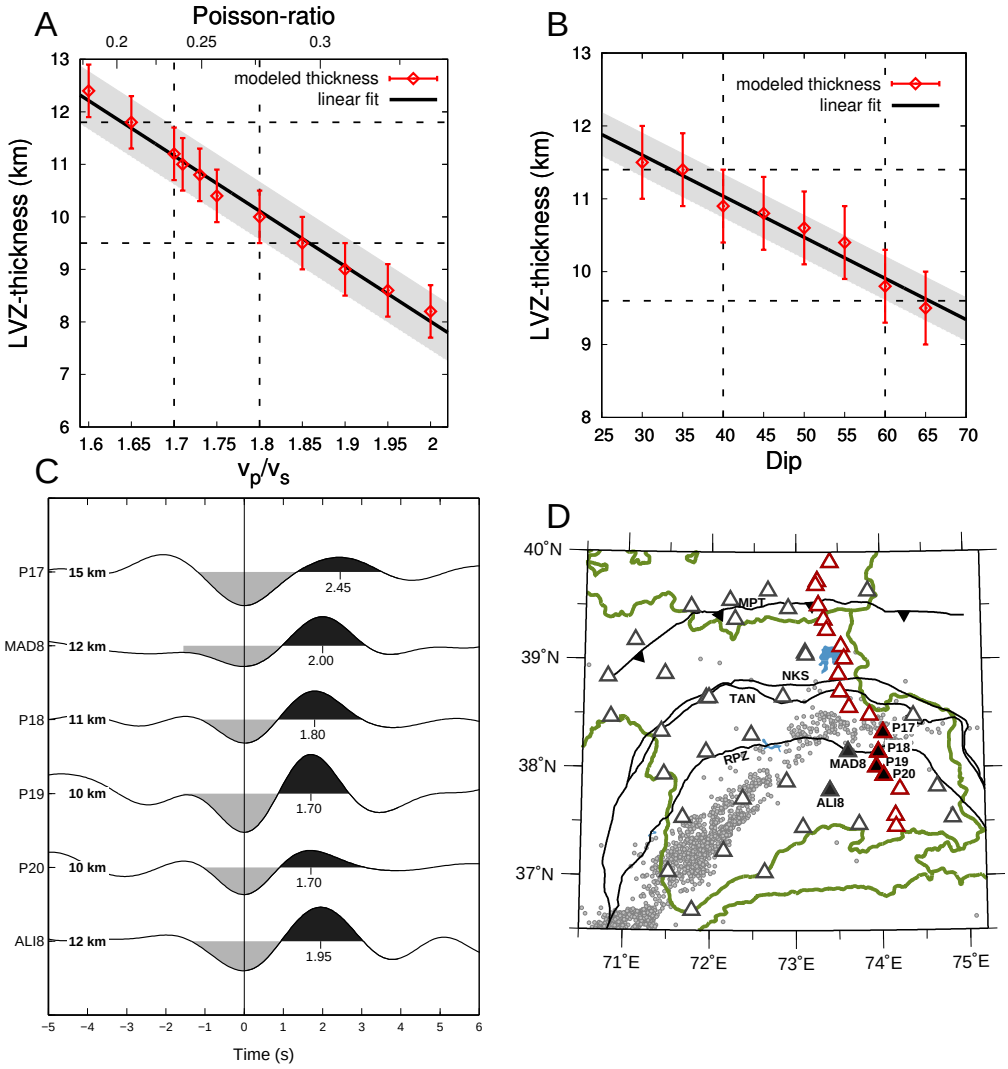

Figure 6.17.: A and B: estimation of the modeling error of the LVZ thickness due to incorrect v_p/v_s - ratio (A) or incorrect inclination angle (B) in the forward model. C: the LVZ phase in the T-component of the RFs at different stations stacked in the azimuth range from 30° to 110°. The corresponding LVZ thickness is written on each trace. D: station locations of stations whose TRF traces are plotted in C are depicted as black filled triangles.

6.5.3. Waveform modeling for thickness and velocity contrast of the LVZ

Modeling waveforms and amplitudes of the slab phases can provide information on the velocity of the LVZ. However, due to diverse sources of noise, lateral heterogeneity, anisotropy and data processing, amplitudes of receiver function summations often underestimate the true velocity contrast. These effects should be similar for the slab and the Moho phases. In Fig. 6.18 we compare modeled amplitudes of the slab phase with those of the Moho conversion for station P18. We examine the most coherent part of the receiver functions in the azimuthal range of 100-110° in order to reduce noise and heterogeneity. We stack QRFs and TRFs and extract the Moho Ps phase from the QRFs and the slab Ps phase from the TRFs. Synthetic QRFs and TRFs are modeled for the same azimuth and slowness values and treated in the same way as the observed data. The summation traces of synthetic and observed seismograms are compared. First, the amplitudes of the data are normalized to fit the velocity contrast (Δv_m) of Vs from 4.6 km/s to 4.15 km/s at the Moho (Mechie et al., 2012). The velocity contrast between the LVZ and the mantle is chosen relative to Δv_m. At station P18, the best fit between modeled and observed amplitudes of the slab Ps phase is achieved for a 10.5 km thick LVZ with a velocity contrast of $0.97\Delta v_m$, implying that the velocity of the LVZ is very similar to that of the lower crust. Assuming an S-wave velocity (v_s) of 4.6 km/s in the upper mantle, we obtain a v_s of 4.16 km/s in the LVZ. Thus we conclude that the LVZ is composed of lower crustal material.

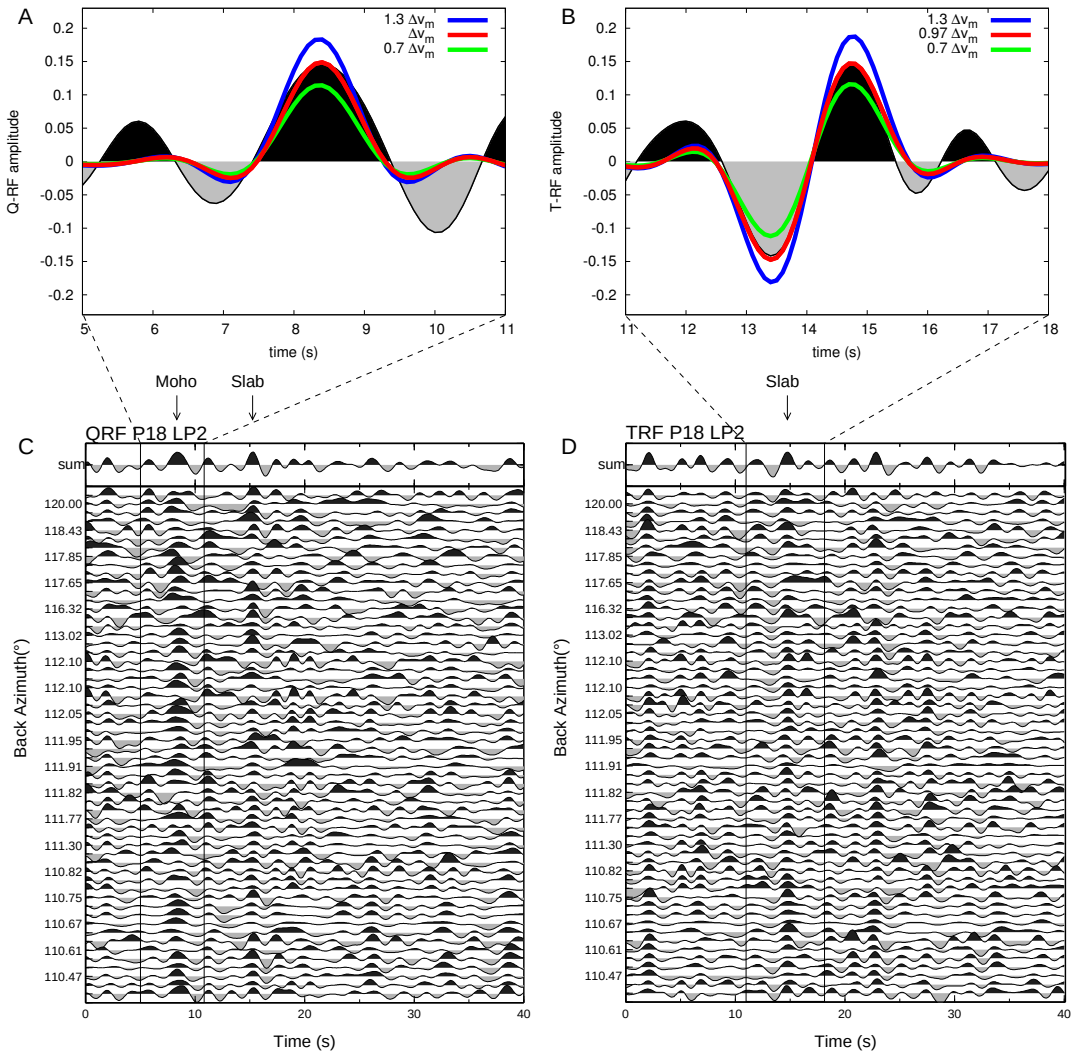

Figure 6.18.: Comparison and modeling of waveforms of (A) the Moho (on the Q component) and (B) the slab (on the T component) phases. To match the amplitudes for the LVZ (slab), the velocity contrast at the base of the LVZ has to be chosen to be very similar (97%) to that at the Moho. Amplitudes of the data are normalized to a velocity drop from v_s=4.6 km/s (mantle) to v_s=4.15 km/s (lower crust) at the Moho (Mechie et al., 2012). QRF and TRF data traces used for the modeling are shown in (C) and (D), respectively.

7. Crustal thickness

7.1. Determining Moho depth and the v_p/v_s velocity ratio

The delay time depth assignment for determining the depth of seismic discontinuities from the Ps phase alone always depends on the velocity model that is used. However, the differential Ps-P time is much more sensitive to the v_p to v_s ratio (v_p/v_s), than to the absolute v_p or v_s values. In Fig. 7.1(a) the dependence of the Moho depth results on v_p/v_s is displayed for different average v_p. If, for example, the Ps-conversion of the Moho appears in the receiver function at a time of 8.2 s, assuming an average crustal v_p of 6.0 km/s and a v_p/v_s of 1.73 results in a crustal thickness of 65 km, whereas assuming a v_p/v_s of 1.8 results in a crustal thickness of 60 km.

Realistic ranges of average v_p for a thick crust are shown in Fig. 7.1(b). v_p and v_s of the 1D reference velocity model is displayed with black and gray lines, respectively. The red line is the calculated average velocity above the current depth for a ray with slowness of 6.4 $s/°$, which has been determined by ray tracing. For a 60 to 70 km thick crust, the average crustal v_p for this model is $6.2 \pm 0.05\, km/s$.

In a realistic range for a 65 km thick crust, i.e. between 6.1 to 6.3 km/s for v_p and between 1.69 to 1.8 for v_p/v_s, the depth error range caused by uncertain knowledge of v_p is 2.5 km, whereas the depth error range caused by uncertain knowledge of v_p/v_s is 10 km, see red and green arrows in Fig. 7.1(a), respectively. Thus the effect on depth determination from uncertainty in crustal v_p/v_s is approx. 4 times higher than from the uncertainty in crustal v_p.

To minimize this kind of error and to determine the proper v_p/v_s ratio a slant stacking algorithm has been introduced by Zhu and Kanamori (2000). In this algorithm, in addition to the Ps phase, the arrival times of $PpPs$ and $PpSs$ multiples are consulted. The data are stacked in a Moho depth vs. v_p/v_s grid as shown in Fig. 7.1(a). Pre-assuming a fixed average v_p above the converter, the data are summed in three steps. First, the RF amplitudes are added to the array using the delay time depth assignment for direct Ps converted waves. In the next two steps the same RF data are added again using the delay time depth assignment for the multiple phases $PpPs$ and $PpSs$. Since the $PpSs$ phase shows

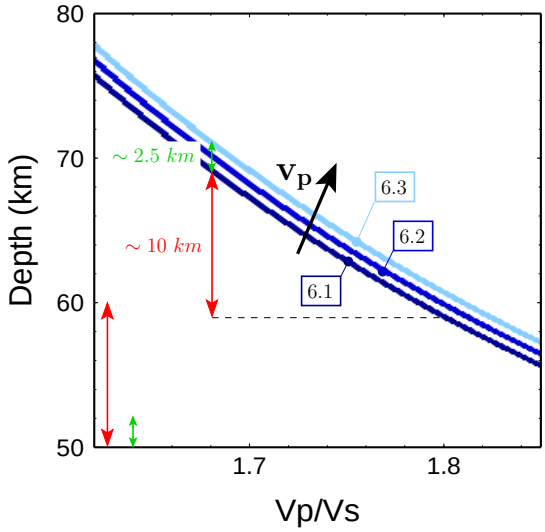

(a) Delay time depth assignment in dependence of average v_p/v_s and v_p above the converter. The three curves are calculated for average v_p of 6.1, 6.2 and 6.3 km/s, as marked. The converter depth would be overestimated by a too large v_p, while it would be underestimated by a too large v_p/v_s.

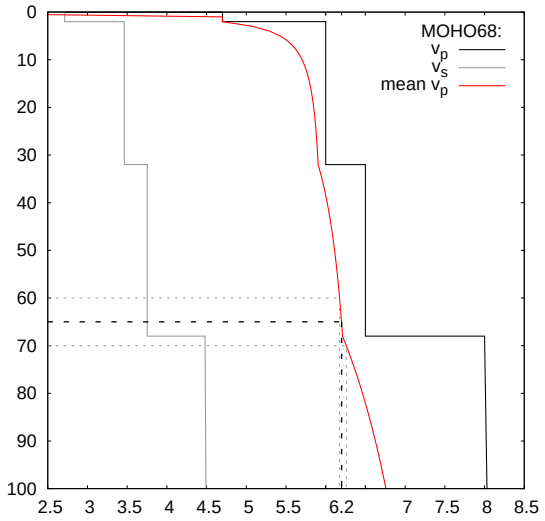

(b) 1D velocity model MOHO68: v_p black, v_s gray. The MOHO68 model is a modified version of the IASP91 model that was adjusted to a 68 km thick crust. The red line is the average v_p above the current depth. For calculation of the average v_p, ray path and travel time is calculated for a P-ray with a slowness of 6.4 $s/°$.

Figure 7.1.: Delay time depth assignment in dependence of model parameters.

opposite amplitudes compared to Ps and $PpPs$ (see for example Fig. 7.2(a) or Fig. 4.17), the sign of the amplitudes is inverted for this phase. Since all phases show different moveout behavior, the dependency of v_p/v_s likewise differs.

Fig. 7.2(a) shows a synthetic receiver function from a simple one layered crust. The first phase originates from the direct Ps conversion, while the later ones are the crustal multiples. Applying the slant stacking algorithm to this ideal case, all three phases of the single converter meet in one point in the v_p/v_s - depth grid, see Fig. 7.2(b). Fig. 7.2(c) shows the summation stack of all three phases. The result of the summation has its maximum, where all three phases meet and the corresponding depth and v_p/v_s values are assumed to be true.

7.2. Application of the slant stacking algorithm to real data

The slant stacking algorithm (Zhu and Kanamori, 2000) has been applied to all stations of the network and the data of each station was manually inspected. In many cases, the algorithm can not be applied without manually inspection and interpretation of the phases. If other crustal converters are present, the multiple phases of these inner crustal discontinuities can obscure the Moho phase. The slant stacking algorithm helps to identify possible candidates of "real" phases, through the association of direct to multiple phases. But in many cases just relying on the result of the maximum stack would result in wrong associations. Hence, an inspection routine is applied to each station to determine the Moho depth and v_p/v_s values. For each station, a combination of figures is inspected, which show different representations of the data. As example, Fig. 7.3 shows the different representations for station P24. First, all RFs are stacked in a depth-v_p/v_s grid. The results with different depth-time relations are plotted on top of each other in blue (Ps), green ($PpPs$) and red ($PpSs$) (see Fig. 7.3, top left). This is helpful for seeing, how many phases join together at one depth v_p/v_s combination, and how reliable the result of the maximum stack is (see Fig. 7.3, top right). In the next step, for the v_p/v_s-depth combination gained from the slant stacking method, curves of theoretical arrival times for the three investigated phases are calculated in dependency of the slowness. The resulting slowness arrival time curves are compared with the individual traces sorted for the slowness, see the lower panel of Fig. 7.3. The advantage of this representation is, that the direct and multiple phases can be distinguished from each other by their slopes (moveout). Direct Ps phases from a horizontal converter Ps have larger travel times for larger slowness, while the multiple $PpSs$ and $PpPs$ phases have shorter travel times for larger slownesses. Thus, in this representation, it can be checked whether the picked phases are assigned correctly by the slant

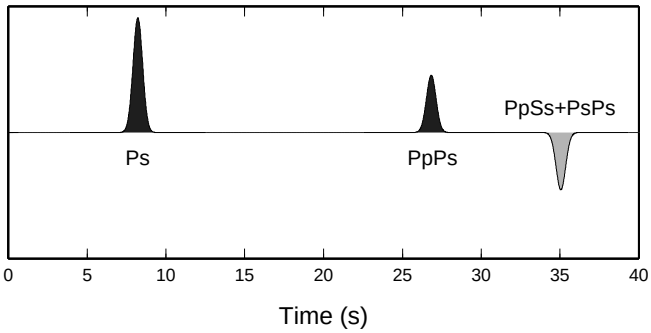

(a) Synthetic receiver function with Ps and $PpPs$ and $PpSs$ phases from the Moho of a 65 km thick crust. The slowness of the event is 8.3 $s/°$.

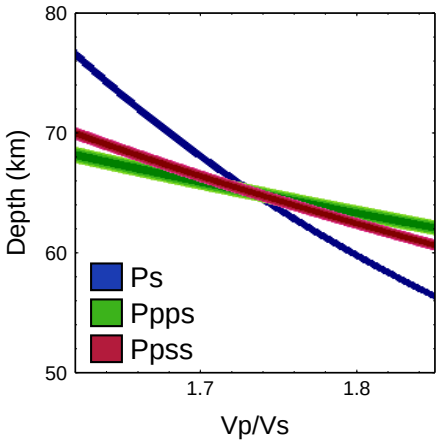

(b) Delay time depth assignment for Ps, $PpPs$ and $PpSs$ in blue, green and red, respectively. An average v_p of 6.0 km/s has been assumed.

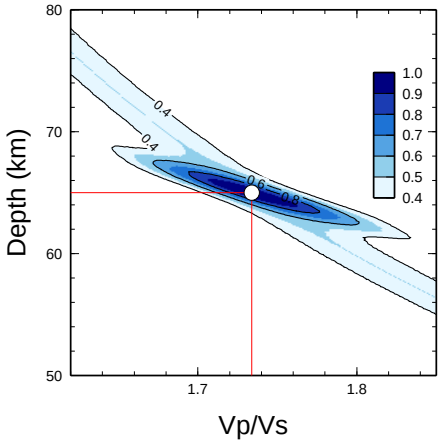

(c) Stacked result of Ps, $PpPs$ and $-PpSs$ with its maximum at a depth of 65 km and $v_p/v_s = 1.73$.

Figure 7.2.: The *slant stacking* - method of Zhu and Kanamori (2000) to determine the converter depth and the average v_p/v_s above the converter stacking the amplitudes of the receiver functions in a depth-v_p/v_s grid. Data are added to the grid three times with the three different delay time depth assignments of Ps $PpPs$ and $PpSs$ phases. In this example, the receiver function shown in (a) is used to test the method. In Figs. (b) and (c) the result of the slant stacking method for this single synthetic RF is shown and the crustal thickness of 65 km and v_p/v_s of 1.73 could be reassessed.

stack algorithm. In the example in Fig. 7.3 all three phases can be seen very clearly. In such a case the v_p/v_s value and the depth is considered robust. In other cases, when the multiple phases can not be identified clearly, but the Ps conversion is clear and shows the right slope in the lower panel representation, only the Ps time is picked, and the crustal thickness is calculated from this Ps time and a v_p/v_s value at the station location deduced through interpolation of v_p/v_s values from neighboring stations.

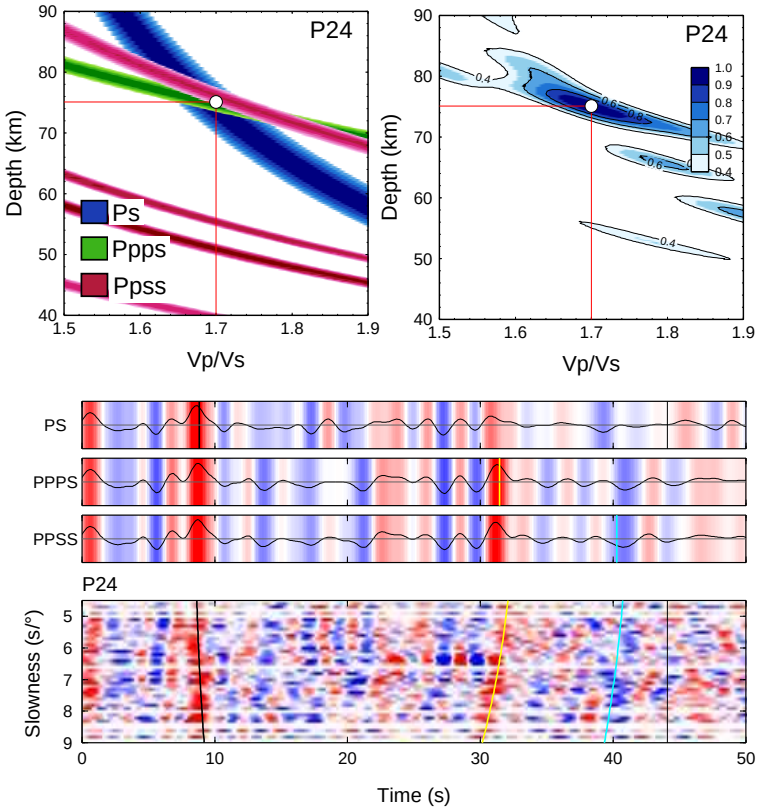

Figure 7.3.: Illustration of the data inspection for the Moho depth and average crustal v_p/v_s determination. Upper left: Ps, $PpPs$ and $PpSs$ phases in a v_p/v_s depth diagram; upper right: stacked Ps, $PpPs$ and $PpSs$ phases. Below individual traces sorted by the slowness for the event and summation traces after moveout correction for the direct and the multiple phases. The black, yellow and turquoise lines mark the theoretical arrival times of Ps, $PpPs$ and $PpSs$ phases calculated from the depth obtained by the slant stacking.

7.3. Ratio of compressional-wave and shear-wave velocity

The v_p/v_s values obtained from the slant stacking algorithm are shown in Figure 7.4(a). The Central Pamir and the eastern part of the South Pamir show very low v_p/v_s values (labeled as L1 in Fig. 7.4(a)), indicating a felsic crustal composition. There are 5 spots showing high v_p/v_s values (labeled as H1-H5 in Fig. 7.4(a)). The largest zones of high v_p/v_s are the Tajik Depression (H1) and the Ferghana Valley (H2). The high average crustal v_p/v_s values in basin areas are interpreted to hint at mafic compositions of the crust (Sippl et al., 2013a). In the Pamir, elevated v_p/v_s values are observed in the southeast at the border to Afghanistan (H3) and at two smaller spots close to station RAN8 at the Chinese border (H4) and in the north east close to the Main Pamir thrust (H5). The southern areas of elevated v_p/v_s are correlated to the location of the Shakhdara dome (H3) in the southwest and the Muskol-Shaput dome in the east (H4), marked as dotted areas in the map. The slightly elevated v_p/v_s values at stations VAN9 and POI8 are also coinciding with the location of the Yazgulom (not shown here) (Stübner et al., 2013b). These domes were exhumed from 30-40 km depth (Schmidt et al., 2011) and are exposing middle to lower crustal rocks. They consist of migmatit that has been created by partial melting of gneiss. From geothermal modeling Stübner et al. (2013a) inferred for the exhumation period very high geothermal gradients of 60°C/km that are relaxing since the the end of exhumation at 2 Ma (Stübner et al., 2013b). However, at present day, still a high geothermal gradient of 40°C/km is estimated, that is confirmed by the occurrence of plenty hot springs in the region. A constant geothermal gradient of 40°C/km would imply at depths deeper than 18 km temperatures exceeding 700°C, which is already higher than the melting temperature of solid rocks. Earthquake tomography shows low v_p values at 15 km and 30 km for this region (Sippl et al., 2013a), indicating that v_s must be decreased even more to match the observation of high v_p/v_s. Thus the observation of decreased values for v_p and high v_p/v_s might be best explained in this region by the presence of partial molten rocks.

7.3.1. Comparison with local earthquake tomography

To first order, the v_p/v_s values gained from receiver function analysis are in agreement with the v_p/v_s results from local earthquake tomography (Sippl et al., 2013a) at mid crustal depths (30 km and 45 km), shown in Fig. 7.4(b). Even if the image of local earthquake tomography looks more patchy, most main features can be correlated to each other. High values for v_p/v_s at locations H1, H3, H4 and H5 and low values in the eastern South Pamir (L1) are consistent to the

tomography values of the mid-crust. The low v_p/v_s values south of the Ferghana Valley (around 40°N, 72°E) seen in mid-crustal depths in the tomography are not seen by the receiver functions. At shallower depth levels, however, low v_p/v_s values are shown in the tomography at this location (Sippl et al., 2013a) (not shown here). Only station PAS8 shows low v_p/v_s values. One explanation for the discrepancy might be, that the v_p/v_s values can be erroneous for stations at the transition between Pamir and Ferghana valley, since the Moho depth changes strongly at this location, which might result in a strongly inclined Moho discontinuity. Since the slant stacking algorithm is assuming horizontal layering, this can lead to wrong v_p/v_s estimates.

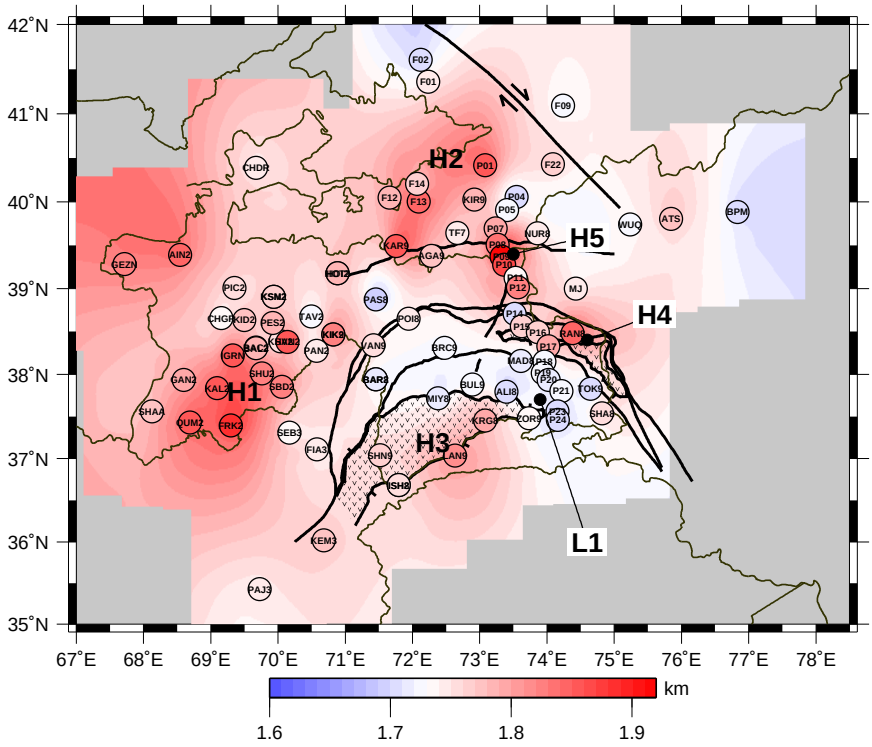

(a)

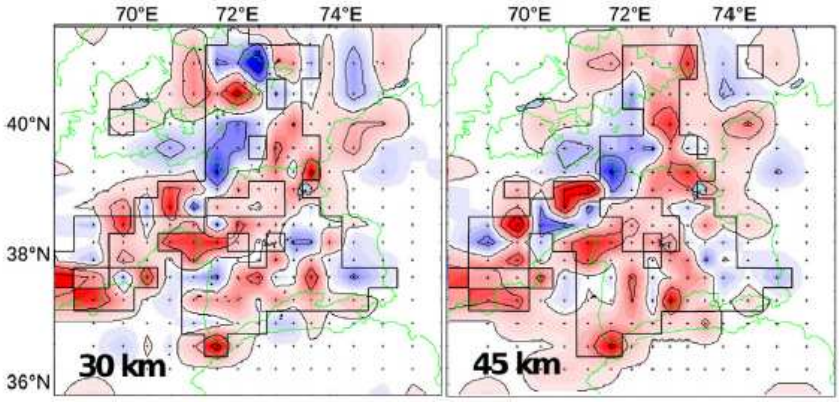

(b)

Figure 7.4.: a: Average crustal v_p/v_s gained from slant stacking technique using Ps, $PpPs$ and $PpSs$ arrivals; the dotted areas mark the locations of the Shakhdara dome in the southwest of the Pamir and the Muskol-Shaput dome east of the Central Pamir. Values for v_p/v_s are interpolated between the stations using the interpolation procedure of Smith and Wessel (1990) with a tension parameter of T=0.25. b: Depth slice at 30 km and 45 km depth of the v_p/v_s from local earthquake tomography (Sippl et al., 2013a).

7.4. Moho map from P-receiver functions

The Moho depth distribution computed from the P-receiver functions is shown in Fig. 7.5(a). At five stations, two Moho phases were detected. In the main Figure the deeper phase is chosen at these five stations, while the inset shows the area of the map that is affected with the shallower converter signal interpreted as Moho. Apart from these five stations, the Moho map distribution shows a 65 to 70 km thick crust at most stations in the Pamir and an increasing thickness of 70 to 75 km in the southeast, while in the basin areas surrounding the Pamir a shallower Moho depth of 40-50 km is detected. In the Pamir, there are two areas that showing strongly deviating Moho depths, one area of low crustal thickness in the eastern Pamir and the area showing the double Moho signal. Both the observation of a shallow and the double Moho signal can be explained as consequences of the same scenario: the arcuate subduction of crustal material in eastern, southeastern to southern direction, which will be shown in the following two sections.

7.4.1. Shallow Moho anomaly in eastern Central Pamir

Around stations RAN8 and P16 the Moho is shallowing to 50 km. In Fig. 7.6(b) the slant stacking results for both stations are shown. Both stations show a clear maximum at the attributed Moho depth. While for station P16 only the PpPs is non-ambiguously detectable, at station RAN8, where the Moho depth has its minimum, the depth is confirmed clearly by both multiple reverberations. The trend of shallowing Moho can also be observed along the profile in the corresponding latitude range at profile stations P12 - P21. From P12 to P16, the Moho depth is shallowing and from P16 to P21 the Moho depth is deepening again. For visualization of this Moho depth minimum, a cross section is shown passing P16 in south-north direction in Fig. 7.6(c). In addition to the migrated data show with the colors, the summation traces of each station is converted to depth, using the same 1D-velocity model as for the migration and then plotted on top of the migrated cross section. Station RAN8 (not shown), where the anomaly reaches its maximum is situated in this projection at the same location as P16 . Note, that v_p/v_s variation and topography are not considered in the cross section and v_p/v_s=1.73 is assumed. The summation trace of station P16 shows its maximum of the Moho phase at ∼57 km depth, that is 53 km below sea level. The increased v_p/v_s at station P16 and RAN8 further reduces the Moho depth to ∼50 km. In the cross section in Fig. 7.6(c) it can bee seen, that the position, where the detected Moho signal is shallowing coincides with the upper end of the low velocity zone (LVZ) that we interpreted as subduction of lower continental crust (Schneider et al., 2013). The detected Moho phase belongs to the southern plate, that overthrusts the LVZ. The shallowing of the Moho

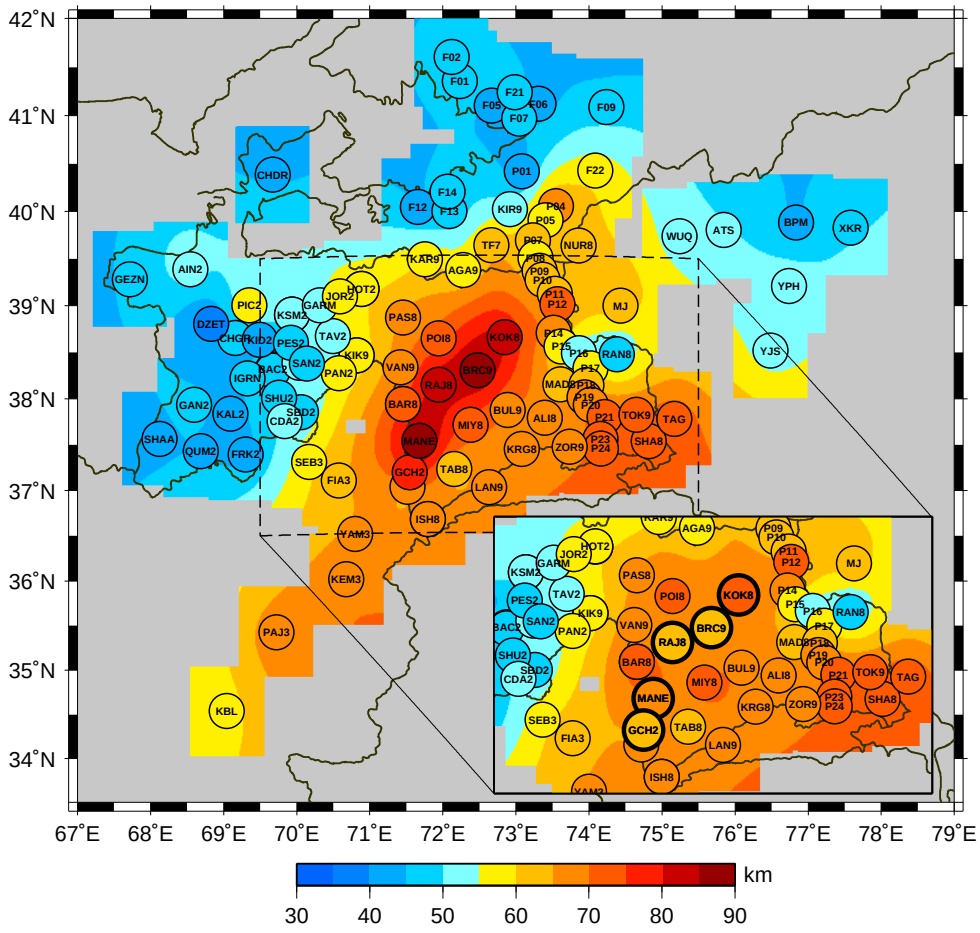

(a)

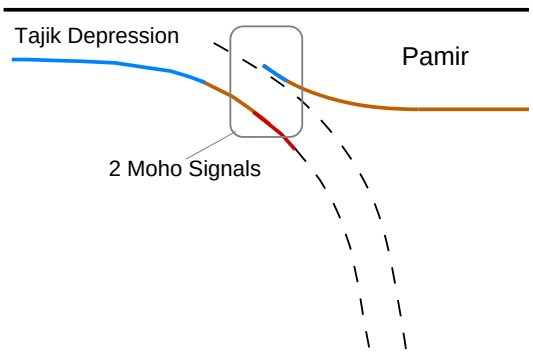

(b)

Figure 7.5.: a: Moho map calculated from P-Receiver functions. At the stations shown in 7.4(a). *Ps* and crustal multiples were stacked to determine the Moho depth, at the other stations only the *Ps* conversion time was taken into account. The inset shows the Moho map with an earlier conversion time interpreted as Moho at five stations marked with thick circles. Values for the Moho depth are interpolated between the stations using the interpolation procedure of Smith and Wessel (1990) with a tension parameter of T=0.25. b: Explanation sketch for double signals at five stations along the subducting plate of the Tajik Depression.

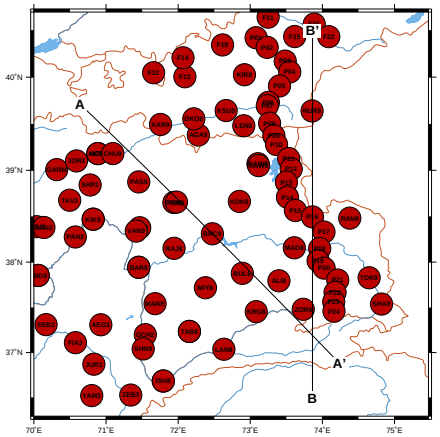

(a) Map showing the position of the cross sections shown in Fig. 7.6(c) and Fig. 7.7(b).

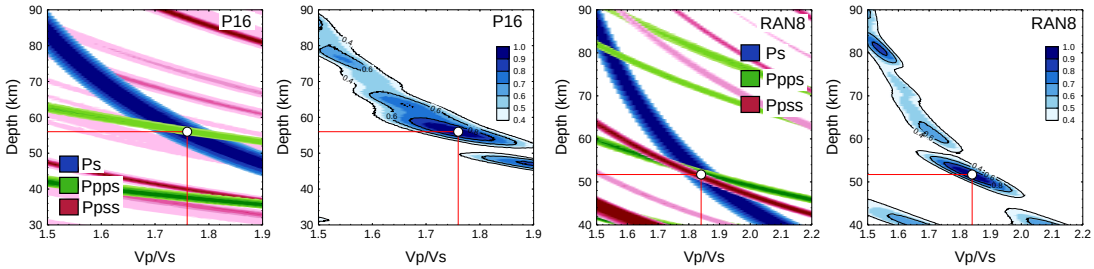

(b) Slant stacking results for stations P16 and RAN8, showing a maximum at 56 km and 52 km depth below surface, respectively.

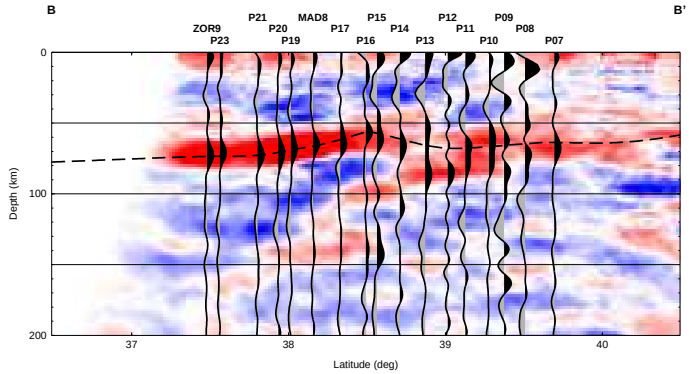

(c) P-RF-cross section in south-north direction passing station P16. The moveout corrected summation trace of each station is converted to depth, normalized to the Moho amplitude and plotted vertically on top of the migrated data (black wiggles).

Figure 7.6.: The shallow Moho anomaly in the eastern Central Pamir.

indicates that a mantle wedge on top of the LVZ exists up to 50 km depth. This anomaly withing the Pamir coincides with the position of the Muskol-Shaput dome, see Fig. 7.4(a).

7.4.2. Double Moho signal

Along a southwest to northeast trending arc, two Moho discontinuities are detected from (37°N,71.5°E) to (38.8°N 73°E). As example, in Fig. 7.7(a) the slant stacking result from station BRC9 is shown. Two prominent maxima are observed at 65 and 88 km depth with a v_p/v_s of 1.72 and 1.75, respectively. Similar to the shallow Moho in the eastern Pamir, the two signals at this locations can be explained by a subduction of the lower crust in southeastern directions. Fig. 7.5(b) shows a sketch describing the situation. At the position where the crust of the Tajik Depression descends, the Moho signal is discontinuous and the Moho signal from both plates are overlapping. Fig 7.7(b) shows a northwest to southeast cross section perpendicular to the strike of the descending plate. While the stations apart from the subduction slab show only one clear Moho phase, at station BRC9 the both plates overlap, resulting in the double Moho phases.

7.4.3. Basin areas surrounding the Pamir

In the basin areas surrounding the Pamir we observe a crustal thickness of 40 to 50 km. Even though the crustal thickness in the basin areas is nearly 40% thinner than in the Pamir, it is thicker than expected in some publications before. Results from a Russian publication of Kulagina et al. (1974) discussed by Burtman and Molnar (1993) show a Moho depth of less than 35 km in the south-west of Tajikistan. They conclude that the basement of the Tajik Depression is thinned. This can not be confirmed by our study. For no single station, a Moho depth of less than 40 km was observed.

However, since this point is important for further geodynamic interpretation, the issue of Moho thickness in the Tajik Depression will be further investigated in the following. Two stations of the area where the thinnest crust was expected are thus regarded in more detail.

Slant stacking for low average v_p

For all slant stack results shown in Fig. 7.5(a) an average v_p of 6.2 km/s was chosen. In the Tajik Depression, the occurrence of a very thick sedimental layer is reported. A 10 km thick layer of sedimentary rocks with $v_p = 4.7$ km/s and a basement with $v_p = 6.2$ km/s would reduce the average crustal v_p in the upper

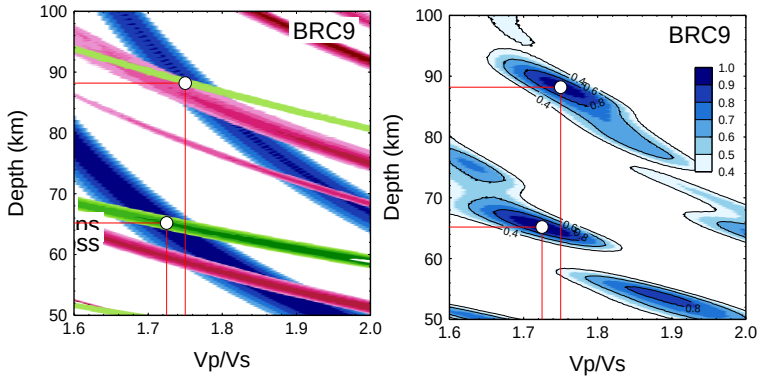

(a) Slant stacking results for BRC9 showing two maxima in the v_p/v_s-depth diagramm.

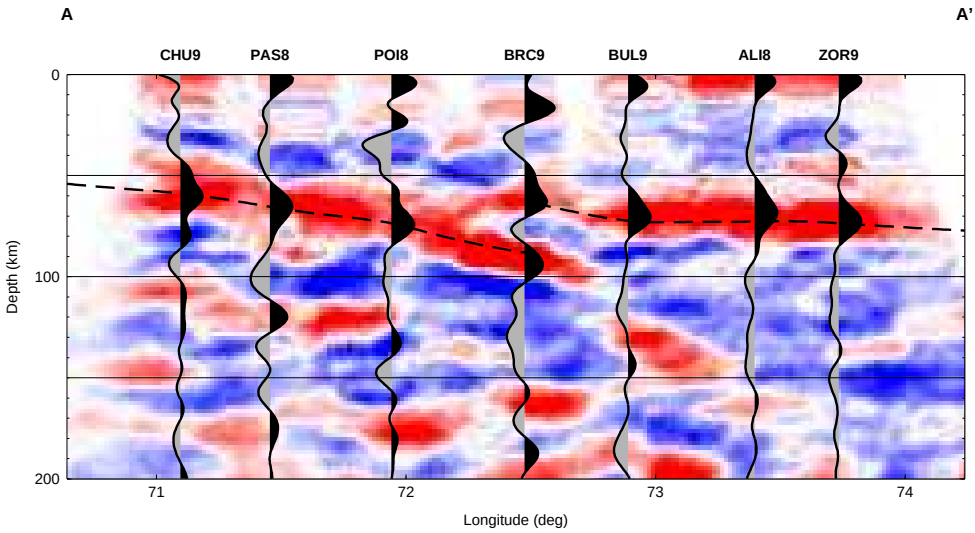

(b) Migrated cross section in northwest to southeast direction passing the station BRC9. the dashed lines are the interpolated Moho depths. While to the northwest of BRC9 the deeper version is plotted, to the southeast of BRC9 the shallower version is shown.

Figure 7.7.: BRC9 as example station with two Moho phases. Above: Slant stacking results; below: migrated cross section with summation traces plotted on top. Location of the cross section on a map, see Fig. 7.6(a).

35 km to 5.7 km/s for a P wave with the slowness of 6.4 $s/°$. However, in local earthquake tomography, the basement of the Tajik Depression is observed to be faster than 6.2 km/s for P-waves (6.4km/s-6.6km/s) (Sippl et al., 2013a), which would again increase the average crustal v_p. Thus the average v_p of 5.7 km/s can be seen as lower boundary for an estimate of the shallowest possible Moho. The slant stack was performed with $v_p = 5.7$ km/s for stations SHAA and QUM2, see Fig. 7.8. Compared to the slant stack result with $v_p = 6.2$ km/s, for the stations SHAA and QUM2, the Moho depth is decreased by 3.6 ± 0.2 km, which yields after subtraction of the topography 40.0 and 41.2 km, respectively.

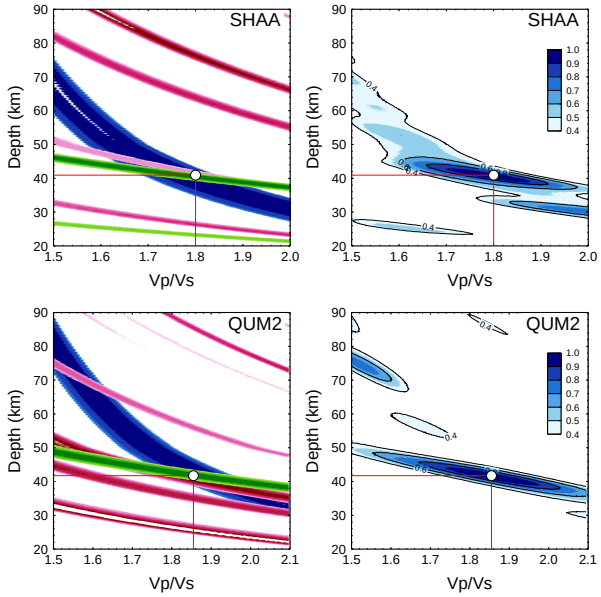

Figure 7.8.: Slant stacking results for station SHAA and QUM2, where the thinnest crustal thickness of the Tajik Depression was expected. Here a very slow average crustal $v_p = 5.7$ has been assumed, which decreases the Moho depth. After correction of the topography the resulting Moho depths are 40.0 km for station SHAA and 41.2 km for station QUM2.

Forward waveform modeling

A further approach for a crustal thickness estimate is the modeling of the whole waveform of the receiver function. Synthetic seismograms are computed using the reflectivity method and compared to the summation trace of the station. Synthetic and observed receiver functions were filtered with a Gaussian low pass filter with 1.5 s corner frequency.

An iterative forward modeling procedure is performed. In Figs. 7.9 and 7.10, the process is illustrated for stations SHAA and QUM2. Following the approach

of Mohsen et al. (2005), one phase is modeled after the other, beginning with the first phase and iteratively adding seismic discontinuities. Like this, higher priority is given to model the sign and the arrival times of the phases than to model the exact amplitude fit, since for the amplitudes the 3-D structure is thought to play an important role.

In the first panel of Fig. 7.9, the first phase is modeled, labeled as S. It produces two strong multiples (m1S and m2S). In the next step, to model the negative amplitude at $\sim 2\ s$, a low velocity zone is included in the model. The negative velocity jump produces a negative amplitude at 2 s (L1) and two multiples (m1L1 and m2L2), all marked with blue labels. The first (m1L1) multiple falls together with the Moho phase, but the second fits to an observed phase after the Moho. The phase of the positive velocity jump (L2) at the lower bound of the LVZ at 22 km depth appears at the same time as the second multiple of the first layer (m2S) and reduces its amplitude. Its multiples (m1L2 and m2L2) fit to observed phases at 11.5 and 15 s. In the next panel a lower crustal converter and the Moho step were included in the model. The direct phases are labeled U and M. The first multiple (m1U) fits to an observed phase, as well as the two multiples of the Moho (m1M and M2m). That the amplitude of the multiples is much smaller and the position is slightly shifted for m1M can be caused by the moveout correction of the observed summation trace, which is adjusted for direct Ps conversions. In the last step a LAB is included in the model to explain the negative phase at $\sim 9\ s$.

In Figure 7.10, forward modeling is performed for station QUM2 in a similar way as described for station SHAA. Note that for station QUM2, the waveform of the first 12 s seconds could be modeled with a 33.5 km thick crust alone, see third panel in Fig. 7.10. However, the waveform fit for $t > 15\ s$ improves significantly by introducing the Moho at 43.5 km depth. Multiple phases labeled as m1M, m2M and m3M appear at the right positions that are not present for a 33.5 km thick crust. Thus, the waveform fit of the multiple reverberations is supporting the Moho depth from the slant stacking method.

For both stations, the final model shows a Moho depth of more than 40 km. However, a lower crustal converter had to be introduced at a depth of 32 and 33.5 km for stations SHAA and QUM2, respectively. At station SHAA the direct phase of the lower crustal phase (U) is observable, as well as the first multiple (m1U). At station QUM2, the direct phase is hidden in the Moho phase, but the first multiple is also observable for this station. The occurrence of a discontinuity at 32 and 33.5 km depth at stations SHAA and QUM2 may explain the observation of a shallower reflector reported by Kulagina et al. (1974), which was interpreted as Moho.

The forward modeling shows, that reasonable models can be found to explain the waveforms that end up with the same Moho depth as the slant stacking

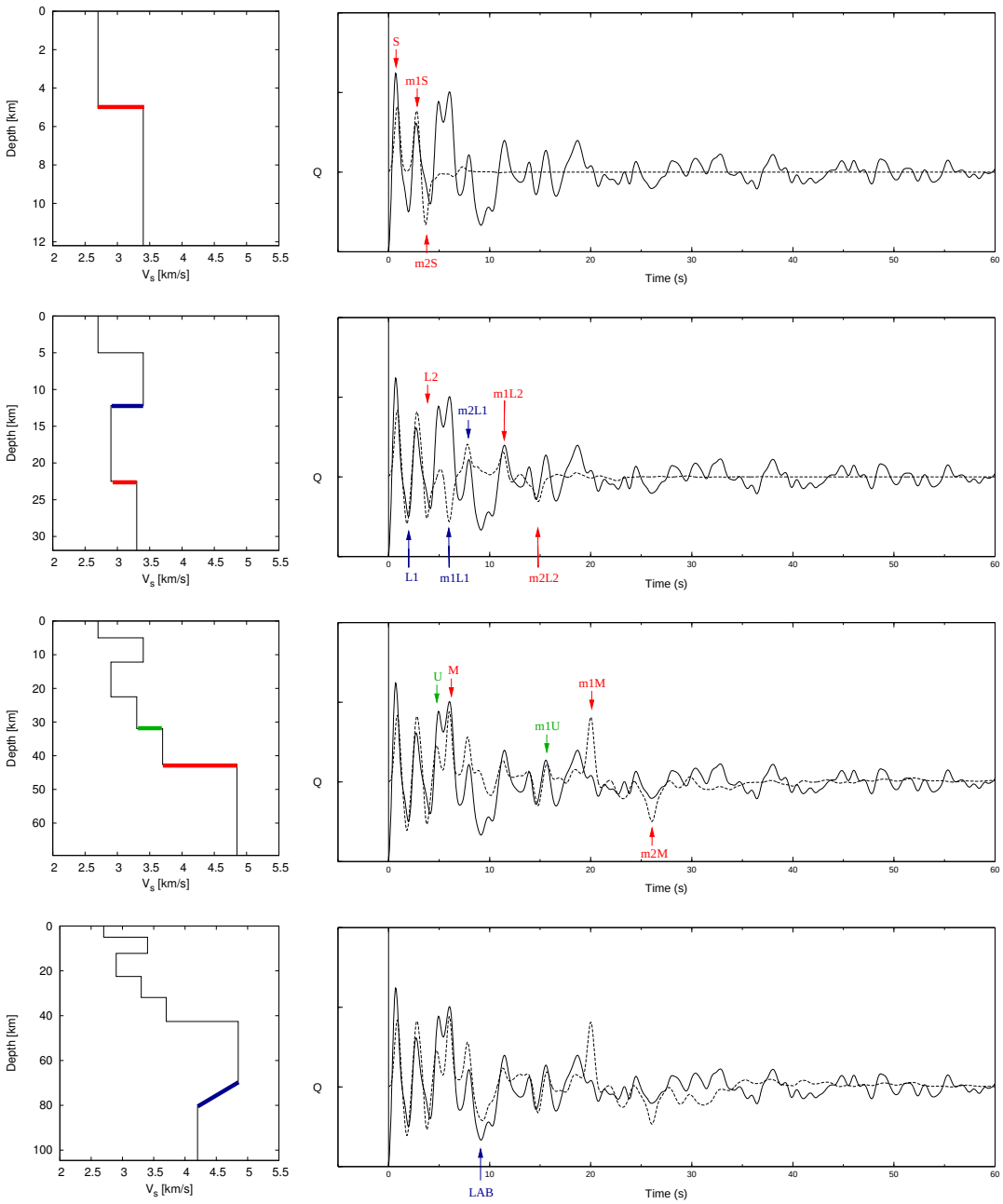

Figure 7.9.: Forward modeling of the P-receiver function at station SHAA in the Tajik Depression. The final model in the bottom figure consists of a 5 km thick sedimentary layer, a 26 km thick basement including a 10 km thick low velocity zone, and an 11 km thick lower crust. The LAB is modeled as a gradient layer in 70 to 80 km depth. For modeling, the layers are successively added starting from top to bottom. Phases and first order multiples of the added layers are labeled as follows: Upper and lower boundary of inner crustal low velocity zone (L1 and L2); Boundary between upper and lower crust (U); Moho (M); Lithosphere-asthenosphere boundary (LAB).

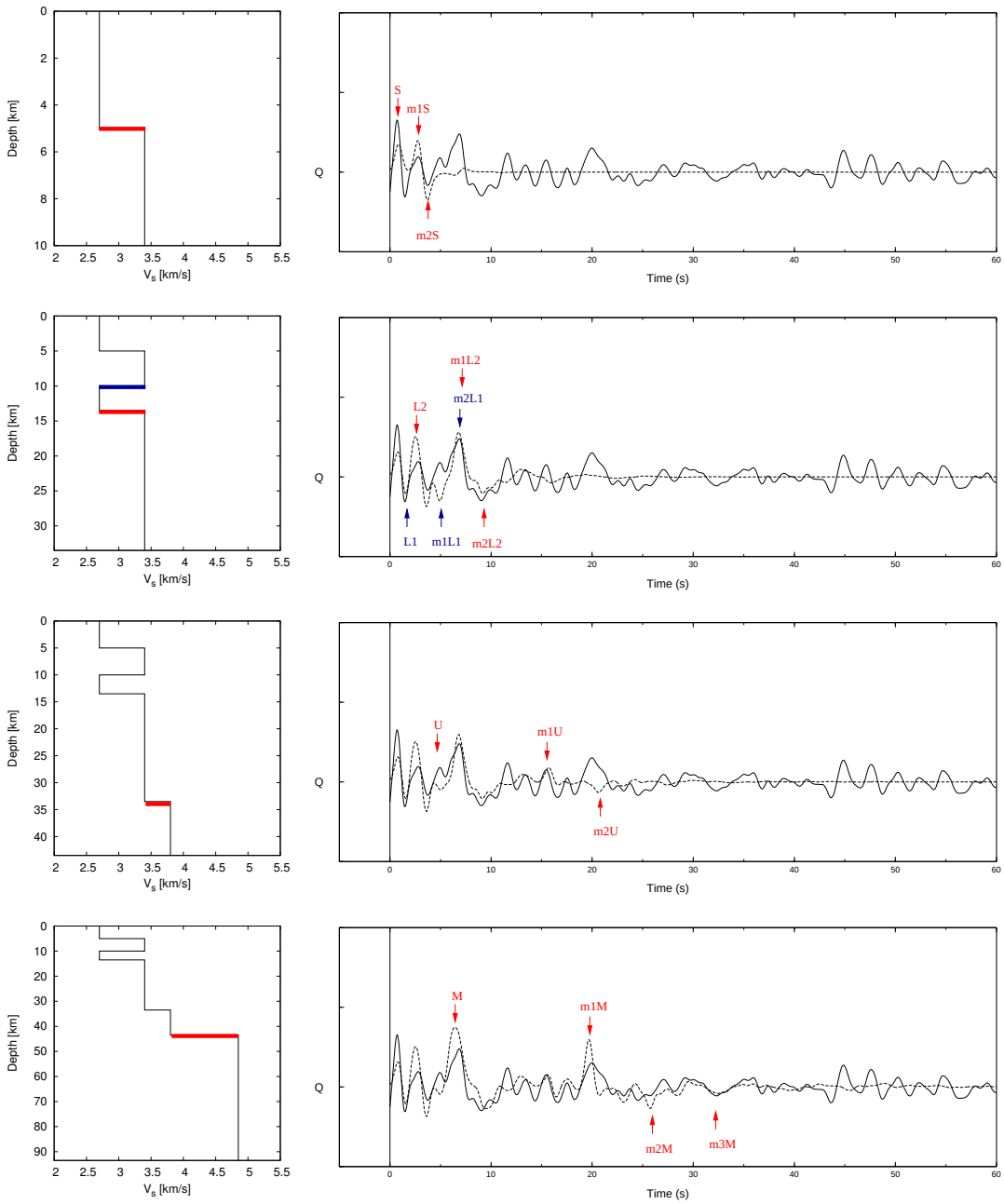

Figure 7.10.: Forward modeling of the P-receiver function at station QUM2 in the Tajik Depression. The final model in the bottom figure consists of a 5 km thick sedimentary layer, a 28.5 km thick basement including a 3.5 km thick low velocity zone, and an 10 km thick lower crust. The LAB is not included in the model. Phases and first order multiples of the added layers are labeled as follows: Contrast between sediment and basement (S); Upper and lower boundary of inner crustal low velocity zone (L1 and L2); Boundary between upper and lower crust (U); Moho (M).

algorithm predicted. However, for station QUM2 we demonstrated that a large part of the seismogram can also be explained by an alternative model with a thin crust due to crustal reverberations. Even if the later phases, interpreted as multiples, support a thick crust, here the non-uniqueness of the inversion problem becomes evident, since the modeled multiple phases could also be caused by direct Ps conversions of structure in the upper mantle. To gain more certainty in the crustal thickness estimate, in the next section the crustal thickness is deduced from another independent observation tool, namely from S-Receiver functions.

7.5. Moho map from S-Receiver functions

In this section, as a complimentary observation to the P-RF Moho map, the crustal thickness is deduced from S to P converted waves using S-RFs. Since the S to P converted waves are precursors of the direct S wave, they are not obscured by its crustal multiple reverberations that arrive after the main S phase. As the offset of the piercing points from S-RFs is large, a station wise analysis is not useful, since the observation areas from different stations overlap. As a rule of thumb one can estimate the Moho depth piercing point offset for S-RFs to be as large as the Moho depth itself ($\sim$ 50 km to 70 km). For a station spacing of 50 km in the Pamir and 20 km along the profile, the overlap between stations is large for S-RFs. To account for smaller Moho depth variations S-RF cross sections are computed using CCP stacking. Then the Moho depth is picked from the cross section.

In Fig. 7.11 all west to east cross sections are shown that have been used for Moho depth determination in the latitude range 37°-40°. The picked Moho depths are shown as green crosses. Note, that the displayed cross sections are gained using a 1D velocity model with constant v_p/v_s. To account for local v_p/v_s variations and to allow comparability with the P-RF Moho map, depth is corrected after picking the S-RF Moho using the interpolated v_p/v_s value at the corresponding coordinates from the v_p/v_s-map from P-RF slant stacking (see Fig. 7.4(a)). Thus, the displayed Moho depths in Fig. 7.11 are not the final values. Fig. 7.12(a) shows the Moho map from S-RF In Fig. 7.12(b) both P-RF and S-RF measuring points are combined in one data set before constructing the Moho surface. While for the P-RF Moho estimates the station locations are used as measuring points (depicted as triangles), for Moho depth estimates from S-RF the locations of the picks along the cross sections are used (depicted as squares). All Moho surfaces are constructed applying interpolation using continuous curvature splines in tension (Smith and Wessel, 1990) implemented in the *surface* tool of *GMT* (Wessel and Smith, 1998). Comparing the S-RF-Moho map to the P-RF-Moho map, the main features are identical. However,

the double Moho phase (inset in Fig. 7.5(a)) is not observed at many locations for S-RFs. In the fourth panel (38°N) of Fig 7.11 a similar situation can be seen as in Fig. 7.6(a). At 72° longitude two Moho phases could have been picked, the lower one with a continuation towards western direction and the shallower one with a continuation towards the eastern direction. In the northernmost part of Afghanistan, where no seismic stations are located so far, the observations could be extended. Comparing the S-RF Moho phase in this part to the P-RF Moho yields a continuation of the deep Moho in the Pamir towards the Tajik Depression.

In Fig. 7.13, three S-RF cross sections are shown that pass through the Hindu Kush. To get a clear Moho signal, strong lateral smoothing had to be applied, leading to a smeared signal. The upper two cross sections in west-east direction were used to determine the Moho phase. The lower one is a south-north cross section, showing the interpolated Moho depth gained from the S-RF observations as a dashed line. The average v_p/v_s along this cross section was calculated from the v_p/v_s data (see map in Fig. 7.4(a)) and used for the migration. Since only west-east cross sections were used, to determine the S-RF-Moho depth the good fit of the Moho in the south-north cross section confirm the picked depth values. Beneath the Hindu Kush, we observe a Moho at 60 to 75 km depth, deepening to southern and eastern directions. Moreover, at a latitude of 36.5° a deeper positive phase is observed (Fig. 7.13 lower panel), which probably originates from the southward subducting Tajik Depression plate . All S-Receiver functions are calculated using stations in the Pamir and Tajik Depression, since the Hindu Kush stations are short period sensors. Since only 3 months of data are available for the Hindu Kush stations, the P-RF Moho depths should also be treated with caution. In the S-RF cross sections the uncertainty is quite high, since a strong smoothing filter had to be applied to get a clear signal. Thus, as well for P-RF as for S-RF Moho depth beneath the Hindu Kush should be treated more as a rough and preliminary estimate.

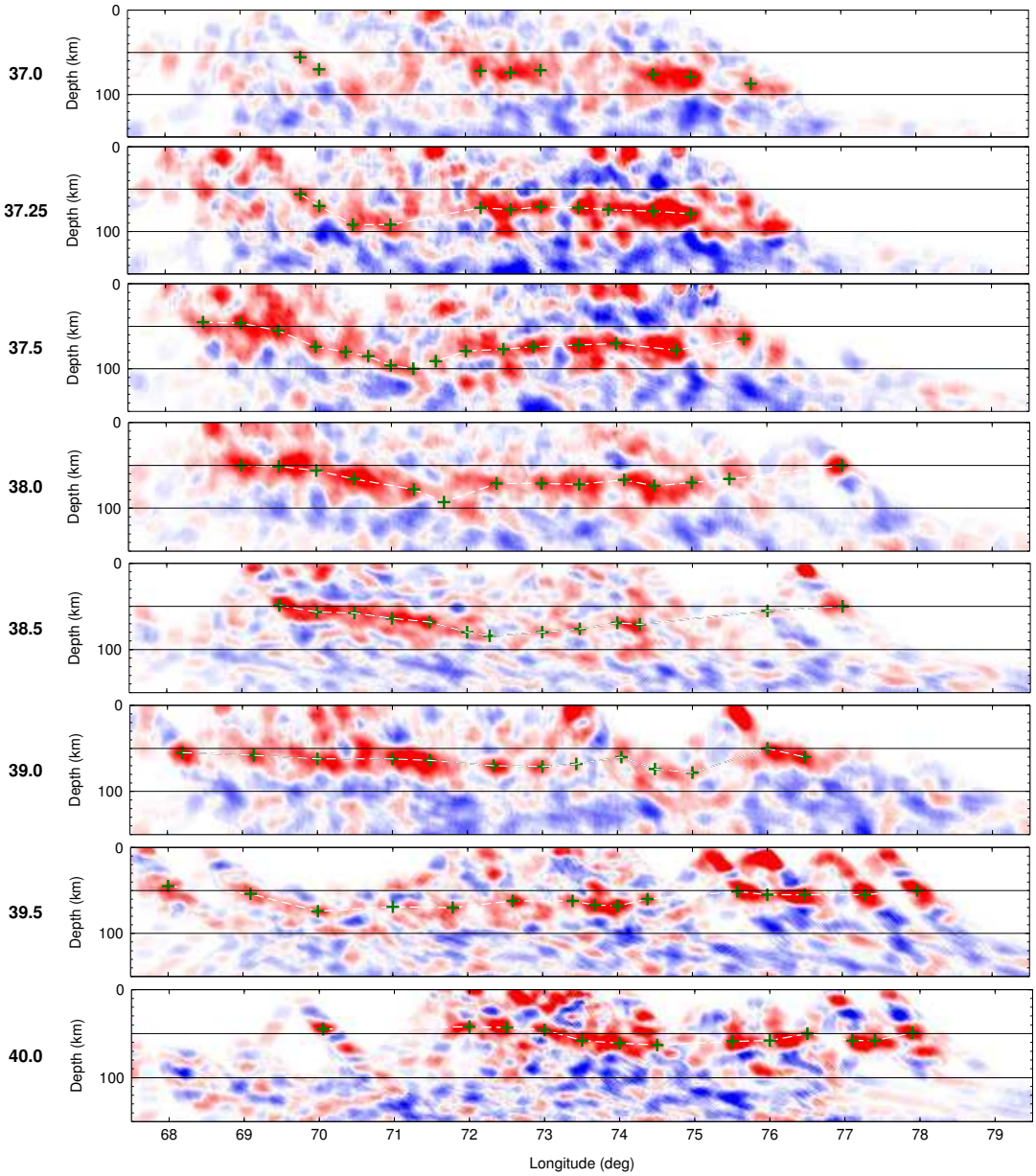

Figure 7.11.: West-east S-RF cross sections with picked Moho depths (green crosses). The center latitude for each cross section is written on the left side for each plot.

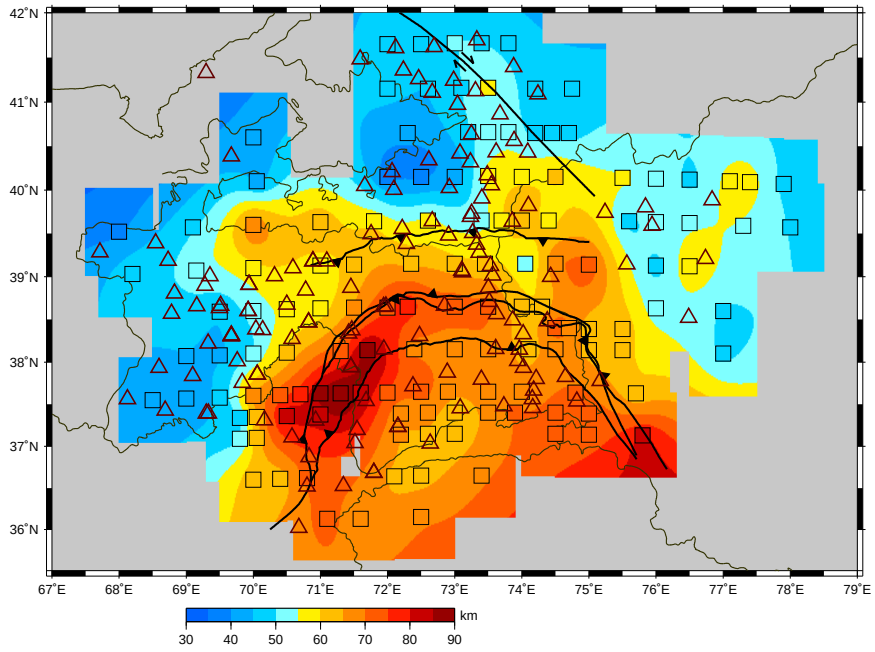

(a)

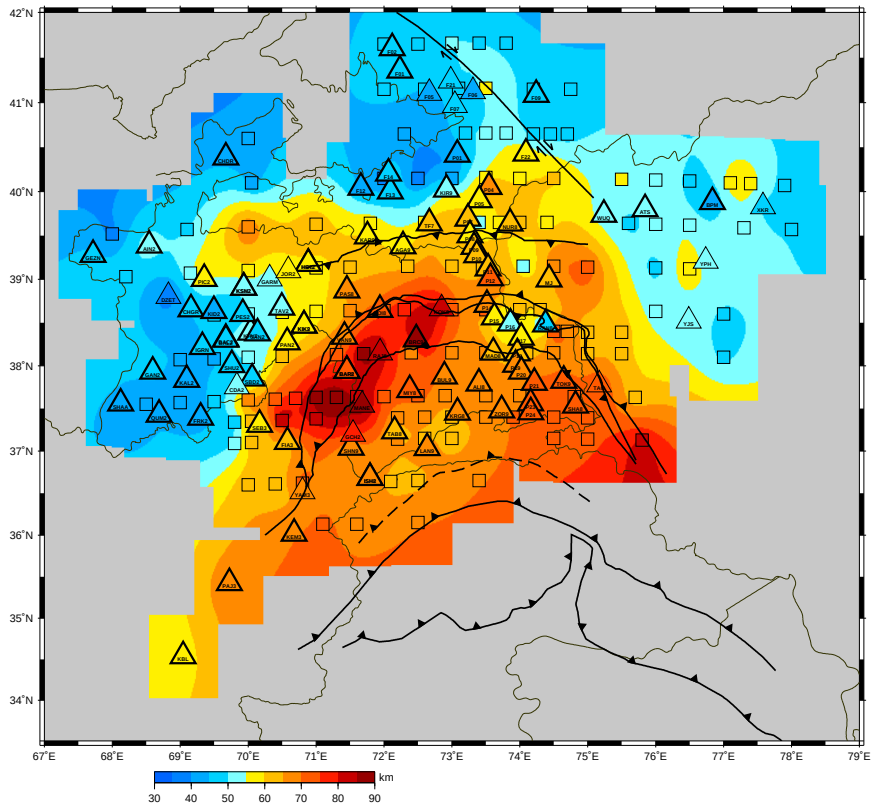

(b)

Figure 7.12.: A: Moho map from S-RF picks. B: Combined Moho map with depth values from P- and S-RF. Squares and triangles show the locations of picked S-RF Moho depths and locations of the seismic stations, that are used as measuring points for the P-RF Moho depth, respectively. Both P-RF and S-RF measuring points are combined in one data set before constructing the Moho surface.

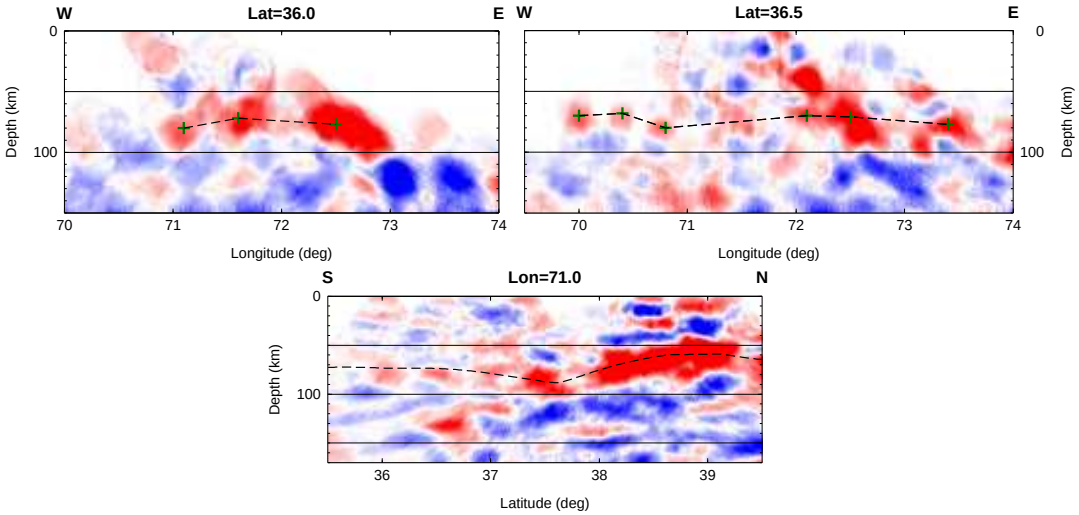

Figure 7.13.: Above: S-RF in west-east cross sections used for Moho depth determination beneath the Hindu Kush. Below: South-north cross section showing the interpolated Moho depth values as dashed lines.

8. Conclusion

8.1. Geometry of the Pamir slab

8.1.1. Southward subduction beneath eastern Pamir

The most important conclusion that can be drawn from the results of this thesis is that beneath the eastern Pamir the subduction zone is directed towards south and that the earthquakes of the Pamir seismic zone are hosted in a thin layer of subducted crust observed as a south dipping low velocity zone (LVZ). The observation of the LVZ is considered to be robust since it has been verified by several tests and forward modeling. It is observed on the Q-component (Fig. 6.1) and on the T-component of the P-RFs (Fig. 6.5) (QRF and TRF) as predicted by synthetic tests (Fig. 6.4). Moreover by applying an imaging method adjusted for inclined converters, it is shown that the earthquakes are located within the LVZ. Furthermore, the signals of the LVZ show a predicted polarity inversion on the T-component (section 6.3). In addition, an isolation of the conversion energy has been successfully tested using theoretical calculated angles for a complex rotation procedure. To get the right back azimuth values for the polarity flip, the dipping direction of the slab had to be pre-assumed (due south). For the complete isolation of the conversion energy on one component, both the dipping direction and the dipping angle has to be assumed. That both of these tests reveal the expected results can be regarded as a confirmation of the assumptions that have been done concerning the geometry. Moreover the geometry of the subduction zone is confirmed from S-RF and local earthquake tomography (see Figs. 5.14 and 8.3 below).

In forward modeling the thickness of the slab is estimated to 10-15 km. For the velocity contrast of the slab, a velocity decrease of approximately the same size as at the Moho is observed leading to the conclusion, that crustal material is subducted. To reveal the geometry of the subducting LVZ a model is constructed by combining a series of migration results taking into account different inclination angles (Fig. 6.6). In Fig. 8.1(a) the main results along the S-N profile are shown in a model sketch compiled by the results of Fig. 6.6 and extended in northern direction by the QRF results of Fig. 6.1. The subduction takes place south of the MPT. However, from the results it is evident, that the crust north of the MPT is much thicker, than the LVZ that is subducted. This leads to our

interpretation that not the entire crust is subducted (Schneider et al., 2013).

The south directed subduction beneath the Pamir implies that tectonic models for the Pamir-Hindu-Kush seismic zone with a single originally north-dipping overturned slab of Indian provenance as proposed by Billington et al. (1977), Pegler and Das (1998) and Pavlis and Das (2000) can be discarded. From the previously introduced models only the two slab models are thus possible. However, alternatively a one slab model is conceivable. Then, the Hindu Kush must be of Asian origin and have been contorted due to the collision of India. Evidences for a southward subduction of the Tajik Depression is gained from S-RFs (see Figs. 5.13 and 8.4, below). However, the zone of intermediate depth seismicity does not appear to align with this observation. They dip in opposite direction which hints the earthquakes to be located in an independent plate with opposite dipping direction.

8.1.2. Conclusion for the 3D geometry

The zone of intermediate depth seismicity beneath the Pamir has been resolved by Sippl et al. (2013b) as an arc dipping to the south in the eastern Pamir changing its dipping direction along arc by 90° to a eastward dipping direction beneath the south-western Pamir. At the eastern end of this arc it was shown, that the earthquakes are located within a LVZ, that connects the earthquake zone to the lower crust north of the MPT. In Fig. 8.1(b) the 3D location of the seismic zone and the P-RF observation is sketched. Since the earthquake zone beneath the Pamir appears to be a relatively smooth connected zone, the earthquakes are probably hosted in the same kind of material. Thus we propose, that the entire arc consists of crustal material.

This idea has been confirmed by several further observations. First a second SE-NW cross section of P-RFs (QRF and TRF) has been constructed that show a similar scenario as along the S-N profile (Schneider et al., 2013). However the resolution is not as good due to a more non linear station geometry. Furthermore, S-RF cross sections in W-E direction (see Figs. 5.11 and 8.2(a), below) and mapping of the Moho discontinuity from P-RF and S-RF (see Figs. 8.6 and 7.12(b)) show a consistent image of a east dipping Tajik Depression in the south and a Moho trough along the arc of intermediate depth seismicity. In addition to the Moho observation, in P-RF and S-RF show a negative phase beneath the Tajik Depression that I interpret as lower boundary of the lithosphere (LAB). This negative signal also shows consistent dip which further confirms the interpretation of the whole arc being a connected subduction zone.

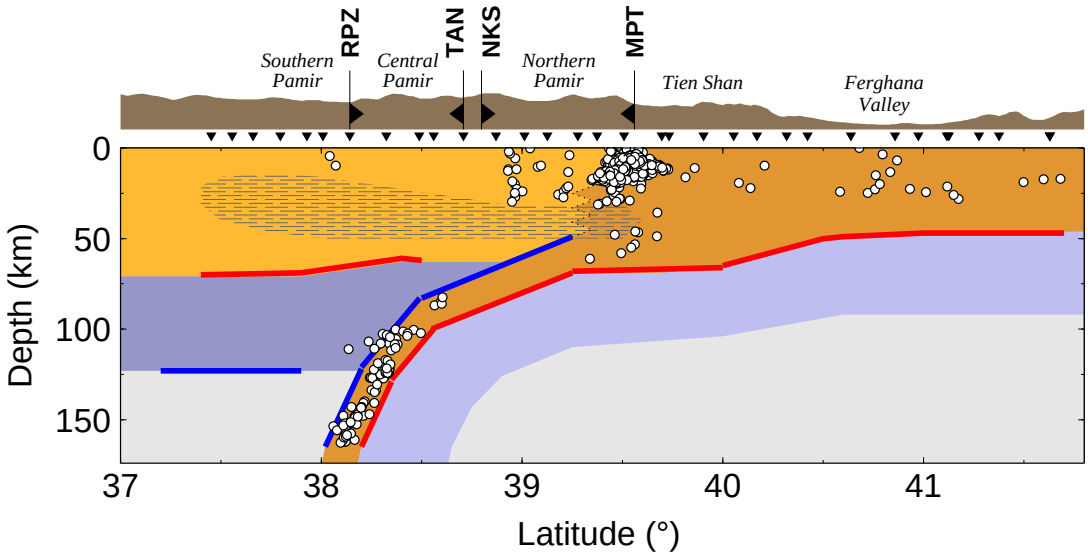

(a)

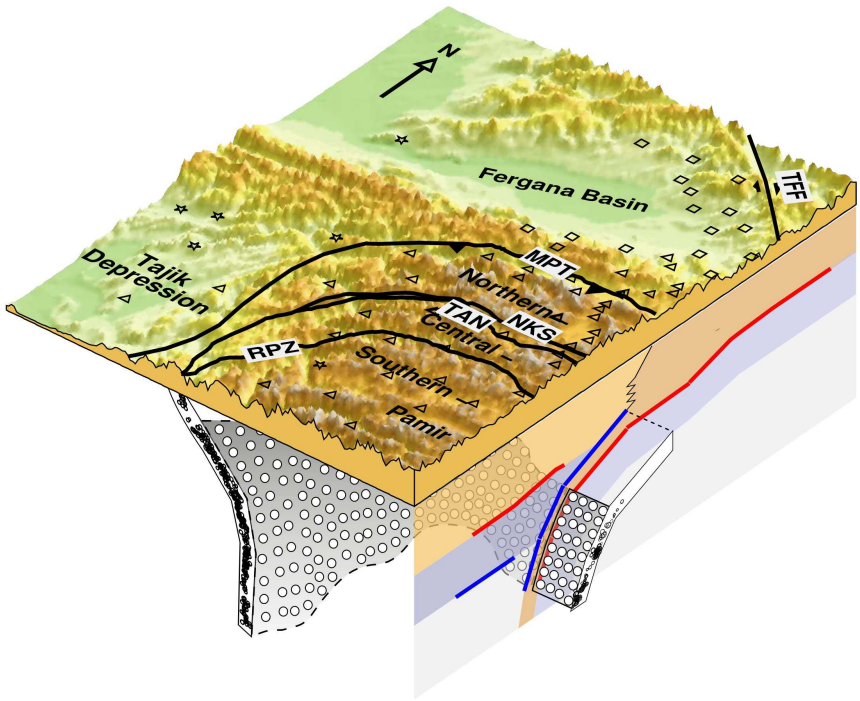

(b)

Figure 8.1.: a) 2D model for the eastern Pamir in S-N direction. This figure compiles the main result from the P-RF analysis along the S-N seismic profile. Red lines show the locations of the Moho and the lower boundary of the subducted slab. Blue lines show the locations of discontinuities with faster material being located above slower material (as LAB and upper boundary of the subducted crust).; b) 3D model showing the location of the S-N profile with respect to the zone of intermediate depth seismicity. The locations of earthquakes in (a) and the form of the seismic zone in (b) were provided by Sippl et al. (2013b).

8.2. Subduction of thin lithosphere

A further important observation obtained from P- and S-RF analysis is a quite thin lithosphere of the subducting Tajik Depression. Burtman and Molnar (1993) argue that the Tajik Depression plate may subduct entirely due to a thin basement of the crust. However, this can not be confirmed by our observations. We observe the crust of the Tajik Depression to be at least 40 km thick (see 7.4.3). However, our observation of the lateral depth variation of the LAB implies that the thick to normal crust is underlain of an only 40 km thick layer of mantle lithosphere. In the following, first the P-RF and S-RF observations are compared with results from tomographic inversion, than possible implications are discussed.

8.2.1. West-east cross section

In Fig. 8.2 RF results from the east-west cross sections are compared with results from local earthquake tomography (Sippl et al., 2013a) and an interpretation model is given. First P-RF and S-RF results are compared with each other and in the second step the comparison with tomography is done. In the left column of Fig. 8.2(a) the main converters from the S-RF cross sections (lower image) are picked and plotted on the P-RF cross section (upper image). In the right column the positions of the main converters are picked in the the P-RF image and ploted on the S-RF cross section. For the Tajik Depression (longitudes $<$ 72°) the Moho and LAB depths of P-RF and S-RF are consistent to each other. In the longitude range 70.5°-72° due to a lack of stations no discontinuities can be observed by P-RFs. However, the observation from S-RF directly connects to the depth and trend of Moho and LAB depths observed by P-RF west of 70.5° (See left column upper image). Similar, west of 69.5°, where the S-RF LAB observation gets diffuse due to a lack of piercing points (see Fig. 5.6), the P-RF observation connects to the depth and trend of the S-RF observations east of 69.5°. Thus, the Moho and LAB observation of the Tajik Depression can be considered as robust. The Moho observation beneath the Pamir is also robust. Both cross sections show the Moho in the same depth. The high velocity zone (HVZ) observed by the S-RF in the longitude range 72.5°-75° is not clearly visible in P-RFs. As discussed in section 5.2.4 this observation in S-RFs is also only observed from waves with high slownesses. P-RFs have in principle lower slownesses and steeper incidence angle that may explain the lack of observations in P-RFs. Moreover, the phases can be obscured in P-RF due to inner crustal multiples. So we will discuss the phases in the following, being aware, that the observation is not so strong.

In Fig. 8.2(b) the converters picked in Fig. 8.2(a) are plotted on top of the results from local earthquake tomography of Sippl et al. (2013a). The tomographic re-

sults are displayed in absolute values (upper image) and relative values compared to a reference model (lower image). For the Tajik Depression upper and lower boundaries of the mantle lithosphere (Moho and LAB) fit well together with an observed high velocity anomaly. Thus the observation in confirmed from all three methods. Beneath the Pamir, the observations from RF and tomography does not match as well as for the Tajik Depression. In the tomography, the transition to lower velocities from mantle to crust is observed at ∼60 km depth, which is 15 km shallower than the RF Moho. The S-RF observation of a HVZ in the upper mantle can also not be confirmed by tomography. However, the location of the S-RF HVZ observation is located at the edge of the area which is supposed to be resolved.

In the lower image all converter positions of S-RF and P-RF are plotted in a sketch. The observation of the subduction plate of the Tajik Depression is the feature with the highest certainty. The mantle lithosphere of the Tajik Depression seems to be very thin. From 68°-69°, where the plate does not appear to be inclined, the LAB is imaged at 80 km depth. The Moho in the Tajik Depression is at least 40 km thick (see section 7.4.3). Thus the mantle lithosphere appears to be only 40 km thick.

8.2.2. South-north cross section

In Fig. 8.3 P- and S-RF cross sections are compared to local earthquake tomography along the main TIPAGE profile in S-N direction. For P-RF along for this section at 73.5° the model including the inclined LVZ was constructed in section 6.2.4. Here the converters from the model are plotted on the tomographic result (see middle plot in Fig. 8.3). An S-RF cross section is constructed along the same meridian (upper figure). Then converter locations are picked and also plotted on the tomography result. P-RF and S-RF Moho depths are consistent to the tomographic inversions and to each other. However, directly south of the south-dipping LVZ the S-RF Moho appears deeper than the P-RF Moho, which hints to an inclined Moho, since inclined layers are imaged at too shallow and too deep locations in P-RFs and S-RFs, respectively. At the northern end of the cross section (41°) the LAB is detected by S-RFs in ∼80 km depth. Towards south the LAB deepens to ∼130 km depth at 39°. The thickness of the mantle lithosphere is around 40 km, which is the same value as observed in the W-E cross section for the Tajik Depression.

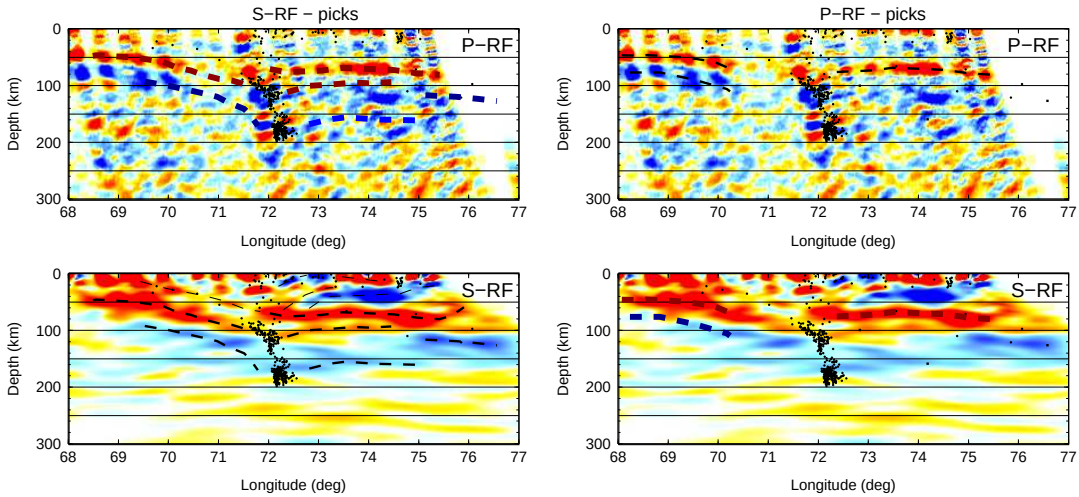

(a)

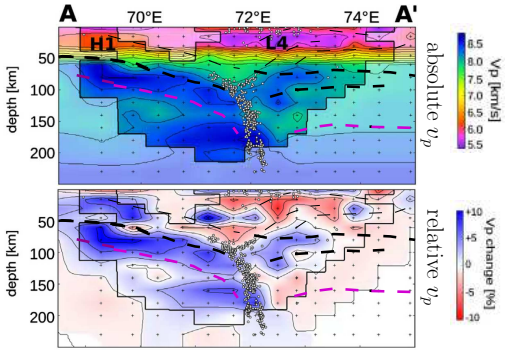

(b)

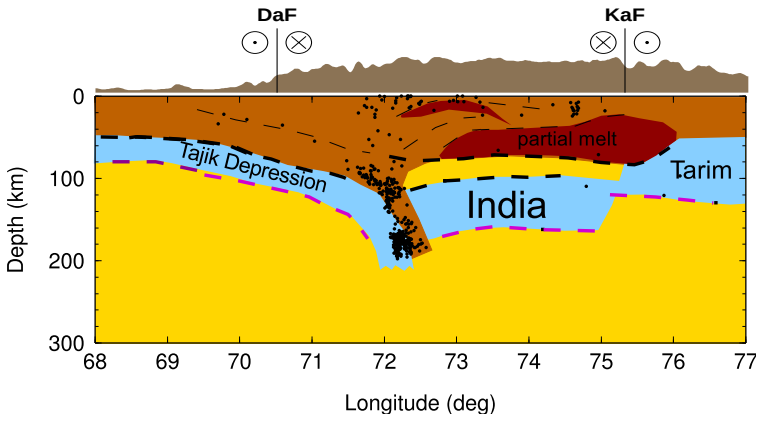

(c)

Figure 8.2.: A: Comparison of P-RFs and S-RFs. Left side: Lines picked from P-RFs are overlain on the S-RF result. Right side: Lines picked from S-RFs are overlain on the P-RF migration.; B: Combined lines from S-RF and P-RF overlain on local earthquake tomography result of Sippl et al. (2013a).; C: Interpretation figure with combined converters of P-RFs and S-RFs.

8.2.3. Is the subducted lithosphere of oceanic or continental composition?

The composition of the subducted lithosphere is still enigmatic. Along the S-N profile, we observe a crustal layer subducting toward the south. In our article (Schneider et al., 2013) we interpreted the material as lower continental crust. The reason for this interpretation is the observation of an at least 40 km thick crust in the Tajik Depression, which we took as a proxy for the crustal thickness of the basin area that had been subducted. Even if 15 km of sediments are subtracted, a 25 km thick crust is too thick to be oceanic. The crustal layer that we observe in the upper mantle is only 10-15 km thick. Thus we concluded, that not the entire crust is subducted. Only the lower crust may undergo a metamorphic transition due to the high pressure that is present at the base of a strongly thickened crust. The observed earthquakes in intermediate depth may be attributed to the eclogitization process. This interpretation is consistent to the absence of Cenozoic volcanism in the region (Schwab et al., 2004) that is present in most oceanic subduction zones. Furthermore, rock records indicating the presence of a remnant ocean basin north of the Indus-Yarlung suture have not been found so far (Burtman and Molnar, 1993).

However, the above introduced P-RF and S-RF analysis of recently obtained data in the Tajik Depression from the TIPTIMON deployment (Kufner et al., 2013) indicate the mantle lithosphere beneath the Tajik Depression to be very thin ($\sim$ 40 km). Thin lithosphere rather hints to oceanic than to continental lithosphere. In addition, the subduction of lower continental crust as proposed by Molnar and Gray (1979) requires the mantle lithosphere as driving force for the subduction. Thus continental subduction appears to be less likely for thin mantle lithosphere. Moreover many authors take the appearance of intermediate depth earthquakes itself as evidence for oceanic composition of the slab.

If we argue that continental crust is subducted here, we have to explain how the mantle lithosphere has been thinned. On the other hand if we argue that oceanic lithosphere is subducted the question arises how the oceanic lithosphere could be preserved longtime during the collision history of the Eurasian margin or where the oceanic crust comes from.

Both could be explained by a scenario related to the back arc dynamics of an Andean-type margin. As such, the Pamiran region is described, prior to the India-Asia collision (Schwab et al., 2004). Oceanic crust could be created due to rifting, and continental lithosphere might have been thinned due to back arc thinning as pre-stage of rifting or due to delamination.

Rifting during oceanic subduction, is caused through back-arc extension, which is induced by pulling forces of the slab (roll-back). The back-arc extension scenario would allow for creation of a small oceanic basin. Thus a relatively young

oceanic basin could be present which would explain its low thickness. However, the crustal thickness in the Tajik Depression is contradicting this scenario. But it can not be precluded that the crust that has already been subducted is of a different composition as the crust that is still observable beneath the Tajik Depression. If we however assume, that the subducted part beneath the Pamir is of the same composition as the crust in the Tajik Depression the observation of at least 40 km crust is difficult to explain by oceanic crust. Thus I favor the interpretation that the Tajik Depression is underlain by continental crust and that beneath the Pamir the lower continental crust is subducted, while the upper crust is incorporated in the thick crust observed in the Pamir.

8.2.4. Onset of Pamir deformation due to delamination event?

Since an extensional thinning of the lithosphere would probably also thin the crust together with the lithospheric mantle, which again would be contradicted by the observation of 40 km thick crust, I propose that rather lithospheric delamination must have been occurred. If we assume that the mantle lithosphere has been delaminated completely, we could roughly estimate the timing of the delamination event from its present day thickness. For oceanic lithosphere one can relate the thickness of the mantle lithosphere to its age (cooling time) (Wiens and Stein, 1983). A 40 km thick lithosphere is related to an age of 20 to 25 million years. Sclater et al. (1980) found that continental basins exhibit the same relation between heat flow and age, as the deep ocean floor. Thus the result of Wiens and Stein (1983) should be applicable for the situation in the Tajik Depression. 20-25 Ma is roughly the time, when the Pamir started to move northwards and of the initiation of major deformation in this region (Thomas et al., 1993; Sobel et al., 2013). Thus one can speculate if the onset of overthrusting of the Pamir was enabled by lithospheric weakening of the basin due to delamination.

8.2.5. The origin of the Hindu Kush seismic zone

In Fig. 8.4 the S-N cross section from S-RFs at 71° longitude is compared with a cross section from teleseismic tomography along the same meridian (Kufner et al. (2013) and pers. communication). In the tomography image a strong high velocity anomaly is observed in 300 to 600 km depth. A high velocity zone reaching down to the mantle transition zone has been also reported by previous tomographic results Koulakov and Sobolev (2006); Negredo et al. (2007). On the tomographic image the earthquake hypocenters of the Hindu Kush seismic zone are plotted (locations from Sippl et al. (2013b)). The seismic

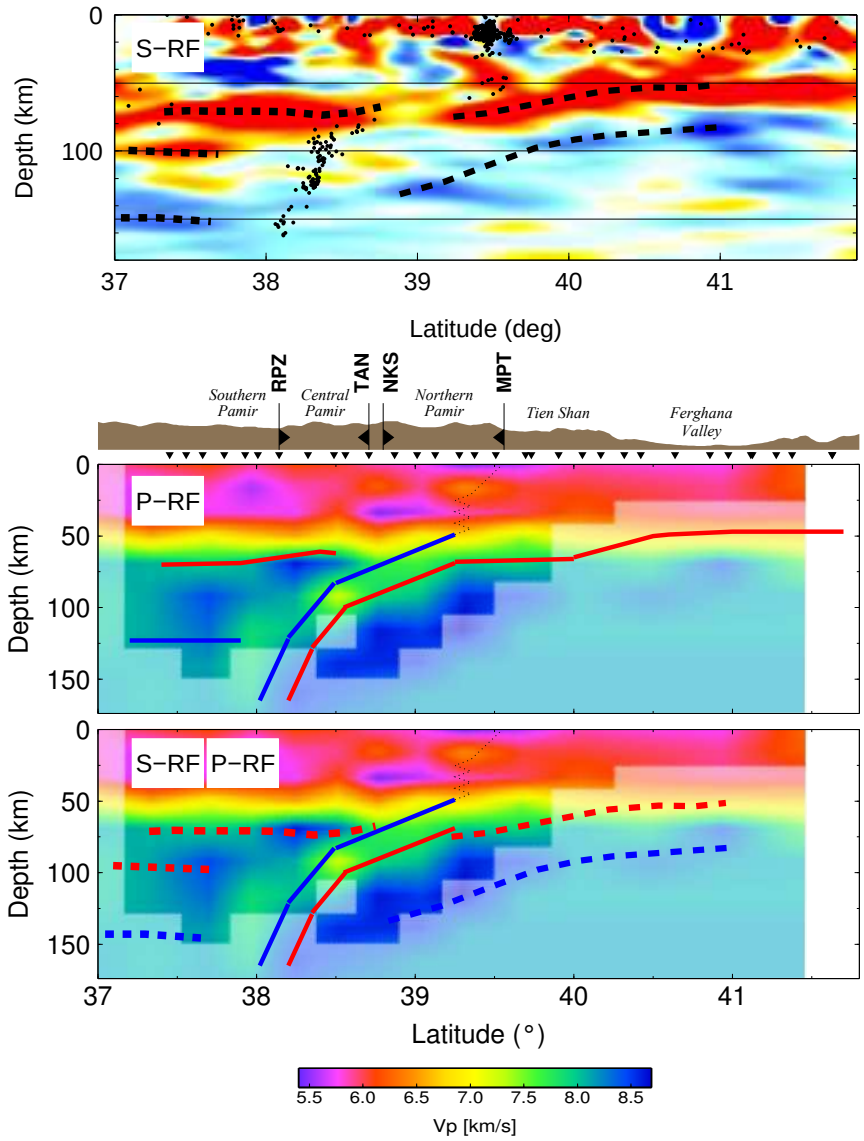

Figure 8.3.: Comparison of P-RF, S-RF and local earthquake tomography along the S-N profile. Central meridian of all cross sections is 73.5°. Upper panel: S-RF cross section. Middle and lower panel: local earthquake tomography (Sippl et al., 2013a) with positions of converters from P-RF (middle panel) and S-RF (lower panel). In the lower panel in addition to the S-RF lines the P-RF lines of the inclined converter are plotted. S-RF lines in the lower panel are picked in the upper panel and plotted with the corresponding colors. The converter of the P-RFs are taken from the model construction (see Figs. 6.6 and 8.1(a)).

zone seems to dip from south to north (compare also to Fig. 5.13). The S-RFs show a positive and negative converter imaging an upper and lower boundary of a high velocity zone that is interpreted as the Tajik Depression plate. In this cross section Tajik Depression plate appears to subduct in northern direction. In the upper image of Fig. 8.4 the positions of the double phase is picked and plotted on top of the tomography result. The double phase interpreted as subducting Tajik Depression plate ends close to the locations of the Hindu Kush seismic zone. Moreover it seems like the Hindu Kush seismic zone is deformed at the location where the Tajik Depression plate connects to it. The high velocity anomaly resolved by the tomographic inversion is located in the prolongation of the Tajik Depression plate. However, it is not clear if the high velocity anomaly is connected to the Tajik Depression plate or if it is connected to a plate subducting from south to north as indicated by the form of the seismic zone.

The geometry of the seismic zone indicates plate subduction from south to north direction. If the seismic zone belonged to the Tajik Depression, the Tajik Depression plate would have been overturned. However, the double phases in Fig. 8.4 does not show contortion. Only earthquakes deeper than 150 km could thus be explained by subduction of the Tajik Depression. Thus I infer, that the Hindu Kush seismic zone belongs to a northward subduction of a separate plate as proposed by various authors (e.g. Burtman and Molnar (1993)). However this conclusion, is still speculative. Further investigation of the area is necessary to resolve the crustal structure beneath and south of the Hindu Kush. Further data from the stations in Afghanistan deployed in the framework of TIPTIMON will be important in this context.

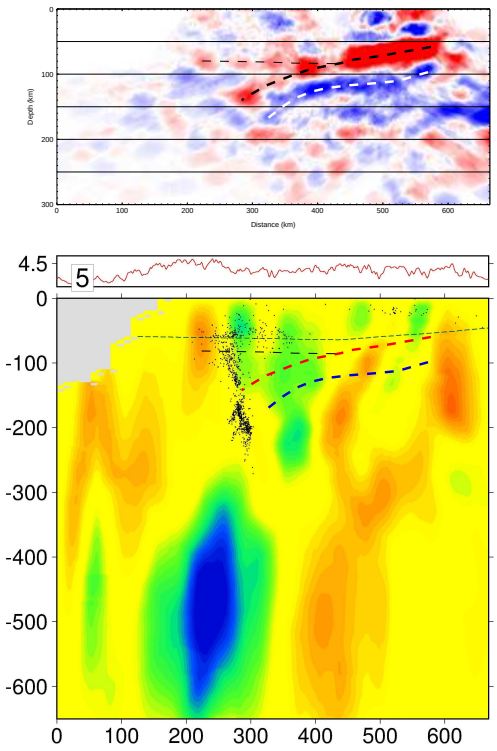

Figure 8.4.: Converters seen from S-RFs overlain on teleseismic tomography (results of Kufner et al. (2013) and pers. communication) on a S-N cross section along the meridian line at 71°. Green to blue colors are indicating high velocity material.

8.3. Crustal thickness map

The crustal thickness of the Pamir reflects the dynamics of continental collision and subduction. In the Pamir a thick crust of 70-75 km is observed. This is a consequence of crustal thickening due to continental collision. Beneath the western part of the Central Pamir, a Moho trough is observed with depths of more than 90 km. This observation reflects the under-thrusting and subduction of the Tajik Depression plate.

8.3.1. Comparison with tomographic results

The observation of a deep Moho trough can be confirmed by comparison with local earthquake tomography (LET). In Fig. 8.5 the Moho map is compared with a depth section at 80 km depth of the LET conducted from the TIPAGE data set (Sippl et al., 2013a). Contour lines of the Moho map are plotted on top of the LET image. In Fig. 8.5 A, contour lines from the P-RF Moho map are plotted, in Fig. 8.5 B the Moho map from the S-RF observations is used. The deep Moho in the western Pamir correlates with low P-velocities (depicted with red colors). The correlation with tomography confirms that crustal material is subducted to depth greater than 80 km at this location. Moreover the area depicted by the Moho trough and the low velocity coincides with the zone of intermediate depth seismicity.

A lateral shift in E-W direction between both results is evident. This may be caused either by the event geometry of the RF-analysis that is dominated by eastern back azimuths. Alternatively, the station geometry used for the tomographic inversion may account for a lateral shift since a station gap exists in northern Afghanistan that is close to the western termination of the anomaly. Moreover the P- and S-RF are sensitive to v_s velocity contrasts while in Fig. 8.5 A and B v_p velocities from tomographic inversion are shown. The comparison with the v_p/v_s results is therefore shown in Fig. 8.5 C and D. Here the red area depicts high v_p/v_s. The area of high v_p/v_s seems to fit better to the RF results. Moreover from this comparison, the trend of a Moho to deepen towards south-eastern direction is also consistent with low P-velocities and high v_p/v_s beneath southeast Tajikistan. The 70 km contour line of the P-RF Moho frames the decreased low v_p in 80 km depth. The Moho map observation and the local earthquake tomography show good correlations and thus both observations can considered to be robust.

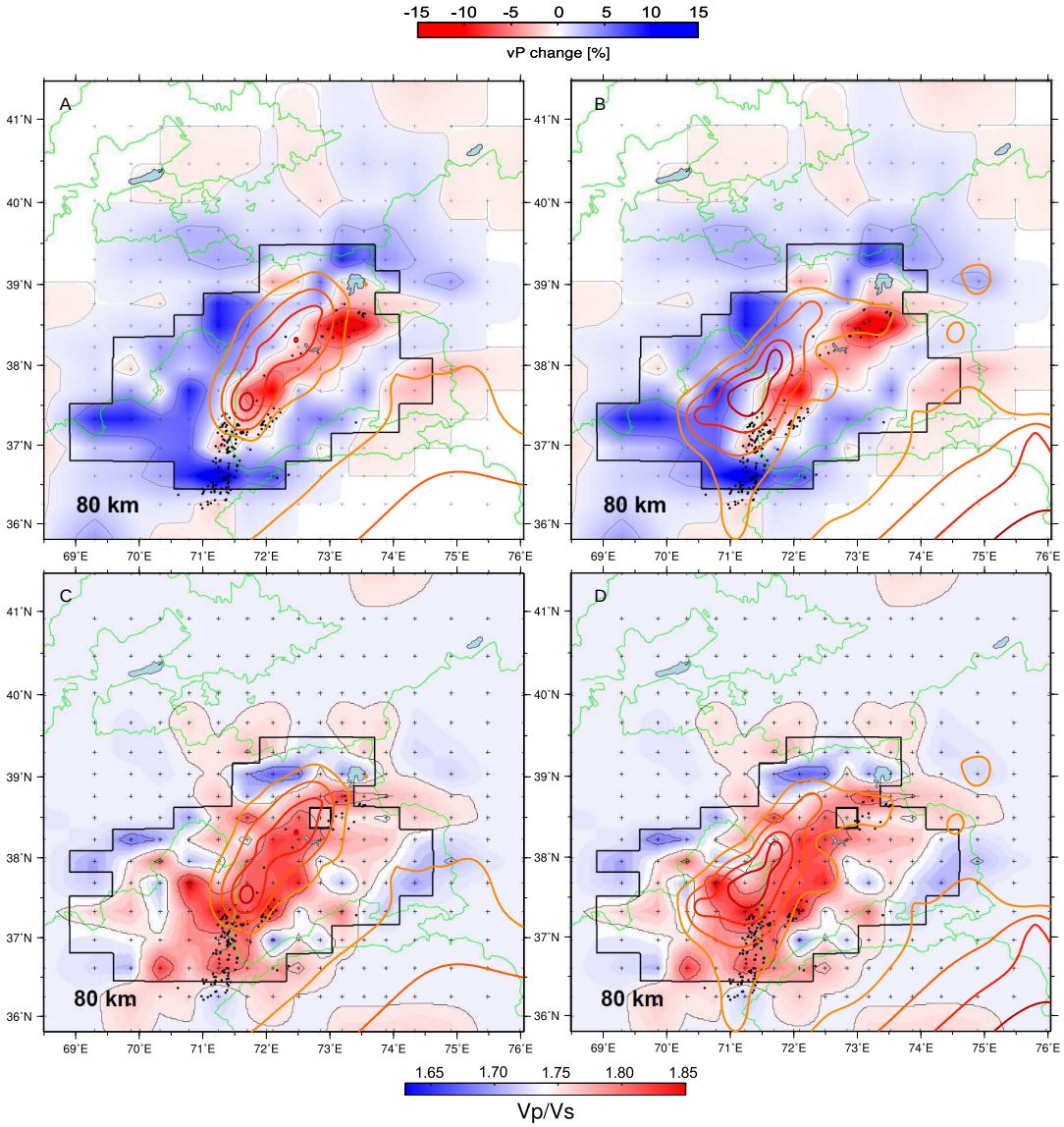

Figure 8.5.: Comparison of crustal thickness from RFs with local earthquake tomography (Sippl et al., 2013a). From the Moho map contours in 70, 75, 80 and 85 km are calculated and plotted in orange to red colors. A, C: contours plotted from P-RF Moho depth (see Fig. 7.5(a)); B, D: contours plotted from S-RF observations (see Fig. 7.12(a)). In A and B contours are plotted on top of the relative v_p - results, in C and D relative v_p/v_s results are shown.

8.3.2. Comparison with gravity results

Steffen et al. (2011) used gravity data to determine the crust-mantle boundary in Central Asia. In addition, this publication provides an isostatic Moho calculated from topographic data. By comparison of crustal thickness results from gravity inversion and from the isostatic Moho and effects of isostatic compensation is inferred. The crustal thickness results from gravity inversion are shown in Fig. 8.6 A. For the Pamir a 65 to 80 km thick crust was deduced, which is consistent to our observations. However, for the Tajik Depression they infer a shallow crust of less than 35 km in the south western corner. Comparing to the isostatic Moho shown in Fig. 8.6 D they infer isostatic under-compensation for the Tajik Depression.

In Fig. 8.6 C the P-RF Moho map is shown using the same color scale as used by Steffen et al. (2011). The crustal thickness deduced from P-RF observations does not drop below 40 km. Thus the contour lines at 50 km (plotted in orange) and 60 km (plotted in red) divide the investigation area in 3 domains with crustal thicknesses of 40-50 km (orange colors), 50-60 km (yellow) and greater than 60 km (green and blue colors). The area in green and blue colors outline the high elevated Pamir, with one exception in the eastern Pamir where a shallow Moho anomaly is observed (see section 7.4.1). In Fig. 8.6 D the contour lines of 50 and 60 km are plotted on the isostatic Moho map deduced by Steffen et al. (2011). Neglecting the Moho anomaly in the eastern Pamir, there is good agreement between contours and the boundaries of the yellow region that is showing the corresponding depth range. In the Tajik Depression the P-RF Moho results are better in agreement with the isostatic model. Thus, if the RF-results imply that the Tajik Depression is today close to isostatic equilibrium, while the gravity inversion would imply ongoing subsidence if not hindered by tectonic forces.

On the other hand, the Moho anomaly in the eastern Pamir as seen from RF imply a isostatic under-compensation in this area. This could induce subsidence and creation of an inter-mountainous basin, if slab roll back allows for isostatic relaxation.

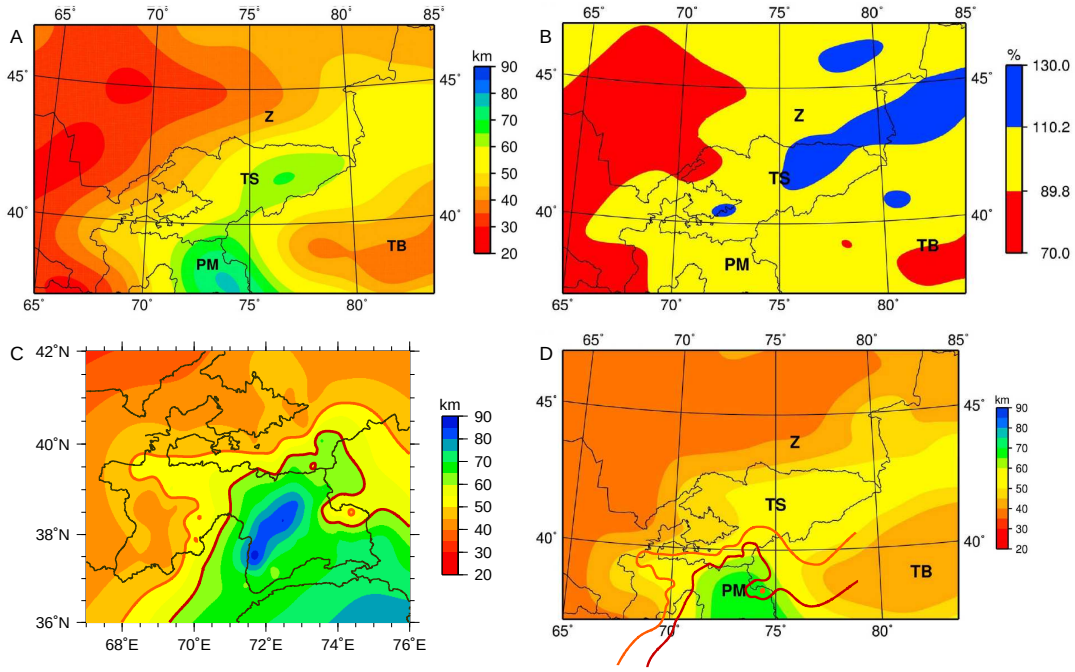

Figure 8.6.: A: Moho map for the Pamir and Tien Shan from gravity inversion (Steffen et al., 2011).; B: Isostatic compensation (ratio between Moho from gravity inversion and the isostatic Moho shown in D. Red, yellow and blue colors indicate under-compensated, equilibrated and over-compensated areas.; C: Moho map from P-RFs with contour lines at 50 km (orange), 60 km (red) depth.; D: Isostatic Moho calculated from topographic information (Steffen et al., 2011). Red and orange lines are the 60 and 50 km contours from the P-RF Moho map), respectively.

8.4. Summary

In the following I summarize briefly the main observations from this thesis.

The model shown in Fig. 8.7 provided by Sippl et al. (2013a) is therefore consulted and slightly modified. The model shows a 3D representation of a lithospheric block in the Pamir with two cross sections at its margins, one in N-S and one in E-W direction.

The Pamir slab describes an arc that bends from north-south strike to an east-west strike. Its upper layer is composed of lower continental crust that hosts intermediate depth earthquakes. Close to its eastern termination the crust of the slab was successfully resolved by receiver functions, see Fig. 6.5. The thickness of the subducted crust is estimated with 10-15 km by forward modeling (see section 6.5). The mantle lithosphere of the subducted slab appears to be only 40 km thin (see Fig. 8.2). This indicates that the mantle lithosphere of the basin area is thinned or have been removed during the collision and accretion history of the southern Eurasian margin.

S-RFs of a certain slowness and azimuth range provide evidence for the presence of Indian lithosphere at roughly the location given in the model (see 5.8). This observation indicate that the Indian slab is inclined and to dips in northern and eastern direction. If the interpretation of this observation is correct, it is likely, that the Indian and Eurasian lithosphere meet or collide in depth, and that the Indian lithosphere is down-welling together with the subducting Asian lithosphere at this location similar to what is observed beneath Tibet (Tilmann et al., 2003; Li et al., 2008).

In the western Pamir in the mid-crustal depths a strong signal is observed by S-RFs indicating a ductile-to-brittle transition at about 20 km depth, see section 5.4. This layer may serve as detachment, that decouples the upper crustal dynamic from lower crustal and mantle dynamics. This detachment layer allows for extensional dynamics of the upper crust in western direction.

The crust beneath the Pamir is 65-75 km thick and forms a deep trough, where the Tajik Depression plate is subduction in eastern direction. At this location probably both, the Tajik Depression lower crust and the Pamir lower crust is pulled down as indicated by the deep Moho phase and a forked up-dip end of intermediate-depth seismicity. In contrast, at the eastern end of the slab a mantle wedge seems to exist on top of the south dipping slab observed by a shallow Moho anomaly in this region (see section 7.4.1). The surrounding basins of the Pamir have a crustal thickness of $\sim$ 45 km. At no single station in the Tajik Depression a crustal thickness of less than 40 km has been observed.

Since we observe a clear connection between the subducted slab towards north and east, it is likely that the crust which has been overthrusted by the Pamir has had the same composition as what is present in the Tajik Depression today.

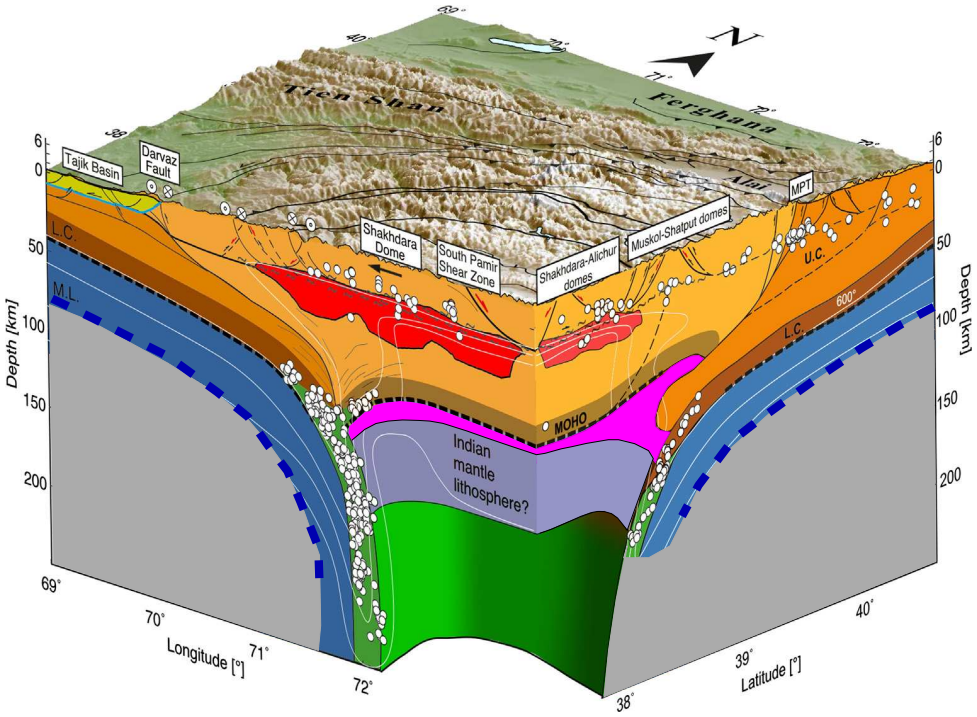

Figure 8.7.: Cross section, summarizing the results from the TIPAGE project (Sippl et al., 2013a). The figure has been slightly modified: The mantle lithosphere of the subducting basin has been thinned and a stronger downwelling of the Indian lithosphere is indicated to match the observation from S-RF. The approximate locations of the LAB-observations are depicted as blue dashed lines.

A. Determining the absolute S-velocity from receiver functions

The P incidence angle at the surface, as seen by a seismometer differs from the incidence angle inside of the medium, since the particle motion at the surface is a superposition of an incident and reflected P wave and a converted SV wave (Svenningsen and Jacobsen, 2007). This complex interaction is refected in the free-surface transfer matrix (Kennett, 1991). For P waves, the apparent incidence angle i_p can be defined as the rotation angle from Z, R, T system into a L, Q, T system for which the energy at $t = 0$ vanishes at the Q-component. The Q-component can be written as

$$Q = V_{QZ}\, Z + V_{QR}\, R. \tag{A.1}$$

The free surface transfer matrix separates the energy for each component.

Even if this matrix is not a rotation matrix, it is possible to calculate the angle between Q and R. This angle can be defined as the incidence angle.

Since Z and R component are orthogonal to each other and Q is the superposition of both vectors, we can calculate the angle between the Q and R vectors by

$$\tan(i_p) = \frac{V_{QZ}}{V_{QR}}, \tag{A.2}$$

which yields

$$\tan(i_p) = \frac{2\, p\, v_s^2 \sqrt{\frac{1}{v_s^2} - p^2}}{1 - 2\, p^2\, v_s^2}\,. \tag{A.3}$$

This expression is equivalent to that given by Svenningsen and Jacobsen (2007)

$$\frac{\sin(\frac{1}{2} i_p)}{v_s} = \frac{\sin(i)}{v_p} = p, \tag{A.4}$$

which can be proven by substitution of Eq. A.4 in Eq. A.3 and making use of trigonometric identities.

The apparent incidence angle of P-waves at the surface thus only depends on the surface shear velocity v_s. This result is surprising since inside the medium the incidence ange of P-waves depends in the velocity for compressional waves v_p.

In a reverse conclusion, by measuring the apparent incidence angle from the data the absolute v_s at the surface can be determined by

$$v_s = \frac{\sin(\frac{1}{2} i_p)}{p}. \tag{A.5}$$

B. Mathematical description of the deconvolution method

The deconvolution method that is used in this study is performing the deconvolution in the time domain. Different deconvolution methods are known such as spectral division or iterative deconvolution. In the following, the mathematical description of the deconvolution process is reviewed as it is realized in the SeismicHandler code (Stammler, 1993) and described by Gubbins (2004).

Let $q[t]$, $t \in \{0, .., n-1\}$ be the record of the Q component and $l[t]$, $t \in \{0, .., m-1\}$ be the wavelet record of the L component around the P-onset which should be deconvoluted from Q.
If we expand $l[t]$ to a $n \times n$ Toepplitz matrix

$$\underline{\underline{L}} = \begin{bmatrix} l_0 & 0 & \dots & 0 & 0 \\ l_1 & l_0 & \dots & \vdots & \vdots \\ \vdots & l_1 & \dots & 0 & 0 \\ l_{m-2} & \vdots & \dots & l_0 & 0 \\ l_{m-1} & l_{m-2} & \dots & l_1 & l_0 \\ 0 & l_{m-1} & \dots & \vdots & l_1 \\ 0 & 0 & \dots & l_{m-2} & \vdots \\ \vdots & \vdots & \dots & l_{m-1} & l_{m-2} \\ 0 & 0 & \dots & 0 & l_{m-1} \end{bmatrix}, \tag{B.1}$$

the convolution of $l[t]$ and the receiver function $R[t]$, $t \in \{0, .., n-1\}$ can be written as

$$q[t] = \left[\underline{\underline{L}}\,\underline{R}\right]_t = \sum_{i=1}^{m} L_{ti} R_i = \sum_{i=1}^{m} l_{t-i} R_i \,. \tag{B.2}$$

Thus we can define an error vector by

$$E[t] = q[t] - \sum_{i=1}^{m} l_{t-i} R_i \,. \tag{B.3}$$

To calculate the receiver function components $R[k]$ the least square method is used, minimizing the squared error

$$S = \sum_{t=1}^{T} E[t]^2 = \sum_{t=1}^{T} \left(q[t] - \sum_{i=1}^{m} l_{t-i} R_i \right)^2 \,. \tag{B.4}$$

In order to minimize S, each R_k is chosen such that $\partial S / \partial R_k = 0$, that is

$$\forall_k : \quad 0 = \sum_{t=1}^{T} 2 \left(q[t] - \sum_{i=1}^{m} l_{t-i} R_i \right) \cdot (-l_{t-k}) \,, \tag{B.5}$$

which can be converted to

$$\forall_k : \quad \sum_{t=1}^{T} l_{t-k}\, q[t] = \sum_{t=1}^{T} \sum_{i=1}^{m} l_{t-i} l_{t-k}\, R_i \,. \tag{B.6}$$

This is equivalent to the matrix representation

$$\underline{\underline{L}}^T \underline{Q} = \underline{\underline{L}}^T \underline{\underline{L}} \underline{R}. \tag{B.7}$$

The receiver function can thus be expressed as

$$\underline{R} = \left(\underline{\underline{L}}^T \underline{\underline{L}} \right)^{-1} \underline{\underline{L}}^T \underline{Q} \tag{B.8}$$

, and the inverse of $\underline{\underline{L}}$ is given by

$$\underline{\underline{L}}^{-1} = \left(\underline{\underline{L}}^T \underline{\underline{L}} \right)^{-1} \underline{\underline{L}}^T \tag{B.9}$$

.

The vector $L^T Q$ is the cross correlation vector of $l[t]$ and $q[t]$.

The matrix $\underline{\underline{L}}^T \underline{\underline{L}}$ is a symmetric Toepplitz matrix of the form

$$\begin{bmatrix} \phi_0 & \phi_1 & \phi_2 & \dots & \phi_{t-1} & \phi_t \\ \phi_1 & \phi_0 & \phi_1 & \dots & \phi_{t-2} & \phi_{t-1} \\ \phi_2 & \phi_1 & \phi_0 & \dots & \phi_{t-3} & \phi_{t-2} \\ \vdots & \vdots & \vdots & \dots & \vdots & \vdots \\ \phi_{t-1} & \phi_{t-2} & \phi_{t-3} & \dots & \phi_0 & \phi_1 \\ \phi_t & \phi_{t-1} & \phi_{t-2} & \dots & \phi_1 & \phi_0 \end{bmatrix}, \tag{B.10}$$

where each entry

$$\phi_i = \sum_k l_k \, l_{k+i} \tag{B.11}$$

is the unnormalized autocorrelation of $\underline{l}$.
This symmetric Toepplitz matrix can be inverted using an Levinson algorithm, which is implemented in SeismicHandler (Stammler, 1993).

C. List of stations used

In table C.1 all stations that have been used as data sources are listed. Stations with network code TI are from the TIPAGE deployment. Stations with network codes TP and AF have been deployed in the framework of the TIPTIMON project and the FH stations were deployed in the FERGANA program. All previously mentioned networks were deployed and operated under the aegis of groups from the GFZ and the instruments were provided by the Geophysical Instrument Pool Potsdam (GIPP). The network codes TJ, XJ and IU are permanents stations in Tajikistan, China and Afghanistan deployed and operated by locale geophysical surveys. Instrument abbreviations and corner periods are listed in table C.2.

Table C.1.: Station list

Station	Network	Instrument	Lat (°)	Lon(°)	Elevation (m)
AGA9	TI	40-T	39.38099	72.28013	3081
ALI8	TI	STS-2	37.79446	73.39701	3940
BAR8	TI	3-T	37.94210	71.45338	2092
BRC9	TI	3ESP	38.30934	72.47467	2663
BUL9	TI	3ESP	37.87693	72.88941	3906
CHU9	TI	40-T	39.17992	71.09527	1858
DKO8	TI	STS-2	39.55383	72.21785	2535
FRK9	TI	3ESP	37.39417	69.32940	461
ISH8	TI	3-T	36.68372	71.79457	2657
KAR9	TI	40-T	39.49321	71.75637	2323
KAW8	TI	L4-3D	39.07097	73.10701	4376
KAW9	TI	40-T	39.05101	73.11608	4442
KIK9	TI	3ESP	38.46850	70.82206	1804
KIR9	TI	40-T	40.02564	72.91926	1847
KOK8	TI	3-T	38.66214	72.84871	3722
KRG8	TI	L4-3D	37.45451	73.08261	4327
KSU9	TI	40-T	39.64314	72.66626	2821
LAN9	TI	40-T	37.03696	72.63419	2922
LEN9	TI	L4-3D	39.47919	72.91007	3630
MAD8	TI	L4-3D	38.15572	73.61028	3550
MIY8	TI	L4-3D	37.71806	72.37804	3175

Continued on next page ...

Table C.1 – continued from previous page

Station	Network	Instrument	Lat (°)	Lon(°)	Elevation (m)
NUR8	TI	STS-2	39.63936	73.85780	2960
P01	TI	40-T	40.41957	73.08028	1677
P02	TI	3ESP	40.31747	73.23361	2040
P03	TI	STS-2	40.17126	73.48503	1758
P04	TI	40-T	40.05566	73.54692	2013
P05	TI	3ESP	39.90567	73.40457	2421
P06	TI	40-T	39.73060	73.25200	3201
P07	TI	3ESP	39.69467	73.23574	3122
P08	TI	40-T	39.50692	73.26760	3482
P09	TI	40-T	39.37368	73.32629	4216
P10	TI	3ESP	39.27826	73.36456	4019
P11	TI	40-T	39.12706	73.53217	3947
P12	TI	3ESP	39.01496	73.56756	3950
P13	TI	3ESP	38.87089	73.50125	3982
P14	TI	40-T	38.70927	73.51652	4120
P15	TI	3ESP	38.56332	73.62463	4443
P16	TI	40-T	38.49299	73.86336	4007
P17	TI	3ESP	38.32936	74.02198	3778
P18	TI	40-T	38.14747	73.96265	3601
P19	TI	3ESP	38.01394	73.93971	3787
P20	TI	3ESP	37.93403	74.02339	3920
P21	TI	40-T	37.80282	74.21336	4290
P22	TI	3ESP	37.66653	74.17580	4106
P23	TI	3ESP	37.56242	74.15748	4176
P24	TI	3ESP	37.45907	74.16130	4280
PAS8	TI	L4-3D	38.87336	71.45415	2546
POI8	TI	L4-3D	38.65086	71.94102	2468
POI9	TI	3ESP	38.65522	71.97576	2476
RAJ8	TI	L4-3D	38.15103	71.94333	2277
RAN8	TI	3ESP	38.48109	74.37959	3815
SBD9	TI	L4-3D	37.85276	70.05899	2091
SHA8	TI	STS-2	37.53764	74.81990	3848
SHN9	TI	40-T	37.04139	71.51593	2743
TAB8	TI	L4-3D	37.23437	72.15613	3111
TOK9	TI	40-T	37.82750	74.64881	3827
VAN9	TI	40-T	38.33863	71.41936	1736
ZOR9	TI	3ESP	37.48012	73.73395	4189
F01	FH	3ESP	41.35862	72.23420	646
F02	FH	3ESP	41.60648	72.12083	910

Continued on next page ...

Table C.1 – continued from previous page

Station	Network	Instrument	Lat (°)	Lon(°)	Elevation (m)
F03	FH	3ESP	41.48158	71.59319	1445
F04	FH	3ESP	41.26156	72.46192	973
F05	FH	3ESP	41.10630	72.66737	849
F06	FH	3ESP	41.12521	73.31060	1372
F07	FH	3ESP	40.97075	73.04316	843
F08	FH	3ESP	41.39481	73.87935	1376
F09	FH	3ESP	41.09009	74.24146	2228
F10	FH	3ESP	40.86269	73.67527	1366
F11	FH	3ESP	40.63679	73.24698	1292
F12	FH	3ESP	40.04762	71.66057	1302
F13	FH	3ESP	40.00466	72.09252	1327
F14	FH	3ESP	40.20624	72.06648	1004
F15	FH	3ESP	40.43226	73.61598	2024
F16	FH	3ESP	40.56270	73.88638	1806
F17	FH	3ESP	41.62026	72.69147	972
F19	FH	3ESP	40.34251	72.61653	1116
F20	FH	3ESP	41.69641	73.32970	1507
F21	FH	3ESP	41.24247	72.98354	1011
F22	FH	3ESP	40.43084	74.08885	2046
AIN2	TP	Tri-120	39.38912	68.54383	1490
BAL2	TP	3ESP	38.30459	69.67062	971
BAR2	TP	3ESP	37.94210	71.45339	2091
CDA2	TP	3ESP	37.75668	69.83372	1061
FRK2	TP	3ESP	37.39438	69.30005	620
GAN2	TP	Tri-120	37.93341	68.59559	641
GCH2	TP	3ESP	37.19937	71.54546	2621
HOI2	TP	Tri-120	39.18008	70.88634	1653
ISH2	TP	3ESP	36.68377	71.79406	2661
JOR2	TP	3ESP	39.10065	70.59066	1557
KAL2	TP	3ESP	37.83819	69.09501	699
KHV2	TP	3ESP	38.38733	70.03655	1654
KID2	TP	3ESP	38.63666	69.49506	1739
KIK2	TP	3ESP	38.46849	70.82207	1811
KSM2	TP	3ESP	38.90668	69.93658	1604
PAN2	TP	3ESP	38.27524	70.57496	1141
PES2	TP	3ESP	38.60176	69.92249	1492
PIC2	TP	Tri-120	39.00646	69.35254	1844
QUM2	TP	3ESP	37.42958	68.68763	447
SBD2	TP	3ESP	37.85275	70.05899	2090

Continued on next page ...

Table C.1 – continued from previous page

Station	Network	Instrument	Lat (°)	Lon(°)	Elevation (m)
SHU2	TP	3ESP	38.01105	69.76023	695
SHP2	TP	Tri-120	38.84075	70.77992	1831
TAB2	TP	3ESP	37.23438	72.15613	3111
TAV2	TP	3ESP	38.67568	70.49674	1724
VAN2	TP	3ESP	38.37526	71.46708	1740
BAC2	TP	3ESP	38.31505	69.67270	938
HOT2	TP	Tri-120	39.18071	70.88660	1660
KSN2	TP	3ESP	38.90642	69.93552	1607
MAR2	TP	Tri-120	39.18675	68.72934	2071
SAN2	TP	3ESP	38.37819	70.13874	1580
BAC3	TP	3ESP	38.31497	69.67271	949
GUL3	TP	3ESP	38.66300	69.51306	1928
PES3	TP	3ESP	38.60197	69.92270	1493
VIS3	TP	Tri-120	38.89579	69.27805	1522
PAJ3	AF	L4-3D	35.42595	69.72396	2260
SEB3	AF	L4-3D	37.31092	70.16776	1728
JUR3	AF	L4-3D	36.87128	70.83173	1561
KEM3	AF	L4-3D	36.02038	70.67809	2551
YAM3	AF	L4-3D	36.52016	70.80148	1853
FIA3	AF	L4-3D	37.10986	70.57675	1477
AEG3	AF	L4-3D	37.30903	70.92823	2541
ZEB3	AF	L4-3D	36.527	71.34221	2615
CHDR	TJ	Tri-40	40.3867	69.67099	580
CHGR	TJ	Tri-40	38.65689	69.1582	1049
DUSH	TJ	Tri-40	38.5688	68.7810	786
GARM	TJ	Tri-40	39.00637	70.31662	1336
GEZN	TJ	Tri-40	39.2833	67.7154	1485
IGRN	TJ	Tri-40	38.2203	69.3266	1284
MANE	TJ	Tri-40	37.54238	71.68008	2312
SHAA	TJ	Tri-40	37.562	68.1228	868
ATS	XJ	3ESP	39.804	75.844	1815
BPM	XJ	3ESP	39.883	76.836	1325
JG	XJ	40T	39.82	74.10	2693
KSH	XJ	CTS-1V	39.145	75.566	1523
KSZ	XJ	3ESP	39.591	75.941	1582
MJ	XJ	40T	39.00	74.43	3468
TAG	XJ	3ESP	37.7799	75.1699	3282
WUQ	XJ	3ESP	39.73970	75.23810	2206
YJS	XJ	3ESP	38.521	76.486	1603

Continued on next page ...

Table C.1 – continued from previous page

Station	Network	Instrument	Lat (°)	Lon(°)	Elevation (m)
YPH	XJ	FSS-3BDH	39.209	76.737	1189
KBL	IU	STS-2	34.5408	69.0432	1913

Table C.2.: Instrument abbreviations and corner periods

abbreviations	instrument	corner period
L4-3D	Mark L4-3D short period	1 s
40T	Güralp CMG-40T broadband	30 s
3ESP	Güralp CMG-3ESP broadband	100 s
STS-2	Streckeisen STS-2 broadband	120 s
Tri40/Tri120	Nanometrics broadband	40 s / 120 s
FSS-3DBH	Chinese manufacturer, short period borehole seismometer	2 s
CTS-1V	Chinese manufacturer, broadband	120 s

Bibliography

Abdrakhmatov, K. Y., Aldazhanov, S. A., Hager, B. H., Hamburger, M. W., Herring, T. A., Kalabaev, K. B., Makarov, V. I., Molnar, P., Panasyuk, S. V., Prilepin, M. T., Reilinger, R. E., Sadybakasov, I. S., Souter, B. J., Trapeznikov, Y. A., Tsurkov, V. Y., Zubovich, A. V., 1996. Relatively recent construction of the Tien Shan inferred from GPS measurements of present-day crustal deformation rates. Nature 384 (6608), 450–453.

Abe, Y., Ohkura, T., Hirahara, K., Shibutani, T., Jun. 2011. Common-conversion-point stacking of receiver functions for estimating the geometry of dipping interfaces. Geophys. J. Int. 185 (3), 1305–1311.

Abers, G., Bryan, C., Roecker, S., McCaffrey, R., Feb. 1988. Thrusting of the Hindu Kush over the Southeastern Tadjik Basin, Afghanistan: Evidence from two large earthquakes. Tectonics 7 (1), 41–56.

Aitchison, J. C., Ali, J. R., Davis, A. M., May 2007. When and where did India and Asia collide? J. Geophys. Res. 112 (B5).

Ali, J. R., Aitchison, J. C., Oct. 2005. Greater India. Earth-Science Reviews 72 (3–4), 169–188.

Ali, J. R., Aitchison, J. C., Jul. 2012. Comment on "Restoration of Cenozoic deformation in Asia and the size of Greater India" by D. J. J. van Hinsbergen et al. Tectonics 31 (4).

Beloussov, V. V., Belyaevsky, N. A., Borisov, A. A., Volvovsky, B. S., Volkovsky, I. S., Resvoy, D. P., Tal-Virsky, B. B., Khamrabaev, I. K., Kaila, K. L., Narain, H., Marussi, A., Finetti, J., 1980. Structure of the lithosphere along the deep seismic sounding profile: Tien Shan–Pamirs–Karakorum–Himalayas. Tectonophysics 70 (3-4), 193 – 221.

Billington, S., Isacks, B. L., Barazangi, M., 1977. Spatial distribution and focal mechanisms of mantle earthquakes in the Hindu Kush-Pamir region: A contorted Benioff zone. Geology 5 (11), 699–704.

Buland, R., Chapman, C. H., Oct. 1983. The computation of seismic travel times. B. Seismol. Soc. Am. 73 (5), 1271–1302.

Burtman, V. S., Molnar, P., Jan. 1993. Geological and geophysical evidence for deep subduction of continental crust beneath the Pamir. Spec. Pap. Geol. Soc. Am. 281.

Chatelain, J. L., Roecker, S. W., Hatzfeld, D., Molnar, P., Mar. 1980. Microearthquake seismicity and fault plane solutions in the Hindu Kush Region and their tectonic implications. Journal of Geophysical Research: Solid Earth 85 (B3), 1365–1387.

Chopin, C., May 1984. Coesite and pure pyrope in high-grade blueschists of the Western Alps: a first record and some consequences. Contrib. Mineral. Petr. 86 (2), 107–118.

Coutand, I., Strecker, M. R., Arrowsmith, J. R., Hilley, G., Thiede, R. C., Korjenkov, A., Omuraliev, M., Dec. 2002. Late Cenozoic tectonic development of the intramontane Alai Valley, (Pamir-Tien Shan region, central Asia): An example of intracontinental deformation due to the Indo-Eurasia collision. Tectonics 21 (6), 1053.

Cowgill, E., 2010. Cenozoic right-slip faulting along the eastern margin of the Pamir salient, northwestern China. Geol. Soc. Am. Bull. 122 (1-2), 145–161.

Crotwell, H. P., Owens, T. J., Ritsema, J., Mar. 1999. The TauP Toolkit: Flexible Seismic Travel-time and Ray-path Utilities. Seismological Research Letters 70 (2), 154–160.

Currie, C. A., Huismans, R. S., Beaumont, C., 2008. Thinning of continental backarc lithosphere by flow-induced gravitational instability. Earth and Planetary Science Letters 269 (3–4), 436–447.

Deuss, A., Woodhouse, J. H., Apr. 2002. A systematic search for mantle discontinuities using SS-precursors. Geophysical Research Letters 29 (8), 90–1.

Ding, L., 2005. Paleocene–Eocene record of ophiolite obduction and initial India-Asia collision, south central Tibet. Tectonics 24 (3).

Duchkov, A., Shvartsman, Y., Sokolova, L., 2001. Deep heat flow in the Tien Shan: Advances and drawbacks. Geologiya i Geofizika 42 (10), 1516–1531.

Engdahl, E. R., Hilst, R. v. d., Buland, R., Jun. 1998. Global teleseismic earthquake relocation with improved travel times and procedures for depth determination. Bulletin of the Seismological Society of America 88 (3), 722–743.

Fan, G., Ni, J. F., Wallace, T. C., 1994. Active tectonics of the Pamirs and Karakorum. J. Geophys. Res. 99, 7131–7160.

Finlay, C. C., Maus, S., Beggan, C. D., Bondar, T. N., Chambodut, A., Chernova, T. A., Chulliat, A., Golovkov, V. P., Hamilton, B., Hamoudi, M., Holme, R., Hulot, G., Kuang, W., Langlais, B., Lesur, V., Lowes, F. J., Lühr, H., Macmillan, S., Mandea, M., McLean, S., Manoj, C., Menvielle, M., Michaelis, I., Olsen, N., Rauberg, J., Rother, M., Sabaka, T. J., Tangborn, A., Tøffner-Clausen, L., Thébault, E., Thomson, A. W. P., Wardinski, I., Wei, Z., Zvereva, T. I., 2010. International Geomagnetic Reference Field: the eleventh generation. Geophys. J. Int. 183 (3), 1216–1230.

Frederiksen, A. W., Bostock, M. G., 2000. Modelling teleseismic waves in dipping anisotropic structures. Geophys. J. Int. 141 (2), 401–412.

Fuchs, K., Müller, G., Sep. 1971. Computation of Synthetic Seismograms with the Reflectivity Method and Comparison with Observations. Geophysical Journal International 23 (4), 417–433.

Gubbins, D., 2004. Time Series Analysis and Inverse Theory for Geophysicists. Cambridge University Press.

Gung, Y., Panning, M., Romanowicz, B., Apr. 2003. Global anisotropy and the thickness of continents. Nature 422 (6933), 707–711.

Haberland, C., Abdybachaev, U., Schurr, B., Wetzel, H., Roessner, S., Sarnagoev, A., Orunbaev, S., Janssen, C., May 2011. Landslides in southern Kyrgyzstan: Understanding tectonic controls. Eos, Trans. Am. Geophys. Union 92 (20), PAGE 169.

Hacker, B., Luffi, P., Lutkov, V., Minaev, V. T., Ratschbacher, L., Plank, T., Ducea, M. N., Patino-Douce, A., McWilliams, M., Metcalf, J., 2005. Near-Ultrahigh Pressure Processing of Continental Crust: Miocene Crustal Xenoliths from the Pamir. J. Petrol. 46 (8), 1661–1687.

Hacker, B. R., Wallis, S. R., Ratschbacher, L., Grove, M., Gehrels, G., 2006. High-temperature geochronology constraints on the tectonic history and architecture of the ultrahigh-pressure Dabie-Sulu Orogen. Tectonics 25 (5).

Haines, S. S., Klemperer, S. L., Brown, L., Guo, J., Mechie, J., Meissner, R., Ross, A., Zhao, W., Jan. 2003. INDEPTH III seismic data: From surface observations to deep crustal processes in Tibet. Tectonics 22, 18 PP.

Hamburger, M. W., Sarewitz, D. R., Pavlis, T. L., Popandopulo, G. A., 1992. Structural and seismic evidence for intracontinental subduction in the Peter the First Range, Central Asia. Geol. Soc. Am. Bull. 104 (4), 397–408.

Hetényi, G., Cattin, R., Brunet, F., Bollinger, L., Vergne, J., Nábělek, J. L., Diament, M., Dec. 2007. Density distribution of the India plate beneath the Tibetan plateau: Geophysical and petrological constraints on the kinetics of lower-crustal eclogitization. Earth and Planetary Science Letters 264 (1–2), 226–244.

Ischuk, A., Bendick, R., Rybin, A., Molnar, P., Khan, S. F., Kuzikov, S., Mohadjer, S., Saydullaev, U., Ilyasova, Z., Schelochkov, G., Zubovich, A. V., 2013. Kinematics of the Pamir and Hindu Kush regions from GPS geodesy. Journal of Geophysical Research: Solid Earth 118 (5), 2408–2416.

Kanasewich, E. R., 1983. Time sequence analysis in geophysics., 3rd Edition. Vol. 11. The University of Alberta Press, Edmonton, Alberta.

Kawakatsu, H., Watada, S., Jun. 2007. Seismic Evidence for Deep-Water Transportation in the Mantle. Science 316 (5830), 1468 –1471.

Kennett, B. L. N., Jan. 1991. The removal of free surface interactions from three-component seismograms. Geophys. J. Int. 104 (1), 153–163.

Kennett, B. L. N., Engdahl, E. R., 1991. Traveltimes for global earthquake location and phase identification. Geophys. J. Int. 105 (2), 429–465.

Kind, R., 1985. The reflectivity method for different source and receiver structures and comparison with GRF data. J. Geophys. 58, 146–152.

Kind, R., Yuan, X., Sep. 2010. Seismic Images of the Biggest Crash on Earth. Science 329 (5998), 1479–1480.

Kind, R., Yuan, X., Kumar, P., Apr. 2012. Seismic receiver functions and the lithosphere–asthenosphere boundary. Tectonophysics 536–537, 25–43.

Kind, R., Yuan, X., Saul, J., Nelson, D., Sobolev, S. V., Mechie, J., Zhao, W., Kosarev, G., Ni, J., Achauer, U., Jiang, M., 2002. Seismic Images of Crust and Upper Mantle Beneath Tibet: Evidence for Eurasian Plate Subduction. Science 298 (5596), 1219–1221.

Koulakov, I., Sobolev, S. V., 2006. A tomographic image of Indian lithosphere break-off beneath the Pamir-Hindukush region. Geophys. J. Int. 164 (2), 425–440.

Krystopowicz, N. J., Currie, C. A., Jan. 2013. Crustal eclogitization and lithosphere delamination in orogens. Earth Planet. Sci. Lett. 361, 195–207.

Kufner, S., Schurr, B., Yuan, X., Schneider, F., Ischuk, A., Murodkulov, S., Bianchi, M., Haberland, C. A., Sippl, C., Mechie, J., Dec. 2013. Evidence for deeply subducting Asian lithosphere beneath the Pamir-Hindu Kush region from teleseismic tomography. AGU Fall Meeting Abstracts.

Kulagina, M., Lukk, A. A., Kulagin, B., 1974. Block structure of the earth's crust of Tadjikstan. In: Searches for precursors of earthquakes in prediction polygons. Nauka, Moscow, Russian Federation (RUS), pp. 70–84.

Kumar, P., Kind, R., Yuan, X., 2010. Receiver function summation without deconvolution. Geophysical Journal International 180 (3), 1223–1230.

Kumar, P., Yuan, X., Kind, R., Kosarev, G. L., Apr. 2005. The lithosphere-asthenosphere boundary in the Tien Shan-Karakoram region from S receiver functions: Evidence for continental subduction. Geophys. Res. Lett. 32.

Lacassin, R., Valli, F., Arnaud, N., Leloup, P., Paquette, J. L., Haibing, L., Tapponnier, P., Chevalier, M., Guillot, S., Maheo, G., Zhiqin, X., Mar. 2004. Large-scale geometry, offset and kinematic evolution of the Karakorum fault, Tibet. Earth Planet. Sci. Lett. 219 (3–4), 255–269.

Leith, W., Alvarez, W., Jul. 1985. Structure of the Vakhsh fold-and-thrust belt, Tadjik SSR: Geologic mapping on a Landsat image base. Geological Society of America Bulletin 96 (7), 875–885.

Li, C., van der Hilst, R. D., Meltzer, A. S., Engdahl, E. R., Sep. 2008. Subduction of the Indian lithosphere beneath the Tibetan Plateau and Burma. Earth and Planetary Science Letters 274 (1–2), 157–168.

Li, X., Yuan, X., 2003. Receiver functions in northeast China - implications for slab penetration into the lower mantle in northwest Pacific subduction zone. Earth Planet. Sci. Lett. 216 (4), 679 – 691.

Mechie, J., Yuan, X., Schurr, B., Schneider, F., Sippl, C., Ratschbacher, L., Minaev, V., Gadoev, M., Oimahmadov, I., Abdybachaev, U., Moldobekov, B., Orunbaev, S., Negmatullaev, S., Feb. 2012. Crustal and uppermost mantle velocity structure along a profile across the Pamir and southern Tien Shan as derived from project TIPAGE wide-angle seismic data. Geophys. J. Int. 188 (2), 385–407.

Mohadjer, S., Bendick, R., Ischuk, A., Kuzikov, S., Kostuk, A., Saydullaev, U., Lodi, S., Kakar, D. M., Wasy, A., Khan, M. A., Molnar, P., Bilham, R., Zubovich, A. V., Feb. 2010. Partitioning of India-Eurasia convergence in the Pamir-Hindu Kush from GPS measurements. Geophys. Res. Lett. 37 (4), L04305.

Mohsen, A., Hofstetter, R., Bock, G., Kind, R., Weber, M., Wylegalla, K., Rümpker, G., Group, t. D., 2005. A receiver function study across the Dead Sea Transform. Geophysical Journal International 160 (3), 948–960.

Molnar, P., Gray, D., Jan. 1979. Subduction of continental lithosphere: Some constraints and uncertainties. Geology 7 (1), 58 –62.

Molnar, P., Tapponnier, P., Aug. 1975. Cenozoic Tectonics of Asia: Effects of a Continental Collision Features of recent continental tectonics in Asia can be interpreted as results of the India-Eurasia collision. Science 189 (4201), 419–426.

Negredo, A. M., Replumaz, A., Villaseñor, A., Guillot, S., Jul. 2007. Modeling the evolution of continental subduction processes in the Pamir–Hindu Kush region. Earth Planet. Sci. Lett. 259 (1-2), 212–225.

Nábělek, J., Hetényi, G., Vergne, J., Sapkota, S., Kafle, B., Jiang, M., Su, H., Chen, J., Huang, B., Team, t. H., Sep. 2009. Underplating in the Himalaya-Tibet Collision Zone Revealed by the Hi-CLIMB Experiment. Science 325 (5946), 1371–1374, PMID: 19745147.

Okay, A., Shutong, X., Sengor, A. M. C., 1989. Coesite from the Dabie Shan eclogites, central China. Eur. J. Mineral. 1, 595–598.

Pandey, S., 2013. High resolution 3D Rayleigh wave velocity model of China and surrounding area. Dissertation. Freie Universität Berlin, Germany.

Patriat, P., Achache, J., 1984. India–Eurasia collision chronology has implications for crustal shortening and driving mechanism of plates. Nature 311 (5987), 615–621.

Pavlis, G. L., Das, S., 2000. The Pamir-Hindu Kush seismic zone as a strain marker for flow in the upper mantle. Tectonics 19 (1), 103–115.

Pegler, G., Das, S., 1998. An enhanced image of the Pamir-Hindu Kush seismic zone from relocated earthquake hypocentres. Geophys. J. Int. 134 (2), 573–595.

Priestley, K., Debayle, E., McKenzie, D., Pilidou, S., Oct. 2006. Upper mantle structure of eastern Asia from multimode surface waveform tomography. Journal of Geophysical Research: Solid Earth 111 (B10), B10304.

Priestley, K., Jackson, J., McKenzie, D., Jan. 2008. Lithospheric structure and deep earthquakes beneath India, the Himalaya and southern Tibet. Geophysical Journal International 172 (1), 345–362.

Reigber, C., Michel, G., Galas, R., Angermann, D., Klotz, J., Chen, J., Papschev, A., Arslanov, R., Tzurkov, V., Ishanov, M., Aug. 2001. New space geodetic constraints on the distribution of deformation in Central Asia. Earth Planet. Sci. Lett. 191 (1–2), 157–165.

Robinson, A. C., Ducea, M., Lapen, T. J., Apr. 2012. Detrital zircon and isotopic constraints on the crustal architecture and tectonic evolution of the northeastern Pamir. Tectonics 31 (2), TC2016.

Robinson, A. C., Yin, A., Manning, C. E., Harrison, T. M., Zhang, S., Wang, X., 2004. Tectonic evolution of the northeastern Pamir: Constraints from the northern portion of the Cenozoic Kongur Shan extensional system, western China. Geol. Soc. Am. Bull. 116 (7-8), 953–973.

Roecker, S. W., 1982. Velocity Structure of the Pamir-Hindu Kush region: possible evidence of subducted crust. J. Geophys. Res. 87, 945–959.

Sass, P., 2013. Magnetotellurische Untersuchung der kontinentalen Kollisionszone im Pamir und Tian Shan, Zentralasien. Dissertation. Freie Universität Berlin, Germany.

Sass, P., Ritter, O., Ratschbacher, L., Matiukov, V. E., Rybin, A. K., Batalev, V. Y., in press. Resistivity structure underneath the Pamir and Southern Tian Shan. Geophys. J. Int.

Saul, J., Kumar, M. R., Sarkar, D., Aug. 2000. Lithospheric and upper mantle structure of the Indian Shield, from teleseismic receiver functions. Geophys. Res. Lett. 27 (16), 2357–2360.

Schmidt, J., Hacker, B. R., Ratschbacher, L., Stübner, K., Stearns, M., Kylander-Clark, A., Cottle, J. M., Alexander, A., Webb, G., Gehrels, G., Minaev, V., Dec. 2011. Cenozoic deep crust in the Pamir. Earth Planet. Sci. Lett. 312 (3-4), 411–421.

Schneider, F. M., Yuan, X., Schurr, B., Mechie, J., Sippl, C., Haberland, C., Minaev, V., Oimahmadov, I., Gadoev, M., Radjabov, N., Abdybachaev, U., Orunbaev, S., Negmatullaev, S., Aug. 2013. Seismic imaging of subducting continental lower crust beneath the Pamir. Earth and Planetary Science Letters 375, 101–112.

Schurr, B., Sippl, C., Yuan, X., Mechie, J., Lothar, R., Apr. 2013. Seismotectonics of the Pamir. In: EGU General Assembly Conference Abstracts. Vol. 15. p. 13663.

Schwab, M., Ratschbacher, L., Siebel, W., McWilliams, M., Minaev, V., Lutkov, V., Chen, F., Stanek, K., Nelson, B., Frisch, W., Wooden, J. L., Jul. 2004. Assembly of the Pamirs: Age and origin of magmatic belts from the southern Tien Shan to the southern Pamirs and their relation to Tibet. Tectonics 23, 31 PP.

Sclater, J. G., Jaupart, C., Galson, D., Feb. 1980. The heat flow through oceanic and continental crust and the heat loss of the Earth. Reviews of Geophysics 18 (1), 269–311.

Searle, M. P., 1996. Geological evidence against large-scale pre-Holocene offsets along the Karakoram Fault: Implications for the limited extrusion of the Tibetan plateau. Tectonics 15 (1), PP. 171–186.

Searle, M. P., Noble, S. R., Cottle, J. M., Waters, D. J., Mitchell, A. H. G., Hlaing, T., Horstwood, M. S. A., Jun. 2007. Tectonic evolution of the Mogok metamorphic belt, Burma (Myanmar) constrained by U-Th-Pb dating of metamorphic and magmatic rocks. Tectonics 26 (3), TC3014.

Shibutani, T., Sambridge, M., Kennett, B., 1996. Genetic algorithm inversion for receiver functions with application to crust and uppermost mantle structure beneath eastern Australia. Geophys. Res. Lett. 23 (14), 1829–1832.

Sippl, C., 2012. Shallow and deep structure of the Pamir-Hindu Kush region from local seismic data. Dissertation. Freie Universität Berlin, Germany.

Sippl, C., Schurr, B., Tympel, J., Angiboust, S., Mechie, J., Yuan, X., Schneider, F. M., Sobolev, S. V., Ratschbacher, L., Haberland, C., Dec. 2013a. Deep burial of Asian continental crust beneath the Pamir imaged with local earthquake tomography. Earth and Planetary Science Letters 384, 165–177.

Sippl, C., Schurr, B., Yuan, X., Mechie, J., Schneider, F. M., Gadoev, M., Orunbaev, S., Oimahmadov, I., Haberland, C., Abdybachaev, U., Minaev, V., Negmatullaev, S., Radjabov, N., 2013b. Geometry of the Pamir-Hindu Kush intermediate-depth earthquake zone from local seismic data. J. Geophys. Res. 118 (4), 1438–1457.

Smith, W. H. F., Wessel, P., Mar. 1990. Gridding with continuous curvature splines in tension. Geophysics 55 (3), 293–305.

Sobel, E. R., Chen, J., Schoenbohm, L. M., Thiede, R., Stockli, D. F., Sudo, M., Strecker, M. R., Feb. 2013. Oceanic-style subduction controls late Cenozoic deformation of the Northern Pamir orogen. Earth Planet. Sci. Lett. 363, 204–218.

Sobel, E. R., Dumitru, T. A., Mar. 1997. Thrusting and exhumation around the margins of the western Tarim basin during the India-Asia collision. Journal of Geophysical Research: Solid Earth 102 (B3), 5043–5063.

Sobel, E. R., Schoenbohm, L. M., Chen, J., Thiede, R., Stockli, D. F., Sudo, M., Strecker, M. R., Apr. 2011. Late Miocene–Pliocene deceleration of dextral slip between Pamir and Tarim: Implications for Pamir orogenesis. Earth Planet. Sci. Lett. 304 (3–4), 369–378.

Stammler, K., 1992. Ein Beitrag zur Untersuchung des oberen Erdmantels mithilfe von PS Konversionsphasen. PhD thesis, Friedrich-Alexander-Universität Erlangen Nürnberg.

Stammler, K., Feb. 1993. Seismichandler—Programmable multichannel data handler for interactive and automatic processing of seismological analyses. Comput. Geosci. 19 (2), 135–140.

Steffen, R., Steffen, H., Jentzsch, G., Oct. 2011. A three-dimensional Moho depth model for the Tien Shan from EGM2008 gravity data. Tectonics 30, 19 PP.

Strecker, M. R., Hilley, G. E., Arrowsmith, J. R., Coutand, I., Feb. 2003. Differential structural and geomorphic mountain-front evolution in an active continental collision zone: The northwest Pamir, southern Kyrgyzstan. Geological Society of America Bulletin 115 (2), 166–181.

Stübner, K., Ratschbacher, L., Rutte, D., Stanek, K., Minaev, V., Wiesinger, M., Gloaguen, R., members, P. T., 2013a. The giant Shakhdara migmatitic gneiss dome, Pamir, India-Asia collision zone: 1. Geometry and kinematics. Tectonics 32 (4), 948–979.

Stübner, K., Ratschbacher, L., Weise, C., Chow, J., Hofmann, J., Khan, J., Rutte, D., Sperner, B., Pfänder, J. A., Hacker, B. R., Dunkl, I., Tichomirowa, M., Stearns, M. A., Members, P. T., 2013b. The giant Shakhdara migmatitic gneiss dome, Pamir, India-Asia collision zone: 2. Timing of dome formation. Tectonics 32 (5), 1404–1431.

Svenningsen, L., Jacobsen, B. H., 2007. Absolute S-velocity estimation from receiver functions. Geophysical Journal International 170 (3), 1089–1094.

Thomas, J., Chauvin, A., Gapais, D., Bazhenov, M. L., Perroud, H., Cobbold, P. R., Burtman, V. S., 1994. Paleomagnetic evidence for Cenozoic block rotations in the Tadjik depression (Central Asia). J. Geophys. Res. 99 (B8), 160.

Thomas, J., Perroud, H., Cobbold, P. R., Bazhenov, M. L., Burtman, V. S., Chauvin, A., Sadybakasov, E., 1993. A Paleomagnetic Study of Tertiary Formations From the Kyrgyz Tien-Shan and Its Tectonic Implications. J. Geophys. Res. 98 (B6), 9571–9589.

Tilmann, F., Ni, J., INDEPTH III Seismic Team, May 2003. Seismic Imaging of the Downwelling Indian Lithosphere Beneath Central Tibet. Science 300 (5624), 1424–1427, PMID: 12775838.

van Hinsbergen, D. J. J., Lippert, P. C., Dupont-Nivet, G., Kapp, P., DeCelles, P. G., Torsvik, T. H., Jul. 2012a. Reply to comment by Ali and Aitchison on "Restoration of Cenozoic deformation in Asia, and the size of Greater India". Tectonics 31 (4), TC4007.

van Hinsbergen, D. J. J., Lippert, P. C., Dupont-Nivet, G., McQuarrie, N., Doubrovine, P. V., Spakman, W., Torsvik, T. H., May 2012b. Greater India Basin hypothesis and a two-stage Cenozoic collision between India and Asia. Proc. Natl. Acad. Sci. U. S. A. 109 (20), 7659–7664.

van Hinsbergen, D. J. J., Steinberger, B., Doubrovine, P. V., Gassmöller, R., Jun. 2011. Acceleration and deceleration of India-Asia convergence since the Cretaceous: Roles of mantle plumes and continental collision. J. Geophys. Res. 116 (B6).

Vinnik, L., Kato, M., Kawakatsu, H., Sep. 2001. Search for seismic discontinuities in the lower mantle. Geophysical Journal International 147 (1), 41–56.

Wessel, P., Smith, W. H. F., Nov. 1998. New, improved version of generic mapping tools released. Eos, Transactions American Geophysical Union 79 (47), 579–579.

Wiens, D. A., Stein, S., Aug. 1983. Age dependence of oceanic intraplate seismicity and implications for lithospheric evolution. Journal of Geophysical Research: Solid Earth 88 (B8), 6455–6468.

Yang, S., Li, J., Wang, Q., 2008. The deformation pattern and fault rate in the Tianshan Mountains inferred from GPS observations. Sci. China Ser. D 51 (8), 1064–1080.

Yin, A., Harrison, T. M., 2000. Geologic Evolution of the Himalayan-Tibetan Orogen. Annu. Rev. Earth Pl. Sc. 28 (1), 211–280.

Yuan, X., Kind, R., Li, X., Wang, R., 2006. The S receiver functions: synthetics and data example. Geophys. J. Int. 165 (2), 555–564.

Yuan, X., Sobolev, S. V., Kind, R., Oncken, O., Bock, G., Asch, G., Schurr, B., Graeber, F., Rudloff, A., Hanka, W., Wylegalla, K., Tibi, R., Haberland, C., Rietbrock, A., Giese, P., Wigger, P., R|[ouml]|wer, P., Zandt, G., Beck, S., Wallace, T., Pardo, M., Comte, D., Dec. 2000. Subduction and collision processes in the Central Andes constrained by converted seismic phases. Nature 408 (6815), 958–961.

Zhu, L. P., Kanamori, H., Feb. 2000. Moho depth variation in southern California from teleseismic receiver functions. J. Geophys. Res. 105 (B2), 2969–2980.

Zoeppritz, K., 1919. Über Reflexion und Durchgang seismischer Wellen durch Unstetigkeitsflächen. Nachrichten der Königlichen Gesellschaft der Wissenschaften zu Göttingen. Mathematisch-Physikalische Klasse., 66–84.

Zubovich, A. V., Wang, X.-q., Scherba, Y. G., Schelochkov, G. G., Reilinger, R., Reigber, C., Mosienko, O. I., Molnar, P., Michajljow, W., Makarov, V. I., Li, J., Kuzikov, S. I., Herring, T. A., Hamburger, M. W., Hager, B. H., Dang, Y.-m., Bragin, V. D., Beisenbaev, R. T., Dec. 2010. GPS velocity field for the Tien Shan and surrounding regions. Tectonics 29, 23 PP.

Acknowledgement

First, I would like to thank Xiaohui Yuan, my adviser and mentor through the years while working on this thesis. He provided great help and support in various ways. He always had an open door for discussions and shared all his knowledge and code that was used and complemented with own scripts for the data analysis. I am moreover grateful for the nice and amicable relation that we share.

I thank my Doktorvater Rainer Kind, whose enthusiasm is inspiring and who will always be a great example for me as a thoughtful and generous chief, who creates a very pleasant and motivating working atmosphere. I enjoyed very much the hospitality of Rainer and his wife at the summer parties in their garden.

I thank Frederik Tilmann head of the seismology section for giving me the opportunity to fulfill this thesis in his group, to organize scientific dialogue within the group in section meetings and for acting as referee for this thesis. His comments on the manuscripts for this thesis as well as for our article published in EPSL were very helpful.

All previously mentioned are thanked for giving me the opportunity to take part on several field campaigns in Tajikistan, Chile, Spain and Madagascar. This work gave me lots of experiences and unforgettable memories. Moreover I thank for the support to travel to several conferences as EGU, AGU, DGG and AG-Seismologie meetings and the Adam Dziewonski symposium.

The seismology colleagues from the TIPAGE and TIPTIMON projects Christian Sippl, Xiaohui Yuan, Bernd Schurr, Jim Mechie and Sofia Kufner are thanked for the good cooperation in data collection in the field as well as in interpreting, presenting and publishing our results. To come to the final steps various meetings and discussions were needed that were always held in a cooperative, productive and pleasant atmosphere. I thank all principle investigators of the TIPAGE project for doing the job of applying the grants from DFG and GFZ.

Our colleagues in Tajikistan and Kyrgyzstan from the Institute of Geology, Earthquake Engineering and Seismology and the CIAIAG are thanked for the good cooperation. Without them, the data collection would have been impossible. I would like to mention here the scientists that I have met personally during the field campaigns: Ilhomjom Oimamahdof, Mustafo Gadoev, Vlad Minaev and Negmat Radjabov. My thanks also goes to all others who did a great job for the data aquisition in the TIPAGE and TIPTIMON projects.

I thank the doctoral candidates and doctors from the TIPAGE and TIPTIMON projects at the GFZ, Christian Sippl, Jens Tympel, Paul Saß, Sarah Schröder, Sofia Kufner and Walja Korolevsk, for the scientific and non-scientific dialogue and exchange of ideas. I also thank all TIPAGE associated scientists for fruitful discussions and Prof. Lothar Ratschbacher from TU Freiberg for his enthusiasm and his stimulation of interdisciplinary dialogue.

The GIPP Potsdam is thanked for providing the instruments. The work was done with financial support of DFG and GFZ.

Special thanks goes to my colleagues Amerika Manzanares, Ben Heit, Frederik Tilmann, Forough Sodoudi, Günter Asch, Joachim Saul, Liane Lauterjung, Mauro Palo, Martina Gassenmeier, Muzli, Peter Gaebler, Rainer Kind, Shantanu Pandey, Suleyman Dundar, Tom Richter, Tuna Eken and Xiaohui Yuan and all other colleagues from the seismology section for the nice atmosphere at work. Especially I thank Tom for the good times in- and outside of the office that we shared.

Sebastian Brandstetter, Anja Schäfer, Frederik Tilmann, Christian Sippl and Alexander Schäfer are thanked for corrections and comments on the manuscript of this thesis.

Great thank goes to my beloved partner Anja Schäfer, my best friend Sebastian Brandstetter, all my friends as well as to my parents Gertrud and Hans-Hermann and my brother Arno Heinrich for their love and mental support during all the years.

Erklärung

Hiermit versichere ich, dass es sich bei der vorliegenden Dissertation um meine eigenständig erbrachte Leistung handelt. Insbesondere beinhaltet dies die folgenden Punkte:

- Ich habe mich keiner unzulässigen Hilfe Dritter bedient und keine andere als die angegebene Literatur benutzt.
- Die Stellen der Arbeit, die anderen Werken wörtlich oder inhaltlich entnommen sind, wurden durch entsprechende Angaben der Quellen kenntlich gemacht.
- Diese Arbeit hat in gleicher oder ähnlicher Form noch keiner Prüfungsbehörde vorgelegen.

Berlin, Mai 2014

Curriculum Vitae

For reasons of data protection,
the curriculum vitae is not included in the online version